The Pennsylvania State University
The Graduate School
Eberly College of Science

EXPLORING THE COSMIC RAY SPECTRUM WITH THE CREAM EXPERIMENT

A Dissertation in
Physics
by
Tyler B. Anderson

Submitted in Partial Fulfillment
of the Requirements
for the Degree of

Doctor of Philosophy

December 2013

The dissertation of Tyler B. Anderson was reviewed and approved* by the following:

Stephane Coutu
Professor of Physics, Astronomy and Astrophysics
Dissertation Adviser, Chair of Committee

Tyce DeYoung
Associate Professor of Physics

Miguel Mostafá
Associate Professor of Physics

Jane Charlton
Professor of Astronomy and Astrophysics

Nitin Samarth
Professor of Physics
Head of the Department of Physics

*Signatures are on file in the Graduate School.

Abstract

The Cosmic Ray Energetics and Mass (CREAM) project endeavors to resolve the cosmic-ray spectrum in an energy range between 10^{10} and 10^{15} eV for all particles with charges in the range $Z = 1$ (hydrogen) to $Z = 26$ (iron). From 2004 to 2011, the CREAM instrument was flown in a succession of long-duration balloon (LDB) missions over the Antarctic continent. To date, it has completed six successful campaigns, for a cumulative 161 days in flight.

Starting in 2011, CREAM began a process of reconfiguration in order to prepare for ISS-CREAM—a three-year mission bound for the International Space Station in 2014. In addition, a subset of detectors from CREAM's balloon flights have been upgraded and reassembled for the Boron And Carbon Cosmic rays in the Upper Stratosphere (BACCUS) mission, which will mount a new LDB campaign during the 2013–2014 Antarctic summer season.

The CREAM project is presented, with a special emphasis on the design, construction, and performance of CREAM's (and BACCUS') Timing Charge Detector (TCD) and ISS-CREAM's Boronated Scintillator Detector (BSD), two instruments originating from the CREAM group at the Pennsylvania State University. Several new endeavors will be described, including the results of the TCD's charge calibration using data from CREAM's fourth flight; a set of newly commissioned readout electronics for CREAM's BACCUS mission; and the results of a 2012 beam test of a prototype version of the ISS-CREAM BSD.

Table of Contents

List of Figures

List of Tables

Acknowledgments

Much of the credit for my professional development goes to the influence and mentorship provided by my thesis advisor, Professor Stephane Coutu. His combination of scientific and technical prowess, personability, ease in communication and quick wit are just a few of the rare qualities I have come to admire in him. Stephane, the lessons you've taught me have been invaluable, and the whole experience of working in your group has been excellent. Thank you.

I would also like to express my appreciation to the collaborators with whom I have worked closely. Professor Scott Nutter taught me much about building and characterizing plastic scintillator systems, and he has also given generously of his time and talent to develop my skills in analyzing data and constructing GEANT4 monte carlo simulations. I have had the pleasure of working with several individuals from NASA Goddard Space Flight Center, notably Dr. John Mitchell and Dr. Jason Link, from whom I have learned a great deal about experimental methods in physics and have enjoyed very fruitful collaboration on the development of the Boronated Scintillator Detector. I am also grateful to Professor James Beatty for the support he provided in working on the Timing Charge Detector. Thanks also go to the CREAM principal investigator, Professor Eun-Suk Seo, for her leadership and oversight of the project.

I have had a number of meaningful interactions with fellow students who graduated ahead of me. Specifically, I would like to thank Dr. Nicholas Conklin, Dr. Samuel Isaac Mognet, Dr. Theresa Brandt, and Dr. Nahee Park, all of whom have provided advice, direction, and encouragement at key points in my journey through graduate school. I have also spent many hours in the laboratory working with fellow graduate and undergraduate students. The list is long and stretches back many years, but I would especially like to thank several individuals with whom I worked over extended periods of time—Matthew Geske, Brian Dingee, John Groh, Michael Grinshpon, and Sai Im.

I learned much as an undergraduate during my time at Geneva College. The late Professor John Pinkerton was particularlly influential, who in addition to being an engaging lecturer, shared stories and insights on his years of detector development at NASA Jet Propulsion Laboratory which inspired many of my first interests in scientific instrumentation. I am also grateful for the educational influence of many others who worked at Geneva College, either now or in the past. In particular, I recall the excellent courses of Professor John Scaefer, Professor Murat Tanyel, Professor David Shaw, and Dr. Brett van de Sande.

To these, and the many others with whom I have had the pleasure of working throughout my graduate and undergraduate career, I offer heartfelt thanks.

I am incredibly thankful to my parents, Michael and Denise, for giving me a loving childhood which balanced healthy boundaries with a need for independence and exploration. I have always enjoyed a close relationship with both my sisters, Kaitlin and Bethany, and I am especially grateful for this. For some portion of my growing up, I had the privilege of living near an

extended family (both the Andersons and the Morrisons) with whom I grew very close. Thank you all for your prayers and support over the years and for still making me feel so welcome every time I visit home.

Thanks also go to my wife's family, the Brubakers and the Zellers, who have lived nearby during my time in graduate school and have adpoted me as a second son, nephew, and grandson.

Though she is still too young to realize it, my daughter, Leila Robbyn, now only nine-months old, provided significant motivation to finish this thesis in a timely manner. Leila, you will almost certainly never remember this, but your habit of crawling over to me every evening while I wrote this dissertation, grabbing onto my leg, and looking up expectantly with those big, blue eyes, led to the best play breaks *EVER*.

My wife, Dawn, gets the majority of the credit for getting me through the hard parts of graduate school. Like a champion, she has endured long hours, long trips, and many years of work, with nary a complaint or word of negativity. Sweetheart, for all of this, and for so much more, this work is as much a credit to you as it is to me.

Finally, thanks be to my Lord and Savior, Jesus Christ, from whom grace abounds in all things.

Chapter 1

An Overview of Cosmic Ray Physics

Our Earth is constantly bombarded by high-energy radiation of a particle nature, which originates from somewhere in the cosmos. The extraterrestrial origin of this radiation was first discovered in the early part of the 20^{th} century by Austrian physicist Victor Hess. Between 1911 and 1912, Hess mounted a series of 17 manned balloon campaigns over the Austrian-Czech, German, and Slovenian countrysides, in which he measured variations in the discharge rates of three identical electroscopes as his ballooncraft climbed to altitudes as high as 5000 m above sea level. After combining the data from all flights, Hess reported a slight decrease in ionization rates (roughly 10%) below 2000 m, followed by a significant increase in ionization rates (as high as twice that at ground level) up to 5000 m. Because this increase in ionization with altitude could not be correlated to meteorological or solar conditions (one flight took place during a partial solar eclipse), Hess concluded that the most likely explanation of his data was that "a radiation of very high penetrating power enters our atmosphere from above, and still produces in the lowest layers a part of the ionization observed in closed vessels" [1].

The results of Hess were confirmed by the German scientist Werner Kolhörster in another series of balloon flights between 1913 and 1919, in which Kolhörster surpassed heights of 9 km above sea level [2]. Further proof came in 1925 when American physicist Robert A. Millikan performed a series of snow-fed lake experiments. Millikan compared ionization rates of submerged electroscopes in California's Muir Lake, which sits at an altitude of 3600 m above sea level, to similar readings taken at Lake Arrowhead, which is located approximately 420 km south of Muir Lake and is only 1600 m above sea level. The difference in atmospheric thickness seen above the two lakes corresponds to 2 m water equivalent, and when Millikan compared ionization readings between the two lakes, he found Lake Arrowhead readings were in good agreement with Muir Lake measurements at a depth of 2 m lower. This measurement convinced Millikan of the observed radiation's extraterrestrial character, and he dubbed it "cosmic radiation" [3]. Victor Hess was finally awarded the 1936 Nobel prize in physics for his discovery of cosmic rays.[1]

[1] Hess shared his prize with Carl Anderson, who discovered the positron (the antiparticle of the electron) by studying cosmic ray behavior in a cloud chamber to which a magnetic field was applied [4].

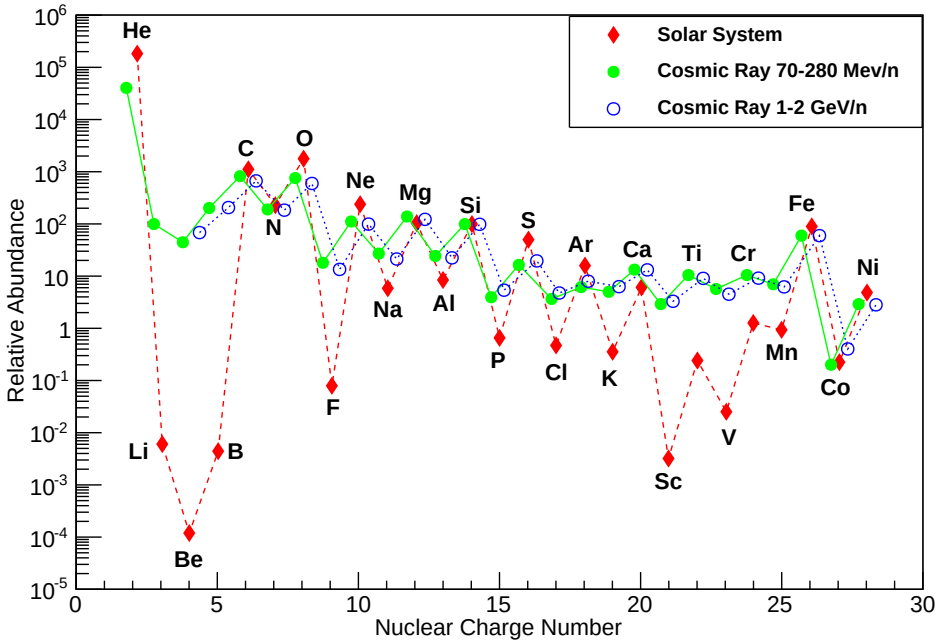

Figure 1.1. The relative abundance of cosmic rays compared with solar abundances. Solid, red diamonds represent solar system abundances. Solid, green circles represent cosmic-ray abundances in the energy range 70–280 MeV/n. Open, blue circles represent cosmic-ray abundances in the energy range 1–2 GeV/n. All abundances are normalized to silicon, which is taken to have an abundance of 100. Adapted from Reference [5].

1.1 Cosmic Rays: The Big Picture

After more than a century of observation, many of the general properties of cosmic rays are well known. The majority of cosmic rays are protons. Helium nuclei are second most common, with an abundance relative to protons of roughly 1 to 10. Electrons, heavy ions, and antimatter particles (positrons and antiprotons) comprise less than 1% of all cosmic rays. Nowadays energetic gamma rays and neutrinos are also studied as part of a comprehensive multi-messenger approach to the study of energetic cosmic phenomena (*e.g.*, with the Astrophysical Multimessenger Observatory Network (AMON) [6]).

Figure 1.1 compares the so-called "relative abundance" of cosmic rays in the energy ranges[2] 70–280 MeV/n and 1–2 GeV/n to the abundance of elements found in the solar system[3]. All abundances are normalized to that of silicon, which is taken to have an abundance of 100. Examining the figure, it is clear that the so-called "primary" cosmic rays (*i.e.*, those elements which are readily produced as the end-products of stellar nucleosynthesis) have abundances which

[2]The electron-volt (eV) is the energy unit used exclusively in particle physics. One electron-volt represents the energy gained by an electron when accelerated through a potential difference of 1 Volt.

[3]Scaling a particle's energy by its number of nucleons is common practice when considering the relative abundance of elements, since most interactions which lead to fragmentation of nuclei tend to preserve this quantity.

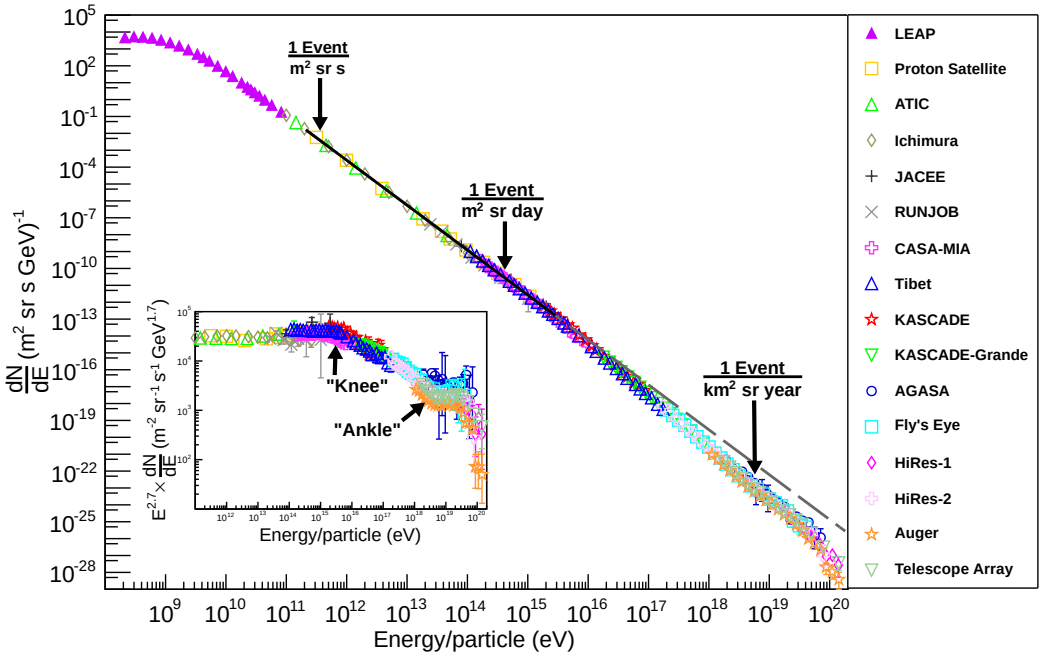

Figure 1.2. the cosmic ray all-particle spectrum. The inset depicts the spectrum with ordinates scaled by energy raised to the 2.7 power. Adapted from References [7], [8], [9], [10], [11], and [12].

track those found in the solar-system relatively closely. They also exhibit the well-known "odd-even effect" of ordinary matter, whereby the formation of elements with an even number of protons is energetically favorable, and thus, more common. The correspondence between the composition of cosmic rays and the materials that comprise the solar system suggests that both originate from a similar bulk material.

Several elements show a much greater prevalence in the cosmic rays than in the solar system. These so-called "secondary" cosmic rays (those which are ***not*** produced in significant quantities by stellar nucleosynthesis) are believed to be created in the cosmic rays by the interaction and subsequent spallation (*i.e.*, breakup) of primary cosmic rays as they pass through the Galaxy. As will be discussed later, measuring how the ratio of secondary-to-primary cosmic rays changes with increasing energy is an important key to understanding cosmic ray propagation history.

Figure 1.2 shows the cosmic-ray "all-particle spectrum", which plots cosmic ray intensity[4] versus energy, as measured by selected balloon, satellite, and ground-based cosmic-ray experiments. For reference, markers have been added to the figure in order to indicate the energy thresholds above which event rates of one particle per second per square meter, one particle per day per square meter, and one particle per year per square kilometer are observed. As can be

[4]Intensity (often also referred to as differential flux) represents the number of cosmic rays observed in the phase space composed of a detector's active area, solid-angle view of the sky, exposure time, and energy range sensitivity. In other words, integrating differential flux over a detector's sensitive energy range and geometrical acceptance (active area × solid angle) gives the cosmic ray event rate in the detector (events/second).

seen from the figure, cosmic rays span an enormous range in both energy (greater than 12 orders of magnitude) and flux (roughly 32 orders of magnitude). The high-energy reach of cosmic rays is truly mind-boggling, extending more than three orders of magnitude higher than the maximum 10^{17} eV lab-frame energy of humankind's most powerful particle accelerator, the Large Hadron Collider (LHC) [13].

Because the overall intensity and energy content represented in the cosmic rays are inconsistent with any potential source found in the solar system (*e.g.*, the Sun), it is widely accepted that most cosmic rays originate from somewhere outside our solar system. There is strong evidence (some of which will be examined in Section 1.4) to suggest that the bulk of cosmic rays are accelerated inside our Galaxy in the shockwaves of supernova remnants (SNR), and that, once these cosmic rays escape their acceleration region, Galactic magnetic fields are capable of confining them for millions of years. However, at sufficiently high energies, the magnetic gyroradius of cosmic rays grows larger than the height of the Galaxy (roughly 300 pc), and the idea of efficient containment of cosmic rays inside of it is challenged. The possibility then arises of an extragalactic component of cosmic rays which may contribute significantly to the overall cosmic-ray intensity at such high energies. However, the energy at which such an extragalactic cosmic ray component might become significant (somewhere above 10^{18} eV), and the exact details of such a transition, are still open questions in cosmic-ray physics.

Below 10^{10} eV, electromagnetic interactions of the solar wind with cosmic rays are strong enough to inhibit some of them from entering our solar system. Thus, the cosmic ray spectrum turns over at low energies, and exhibits significant variability with the eleven year solar cycle below 10^{10} eV, reaching its point of highest (lowest) intensity near the time when solar activity is at a minimum (maximum). Data from the Low Energy AntiProton (LEAP) balloon-borne experiment (which was collected during the solar minimum of 1987) [14] has been incorporated in Figure 1.2 as representative of the regime where the effects of solar modulation are prominent.

Between 10^{11} eV and 10^{15} eV, the intensity, dN/dE, of the all-particle spectrum is well described by a power-law in energy, E, of the form

$$\frac{dN}{dE} = \Phi_0 E^{-\alpha} \tag{1.1}$$

where Φ_0 is a normalization constant and the spectral index, α, has a value near 2.7. A trend line (black, solid line) has been added to Figure 1.2 in order to emphasize this behavior. This is the *observed* spectrum at Earth, to be distinguished from the spectrum at the source, expected from modeling of cosmic-ray shock acceleration to have something like a E^{-2} dependence. The steepening of the spectrum to $E^{-2.7}$ arises from propagation effects, discussed in Section 1.3 below. Below 10^{15} eV, cosmic ray event rates are large enough that they can be studied effectively via "direct measurement" methods, which determine the properties of cosmic rays via the modern methods of particle physics (*e.g.*, magnetic spectrometers, calorimeters, etc.). Because the interaction of cosmic rays with Earth's atmosphere (thankfully) prevents them from reaching ground level, these direct measurements are required to take place high above most of the atmosphere,

either on balloons, with flights lasting upwards of 30 days, or on space-based missions, which are often in excess of a year. Direct measurement techniques excel in their ability to provide precision cosmic-ray energy spectra and composition data. However, the current generation of detectors is hindered in their energy reach by logistical constraints on geometry and mass imposed on these flight missions.[5]

Around 3×10^{15} eV, the all-particle spectrum exhibits a sudden break from its previous power law—the so-called "knee" in the cosmic-ray spectrum. In Figure 1.2, the trend line below the knee has been extrapolated (dark gray, dashed line) in order to emphasize this break. The cause of the knee, and the processes at work on cosmic rays at energies near it, are still open questions. The most popular hypothesis is that the knee represents a cutoff in the maximum energy attainable via acceleration in SNR, and is thus a signature of cosmic-ray acceleration via this mechanism.[6] Many variations of the theory exist, and ultimately, precision measurements of the composition of the cosmic-ray spectrum are required in order to constrain the various models [17].

Spectral features above the knee are made more prominent in the inset of Figure 1.2, where cosmic-ray intensity is scaled by $E^{2.7}$. As can be seen, the cosmic-ray spectrum follows a new power law with spectral index near 3.0 in this energy range, up to roughly 3×10^{18} eV where it again hardens—the so-called "ankle" of the all-particle spectrum. The origin of cosmic rays above the knee and the cause of the ankle feature are still very unclear. Some theories speculate that cosmic rays above the knee originate primarily from extragalactic sources. Others argue that cosmic rays between the knee and the ankle are of Galactic origin (possibly being accelerated in non-standard SNR), and that the ankle represents a transition to an extragalactic component. Still others suggest the ankle originates from a pileup of protons, originally of a higher energy, which experience energy loss during propagation via pair-production interactions with the cosmic microwave background [18]. More experimental data (especially precision composition measurements) are needed in order to distinguish between these types of models.

Somewhere between 10^{19} eV and 10^{20} eV, most experiments report a steep cut-off in the all-particle spectrum. This might be related to the Greisen-Zatsepin-Kuz'min limit, which suggests that cosmic rays originating from distant sources with energies above $\sim 5 \times 10^{19}$ eV should be highly suppressed by interactions with the cosmic microwave background [19] [20].

Above the knee, event rates are too low to be studied via direct measurement techniques, and so-called "indirect" methods are required. Indirect methods compensate for the low intensity of cosmic rays above the knee by using detectors with a large geometrical acceptance, measuring the properties of cosmic rays by the extensive air showers (EAS)—the burst of photons, electrons, muons, and other secondary particles—which are produced as these high-energy cosmic rays interact in the atmosphere. Modern air-shower experiments are comprised of either large-area

[5] At 5 m^2sr, the Transition Radiation Array for Cosmic Energetic Radiation (TRACER) is the instrument which performed direct measurements with the largest geometrical acceptance in recent years [15].

[6] The idea that the knee might represent new physics in an unexplored energy regime of the standard model was also considered in the past. However, this now seems extremely doubtful, since the LHC, which began successful long-term operation in 2009, has fully explored this energy regime for proton-proton collisions, finding no evidence of unexpected phenomena [16].

arrays of charged-particle detectors or of telescopes which measure the Cherenkov radiation or nitrogen fluorescence produced by shower secondaries in the atmosphere. Currently, composition measurements via indirect techniques are significantly limited by a lack of accelerator data on the interactions of particles at these energies. While these models are constantly improving, the most recent analyses are able to resolve only the most prominent elements, or groups of elements, in in the data [21].

1.2 Cosmic Ray Energetics And Mass

The general properties of cosmic rays just discussed raise some intriguing questions. What astrophysical sources are at work in the Galaxy which are capable of imbuing cosmic rays with their phenomenal energy reach? What interactions do cosmic rays undergo as they travel from their acceleration site to their point of detection, and how do such propagation considerations modify the spectra we measure at Earth? Can reacceleration of cosmic rays take place during interstellar transport? What mechanisms create the prominent features in the all-particle spectrum, and what can composition-resolving studies near these features tell us about the acceleration and propagation of cosmic rays?

The Cosmic Ray Energetics and Mass (CREAM) project contributes to the answers of these questions by measuring the individual spectra of each cosmic-ray species with a nuclear charge number between $Z = 1$ (protons) and $Z = 26$ (iron) in the energy range 10^{10} eV to 10^{15} via direct measurement techniques, both in a series of balloon flights and in an upcoming mission to the International Space Station. In so doing, CREAM's measurements provide new data on Galactic cosmic rays at energies approaching the knee and aid in the exploration of the acceleration and propagation mechanisms at work in this fascinating energy range. As an experiment which performs a high-statistics direct measurement, CREAM's precise charge spectra help bridge the gap between lower-energy direct measurements and the indirect techniques required at much higher energies. The multi-faceted details of the CREAM instrument, its science results, and its future missions are the focus of subsequent chapters. The remainder of this chapter will consider some aspects of cosmic-ray propagation and acceleration theory which motivate the CREAM program.

1.3 Cosmic-Ray Propagation

The Galactic disk is permeated by magnetic fields with typical magnitude $B_{ISM} \sim 3\ \mu$G whose average orientation is parallel to the Galactic disk, but whose direction fluctuates randomly over length scales as large as $l_{max} \sim 100$ pc [22]. These magnetic fields are maintained primarily by the ionized gas which pervades the Galaxy, which has a number density $n_{ISM} \sim 1$ proton/cm^3 [23].

Cosmic rays propagating through Galactic magnetic fields move with a trajectory that is randomized by scattering on magnetic irregularities of scale size larger than the cosmic ray's a

magnetic gyroradius r_g. The exact details of the interactions of the ionized gas which maintains the Galaxy's magnetic fields and the cosmic rays which propagate through them are quite complicated. The system as a whole forms a magnetohydrodynamic fluid, in which the motion of cosmic rays generates field disturbances, which in turn create new inhomogeneities for scattering [24]. In this regard, it is instructive to compare the relative energy density of Galactic magnetic fields to that found in cosmic rays. The magnetic energy density of the Galaxy is

$$u_B = \frac{B_{ISM}^2}{8\pi} \approx 3.6 \times 10^{-13}\,\mathrm{erg/cm^3} \sim 0.2\,\mathrm{eV/cm^3} \tag{1.2}$$

while the local interstellar energy density of cosmic rays (*i.e.*, the energy density thought to be observed just outside the solar system) has been calculated as $\rho_E \sim 0.5$ eV/cm^3 by combining low-energy cosmic-ray spectra with models of solar modulation [23]. Thus, the similarity of these two energy densities is highly suggestive of their coupling.

Intuitively, Galactic magnetic fields should be capable of providing a level of confinement for cosmic rays up to the point where r_g is equal to l_{max}. Quantitatively, the energy of maximum confinement can be estimated using the well-known relation,

$$\frac{pc}{r_g} = ZeB \tag{1.3}$$

where p is the magnitude of particle momentum, c is the speed of light, Z is the particle's nuclear charge number, e is the electron charge, and B is the magnetic field seen by the particle. Thus, for an ultrarelativistic[7] cosmic ray, the energy of maximum confinement is estimated to be

$$E_{max} \approx Ze\,l_{max}\,B_{ISM} \sim Z \times 3 \times 10^{17}\,\mathrm{eV}. \tag{1.4}$$

Again, the exact details of the dynamical interactions of cosmic rays with Galactic magnetic fields are quite complicated, and such a calculation only suggests a very crude maximum energy (*i.e.*, probably correct within an order of magnitude or two). However, such estimates are still useful considering the many orders of magnitude spanned by the energy spectra of cosmic rays. In any case, the Z dependence of the dynamics of cosmic-ray propagation should be a general feature, suggesting that models of cosmic-ray propagation are best parameterized in terms of magnetic rigidity,

$$R = r_g B = \frac{pc}{Ze}. \tag{1.5}$$

Such a parameterization effectively removes Z from the dynamical description.

A simple, but instructive, model of cosmic-ray propagation is the so-called "leaky box" model.[8] In this model, cosmic rays are treated as disappearing (*i.e.*, "leaking") from the containment volume of the Galaxy (*i.e.*, the "box") with a constant probability per unit time τ_{res}^{-1}. The rigidity-dependent number density $N_i = N_i(R)$ of the i^{th} cosmic-ray species in the containment

[7] The term "ultrarelativistic" will be taken throughout the text to describe situations in which the relation $E = \sqrt{(pc)^2 + (mc^2)^2} \approx pc$ is a sufficiently good approximation for the situation of interest.

[8] The discussion here follows the presentation of Gaisser quite closely [23].

volume is then determined by a transport equation of the form

$$\frac{\partial N_i}{\partial t} = Q_i\left(R\right) + \beta c n \left(\sum_{k>i} \sigma_{ki} N_k - \sigma_i N_i\right) - \frac{N_i}{\tau_{res}}. \tag{1.6}$$

Considering the right-hand side of the equation, the first term is the "source term", and represents the spectra of cosmic rays when they are ejected from their acceleration site. The second term accounts for cosmic-ray spallation, representing the break-up of cosmic-ray nuclei as they interact with the material in the containment volume. Here, n is the number density of nuclei in the containment volume and the quantity $\beta = v/c$ is particle speed v divided by the speed of light. The spallation term accounts for both feed down (*i.e.*, heavier nuclei of type k interacting to create nuclei of type i) and the loss of the i^{th} species due to interactions with the enclosure's gas, with nuclear interaction cross sections σ_{ki} and σ_i, respectively. The final term is the one which models the leaky box mechanism.

How do the spectra observed at Earth compare to those generated by cosmic accelerators? In the context of the leaky box model, this question can be answered directly from Equation 1.6.[9] Considering a primary species, of type X whose abundance is large enough that feed down can be neglected, evaluated in equilibrium, Equation 1.6 becomes

$$Q_X\left(R\right) - \beta c n \sigma_X N_X - \frac{N_X}{\tau_{res}} = 0 \tag{1.7}$$

and the observed spectrum is found to be

$$N_X = \frac{Q_X\left(R\right)\tau_{res}\left(R\right)}{1 + \lambda_{res}\left(R\right)/\lambda_X}. \tag{1.8}$$

A relation between the source spectrum and the observed spectrum has now been found. Provided the energy range is low enough, the quantity $\lambda_X\left(R\right)$ can be obtained from accelerator measurements, but an independent means of determining $\lambda_{res}\left(R\right)$ is still needed in order to evaluate the relation.

The well-known solution to this problem comes from measuring cosmic-ray secondary-to-primary ratios as a function of rigidity. Of the possible ratios which might be considered, the boron-to-carbon ratio is the one which has been most explored. Because boron is not present in significant quantities in normal Galactic matter (see Figure 1.1), its source term, $Q_B\left(R\right) \approx 0$, and so decouples from the problem. Evaluating Equation 1.6 in equilibrium for boron (and including feed down from the spallation of carbon) results in the relation

$$\beta c n \sigma_{CB} N_C - \beta c n \sigma_B N_B - \frac{N_B}{\tau_{res}} = 0 \tag{1.9}$$

[9] Any characteristic time over which some process occurs τ (units of seconds) can also be expressed in terms of the density-weighted mean-free path for the process λ (units of g/cm^2) or in terms of the interaction cross section for the process σ (units of barns or cm^2) via the relations $\lambda = nm\beta c\tau = m/\sigma$, where m is the average nucleon mass in the containment volume. In the following discussion, such conversions will be performed whenever convenient.

which yields

$$\frac{N_B}{N_C} = \frac{\lambda_{res}/\lambda_{CB}}{\lambda_{res}/\lambda_B + 1}. \tag{1.10}$$

Thus, λ_{res} can be found as a function of rigidity by fitting Equation 1.10 to a measurement of the boron-to-carbon ratio. Below 10 GV, most experiments measure a boron-to-carbon ratio consistent with an expression of the form $\lambda_{res} = \lambda_0\beta$, with $\lambda_0 \sim$ between 10 g/cm^2 and 11 g/cm^2, thus yielding a residence time which remains constant with rigidity [23]. The current status of boron-to-carbon measurements at higher rigidities is discussed in Section 3.2 in the context of CREAM science results, and so an examination of the empirically derived data will be delayed until then. For now, it is sufficient to state that most recent measurements show good agreement with those of CREAM up to ∼600 GV, and that CREAM finds λ_{res} in the form

$$\lambda_{res}(R) = \lambda_0 \left(\frac{R}{R_0}\right)^{-\delta} \tag{1.11}$$

with $R_0 = 10$ GV, $\lambda_0 = 10$ g/cm^2, and $\delta = 0.6$.

Considering again Equation 1.8, in the case of protons, $\lambda_X = \lambda_P$ is roughly 50 g/cm^2 in the range 1 GV to 1000 GV [23], and thus $\lambda_{res} \ll \lambda_P$, yielding a relation between the observed spectrum and the source spectrum of

$$N_P \propto Q(R)\, R^{-0.6}. \tag{1.12}$$

From Section 1.1, given a measured spectral index of 2.7, this translates to a source spectrum of roughly 2.7 - 0.6 = 2.1. Heavier elements have somewhat smaller values of λ_X (iron, for instance, has $\lambda_{Fe} \sim 2$ g/cm^2 in this energy range) and approach the spectral modification of lighter elements asymptotically.

Secondary-to-primary ratios of other species are similarly useful, and CREAM's precise composition measurements hold the potential to make significant contributions to new knowledge of them. In addition to the boron-to-carbon ratio, measurements of the nitrogen-to-oxygen ratio have been reported by the CREAM experiment and will be discussed in Section 3.2. The nitrogen-to-oxygen ratio is interesting in particular because nitrogen is known to be created in stellar nucleosynthesis, and thus, its source abundance can be inferred from the nitrogen-to-oxygen measurement. Various ratios from the "sub-iron" group (scandium, titanium, vanadium, chromium, and manganese—all of which are secondary products of iron) to iron are also accessible to CREAM, although measurements of sub-iron spectra are significantly more challenging than measurements of the spectrum of boron, due to the relative suppression of the sub-iron group in the cosmic rays (see Figure 1.1). Analyses of sub-iron-to-iron spectra are currently in progress by the CREAM collaboration.

While the leaky box model is useful in that it yields simple results which highlight the main features of cosmic-ray propagation, more complicated models are required in order to trace the features of observable cosmic-ray spectra back to the mechanisms at work in the Galaxy. The

GALPROP numerical simulation code-base has been adopted by most recent experiments for this purpose [25]. It treats propagation as a diffusion process, with diffusion coefficient $D(R) \propto R^{-\delta}$ representing the rigidity-dependent behavior of cosmic rays. Other propagation mechanisms can also be studied, including convection in Galactic winds and reacceleration of cosmic rays during their encounters with Alfvén waves as they propagate through the Galaxy. Ultimately, constraining the relative contributions of convection, reacceleration, and other propagation mechanisms requires rather precise measurements of secondary-to-primary ratios over a wide energy range [26], and the precision composition measurements provided by CREAM are valuable in this effort.

1.4 Cosmic-Ray Acceleration

In the quest to identify an astrophysical accelerator for the bulk of Galactic cosmic rays, several observational clues provide useful guidance. The sustained intensities and featureless power-law behavior seen in the all-particle spectrum up to the knee suggest that a single class of sources may be responsible for accelerating the majority of cosmic rays. A power-law spectrum may arise naturally in astrophysical particle accelerators if one considers a mechanism by which cosmic-ray energy grows fractionally over the course of many encounters with the accelerator, an idea first proposed by Fermi in 1949 [27]. Let E_0 be the starting energy of the cosmic ray, and the fractional energy gain per encounter be ξ. After k encounters, the cosmic ray's energy E will be

$$E = E_0 (1 + \xi)^k . \tag{1.13}$$

If the cosmic ray has a probability of escaping the acceleration region, P_{esc}, then, given a starting population of N_0 particles, the number which remains near the accelerator after k encounters is

$$N = N_0 (1 - P_{esc})^k . \tag{1.14}$$

Equating k in Equations 1.13 and 1.14 leads to the expression

$$N = N_0 \left(\frac{E}{E_0} \right)^{\frac{\ln(1-P_{esc})}{\ln(1+\xi)}} . \tag{1.15}$$

Taking the derivative with respect to energy, Equation 1.15 is found to be proportional to Equation 1.1, if the spectral index is assigned the value

$$\alpha = -\frac{\ln(1 - P_{esc})}{\ln(1 + \xi)} + 1. \tag{1.16}$$

Any viable acceleration candidate should be able to reproduce the power-law behavior observed below the knee and (after sufficient consideration has been taken of propagation effects) its spectral index of 2.7.

Measurements of the relative abundance of the proton-rich isotope ^{59}Ni (which decays exclusively via electron capture) to its daughter ^{59}Co in cosmic rays indicate a ratio most consistent with the total decay of all source ^{59}Ni. This sets a lower limit on the time between the synthesis of ^{59}Ni and its acceleration, given by its half life of 7.6×10^4 years, since for shorter time scales, ^{59}Ni would be easily stripped of all of its orbital electrons, being rendered stable to electron-capture decay, and found in greater abundance in cosmic rays [28]. Thus, the picture emerges of an accelerator which sweeps up nearby, pre-existing materials, rather than one that only self-generates its source material during acceleration.

Another clue comes in considering the power output required to keep our Galaxy's cosmic rays in constant supply. As was mentioned in Section 1.3, the local interstellar energy density of cosmic rays has been calculated to be roughly $\rho_E \approx 0.5$ eV/cm$^3 \approx 8 \times 10^{-13}$ ergs/cm^3. Measurements of the relative abundances of radioactive parent isotopes to their daughter isotopes in cosmic rays have been used as "cosmic-ray clocks" (the best studied examples being ^{10}Be/^{9}Be, ^{26}Al/^{27}Al, and ^{36}Cl/$^{35+37}$Cl) to determine that the mean escape time for cosmic rays from the Galaxy is roughly 17 million years [24] [29]. Given the $R_g \approx 15$ kpc radius and $D_g \approx 300$ pc thickness of the Galactic disk, the energy-leakage rate of cosmic rays from the Galaxy is found to be

$$P_{cr} = \frac{\pi R_g^2 \, D_g \, \rho_E}{\tau_{esc}} \approx 9 \times 10^{39} \text{ erg/s}. \tag{1.17}$$

The considerations presented above strongly favor the acceleration of cosmic rays in SNRs. SNRs are formed as the result of supernova explosions. When a massive star (greater than 8 solar masses) reaches the end of its life, the radiation pressure generated by fusion in its core becomes insufficient to maintain the hydrostatic equilibrium necessary in order to prevent its gravitational collapse.[10] The star then begins a process which leads to the collapse of its interior, followed by a powerful explosion—the supernova event. The supernova event results in the generation of plasma shockwave which flows into the surrounding interstellar medium (ISM). This shockwave, and the ISM it absorbs as it expands, is the SNR. Most SNRs continue to develop as fast-moving shocks for hundreds to thousands of years and so are likely active particle accelerators throughout this period of their lifetime [31].

Many lines of reasoning have led to the favoring of the SNR as the site for acceleration of the bulk of cosmic rays. Measurements of the non-thermal x-ray and gamma-ray spectra emitted from SNR indicate electron acceleration up to TeV energies [32] [33], with some datasets showing an additional gamma-ray component for which pion-decay from the interaction of high-energy hadrons is a plausible explanation [34]. Furthermore, based on arguments originally presented by Ginzburg and Syrovatskii [35], Stanev [24] notes that the typical supernova explosion in our Galaxy may eject $M \sim 10$ solar masses (2×10^{34} g) of material, and that the resulting shockwave may move with an average speed $U \sim 5 \times 10^8$ cm/s. Such supernova events are thought to occur

[10] The explosion mechanism described here is for core-collapse supernovae. In type Ia supernovae, the explosion is generated by the ignition of carbon-oxygen fusion in the white dwarf of an accreting binary system [30].

in our Galaxy at a rate T_{SNR}^{-1} of roughly 3 per century, leading to a total power output of

$$P_{SNR} = \frac{MU^2}{2\,T_{SNR}} \approx 2.6 \times 10^{42}\,\mathrm{erg/s}. \tag{1.18}$$

Thus, the processes in SNR which might accelerate cosmic rays need only be ∼1% efficient in order to account for the energy density of cosmic rays in the local ISM.

The shocks of SNR also provide a convenient explanation for a power-law spectrum, as derived from the Fermi mechanism. While the exact details of the processes at work in accelerating cosmic rays in SNR shocks are still somewhat unclear (and likely quite complicated) a simple, but powerful, model will be presented here for illustration.[11] The basic idea is that cosmic rays cross back-and-forth along the SNR shock front many times, and in each crossing, receive an energy boost equivalent to a fraction of their pre-shock crossing (kinetic) energy. Obviously, such a model requires a mechanism for scattering cosmic rays on both sides of the shock and confining them in the acceleration region for long periods of time. Behind the shock (*i.e.*, the "downstream" region), turbulent magnetic fields generated by the SNR's plasma create scattering centers for cosmic rays. Of course, magnetic fields "do no work", and are thus incapable of accelerating particles in the reference frame where the plasma is at rest. However, when these magnetic fields are viewed in the rest frame of the ISM, the plasma is in motion, and the ISM sees electric fields generated in the turbulence as a result of the reference-frame change (*i.e.*, $\vec{v} \times \vec{B}$ electric fields).[12] Meanwhile, ahead of the shock (*i.e.*, the "upstream" region) streaming instabilities generated when the cosmic rays cross the shock front have been shown capable of creating magnetohydrodynamic waves which can efficiently scatter, isotropize, and confine cosmic rays, sending them again back toward the shock front [37]. Again, the fine details of confinement, scattering, and acceleration are still open questions in the field, and the discussion presented here is only meant to motivate an intuitive picture.

Figure 1.3 depicts the three reference frames important for the model. The shock's speed with respect to the ISM, U, is taken to be much less than the speed of light, c, so $U/c \ll 1$. Also, the radius of the shock is considered large relative to the length scale for cosmic-ray scattering, such that the shock can be approximated as a plane. The left side of Figure 1.3 depicts the situation in the rest frame of the stationary shock. The upstream medium rushes toward the shock with velocity $v_2 = -U$, while the downstream medium rushes away from the shock with velocity v_1. Using the condition of continuity of mass flow across the shock boundary [23], it is found that

$$\frac{v_2}{v_1} = \frac{(c_p/c_v + 1)\,M^2}{(c_p/c_v - 1)\,M^2 + 2} \tag{1.19}$$

[11] The presentation shown here follows that of Longair [36].

[12] Note that hot plasmas are incapable of generating significant static electric fields in their own reference frame, since the plasma re-adjusts quickly to cancel potential differences.

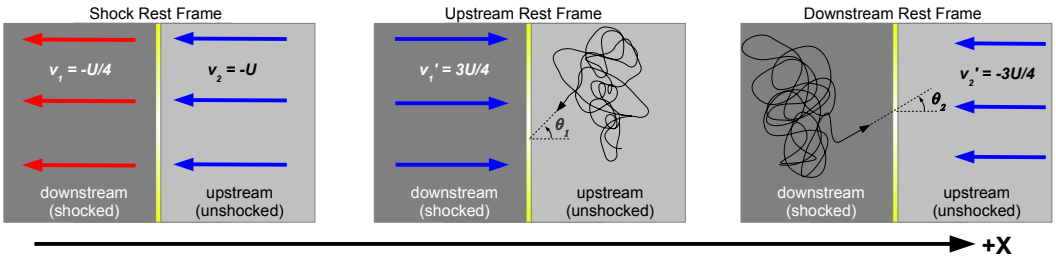

Figure 1.3. Three reference frames important for cosmic-ray acceleration in SNR. Left: the reference frame in which the shock is at rest. The upstream medium rushes toward the shock with velocity $-U$, while the downstream medium rushes away from it with speed $-U/4$. Center: the reference frame in which the upstream medium is at rest. A cosmic ray crossing the shock sees the downstream medium rushing toward it with speed $3U/4$. Right: the reference frame in which the downstream medium is at rest. A cosmic ray crossing the shock sees the upstream medium rushing toward it with speed $-3U/4$. The circuitous paths shown in the center and right-most panels are meant to represent the scattering and isotropization of cosmic rays on each side of the shock. No other inference should be drawn from their physical extent or geometry.

where $c_p/c_v = 5/3$ is the ratio of the specific heats for a plasma, and $M \gg 1$ is the Mach number for a supersonic shock. Taking the limit where M^2 goes to infinity, the velocity of the shocked medium in this reference frame is found to be $v_1 = -U/4$.

The center of Figure 1.3 shows the situation in the reference frame where cosmic rays cross the shock from the upstream side. Here, $v_1' = -U/4 - (-U) = 3U/4$, and thus, a particle crossing the shock sees the downstream medium rushing toward it. Meanwhile, the right side of Figure 1.3 shows the reverse situation, where the cosmic ray crosses from downstream to upstream. This time, $v_2' = -3U/4$, and a particle crossing the shock again sees the upstream medium rushing toward it. It's worth noting that the symmetry of approaching medium from both directions of shock crossings is exactly what allows for the efficient acceleration of cosmic rays in this theory.

The fractional average energy gained in a single set of crossings (*i.e.*, back-and-forth), ξ from Equation 1.13, can be calculated in a straightforward manner. Consider first a cosmic ray traveling upstream-to-downstream (the center panel of Figure 1.3), with an energy and magnitude of momentum in the rest frame of the upstream medium E_1 and p_1, respectively, and a pitch-angle relative to the shock normal $\pi + \theta_1$. The cosmic ray is assumed to be ultrarelativistic, such that $E_1 \approx p_1 c$ is a good approximation. Then, in the downstream reference frame, the incoming particle has an energy

$$E_1' = E_1 + p_1 v_1' \cos\theta_1 = E_1 \left(1 + \frac{3U}{4c} \cos\theta_1\right) \tag{1.20}$$

which is obtained via standard Lorentz transformation, taking the Lorentz factor of the non-relativistic, shocked medium to be unity.

While being scattered in the rest frame of the downstream medium, only magnetic fields are at work, and so the cosmic ray's energy E_1' and magnitude of momentum p_1' are unchanged during this process. Upon re-crossing the shock from downstream-to-upstream (the right panel

of Figure 1.3), the particle now has an energy in the original rest frame

$$E_2 = E_1' - p_1' v_2' \cos\theta_2 = E\left(1 + \frac{3U}{4c}\cos\theta_1\right) + \frac{E}{c}\left(1 + \frac{3U}{4c}\cos\theta_1\right)\frac{3U}{4}\cos\theta_2. \tag{1.21}$$

The fractional energy gain due to one back-and-forth set of shock crossings is then

$$\frac{\Delta E}{E} = \frac{3U}{4c}\left(\cos\theta_1 + \cos\theta_2\right) + O\left(\frac{U^2}{c^2}\right). \tag{1.22}$$

Since $U/c \ll 1$, only the first order term makes a significant contribution.

In order to calculate the average fractional energy gain ξ, it now remains to average $\cos\theta_1$ and $\cos\theta_2$ over all arrival directions. Considering a single patch of the shock front with differential area vector $d\vec{A}$, the number of particles incident on it, dN, in a time interval dt, arriving from a patch of sky which subtends a solid angle $d\Omega = \sin\theta_1 d\theta_1 d\phi_1$ is

$$dN = \frac{1}{2}\, n_{cr}\, d\Omega\, \vec{v}_{cr} \cdot d\vec{A}\, dt = \frac{1}{2}\, n_{cr}\, c\, \cos\theta_1 \sin\theta_1 d\theta_1 d\phi_1\, dA\, dt \tag{1.23}$$

where n_{cr} is the cosmic-ray number density and $\vec{v}_{cr}$ represents the isotropic cosmic ray velocity vector field. The factor of $1/2$ appears because the flux of cosmic rays just in front of the shock front is isotropic, and so, at least half of them will be headed away from the shock.

Converting Equation 1.23 to a normalized probability density in θ_1 leads to the expression,

$$\frac{dn}{d\theta_1} = 2\sin\theta_1\cos\theta_1. \tag{1.24}$$

Finally, averaging over $\cos\theta_1$,

$$\langle\cos\theta_1\rangle = \int_0^{\pi/2} 2\cos\theta_1 \frac{dn}{d\theta_1} d\theta_1 = \int_0^{\pi/2} 2\cos^2\theta_1 \sin\theta_1 d\theta_1 = \frac{2}{3}. \tag{1.25}$$

By symmetry, $\langle\cos\theta_1\rangle = \langle\cos\theta_2\rangle$, and so from Equation 1.22, ξ is calculated to first order as

$$\xi = \langle\frac{\Delta E}{E}\rangle = \frac{3U}{4c}\langle\cos\theta_1 + \cos\theta_2\rangle = \frac{3U}{4c}\left(\frac{2}{3} + \frac{2}{3}\right) = \frac{U}{c}. \tag{1.26}$$

Thus, ξ is small, and the acceleration of cosmic rays to very high energies relies on many shock crossings over the lifetime of the SNR.

The escape probability, P_{esc}, can also be calculated in this framework. Appealing again to Equation 1.22, the number of cosmic rays which cross the shock from upstream-to-downstream per-unit-time, per-unit-area patch of shock front, averaged over solid angle is,

$$\frac{dN}{dAdt} = \frac{1}{2}\, n_{cr}\, c\, \frac{\int_0^{\pi/2}\cos\theta\sin\theta d\theta \int_0^{2\pi} d\phi}{\int_0^{\pi/2}\sin\theta d\theta \int_0^{2\pi} d\phi} = \frac{1}{4}\, n_{cr}\, c. \tag{1.27}$$

It is interesting to note that this is the same as the "impingement rate" of a gas on the sidewalls of its container, as derived from classical kinetic theory [38]—an observation which agrees with intuition, since the model specifies that the SNR contains the cosmic rays.

In the downstream region, the medium is advected away from the shock at a speed $U/4$, and thus, cosmic rays escape the accelerator region at a rate per-unit-time, per-unit-area, of $n_{cr}U/4$. The escape probability is then found to be

$$P_{esc} = \frac{\text{number leaving shock region}}{\text{number crossing shock}} = \frac{\frac{1}{4}\, n_{cr} U}{\frac{1}{4}\, n_{cr} c} = \frac{U}{c}. \tag{1.28}$$

As mentioned previously, U/c is small because the shock moves non-relativistically, and thus, the probability of escape in a single crossing is low.

Substituting these values into Equation 1.16, the spectral index is found to be

$$\alpha = -\frac{\ln(1 - P_{esc})}{\ln(1 + \xi)} + 1 \approx \frac{P_{esc}}{\xi} + 1 = \frac{\frac{U}{c}}{\frac{U}{c}} + 1 = 2. \tag{1.29}$$

This result is perhaps the most impressive aspect of the theory, since, when the spectral index is increased by $\delta = 0.6$, in accordance with the effects of propagation, the behavior of the all-particle spectrum below the knee is re-produced almost exactly. It is also interesting to note that U, the speed of the SNR shockwave in the rest frame of the upstream medium, cancels in the final result, making the spectral index somewhat insensitive to the physical parameters of the SNR.

The maximum particle energy achievable through shock acceleration can be estimated by an intuitive argument [24]. The average rate of energy gain by cosmic rays can be taken as

$$\frac{dE}{dt} \approx \frac{\xi E}{T_{enc}} \tag{1.30}$$

where T_{enc} is the time between shock crossings. The value of T_{enc} can be approximated as the mean-free path for scatters λ_s divided by the shock speed U. The shock will be efficient in accelerating cosmic rays up to a time T_{acc}, at which point the magnetic gyroradius of the cosmic rays significantly exceeds λ_s. For an ultrarelativistic particle, the gyroradius is

$$r_g \approx \frac{E}{ZeB} \tag{1.31}$$

where B is the local magnetic field and e is the fundamental charge. Quantitatively, taking $r_g = \lambda_s$ to occur at $t = T_{acc}$, Equation 1.30 becomes

$$\frac{dE}{dt} \approx \frac{\xi E}{r_g/U} \approx \frac{(U/c)EU}{E/(ZeB)} T_{acc} = Z\frac{U^2 eB}{c}. \tag{1.32}$$

Thus, the rate of energy gain is independent of energy at late times. Gaisser argues that the typical SNR remains an efficient accelerator for $T_{acc} \sim 1000$ years, at which point it will have swept up

an ISM mass equivalent to its ejected mass [23]. Integrating Equation 1.32 for $U = 5 \times 10^8$ cm/s and $B = 3$ μG typical interstellar magnetic field ahead of the shock, we find

$$E_{max} \approx Z\frac{U^2 eB}{c}T_{acc} \approx Z \times 2.4 \times 10^{14}\,\text{eV}. \tag{1.33}$$

The maximum energy of acceleration is Z dependent (as might have been guessed from the fact that the forces at work to accelerate cosmic rays in SNR are electromagnetic in nature, and so couple to Z), and thus indicates a maximum rigidity for acceleration. Thus, a signature of the mechanism would be a composition change in the cosmic-ray spectrum, with each element demonstrating a cutoff energy corresponding to its nuclear charge number.

It has often been suggested that the knee in the all-particle spectrum might correspond to the maximum energy achievable via acceleration in the shocks of SNR. In this regard, it is interesting to note that numerical models of self-generating magnetic fields in SNR shocks yield a cutoff energy of 3×10^{15} eV—exactly the position of the knee in the all-particle spectrum [39]. Furthermore, the KArlsruhe Shower Core And Array DEtector (KASCADE) has claimed to observe a composition change at the knee corresponding to the steepening of the spectra of the light mass group [40], while its high-energy extension (KASCADE-Grande) reports a dominance of the heavy mass group up to 80×10^{15} eV, after which point the iron spectrum also steepens [21]. These results are very much in line with the expectations of the theory, though perhaps not conclusive proof of it.

It should be noted that the simple treatment of SNR shock acceleration presented here, while being extremely powerful in its ability to explain some general features of cosmic-ray spectra, includes many assumptions which neglect potentially vital aspects. Two such aspects—modifications of the acceleration mechanism and the environment into which SNR expand—are discussed below.

While the acceleration mechanism discussed above predicts a smooth power-law spectrum, most detailed models suggest that precise composition measurements should reveal more complex spectral structures associated with the specific details of shock acceleration. For example, the case presented above tacitly assumes a "parallel shocks", wherein the magnetic field is directed parallel to the direction of shock flow, thereby yielding a spectral index of 2.0. In contrast, shocks may also arise with a flow component perpendicular to the magnetic field. These so-called "quasi-perpendicular shocks" generate additional electric fields in the rest reference frame of the medium into which they expand. The resulting electric fields are capable of accelerating particles significantly more efficiently than parallel shocks, although they result in a somewhat softer spectral index of 7/3 [41] [42].

The dynamic effects of cosmic rays on the shocks which accelerate them may also be important. The above treatment assumed that cosmic rays crossing the shock from both directions see a discontinuity between the shocked and unshocked region, and that their crossing has no effect on the evolution of the shock (the "test particle" approximation). In reality, the pressure of the cosmic rays impinging on the shock deforms it, making it more difficult for low-energy

particles to cross it. The result is a non-linear acceleration theory, with concavity appearing in the spectrum at energies approaching maximum [24].

The environment into which SNRs expand can also play an important role. SNRs which are created in the local ISM should accelerate the abundant protons found there in great dominance, a characteristic which has long been known of cosmic rays. However, recent measurements from the Advanced Composition Explorer's Cosmic Ray Isotope Spectrometer (ACE/CRIS) show relative abundances of some nuclear isotopes (notably $^{22}Ne/^{20}Ne$) consistent with a fractional composition reflecting $\sim$80% normal solar material but $\sim$20% the outflow of Wolf-Rayet stars—massive supernova progenitors typically found in OB associations with strong stellar winds and a richness of nuclei heavier than hydrogen [43]. This idea is further supported by recent results from the Trans-Iron Galactic Element Recorder (TIGER) experiment, who claim a prevalence of refractory elements (*i.e*, those which more naturally condense to form grains) over volatile elements in ultra-heavy cosmic rays [44]. Thus, it seems that at least some portion of cosmic rays are accelerated in an environment quite different from that of the local ISM.

Chapter 2

The CREAM Experiment

The CREAM experiment will be discussed, including an overview of its balloon program and an examination of its detector systems and measurement techniques.

2.1 The CREAM Balloon Program

CREAM explores questions of cosmic ray acceleration and propagation by making direct measurements of the cosmic ray energy spectrum at energies approaching the spectral knee, with sufficient charge resolution to resolve the different spectra for all Z = 1 (proton) through Z = 26 (iron) charge species. Since 2004, CREAM has performed these measurements as part of NASA's long duration balloon program, whereby the CREAM payload is attached to a 40 million cubic foot zero-pressure helium balloon and launched annually from McMurdo Station during the Antarctic summer season. Ideally, once CREAM reaches its float altitude (roughly 40 km above sea level), it is guided around the outskirts of the Antarctic continent by the "polar vortex", a circular wind pattern which sets up seasonally around the south pole. Provided such a trajectory can be achieved, multiple orbits around the continent are possible, with flights lasting upwards of 30 days. This is exemplified by the CREAM I mission in 2004/2005, whose trajectory (shown in Figure 2.1) allowed for three circumnavigations of the continent, for a total of 42 days of flight time.[1] Upon termination of the flight, CREAM parachutes to the ground, where it is recovered, re-furbished, and re-flown in subsequent seasons.

CREAM has flown in a variety of detector configurations over the years, with the set of detectors available at the time of system integration determining the detector configuration flown that year. The CREAM I instrument configuration, which utilizes the fullest complement of detectors, is shown in Figure 2.2. Broadly speaking, this instrument configuration can be broken down into two components—the upper structure detectors and the instrument pallet detectors—each of which is capable of independent measurements of cosmic ray energy and charge.

[1] In fact, this was a scientific ballooning flight duration record until 2012/2013 when the SuperTIGER instrument had a 55 day flight.

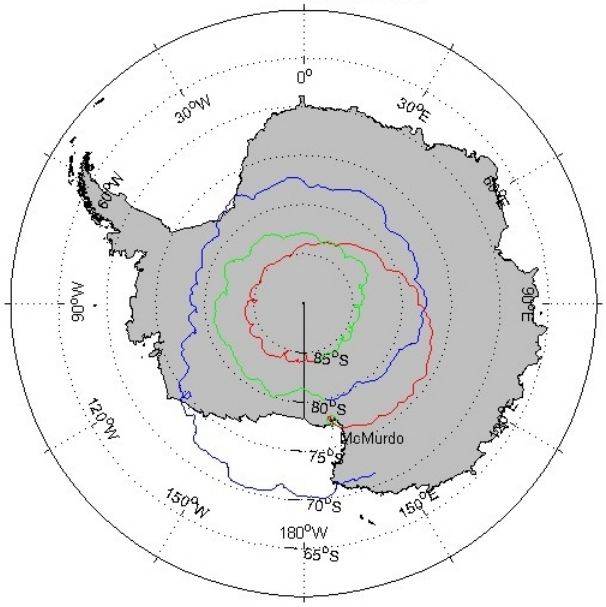

Figure 2.1. The CREAM I flight trajectory in 2004/2005. Its first (red), second (green), and third (blue) circumnavigations are shown.

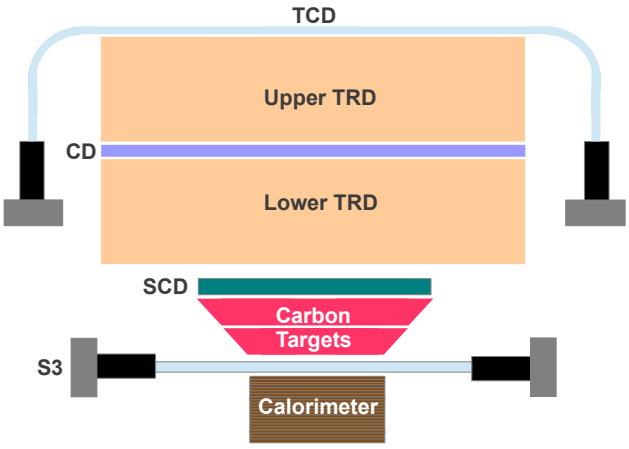

Figure 2.2. The CREAM I instrument configuration.

Flight	Length	TCD	TRD	CD	SCD	CAL	S3	CHERCAM
CREAM I	42 days	✓	✓	✓	✓	✓	✓	X
CREAM II	28 days	✓	X	✓	✓	✓	✓	X
CREAM III	29 days	✓	X	✓	✓	✓	✓	✓
CREAM IV	19 days	✓	X	✓	✓	✓	✓	✓
CREAM V	37 days	✓	X	✓	✓	✓	✓	✓
CREAM VI	6 days	X	X	X	✓	✓	✓	✓

Table 2.1. CREAM Flights.

The upper structure detectors consist of the Timing Charge Detector (TCD), the Transition Radiation Detector (TRD), and the Cherenkov Detector (CD). Attaching primarily to the upper portion of CREAM's instrument support structure, this set of detectors benefit from a large geometry factor (2.2 m^2 sr) and low mass thickness (6.9 g/cm^2 vertically). As will be described in detail later, the TCD and TRD measure the charge and energy of the incoming cosmic ray, primarily via specific ionization losses in their detector media. The CD allows identification of relativistic particles (whose Cherenkov radiation produces sizable signals in the CD), which are of the greatest interest to CREAM, while also rejecting much of the low-energy, charged particle (primarily Z=1) background which is abundant in flights over Antarctica, due to the small geomagnetic cutoff rigidity there.

The instrument pallet detectors are primarily the combination of a Silicon Charge Detector (SCD) and two "carbon" (*i.e.*, graphite) targets (whose thickness totals to roughly 1/2 of a nuclear interaction length) stacked on top of a tungsten electromagnetic sampling calorimeter. The SCD measures cosmic-ray charge via the signals produced in a pixelated, silicon-strip detector. The carbon targets initiate the interaction of the primary cosmic ray, while the calorimeter images the resulting 3-dimensional shower as it develops along each of its 20 tungsten plates (each of which is one radiation length thick), thereby providing a measure of the primary particle's energy.

CREAM's diverse complement of detectors is highly advantageous, as the results from each detector subsystem can be compared and cross-checked, thereby improving measurement resolution and decreasing systematic errors. Table 2.1 summarizes all CREAM balloon campaigns completed so far, along with their duration and detector configuration. The TRD was only present for the CREAM I flight. Starting with the CREAM III flight, a ring-imaging Cherenkov camera (CHERCAM) was developed as a backup detector for CREAM's baseline configuration, thereby utilizing the space normally occupied by the bottom TRD module with an additional means of charge measurement. For the CREAM VI flight, the TCD and CD groups opted not to fly, utilizing the opportunity to instead perform an update on their readout electronics, the results of which are detailed in Chapter 5. To date, CREAM has collected 161 days of flight data.

2.2 The TCD

The TCD[2] sits as the top counter in the set of upper structure detectors, measuring the charge of cosmic rays as they pass through two layers of 0.5 cm-thick BC-408 [45] plastic scintillator.[3] Each layer of the TCD consists of four scintillator "paddles", each with dimensions 120 cm × 30 cm in area. Paddles in the TCD's two layers are oriented in perpendicular directions, with the so-called "Y-paddles" (*i.e.* those whose centerlines have different Y coordinates in the CREAM coordinate system) on top, and the so called "X-paddles" (*i.e.* those whose centerlines have different X coordinates) at the bottom. Right-angle light guides on each end of the paddle direct photons to Photonis XP2020 [46] photomultipler tubes (PMTs) which measure light production in the paddles. PMT signals are read out by stacks of electronics positioned around the instrument, known as "TCD concentrator stacks". Figure 2.3 provides a view of the assembled TCD during system integration in 2012. In this view, light-guides appear as the 8 inverted black triangle-like shapes lining the upper section of the instrument, while concentrator stacks are visible as the white boxes positioned between them.

When charged particles pass through plastic scintillator, their Coulomb interactions with the scintillator's atomic electrons result in the production of optical photons. To first order, the number of photons generated should be proportional to the energy deposited in the scintillator, as described by the Bethe-Bloch formula, which Leo [47] writes as (for energy loss per unit distance traveled in the material),

$$-\frac{dE}{dx} = 2\pi N_a r_e^2 m_e c^2 \rho \frac{Z_T}{A_T}\frac{Z^2}{\beta^2}\left[ln\left(\frac{2m_e\gamma^2 v^2 W_{max}}{I^2}\right) - 2\beta^2\right] \tag{2.1}$$

Here, N_a is Avogadro's number. The quantities r_e and m_e are the classical electron radius and mass, respectively, while Z_T, A_T, and ρ are the target material's atomic number, atomic weight, and density, respectively. The "mean excitation potential", I, is mainly a function of Z_T, and has been measured experimentally for a variety of materials [48]. The quantity $\beta = v/c$ is the primary particle's relativistic speed v normalized to the speed of light c, while $\gamma = (1-\beta^2)^{-1/2}$ is its Lorentz factor, which is related to particle kinetic energy by the relation $E_K = mc^2(\gamma - 1)$, m being the particle's rest mass. W_{max} is the energy transferred in a "head-on" collision, which, for the case of hadronic cosmic rays, where the primary particle's mass is much greater than the electron mass, is well approximated by $W_{max} \approx 2m_e c^2\beta^2\gamma^2$. For the purposes of building a charge detector, the most important feature of Equation 2.1 is its proportionality to Z^2, which dictates that energy deposit is highly sensitive to the primary particle's charge.

An ideal charge detector would be insensitive to primary particle β, and thereby γ. However, examination of Equation 2.1 shows that this is clearly not the case. Figure 2.4 plots energy

[2]The TCD is described here with the goal of providing a detector overview. However, because the design, construction, and support of the TCD forms a significant portion of the work for this thesis, its implementation details will be presented more fully in Chapter 4. Furthermore, significant TCD hardware and software upgrades have been performed for the BACCUS (see Chapter 3) mission. These are described in detail in Chapter 5.

[3]In some configurations, the alternative but essentially equivalent formulations BC-408V and EJ-200 are used instead.

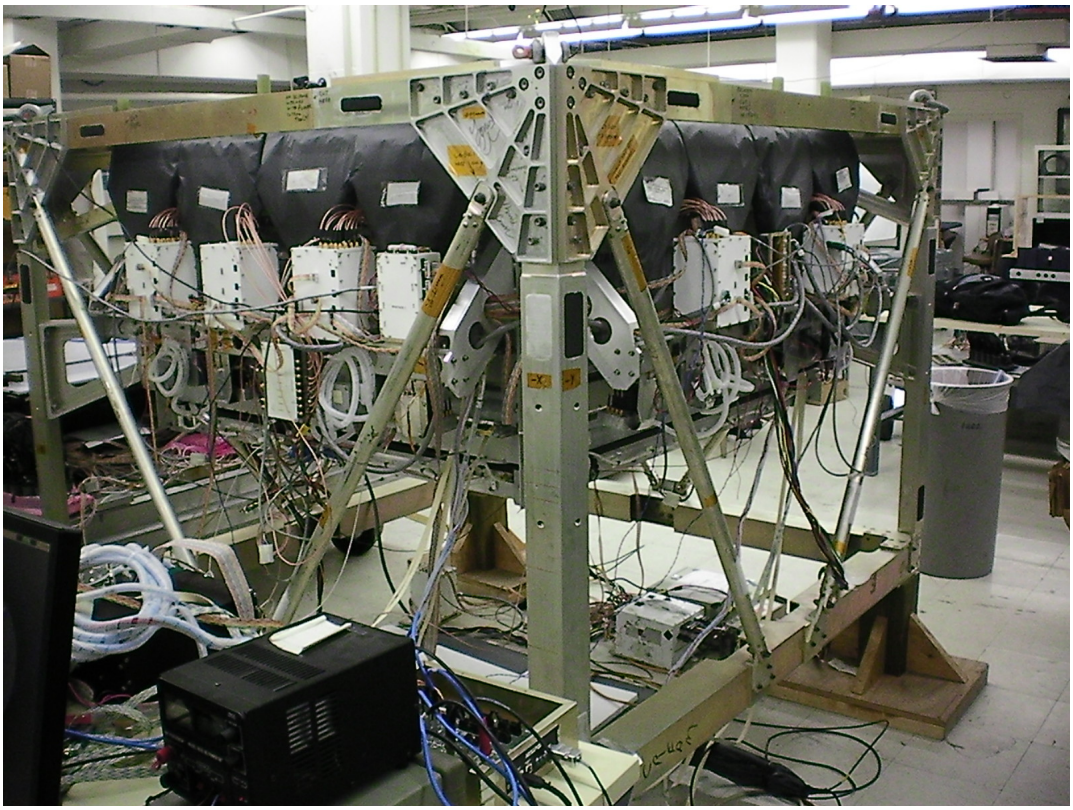

Figure 2.3. The TCD during 2012 BACCUS (see Chapter 3) instrument integration at the University of Maryland.

deposit in the TCD (normalized by Z^2) versus primary particle γ for carbon atoms, as predicted by a detailed instrument monte carlo simulation performed in GEANT4 [49].[4] This "response function" plot exemplifies the main features of Equation 2.1. At low energies, Equation 2.1 displays an inverse relationship between energy deposit and particle velocity, dominated by β^{-2} behavior. This behavior continues until an ionization minimum is reached, which occurs near $\log_{10}(\gamma) \sim 0.6$. Above this minimum ionizing point, β is near 1, and so, Equation 2.1 predicts a slowly rising, logarithmic relationship between energy deposit and particle γ. The combination of a strong dependence on primary cosmic-ray charge and a weak dependence on particle γ above the point of minimum ionization is exactly what makes plastic scintillator an excellent medium for the determination of charge for the relativistic hadrons of interest to the CREAM experiment.

The detailed response of the TCD's scintillator deviates from that predicted by Equation 2.1 in two key ways. The so-called "density effect" [50] results from the fact that highly energetic particles tend to polarize the atomic electrons local to their path, which in turn shields more distant electrons from the primary particle's influence. The density effect is included in GEANT4's physics models, and accounts for the flattening of Figure 2.4 above $\gamma \sim 1.5$. Moreover, an effect

[4]This GEANT4 model of the CREAM instrument was developed and is maintained by CREAM TCD collaborator Professor S. Nutter of Northern Kentucky University.

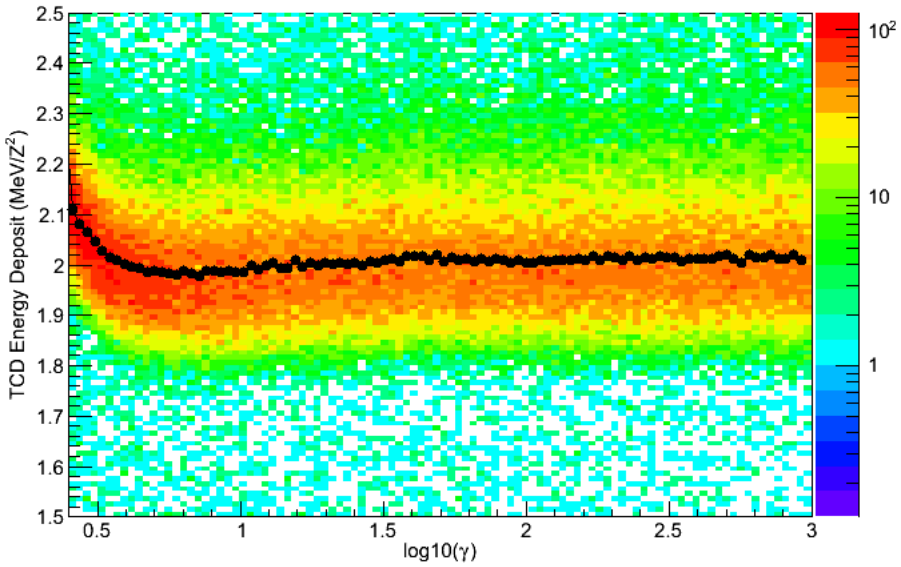

Figure 2.4. The normalized TCD response function, which is derived from the predicted energy deposit of carbon nuclei passing through the TCD. Solid black circles represent the means obtained from a Gaussian fit to the data in each abscissa bin, projected into a 1-dimensional histogram.

known as "scintillator saturation" [51] causes energy deposit to be dissipated non-radiatively for high Z particles, leading to a greatly decreased response for cosmic rays with Z approaching 26 (iron). Conklin [52] has successfully accounted for the effects of scintillator saturation in the response of the CREAM I TCD by fitting the Birks-Tarle-Voltz model [53] to the various charge peaks seen in the flight data.

The interactions of cosmic rays in CREAM's calorimeter tend to create many $Z = 1$ secondary particles. Some of these secondary particles back-scatter into the TCD, and so, may generate delayed scintillation light. However, the ∼100 cm separation between the TCD and the top of the calorimeter means that even the fastest back-scattered particles arrive several nanoseconds after the passage of the primary cosmic ray. Thus, a high speed measurement which completes within a few nanoseconds of the passage of the primary particle will be free of back-scatter contamination. Considering the 0.9 ns rise time of the TCD's BC-408 plastic scintillator, such a fast measurement is feasible, given sufficiently high-speed electronics.

This high-speed electronics requirement manifests in the form of the TCD's ultrafast ***peak detector*** circuits and its high speed ***time-to-digital converter*** (TDC) circuits. Peak detector circuits keep a free-running measurement of the maximum amplitude of the signals from each PMT pulse, and, with a slew rate near 1 V/ns, easily track PMT pulse heights. TDC circuits operate in pairs, each maintaining a differing discriminator threshold on the PMT signal. When a threshold crossing is detected, the TDC circuit starts a precision (roughly 200 ps resolution) clock. All of the TCD's TDCs are later stopped at the same instant, and signal rise time can be

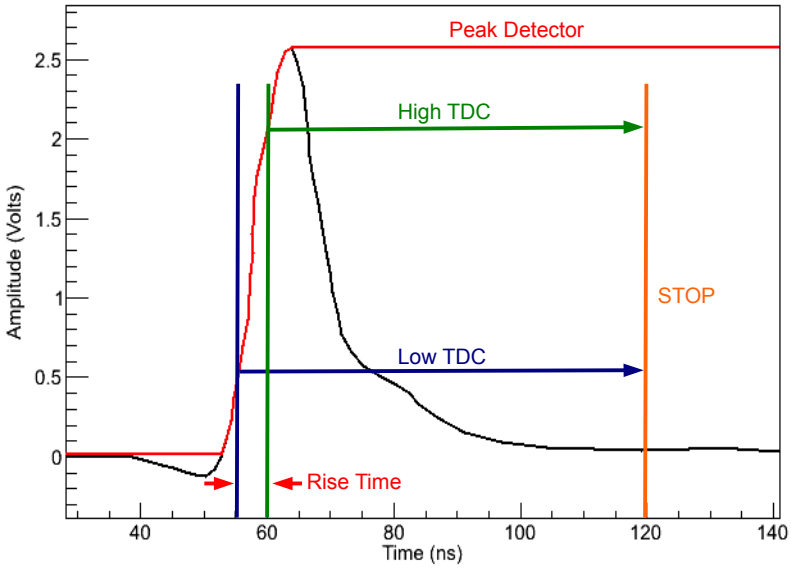

Figure 2.5. Action of the TCD peak detector and TDC circuits on PMT signals. Shown here is the dynode signal, where the anode would produce a signal with negative polarity.

determined from the difference in the resulting TDC values. Figure 2.5 illustrates the action of peak detector and TDC circuits graphically.

CREAM's goal of measuring spectra for charge species up to iron means that the TCD requires a dynamic range of roughly $Z_{Fe}^2/Z_H^2 = 676$. Because measurements from a single PMT anode would saturate over such a large signal range, multiple dynode taps are read out, with each tap corresponding to either a single peak detector circuit or a pair of TDC circuits. Table 2.2 details the mapping of TCD PMT signal taps and lists the target charge range in each case. Originally, TDC0 and TDC1 were planned for proton/helium discrimination, the thought being that the $Z_{He}^2/Z_p^2 = 4$ times larger signal generated by helium nuclei should correspond to signal rise times significantly smaller than those observed for protons. However, analysis by S. Mognet [54] of the CREAM I–II TDC0 and TDC1 flight data revealed no separation between proton and helium populations. Using a detailed optical simulation of the TCD, Mognet has traced this lack of differentiation to the statistical nature of photon arrival times at the face of the PMT. Thus far, no means of deriving separate proton and helium charge populations from the existing TDC strategy has been found. In any case, this charge range is also covered by peak detector measurements on dynode 12.

In addition to measuring signal rise times, TDC differences across paddles (*i.e.*, the paddle's "end-to-end timing" measurement) can be used to derive hit locations in the TCD. This TDC method of hit location determination relies on the fact that, once individual electronics offsets have been removed, the resulting difference in TDC values between two PMTs viewing the

PMT Tap	Readout	Z Range
Anode	TDC0/TDC1	$1 \leq Z \leq 2$
Dynode 12	PD0	$1 \leq Z \leq 2$
Dynode 11	TDC2/TDC3	$Z \geq 4$
Dynode 10	PD1	$2 \leq Z \leq 10$
Dynode 9	PD2	$10 \leq Z \leq 14$
Dynodes 7	PD3	$Z > 14$

Table 2.2. TCD PMT gain stages.

same TCD scintillator paddle is proportional to the hit location's distance from paddle center. By using TDC information from both the X and Y layers of the TCD's scintillator paddles, Mognet has shown that TCD hit position can be determined accurately with ∼3.0 cm position resolution [54]. For flights where no TRD was present, and thus where no TRD tracking could provide an extrapolated TCD hit localization, the resulting timing-derived hit location can be used to generate mapping corrections in the TCD. When combined with hit location information from one or more other CREAM detectors, it can be used to generate pathlength corrections. Figure 2.6 presents the method of TCD hit determination via end-to-end timing measurements diagrammatically.

The placement of a scintillating fiber detector, known as the "S3 detector", just above the CREAM calorimeter also allows the TCD's TDCs to be used in determining whether particles were downward going or upward going. The S3 detector is shown in Figure 2.7. It is composed of a row of 2 mm x 2 mm square scintillating fibers, held taut in an aluminum frame. The light produced in S3's fibers is read out on two sides using the same XP2020 PMTs and electronics which read out the TCD scintillator paddles. If T_{tcd} is the offset-corrected average of the TDCs for a hit TCD paddle, and T_{s3} is the offset-corrected average of the TDCs from the two S3 PMTs, then the distribution $T_{tcd} - T_{s3}$ should be bimodal, with the population of larger mean time (typically positive) corresponding to the downward-going particles of interest to CREAM, and the population of smaller mean time (typically negative) corresponding to upward-going particles which are, most likely, back-scattered $Z = 1$ secondaries from the calorimeter's shower (or alternatively albedo particles from the atmosphere underneath the instrument).

The charge-measurement capabilities of the TCD were verified during a pre-flight beam test at the European Organization for Nuclear Research (CERN) in the H2 beam line [55]. Fragments from a 158 GeV/n indium beam were fired at two crossed TCD paddles. The results suggested charge resolutions of 0.2 charge units (cu) for oxygen and 0.35 cu for iron were possible [56]. However, such impressive charge resolution requires precise particle tracking in order to generate TCD detector pathlength and non-uniformity corrections. For analysis of the CREAM I data, Conklin used the TRD's ∼1 mm track resolution to obtain charge resolutions very close to those predicted by the CERN data—0.20 cu for oxygen, and 0.42 cu for iron [52]. However, the absence of a TRD in subsequent flights meant that an alternate method of deriving particle track information was required. For analysis of the CREAM II TCD charge data, Mognet used

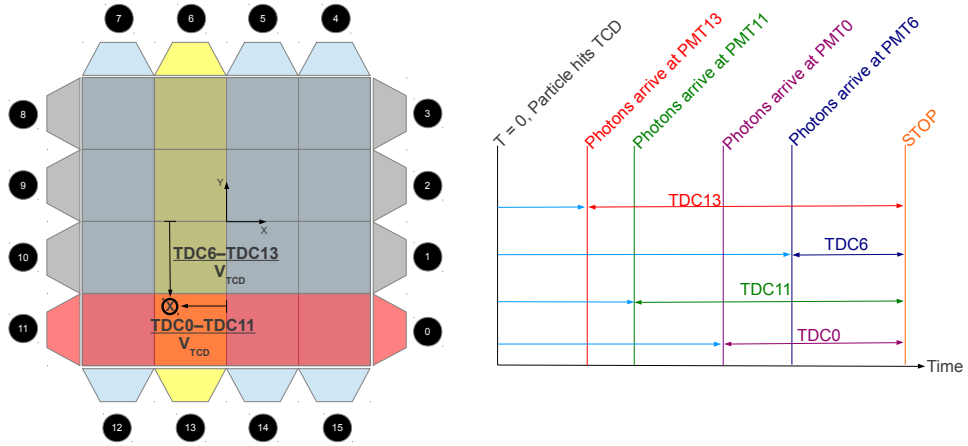

Figure 2.6. The use of TCD's end-to-end timing measurement in determining hit location is demonstrated graphically. On the left, a cosmic-ray hit (circled X) generates light in both an X paddle (salmon) and a Y paddle (maize). On the right, a timing diagram depicts the time required for light to reach each PMT (light blue arrows), with the corresponding timing marker for the start of each TDC signal shown as a color coded vertical line. The resulting TDC0-TDC11 end-to-end timing is proportional to the X hit location, as referenced from paddle center. Likewise, the resulting TDC6-TDC13 end-to-end timing is proportional to the Y hit location, as referenced from paddle center. Formally speaking, the mean group velocity of light propagating in the paddle, V_{TCD}, is required in order to convert end-to-end timing to hit location. In reality, this conversion can be performed either by 1.) comparing the end-to-end timing information with other detector systems which make a calibrated position measurement (*e.g.*, the TRD or calorimeter) or, 2.) by using the shapes of the resulting TDC distributions to identify markers of known position (*e.g.*, the ∼1 mm gaps between adjacent TCD paddles).

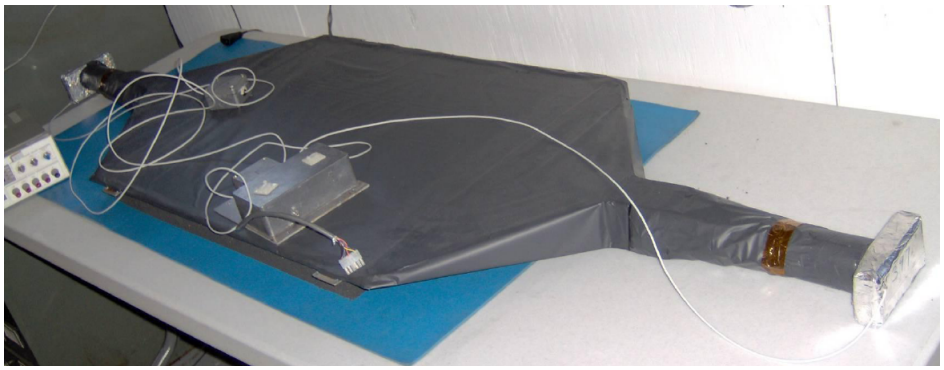

Figure 2.7. The S3 detector.

correlated hit positions in the TCD and SCD to generate particle tracking information, which yielded a somewhat reduced charge resolution of 0.42 cu for oxygen, the highest Z charge species studied in that analysis [54].

The TCD's fast response characteristics also make it ideal for use in CREAM's event trigger formation. The TCD provides two hardware trigger flags, ***RAWZLo*** and ***RAWZHi***, to CREAM's trigger electronics, which, as will be discussed in Section 2.7.2, are used as part of the trigger formation decision. The RAWZLo flag is formed from the three-fold coincidence of TDC0 discriminators firing from at least three sides of the instrument while also having at least one of S3's TDC0s active. Because threshold values for TDC0 are set to roughly 1/2 the pulse height expected for a proton, RAWZLo is generated for all charged particles in geometry for both the TCD and S3. The RAWZLo rate is typically in the range of several kilohertz during flight. The RAWZHi flag is formed from the three-fold coincidence of TDC2 firing from three sides of the instrument while also having the sum of all CD PMTs above a programmable threshold. It is typically tuned to trigger near $Z = 3.5$, such that triggers for boron nuclei ($Z = 5$) are detected with 100% efficiency. The RAWZHi rate is typically near 30 Hz in flight. The hardware implementation details of RAWZHi and RAWZLo formation are discussed fully in Section 4.6.

2.3 The TRD and CD

The TRD and CD provide the primary energy measurement for the upper structure detectors. The composition of the TRD is divided between identical "upper" and "lower" TRD modules. Inside each module are four 120 cm $\times$ 120 cm blocks of Dow Ethafoam 220, each embedded with two rows of 32 proportional tubes. The proportional tubes are 2 inches in diameter and are constructed from thin-walled aluminized mylar, with the tube's central sense wire held at $\sim$1.5 kV relative to the grounded tube walls. The positions of the two layers of proportional tubes inside each foam block are laterally offset from each other, such that any particle passing through the TRD intersects at least one tube in each foam block, hence providing a minimum of 8 separate proportional tube measurements in each event. The orientation of consecutive foam blocks inside each TRD module rotates by 90°, such that incident cosmic rays encounter alternating rows of y-going, x-going, y-going, etc., proportional tubes as they traverse the TRD. During flight, the proportional tubes are filled with a 95% xenon and 5% methane gas mixture. Signals from the sense wires of the proportional tubes are read out by CERN's AMPLEX 1.5 charge-integrating, application specific integrated circuits (ASICs) [57]. The CD is sandwiched between the upper and lower TRD modules, and is composed of a large slab of acrylic plastic viewed by eight XP1910 PMTs through wavelength shifting bars. Figure 2.8 shows a side view of the CREAM I instrument, as modelled in the geometry file for the instrument monte carlo simulation. The outline of the TRD is shown in blue, while the placement of its staggered proportional tubes is shown as filled green circles. The placement of the CD is denoted by the yellow box seen between the two modules.

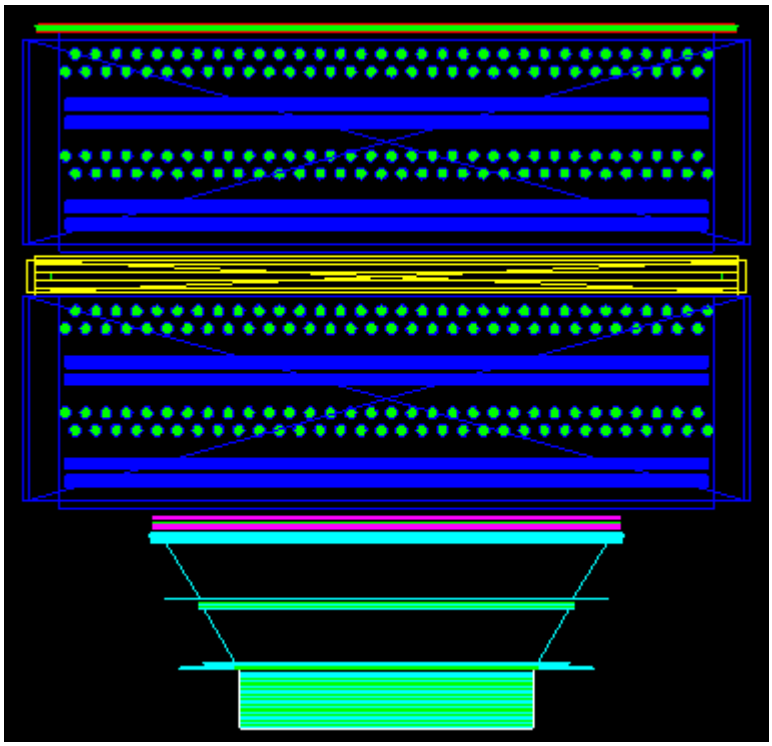

Figure 2.8. The CREAM instrument as modelled in the instrument monte carlo simulation. The TRD can be seen in blue, with its perpendicular layers of proportional tubes filled in as solid green circles. The CD is shown as the yellow box positioned between the two detectors.

The response functions of the TRD and CD are shown in the left and right sides of Figure 2.9, as derived by Conklin [52] from a combination of instrument monte carlo simulations and CERN beam test results [58]. Below $\gamma \sim 10^3$, the TRD's response is dominated by ionization losses, and so, is well described by the Bethe-Bloch equation presented in Section 2.2. The properties of the xenon/methane gas mixture used in the TRD lead to values of the constants in Equation 2.1 which cause TRD signals to vary noticeably over the γ range of interest to CREAM. The overall Z^2 scaling behavior of the Bethe-Bloch equation means that an estimate of primary particle charge (*a la* the TCD) is required in order to derive particle γ from the TRD's signal. Above $\gamma \sim 10^3$, the TRD's response becomes dominated by the production of "transition radiation", a phenomenon which occurs as the result of the cosmic ray abruptly crossing numerous boundaries between alternating materials of differing dielectric constants [59].[5] These transitions create an oscillating electric field in the material, thereby generating X-ray radiation, which in turn greatly enhances gas ionization in the proportional tubes. The combination of a sensitivity to particle Lorentz factor and multiple measurements via two identical TRD modules makes the TRD useful in energy determination above the point of minimum ionization.

[5] In the case of the TRD, this abrupt boundary crossing is generated by the material-to-air-bubble transitions in the TRD's foam block radiators.

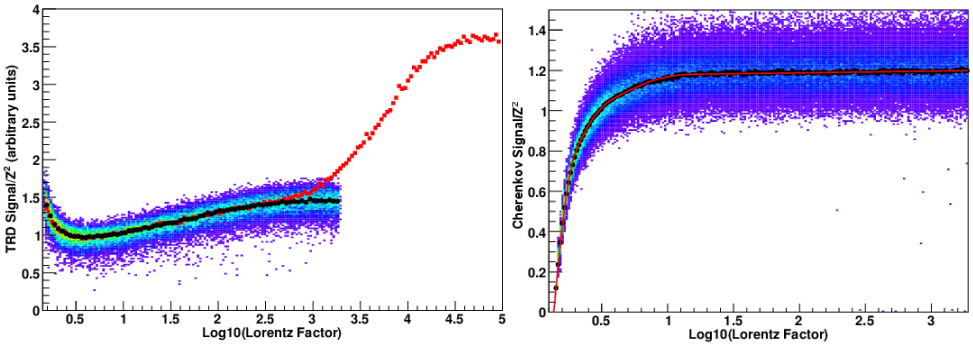

Figure 2.9. The TRD (left) and CD (right) response functions for carbon nuclei, as derived by Conklin [52] from a combination of S. Nutter's instrument monte carlo simulations and a detector beam test at CERN. Black dots correspond to the means obtained from a Gaussian fit to simulation data in each abscissa bin, projected onto a 1-dimensional histogram. On the left, the addition signal enhancement caused by the onset of transition radiation near $\gamma = 10^3$ measured in the TRD's CERN beam test [58] is depicted by red squares.

On its own, the TRD's signal is insufficient to uniquely determine primary particle γ, since, as can be seen from the left side of Figure 2.9, the same TRD signal corresponds to a Lorentz factor both above and below the point of minimum ionization. This degeneracy in the TRD's response is broken by the CD, whose response function, shown on the right side of Figure 2.9, is a steeply increasing function of γ, which begins to saturate near $\gamma = 0.5$. Cherenkov light is generated by the constructive interference of the electric field induced in a medium by a charged particle travelling faster than the speed of light in that medium. In the limit of an infinite radiator, $\beta > 1/n$ is the condition for the onset of Cherenkov radiation, where n is the index of refraction of the radiating medium. The resulting Cherenkov radiation will then be emitted in a forward going cone, with opening angle $\cos(\theta_c) \sim (\beta n)^{-1}$. Leo [47] writes the number of photons produced per unit pathlength traveled per unit wavelength of emitted Cherenkov light as

$$-\frac{d^2N}{d\lambda dx} = \frac{2\pi\alpha Z^2}{\lambda^2}\left(1 - \frac{1}{\beta^2 n^2}\right) \tag{2.2}$$

where λ is the wavelength of emitted light, α is the fine structure constant, and $n = 1.5$ for the CD's acrylic radiator. When compared to Equation 2.2, the saturated response of CREAM's CD will be increased somewhat by the generation of delta rays in the upper TRD module.[6] However, the instrument monte carlo simulation includes physics models for delta ray generation, and so, this effect is included in the response function shown in Figure 2.9.

To summarize the discussion of energy determination using the TRD and CD, at low energies, cosmic rays can be identified, and, provided saturation has not become too severe, their energy can be measured by referring to the CD's response function. At energies above the CD's saturation point, cosmic ray energy is derived primarily from the TRD's response. Note that, because the CD has a response function with a γ dependence which differs from that of the

[6]These are secondary electrons which are accelerated to relativistic speeds by head-on collisions with the primary particle. They are then capable of generating their own Cherenkov light as they pass through the CD.

Bethe-Bloch equation, scatter plots of TCD signal versus CD signal are useful in studying the velocity dependence of these detector systems.

In addition to providing an energy measurement, the TRD also serves the important role of a precision tracker for the upper structure detectors. By using a three-stage tracking routine in which the envelope of hit proportional tubes in both the x and y planes is gradually reduced, particle tracks can be determined with 1 mm precision [60]. As mentioned previously, such precise tracking is critical in determining detector pathlength and non-uniformity corrections in the TCD and CD.

The TRD's response function was verified in a 2001 CERN beam test, where a single layer of the TRD was exposed to a range of electrons, protons, and pions with differing radiator thicknesses and foam types [58]. The energy resolution of the TRD was studied by treating the xz and yz planes as independent measures of TRD signal. By using one plane as a "fixed" reference, variations in the other plane can be studied. Since both TRD planes function identically, the combined resolution is decreased roughly by a factor of $1/\sqrt{2}$ relative to the resolution of a single plane. An energy resolution of $\sim$10% was found for oxygen nuclei [60].

2.4 The SCD

The SCD provides CREAM with a charge detector capable of a high degree of pixelation. A single layer of the SCD is 77.9 cm $\times$ 77.5 cm in active area, and is composed of 182 silicon detectors of dimension 1.55 cm $\times$ 1.37 cm $\times$ 0.38 mm, arranged in a rectangular 13 $\times$ 14 grid. Each silicon wafer contains 16 pixels, and is read out by a 16-channel AMPLEX CR-1.4 charge integrating ASIC circuit [61] mounted on a PCB which is positioned directly below each sensor. Digital control boards are placed at the edges of the detector in order to readout the ASICs and distribute power and high-voltage bias to the ASIC boards. For CREAM I, only a single-layer SCD was present. However, the SCD was upgraded to two layers for all other CREAM flights. Figure 2.10 shows the dual-layer SCD with its dust cover removed. [62]

The SCD's silicon sensors are operated as PIN diodes with 100 V reverse bias. Only a small leakage current is present under normal conditions. However, when a cosmic ray passes through the sensor, the resulting ionization generates electron-hole pairs which are accelerated by the bias field, thereby forming the charge-pulse which acts as the SCD's signal. Because the SCD's signal is created by ionization from the cosmic ray, it is described by Equation 2.1, and so derives its charge detection capability from the previously discussed combination of a Z^2 dependence on charge and a relatively flat response with energy. The pixelated nature of the SCD renders it relatively immune to backscattered secondaries from calorimeter showers for primaries with $Z \geq 3$, since these secondaries are mostly $Z = 1$, and so, should create a quite small signal when compared to the primary cosmic ray. For protons and helium, the calorimeter's reconstructed particle track can be used to identify the SCD's hit pixel, with a very low probability of encountering a back-scatter particle which has the "just right" trajectory to intersect the same pixel as was hit by the primary cosmic ray.

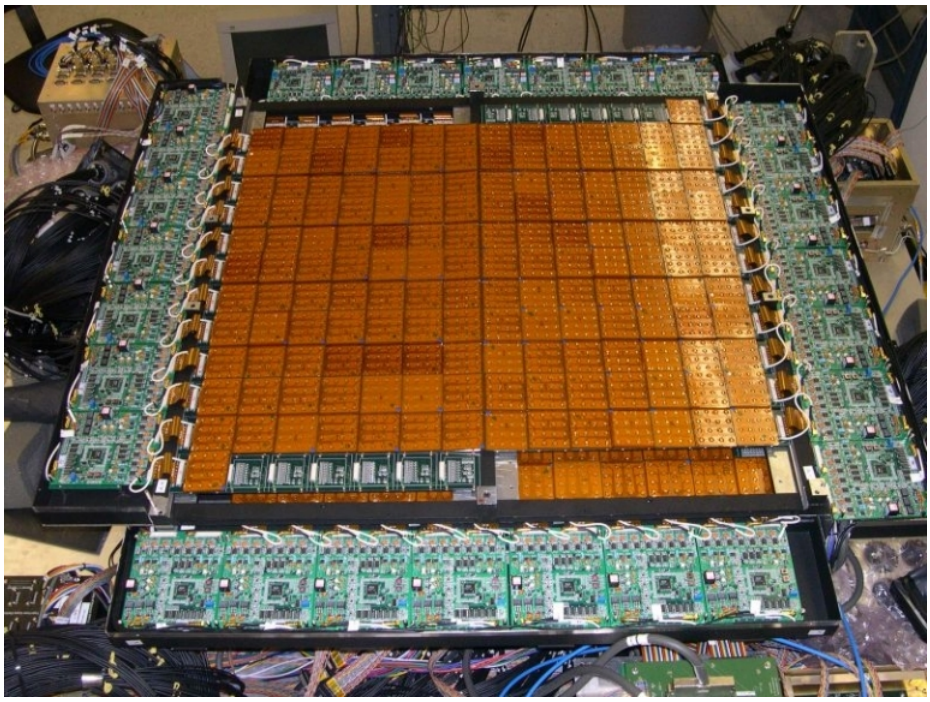

Figure 2.10. The dual-layer SCD with its dust cover removed. Several silicon sensors at the bottom of the figure are missing, revealing the underlying charge integrating ASIC boards. Digitization electronics can be seen at the edges of the detector.

The SCD's charge measurement capabilities were verified in the CERN H2 beam line [55] using a fragmented 158 GeV/n indium beam. The stated charge resolution from this test was 0.1 cu for helium nuclei and 0.3 cu for iron [63]. Analysis of SCD data from the first two flights has yielded a charge resolution near 0.2 cu for most charge species [64].

2.5 The Calorimeter

The CREAM calorimeter detector system is shown in Figure 2.11. Two densified graphite targets (the so-called "carbon targets"), each 9.5 cm thick, are mounted over a 20-layer tungsten scintillating fiber calorimeter. The sides of the carbon targets are flared so as to maximize geometrical acceptance in the calorimeter. The calorimeter's tungsten plates are 50.1 cm $\times$ 50.1 cm $\times$ 3.5 mm, with 0.5 mm thick scintillating fiber ribbons sandwiched between each tungsten plate. The x or y-going directions of the fibers in each layer alternate between layers, thus allowing three dimensional shower imaging and track reconstruction. The scintillation light generated by the secondary particles produced in calorimeter showers is piped to a readout module based around ten 73-pixel Delft Electronics Products BV PP0380BB hybrid photo-diodes (HPDs) through a 48-strand, fiber-optic cable [65]. In order to achieve the calorimeter's full dynamic range requirement, three gain stages are implemented via a combination of division of the 48 fibers (37+5+1, with 5 fibers not readout) and optical neutral density filters. The IDEA's VA32HDR2, a 32-

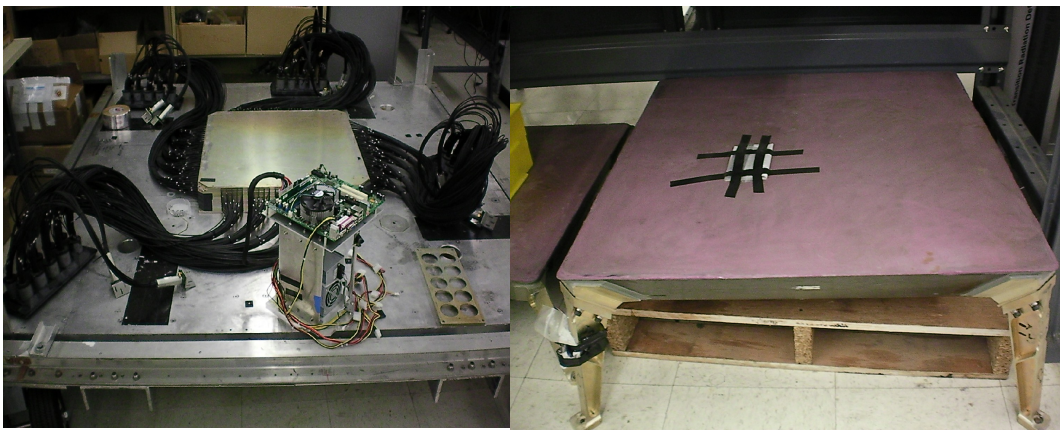

Figure 2.11. The CREAM calorimeter (left) and one carbon target (right).

channel, high dynamic range (effectively 11-bit), charge-sensitive amplifier, reads out each HPD module [66]. The calorimeter's trigger flag is formed via the IDEA's TA32C discriminator chip, which allows implementation of a programmable multi-layer trigger condition. In flight, this trigger condition is set to require >40 MeV in at least six consecutive layers of the calorimeter [67].

The 9.5 cm thickness of each of the carbon targets correspond to roughly 1/2 of a nuclear interaction length, thereby serving to initiate shower development. For the TeV/nucleon particles of interest to CREAM's calorimeter, simulations show that roughly 1/2 of all protons will interact in these carbon targets [65]. Graphite was chosen because it combines low mass (which is critical for ballooning) with a relatively short nuclear interaction length (which allows increased geometrical acceptance through a squat target design). Shower development in the calorimeter's tungsten plates can be thought of as the gradual dissolution of the cosmic ray's energy over N secondary particles, where the average secondary carries E/N of the primary particle's energy. Considering the electromagnetic core of the shower, which is the dominant shower component imaged by CREAM's calorimeter, gamma ray creation via electron bremsstrahlung and subsequent electron and positron pair creation by gamma ray interactions in tungsten are the alternating processes which promote shower growth [8]. The production length for both processes is characterized by X_0, the electron radiation length in matter.[7] When the mean energy of shower electrons reaches the so-called "critical energy", ionization losses begin to dominate bremsstrahlung, and so, shower development ceases [8]. CREAM's calorimeter has an overall sampling fraction near 0.3% and its 20 X_0 depth is sufficient to contain shower maximum for multi-TeV hadronic cosmic rays [65].

The performance of CREAM's calorimeter has been characterized in multiple beam tests. The calorimeter was found to have a 0.15% sampling fraction for protons with energies of 150 GeV, 250 GeV, and 350 GeV, with an energy resolution near 50%. CERN's H2 beam line was used

[7] In a distance X_0, bremsstrahlung causes an electron's energy to be reduced by a factor $1/e$, while a photon's mean free path for pair creation is $\frac{7}{9}X_0$.

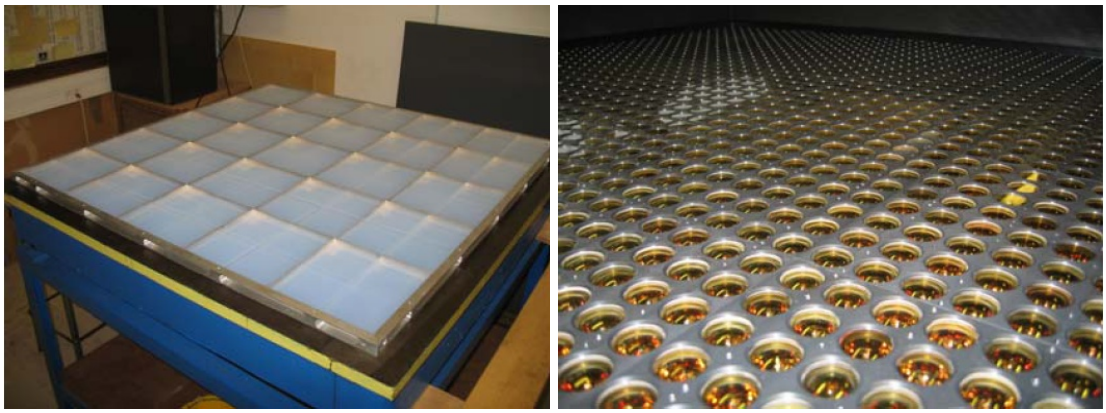

Figure 2.12. The CHERCAM detector's aerogel radiator (left) and PMTs (right).

to study the calorimeter's response to heavy nuclei using a 158 GeV/n indium fragment beam. Energy resolutions of ∼46% and ∼21% were found for carbon nuclei near 1.9 TeV and iron nuclei near 8.2 TeV, respectively [68]. In addition to these performance verification tests, the gain response of the calorimeter's scintillating fiber ribbons was calibrated before each flight in CERN's H2 beam line by performing a 150 GeV electron beam scan, stepped along the surface of the calorimeter in 1 cm increments [69] [70] [71].

2.6 CHERCAM

CHERCAM is a Cherenkov imaging charge detector, which first debuted as part of the CREAM III mission. Its 110 cm x 110 cm active detector area is composed of 100 squares of 2 cm thick aerogel radiator, each 10.5 cm x 10.5 cm in area, supported by an aluminum frame. A 40 x 40 grid of circular, 1 inch diameter, Photonis XP3112 PMTs situated below the aerogel radiator views the Cherenkov light produced by downward-going cosmic rays through an 11 cm expansion gap. Blocks of 16 PMTs are read out and controlled by a common electronics board, which is based around a 16-channel charge-integrating ASIC[8]. In order to create a compact detector, these readout circuits are positioned just below the PMT plane. Figure 2.12 shows the CHERCAM detector with its dust cover removed [73].

The Cherenkov radiation mechanism was already described in Section 2.3. Its Z^2 dependence is what allows CHERCAM to function as an effective charge detector. CHERCAM also makes use of the fact that emitted Cherenkov radiation forms a forward-going cone with opening angle

$$\theta_c = \cos^{-1}\left(\frac{1}{\beta n}\right) \tag{2.3}$$

where $n = 1.05$ is the index of refraction for aerogel, leading to an opening angle approaching 18° for relativistic particles. By allowing the Cherenkov cone to expand through a 11 cm air gap, at least one (often more) PMT is hit in each event. Also, because Cherenkov radiation is

[8]This is the same ASIC used by the AMS experiment's Ring Imaging Cherenkov detector [72]

emitted in a forward direction, by placing an optical absorber on the lid of the enclosure, the light created by upward-going, backscattered secondaries in CREAM's calorimeter showers is effectively rejected. While an official charge spectrum for CHERCAM has not yet been made public, results from a CERN beam test using pions, protons, and electrons of 100 GeV/c to 300 GeV/c momentum found a charge resolution near 0.2 cu for these $Z = 1$ particles [74].

2.7 CREAM Common Electronics

The so-called CREAM "common electronics" are ancillary systems, designed and maintained by the University of Maryland, which support the main detectors of CREAM. These include the science flight computer (SFC), the instrument trigger system, the power system, and the housekeeping system. Each will be discussed briefly.

2.7.1 The SFC

The CREAM SFC has the responsibilities of dispatching detector commands, reading event data and writing it to disk, and interfacing with the balloon craft[9]. In CREAM I, most detector sub-systems interfaced to the SFC via a PC-104 interface, the main exception being the TCD concentrator stacks, which utilized a TCP/IP over Ethernet readout scheme (see Chapter 4). Starting in CREAM II, the USB 2.0 standard was adopted as the primary instrument interface protocol, with most detector systems gradually changing over to this scheme in subsequent flights. Also starting with CREAM II, redundant SFCs were implemented in CREAM, thereby removing the single-point failure risk of having only one computer.

The SFC uses the Linux kernel. Its primary software routines reside in a package known as the CREAM Data Acquisition software (CDAQ) [75]. Inside the CDAQ, separate processes control the tasks of instrument commanding, detector interfacing, packet parsing, networking, and housekeeping control. For the purposes of modularity and ease of maintenance, the CDAQ is developed using the object-oriented data structures of C++. With each new flight, the CDAQ has undergone extensive revisions necessitated by new detector configurations and improvements deemed necessary as the result of experiences in previous flights.

2.7.2 The Trigger System

CREAM event collection proceeds via formation of an overall instrument trigger, which is determined by the CREAM instrument master trigger board. The instrument master trigger board accepts trigger flags from the TCD, calorimeter, and SFC, and determines event trigger formation based on a group of commandable settings, the sum of which defines the active "trigger modes" which might be used to form an overall instrument trigger. Each trigger mode is based

[9]The Command and Data Module (CDM) in CREAM I–IV and the Science Interface Package (SIP) in CREAM V and VI are the balloon craft control systems used on the CREAM project. Designed and supported by NASA's Columbia Scientific Ballooning Facility (CSBF), these systems manage all aspects of command and data telemetry and balloon craft control.

Mode	CREAM I	CREAM II–V	CREAM VI	Description
ZLo	RAWZLo	RAWZLo	NA	$Z > 1$
ZHi	RAWZHi	RAWZHi	NA	$Z > 3$
ZCLB	software	software	software	calibration
ELo	RAWZLo + S3Hi	RAWZLo + S3Hi	NA	$Z > 1$
EHi	CAL	CAL	CAL	calorimeter trigger

Table 2.3. CREAM trigger modes.

on a set of "trigger conditions" (*e.g.*, trigger flags from CREAM detectors). The set of active trigger modes and their corresponding trigger conditions change from flight-to-flight according to the available instrument detector configuration and science priority for that flight. Table 2.3 enumerates all CREAM trigger modes. A prescalar setting exists for each trigger mode, such that triggers of high scientific interest may be read out preferentially.

The ***ZLo*** and ***ZHi*** trigger conditions reflect the TCD RAWZLo and RAWZHi trigger flags, whose formation was discussed in Section 2.2. In CREAM I, the presence of the TRD meant that energy measurements were possible for events which were out of geometry for the calorimeter, and so, these triggers were of scientific interest, and thus were given a high priority. However, because no TRD was present in subsequent flights, ZHi and ZLo were useful only for TCD and CD calibration, and so, were prescaled to a total rate of roughly 3 Hz. The ***ZCLB*** trigger is used to provide periodic calibration pulses to the SCD and calorimeter systems. The ***ELo*** trigger mode corresponds to events which cross a programmable threshold in S3, known as ***S3Hi***. Because S3 is positioned directly above the calorimeter, the ELo trigger condition can be used to study events which are in-geometry for the calorimeter, but do not meet the minimum energy deposit requirement to trigger it. The ***EHi*** trigger condition corresponds to events for which the calorimeter has six consecutive layers each with >40 MeV energy deposit. EHi was given the highest priority in all CREAM flights, and so, was not prescaled. It has a rate near 1/2 Hz.

A secondary function of the instrument master trigger board is to serially transmit the value of a 32-bit event counter to each detector system, which is incremented for each new event. These "instrument event numbers" are distributed to each detector system via a three-wire protocol, starting at the moment of instrument trigger formation. Each detector system receives the event number and packages it into the event data it sends to the SFC. Event numbers can then be used to verify read out synchronization between detector systems in offline analysis.

2.7.3 The Power System

CREAM power is provided via the +31 V line derived from the balloon craft's solar panels, and regulated by external balloon craft circuitry. Power to each detector system is switchable and fused, allowing the possibility of real-time power cycling during the flight [65]. Inside each detector system, internal regulation and filter circuits convert incoming +31 V to the levels necessary to operate that system.

2.7.4 The Housekeeping System

CREAM's common electronics also includes an analog housekeeping system, whereby all detector systems may send the outputs of sensors which monitor detector health for real-time feedback in flight. Converted voltage levels, current draws, high voltage monitors, temperature sensors, and pressure sensors are all examples of the values monitored by the housekeeping system. Housekeeping data is downlinked every 5 seconds during flight.

Chapter 3

CREAM Science Results and Upcoming Missions

A review of CREAM science results published to date will be presented, and these results will be examined in the context of their broader relevance to cosmic-ray physics. In addition, CREAM's soon-to-be deployed Boron And Carbon Cosmic rays in the Upper Stratosphere (BACCUS) campaign will be described, and the ISS-CREAM mission—a ruggedized version of CREAM, bound for the International Space Station in 2014—will be discussed.

3.1 CREAM Primary Cosmic Ray Spectra

Multiple papers have been published updating the on-going process of extracting cosmic ray spectra from the CREAM I and CREAM II calorimeter data. As a first step for these analyses, particle tracks through the calorimeter are reconstructed via a χ^2 fit to the hit pattern and signal magnitudes observed in each layer of the calorimeter. This tracking data is then used to calculate pathlength corrections on the SCD data. Charge peaks are identified via multi-Gaussian fits to the combined signals from both layers of the SCD (for CREAM II, the single layer SCD for CREAM I). Figure 3.1 shows the resulting SCD charge histograms as obtained from the first and second CREAM flights. A charge resolution of 0.15 cu has been found for protons, while a 0.2 cu resolution has been obtained for helium, carbon, nitrogen, oxygen, neon, magnesium, and silicon. A $\sim$0.5 cu resolution was found for iron [64] [76] [77]. While the relative abundance of the elements shown in the figure requires additional corrections, a rough correspondence to the general features of Figure 1.1 (*i.e.*, the odd-even effect and the prevalence of cosmic-ray secondaries relative to primaries) is apparent.

Cosmic-ray energy is determined by correlating calorimeter total energy deposit with calibration data from beam tests at CERN and a FLUKA [78] monte carlo simulation. Corrections for energy misidentification, track-reconstruction efficiency, charge-identification efficiency,

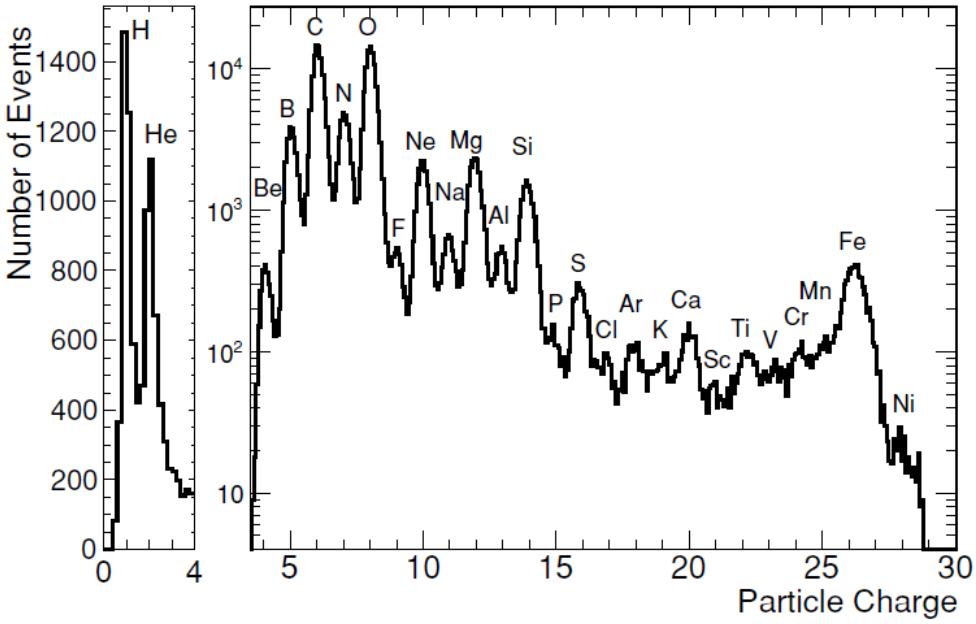

Figure 3.1. SCD charge spectra from CREAM I and II calorimeter-based analyses [64].

quality-cut efficiency, and charge-changing interactions above the SCD are also calculated via the calorimeter's FLUKA simulation.

Figure 3.2 compares CREAM's proton spectrum (left) and helium spectrum (right) with selected results from other recent experiments. The error bars shown for CREAM are statistical only, as systematic errors have been folded into the uncertainties reported on the fits to spectral-indices (see below). All flux measurements are scaled by energy to the 2.7^{th} power in order to facilitate visual comparison of the datasets.

CREAM's role in the broader context of current global efforts to measure cosmic-ray proton and helium spectra is demonstrated well by this figure. Below 1 TeV/n, the Balloon-borne Experiment with a Superconducting Spectrometer (BESS), the Payload for Antimatter-Matter Exploration and Light-nuclei Astrophysics (PAMELA), and the Alpha Magnetic Spectrometer (AMS-02) demonstrate small uncertainties, but are limited in their energy reach.[1] Measurements from the Advanced Thin Ionization Calorimeter (ATIC) help span the range between 50 GeV/n and 30 TeV/n.

[1]Below 10 GeV/n, variations in the fluxes reported by these three experiments can be attributed to their measurement periods occurring in different parts of the solar cycle. However, PAMELA and AMS-02 do show some disagreement in the energy range 100 GeV/n to 1 TeV/n, with PAMELA reporting changes to softer spectra at 80 GV (they report in units of rigidity since they are a magnetic spectrometer-based experiment), followed by significant hardening at larger rigidities (∼232 GV for protons and 243 GV for helium). The AMS-02 collaboration has not yet reported spectral indices on their preliminary data, however, it clearly shows fewer features. The cause of this discrepancy is currently a mystery.

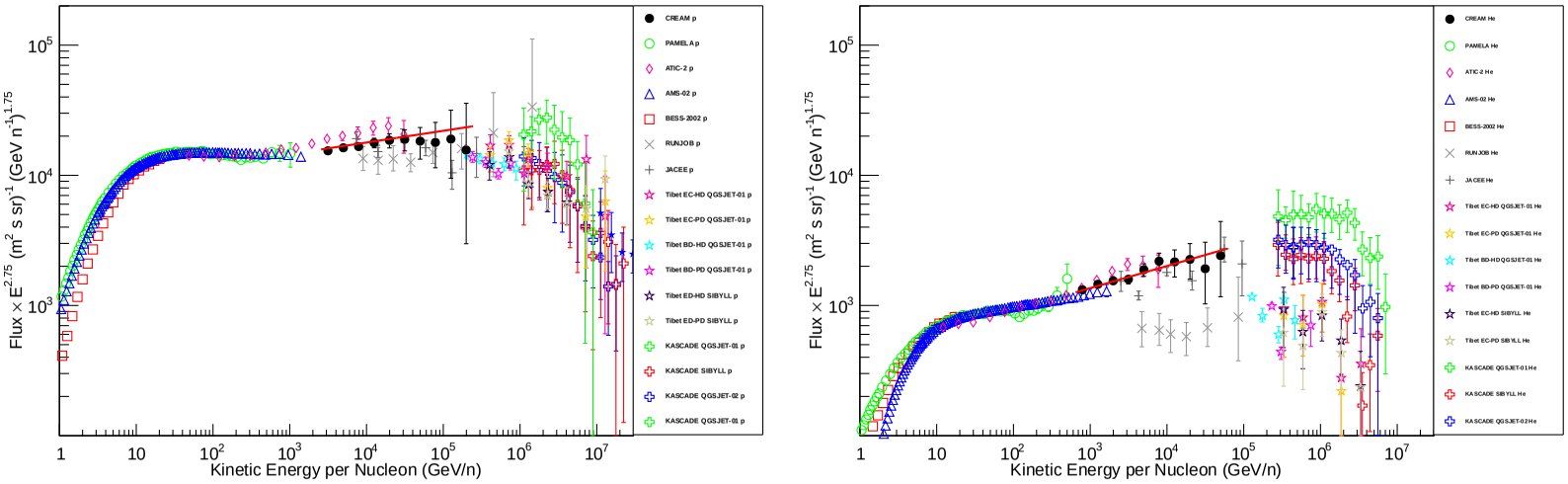

Figure 3.2. CREAM's proton (left) and helium (right) spectra are compared to direct measurements from PAMELA [79], ATIC [80], AMS-02 (preliminary) [81], BESS-2002 [82], RUNJOB [83], and JACEE [84]. Also shown are recent results from the Tibet Air Shower Array [85] and KASCADE [40]. Red lines represent fits to the CREAM spectra.

Measurements above 300 TeV/n are covered by a number of air-shower experiments, and recent results from the Tibet Air-Shower Array and KASCADE are included in Figure 3.2 in order to represent indirect measurements at high energies. As can be seen, both experiments demonstrate strong dependencies on the hadronic physics model employed (SIBYLL, QGSJET-01, or QGSJET-02), since they are indirect, ground-based experiments, leading to significant uncertainties in the final results.

The highest-energy direct measurements performed to date have been by CREAM and the nuclear emulsion-based calorimeter experiments. Results from the most recent emulsion experiments, the Japanese-American Collaborative Emulsion Experiment (JACEE) and the RUssian Nippon JOint Balloon experiment (RUNJOB), are shown in Figure 3.2. The JACEE and RUNJOB experiments mounted long series of high-altitude balloon flights over the course of many years in order to obtain their significant high-energy reach. However, the charge resolution of these experiments is systematically limited by the uncertainty inherent in deriving composition information from emulsion-track grain densities. Thus, in making a direct-measurement of elemental spectra up to 10^{15} eV, CREAM serves a unique role in extending the reach of direct detectors, while also anchoring the indirect measurements of air-shower arrays.

Fits to the CREAM spectra for protons and helium are shown as solid red lines in Figure 3.2. In the energy range 2.5 TeV/n to 250 TeV/n, the proton spectrum was fitted and found to have a spectral index of 2.66 $\pm$ 0.02, while in the energy range 0.63 TeV/n to 63 TeV/n, the helium spectrum was fitted and found to have a spectral index of 2.58 $\pm$ 0.02 [76]. Thus, the spectra of protons and helium differ outside of the errors, and from the figure, it is also clear that both spectra are significantly harder than those seen below 100 GeV/n. Differing spectral indices were first reported by the JACEE collaboration [84]. The ATIC experiment also reports differing spectral indices for protons and helium, and their data also shows signs of hardening above 200 GeV/n [80]. Recent results from the PAMELA collaboration report significant spectral hardening for both proton and helium spectra near 240 GV, with a proton spectral index of 2.67 $\pm$ 0.03 (stat) $\pm$ 0.05 (sys) and a helium spectral index of 2.48 $\pm$ 0.06 (stat) $\pm$ 0.03 (sys) above the break point. The spectral indices reported by PAMELA are compatible with those found by CREAM within errors [79].

Figure 3.3 compares CREAM's primary spectra [77] for carbon, oxygen, neon, manganese, silicon, and iron to those obtained by ATIC [86], the Spacelab-2 Cosmic-Ray Nuclei experiment (CRN) [87], the High-Energy Astrophysical Observatory-3 C2 experiment (HEAO-3-C2) [88], and TRACER [15] [89]. All spectra fit well to a power-law, with a spectral index ranging between 2.61 $\pm$ 0.07 and 2.72 $\pm$ 0.10, in good agreement with previous measurements. While the statistical yield from any one of these primary spectra is somewhat low, fitting all heavy spectra together suggests a hardening above 200 GeV/n [64], providing the first hints of structure at high energies in heavy nuclei.

Taken together, the measurements discussed here are demonstrating subtle structure in cosmic-ray spectra which were previously unobserved. Theories have proliferated which attempt to explain the spectral hardening observed by PAMELA, ATIC, CREAM, and JACEE, some of

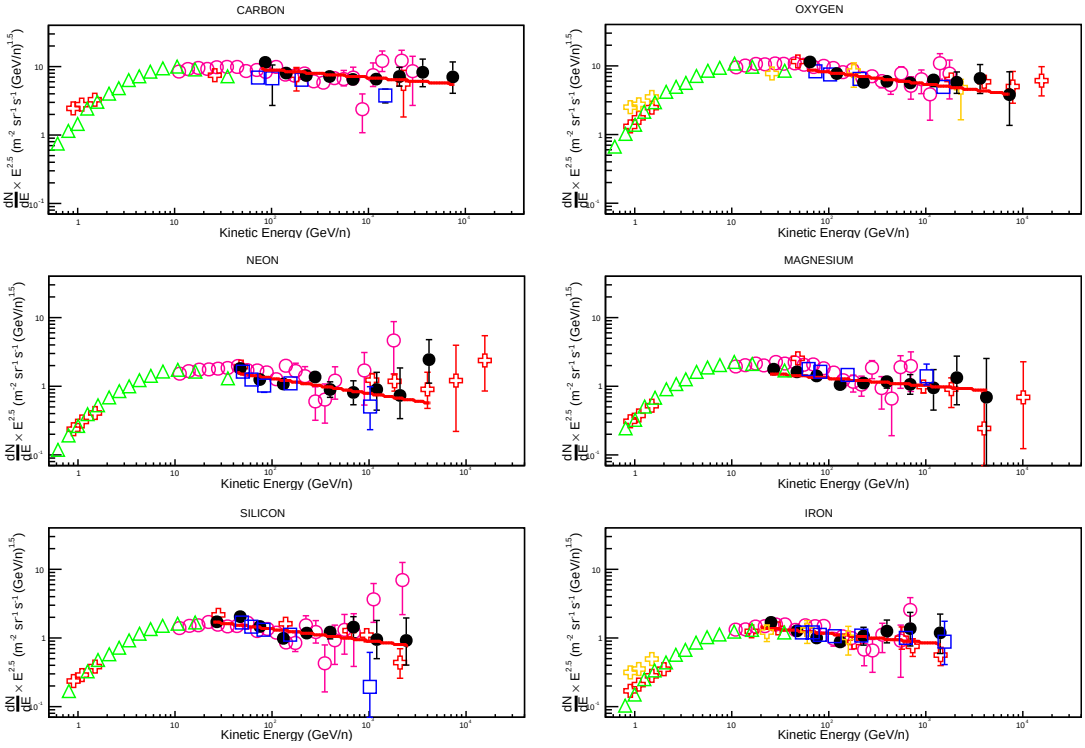

Figure 3.3. Measurements of spectra from the CREAM calorimeter-based analysis of heavy primary events (black, filled circles) [77] are compared with those from, ATIC [86] (pink, open circles), CRN [87] (blue, open squares), HEAO-3-C2 [88] (green, open triangles), and TRACER [15] [89] (red, open crosses). Red lines represent fits to the CREAM spectra.

which are discussed below. As will be seen, most theories invoke some combination of the source environment of cosmic rays, the dynamics of their interactions with the shock front, or variations in the source characteristics.

One recent approach seeks to make a very detailed accounting of the dynamic effects of particles on shocks (see Chapter 1), including Alvènic drift, streaming instabilities, magnetic field amplifications, and differences in scattering off forward and reverse shocks. The resulting spectra are found to reproduce the data quite well, with a spectral hardening observed near ∼120 GeV/n. Helium was found to have a harder spectral index than protons, which was attributed to helium's resonant scattering off reverse-going shocks [90] [91].

A natural means of explaining the differing spectral indices of protons and heavier elements comes in considering the diversity of environments into which SNRs might expand. As was discussed in Chapter 1, SNRs expanding into the interstellar medium should predominantly accelerate the abundant protons found there. Meanwhile, those which expand into the stellar winds of red supergiants should accelerate a higher amount of helium, and those expanding into the progenitor winds of Wolf-Rayet stars should result in an enhanced composition from the carbon and oxygen group. A recent calculation which folds in the effects of propagation,

the progenitor environment of the SNRs, and both types of parallel and perpendicular shock acceleration mechanisms suggests that the spectra observed at low energies should correspond to an index of 8/3, reflecting the perpendicular shock which accelerates all cosmic-ray species, but that at energies approaching the maximum for the accelerator, the spectral indices for helium and other heavy nuclei should harden significantly due to an increasingly-dominant polar-cap component, approaching 7/3 in the limit. While it is still too early to tell if such asymptotic behavior is reflected in the hardening already observed in the CREAM data, future detailed observations of the spectra of helium and other heavy cosmic rays have the potential to shed significant light on this idea [92] [93].

Considering the spectra observed at Earth as the average over multiple classes of SNR may also be important.[2] Zatsepin and Sokolskaya show that a three-component model—wherein the cosmic ray spectrum originates from the combination of a soft-spectral component originating in nova explosions (cut off near 300 GeV/n), a somewhat harder component due to protons accelerated by SNRs in the ISM (cut off near 25 TeV/n), and a hardest component originating from SNRs which expand into the local superbubble (cut off just above the knee)—reproduces experimental observations after proper accounting has been made for propagation effects [94].

Taking a more general approach on a multicomponent model, a recent work by Yuan et al. [95] considers the spectral indices produced by SNRs as a uniform distribution spanning a minimum and maximum range. The spectra observed at Earth should then reflect the average spectral index at low energies, but begin to reflect the characteristics of the hardest accelerators at energies approaching the maximum. Simulations of this idea are capable of reproducing the spectral features observed in the data reasonably well, although the authors incorporate a propagation modification $\delta = 0.33$, somewhat lower than that favored by most experiments at energies above 10 GeV/n (see Section 3.2).

Another recent effort attempts to trace the spectral hardening in the range 500 GeV/n to 1 TeV/n back to enhancements from nearby SNRs. The cosmic-ray flux observed at Earth is modeled as dominated by a constant background source with an addition component based on the characteristics of ten select SNRs located within 1 kpc of Earth. One interesting prediction of this model is that local sources will not affect the boron-to-carbon ratio, since the nuclear spallation time is much longer than the travel time from sources < 1 kpc away. Spectral hardening was found in the range 0.5–1 TeV/n, with heavier elements hardening earlier than lighter ones. The spectral hardening in this model was predicted to cease near 10 TeV/n [96] [97].

The various theories presented above are not necessarily exclusive, and the exact mechanisms at work in the Galaxy may require a combination of several of them. In any case, continuing precise composition measurements over a wide range of energies in key to constraining, and verifying these models. More data is needed, especially at the high energies where CREAM makes its measurement.

[2] Recall from Chapter 1 that, while the active acceleration time of a typical SNR is thought to be only hundreds to thousands of years, secondary-to-primary ratios from radioactive isotopes suggest that the average escape time for cosmic rays is much larger—roughly 17 million years. Thus, that the spectra observed at Earth represent the total contribution of the spectra from many thousands of SNR is believable.

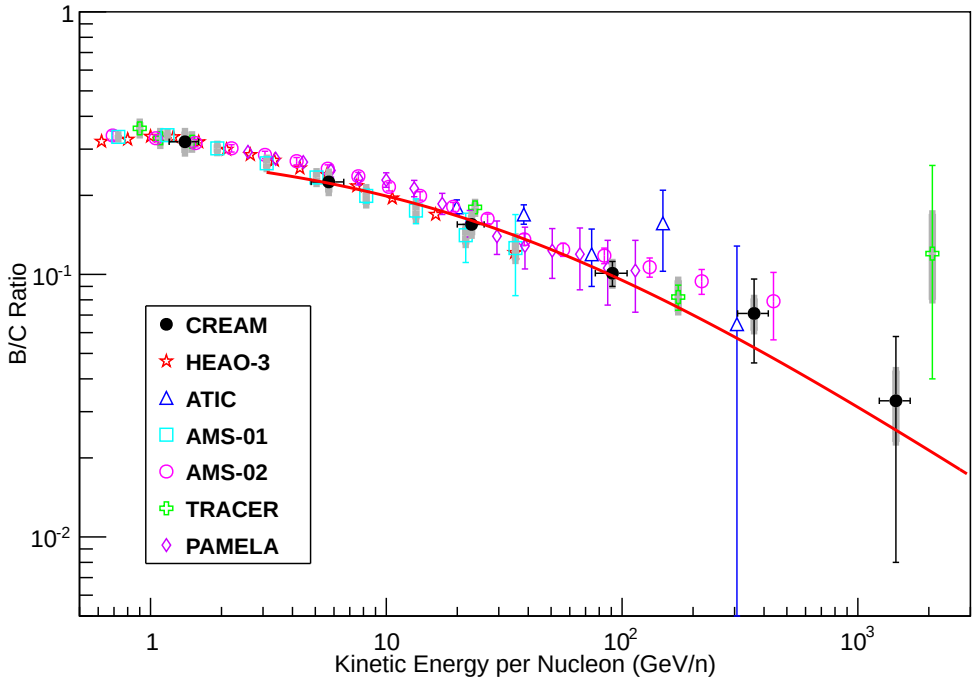

Figure 3.4. Boron-to-carbon ratio for the CREAM I TRD-based analysis [60] is compared to HEAO-3 [88], ATIC [98], AMS-01 [99], preliminary AMS-02 [100], and TRACER [89]. For CREAM, TRACER, and AMS 01 results, thin vertical error bars represent statistical uncertainties, while gray bands denote systematic errors. ATIC and HEAO-3 did not report systematic and statistical uncertainties independently, so the thin vertical error bars on these measurements represent total uncertainty. The theoretical boron-to-carbon ratio predicted by a leaky box model with $\delta = 0.6$ (which provides the best fit to the CREAM data above 3 GeV/n) is shown (red line).

3.2 CREAM Secondary-to-Primary Ratios

A TRD-based analysis of the CREAM I data has been reported which measures the ratios of boron-to-carbon and nitrogen-to-oxygen between 1 GeV/n and 4000 GeV/n [60]. As discussed in Chapter 1, measurements of cosmic-ray secondary-to-primary ratios as a function of increasing energy are extremely useful in constraining models of cosmic-ray propagation, especially for those secondaries which are not produced in abundance during stellar nucleosynthesis, such as elemental boron.

The TRD's tracking capabilities were used to perform precision mapping and pathlength corrections on the TCD, CD, and SCD signals. By then combining the charge detection capabilities of the TCD and SCD, excellent charge resolution was obtained for elements $Z = 5$ through 8, with an overall performance metric of 0.16 cu quoted for carbon. Particle energy determination was performed via a chi-square minimization routine which utilized the TRD and CD response functions discussed in Section 2.3. The resulting energy spectra were corrected for the instrumen-

tal effects of charge and energy mis-identification using a detailed GEANT4 instrument monte carlo simulation. The spectra were also corrected for the effects of charge-changing interactions inside the CREAM instrument and between the top of the CREAM instrument and the top of the Earth's atmosphere.

Figure 3.4 compares the boron-to-carbon ratio measured by CREAM to measurements by HEAO-3, ATIC, AMS-01, AMS-02 (preliminary), and TRACER. The red line shows predictions from the leaky-box model with a spectral modification parameter $\delta = 0.6$, which is representative of much of the dataset. Below 300 GeV/n, most measurements display reasonable agreement with each other. Up to 300 GeV/n, the boron-to-carbon ratio indicates a decrease with energy, consistent with the idea that cosmic rays leak out of the Galaxy more quickly with increasing energy.

Only TRACER and CREAM report data above 300 GeV/n, with these two points representing the highest-energy measurements of the boron-to-carbon ratio to date. The error bars are large and dominated by statistical errors in this region, but it is interesting to note that TRACER reports a significantly higher boron-to-carbon ratio than what is predicted by extrapolation of the leaky-box model from lower-energy measurements, while CREAM's data point is much lower and more consistent with predictions from the leaky-box model.

Clearly, the increased statistical sample which might be gained by additional flights would be advantageous, especially in the region above ∼100 GeV/nucleon, where statistical uncertainties become larger than systematic uncertainties. However, it's also worth noting that, above 100 GeV/nucleon, the uncertainty in the cross section for charge-changing interactions with the atmosphere becomes the dominant term in the systematic error. Until these cross sections can be determined more accurately by particle collider experiments, the accurate measurement of the spectra of cosmic-ray secondaries, such as boron, above ∼1 TeV/nucleon will require experiments performed outside the Earth's atmosphere, such as those on satellites or the International Space Station. Further work is required in order to extend this analysis to higher Z elements. For such elements (even more so than for $Z = 5$ through 8) large statistics are key, since the occurrence of such heavy particles is highly suppressed in cosmic-ray data, especially at the high energies examined by CREAM.

Figure 3.5 shows the nitrogen-to-oxygen ratio as measured by the CREAM I TRD-based analysis, the CREAM II calorimeter-based analysis, HEAO-3, CRN, and ATIC-2. As was mentioned in Chapter 1, the nitrogen-to-oxygen ratio is particularly interesting because nitrogen is produced in some abundance via stellar nucleosynthesis, but also in spallation of oxygen. Leaky-box calculations reflecting nitrogen-to-oxygen source abundances of 10% (solid line), 5% (dot-dashed line), and 15% (dotted line) are shown for reference. CREAM data shows good agreement with the measurements of HEAO-3 and ATIC-2 where they overlap, and seems to favor a source abundances of 10% up to 300 GeV/n. However, at higher energies, CREAM begins to show evidence of a decrease in the nitrogen-to-oxygen ratio, which may be providing a first indication of a transition to the purely primary component of cosmic-ray nitrogen. As was the case with the boron-to-carbon ratio, error bars at high energies are large, and more data will prove beneficial.

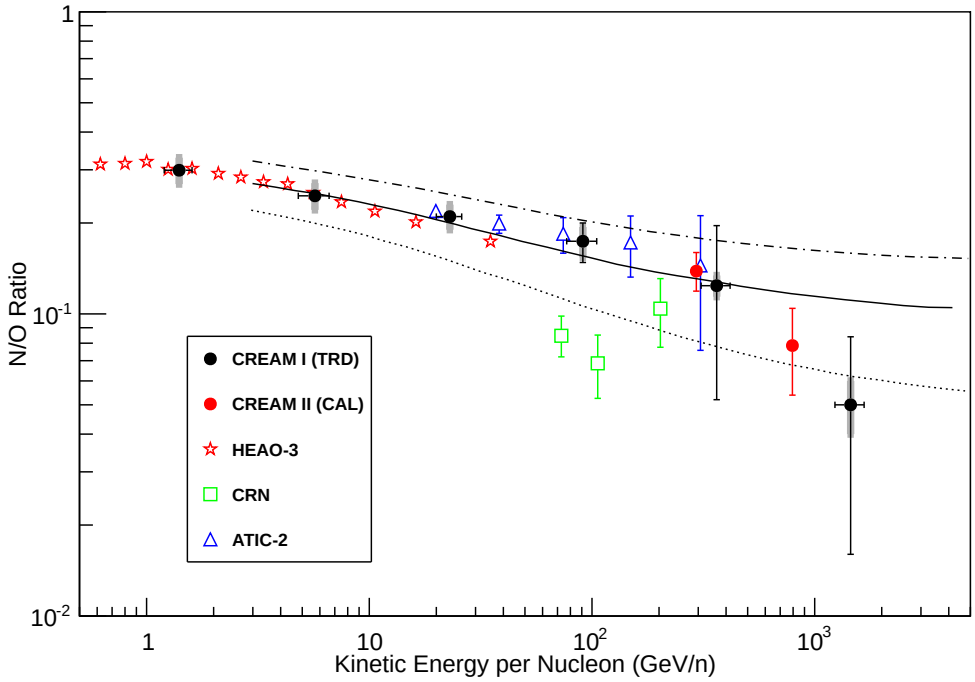

Figure 3.5. The CREAM nitrogen-to-oxygen ratios as derived from the TRD [60] and calorimeter [101] analyses are compared with measurements from the HEAO-3 experiment [88], the CRN experiment [87], and the ATIC experiment [98]. On the data points from the TRD-based analysis, thin vertical error bars represent statistical uncertainties, while gray bands denote systematic errors. Leaky-box calculations reflecting nitrogen-to-oxygen source abundances of 10% (solid line), 5% (dot-dashed line), and 15% (dotted line) are shown for reference.

3.3 ISS-CREAM

The discussion of CREAM results in the previous section reveals several hurdles to achieving the project's science goals via continued balloon missions. Using the 42 days of data collected from the CREAM I flight, the cosmic-ray proton spectrum has been pushed up to the ∼100 TeV energy regime. Extrapolating the observed spectral behavior up another decade in energy, the number of proton events incident through the calorimeter and SCD's $GF = 0.46$ m^2 sr geometric factor with energies between 100 TeV and 1 PeV can be estimated as

$$(GF \times T \times \epsilon \times \Phi_0) \int_{100\ TeV}^{1\ PeV} \left(\frac{E}{1\ GeV}\right)^{-2.66} dE \tag{3.1}$$

where T is the length of the flight, ϵ represents the overall instrument livetime and trigger efficiency, and $\Phi_0 = 7.8 \times 10^3 \left(\text{m}^2 \text{ sr s}\right)^{-1} (\text{GeV})^{-1.66}$. Equation 3.1 evaluates to ∼27 protons

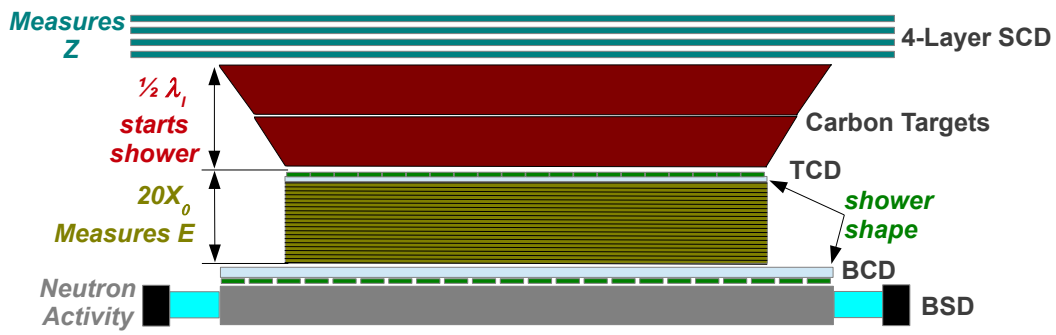

Figure 3.6. Schematic representation of the ISS-CREAM instrument configuration.

for a typical $T = 30$ day balloon flight[3]—a very small statistical yield for the year's worth of work required to execute a campaign. Furthermore, at 100 TeV proton energies, error bars from the 42 day flight are currently dominated by a statistical uncertainty near 100%. Since errors decrease as the inverse square root of sample size, using CREAM's total data set of 161 days will lead to a reduction in the statistical error in this energy bin of ∼50%—a factor two improvement in resolution for five additional years of work. Finally, as described Section 3.2, atmospheric overburden also produces some limitations, since the corrections due to charge-changing interactions through the residual atmosphere above CREAM can be quite significant, especially for the less abundant charge species.

In order to overcome these hurdles, portions of the CREAM experiment are being reconfigured for ISS-CREAM [102]—a three-year mission to be launched to the International Space Station (ISS) in 2014 by SpaceX, docking on the ISS Japanese Experiment Module Exposed Facility (JEM-EF). The planned 1000 day mission will allow the determination of spectra above 1 PeV/particle, while also removing the systematic limitations of an experiment flown under the residual atmosphere seen at balloon altitudes.

Figure 3.6 shows ISS-CREAM's planned detector configuration. In keeping with the approach of the legacy balloon experiment, ISS-CREAM's primary charge detector is composed of a 4-layer SCD, with each layer designed and operated in essentially the same way as was described in Section 2.4. Its energy detector is the same calorimeter system as was used on the balloon payload—a set of flared $0.5\lambda_I$ carbon targets which initiate the primary particle's interaction, followed by a 20-layer tungsten calorimeter which mainly samples the shower's electromagnetic core. With the addition of three new detectors—the Top Counter Detector (TCD[4]), the Bottom Counter Detector (BCD), and the Boronated Scintillator Detector (BSD)—ISS-CREAM will take on the new science goal of measuring the cosmic ray electron spectrum above 100 GeV.

[3]CREAM's trigger efficiency is near 100% for particles with energy above 1 TeV. The livetime efficiency has varied from flight-to-flight, but is taken as 100% for this illustrative calculation.

[4]While ISS-CREAM's "Top Counter Detector" TCD is also a scintillation-based detector system, it is important to distinguish this from the "Timing Charge Detector" TCD flown on the balloon instrument. The two detectors are constructed completely differently and have significantly different measurement goals.

Measurement of the high-energy electron spectrum is of significant scientific interest, particularly because cosmic-ray electrons tend to lose energy quickly via synchrotron radiation in Galactic magnetic fields and inverse-Compton scattering on the cosmic microwave background. Thus, such a high-energy electron measurement has the potential for identifying local sources of cosmic-ray acceleration. While current measurements of the electron spectrum extend only up to $\sim$1 TeV [22], ISS-CREAM has the potentital to extend this measurement by an order of magnitude or more. However, spectral measurements of cosmic-ray electrons at high energies are complicated by the fact that misidentification of the far more abundant cosmic-ray protons as candidate electrons can significantly distort results. Hence, a large hadronic rejection power is critical.

The TCD and BCD [103] are scintillator-based detectors positioned just above and below the calorimeter which provide a measure of lateral shower dimensions and penetration depth. The TCD is comprised of a 50 cm $\times$ 50 cm $\times$ 0.5 cm slab of EJ-200 plastic scintillator [104], viewed by a 20 $\times$ 20 grid of 2.3 cm $\times$ 2.3 cm custom-designed photodiodes. Similarly, the BCD is comprised of a 60 cm $\times$ 60 cm $\times$ 1 cm slab of EJ-200 plastic scintillator, also viewed by a 20 $\times$ 20 grid of photodiodes, with photodiodes spaced slightly farther apart in the BCD in order to cover its larger area. Because showers of a hadronic origin tend to have much larger lateral dimensions than those of a purely electromagnetic origin, such a pixelated view of shower development is expected to provide a significant increase in ISS-CREAM's ability to identify and reject hadronic cosmic rays from electron samples. As a fast-response scintillation detector, the ISS-CREAM TCD also provides a charge-based trigger flag for the system. Work to characterize the hadronic rejection power provided by the TCD and BCD using instrument simulations and analysis of data taken during a 2012 CERN beam test is ongoing.

ISS-CREAM's BSD [105] is a boron-loaded scintillator-based detector which sits at the bottom of the ISS-CREAM instrument, sampling neutron production in the shower. Because showers originating from hadronic cosmic rays tend to produce many more neutrons than electron-generated showers, such a measurement can add significantly to ISS-CREAM's overall hadronic rejection power. The design, construction, and verification of the BSD are discussed in detail in Chapter 6, and so, all further discussion on the BSD will be delayed until then.

3.4 BACCUS

While ISS-CREAM is poised to address questions of cosmic ray physics at the highest energies achievable via direct measurement, further TRD-based missions performed on a balloon, of the style discussed in Section 3.2, hold promise of new science, especially for the spectra of higher-Z elements not addressed in that analysis. With this in mind, the BACCUS instrument was developed as on off-shoot of CREAM's balloon program. BACCUS is scheduled to be flown as an LDB payload from McMurdo Station, Antarctica in the 2013–2014 summer season. The BACCUS instrument's tracking and primary energy measurement are based around a newly-constructed double-module TRD, similar to the one flown on CREAM I [106]. BACCUS also

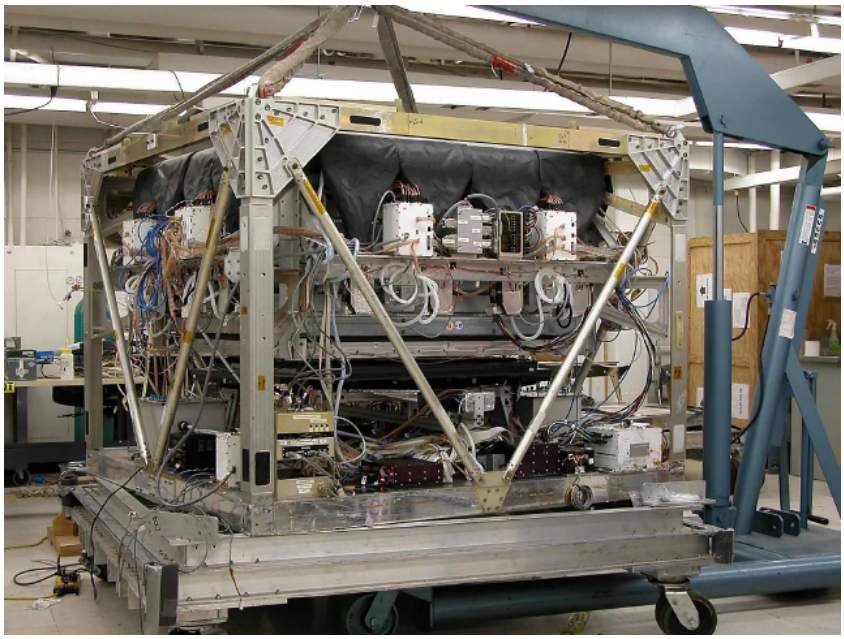

Figure 3.7. The BACCUS instrument integrated at the University of Maryland [106].

combines balloon-CREAM's dual-layer SCD with the TCD, CD, and S3 detectors, whose readout electronics have been significantly upgraded (see Chapter 4). Figure 3.7 shows the fully integrated BACCUS instrument. A detector performance similar to that derived from CREAM I should be achievable.

Chapter 4

The Design, Construction, and Qualification of the CREAM TCD

CREAM's TCD system is an integral part of the overall charge measurement and trigger schemes of the CREAM instrument. Because the design, fabrication, integration, and support of this detector form a major portion of my thesis work, the TCD will be described here in detail.

4.1 Scintillator Paddles and Light Guides

As described in Chapter 2, the TCD's primary detection medium consists of two layers of 120 cm × 30 cm plastic scintillator paddles, each 5 mm thick, with the direction of paddles in the TCD's bottom layer rotated by 90° relative to its top layer. For CREAM I–II, TCD paddles were cast by Saint-Gobain Crystals, using their low outgassing, BC-408V scintillator formula. This reduced outgassing formula was later deemed unnecessary, so instead, the less expensive BC-408 formula was chosen for CREAM III–V [45]. For BACCUS, Eljen Technologies cast the TCD scintillator paddles at a greatly reduced cost and lead time, using their identical EJ-200 [104] scintillator formula.[1]

The photons generated by the charged particles which pass through the scintillator paddles are piped to PMTs at each end of the paddle via adiabatic light guides, which were manufactured by Saint-Gobain Crystals [107]. The light guides meet the scintillator paddles along opposing, 1 cm wide, 0.25 cm deep polished steps which couple in a lap joint. The joints are optically and mechanically joined using Saint-Gobain Crystal's BC-600 optical epoxy [108]. The light guides were designed to maintain constant cross-sectional area along their length, thereby minimizing escaped light, and were handmade using UV absorbent Lucite, thereby minimizing the production of Cherenkov light in the light guide. Figure 4.1 shows the various stages of paddle assembly.

[1] In fact, both formulations have been confirmed to be exactly the same, and both were designed by the same engineer, Chuck Hurlbut.

The TCD's PMTs are optically coupled to the light guides via a pair of mating Lucite cookies, with one cookie glued to the light guide and the other glued to the PMT. General Electric Silicone's RTV615 [109] is used to attach these cookies to the light guides and PMTs. The cookies are optically coupled together using a thin layer of BC-630 optical grease [110]. The cookies are held together via a pair of custom designed aluminum PMT attachment rings. For flights where a TRD is present (CREAM I and BACCUS), the TCD paddles rest directly on top of the TRD. For all other flights, the TCD paddles rest on a light-weight, aluminum support structure. The weight of the PMTs is supported by holding brackets attached directly to TCD outrigger arms. These outrigger arms then bolt to either the TRD (CREAM I and BACCUS) or the TCD support structure (CREAM II through CREAM V). Figure 4.2 shows the CREAM I/BACCUS configuration, where the TCD outrigger arms are bolted directly to the TRD.

When scintillation photons encounter the scintillator's boundaries, those photons incident at an angle greater than the critical angle[2] for scintillator (about 39°) experience total internal reflection and remain captured in the scintillator. However, some portion of those with an incident angle less than the critical angle escape the scintillator, and hence would be lost for detection. In an effort to recapture this lost light, the scintillator is covered with crinkled aluminum foil. The many crinkles in the foil re-reflect escaping photons toward the scintillator at random angles, hence allowing some photons to re-enter the scintillator and be captured.

Paddle assemblies are wrapped in two layers of 0.004 in thick black Tedlar [111], a Dupont film whose high durability, light-weight, and extreme opacity make it ideal for blocking external photons from entering the TCD paddles. Seams from the Tedlar wrapping are sealed using homemade "Tedlar tape," which is created by placing 3M's 966 transfer tape [112] onto strips of Tedlar. The 966 transfer tape is a clear, double sided film which, once in place, provides reliable adhesion between layers of Tedlar, even at the low temperatures experienced in Antarctica or in flight.

4.2 PMT Modules and High Voltage Testing

The TCD uses Photonis XP2020 PMTs [46]. These are 12-stage, 2-inch, linear-focused PMTs which make use of a bialkali photocathode viewed through borosilicate glass, and exhibit a maximum gain of 3×10^7. The design goals of the TCD mean that its PMTs must remain unsaturated for charge responses between Z = 1 (hydrogen) to Z = 26 (iron), which roughly corresponds to a dynamic range of $26^2 = 676$. Combining this dynamic range requirement with the low power requirements for flight leads to the implementation of several advanced design techniques. The high voltage distribution scheme (*i.e.*, "base circuit") for these tubes is shown in Figure 4.3. The high voltage bias for all the dynodes is provided via a resistive voltage divider network buffered by a chain of emitter followers. The high input impedance and low

[2]The critical angle is referenced relative to the normal of the surface upon which light is incident and is defined as the minimum incident angle at which all light traveling from a medium of larger index of refraction n_1 to smaller index of refraction n_2 is completely reflected. It can be calculated using Snell's Law: $\theta_c = \arcsin(n_2/n_1)$.

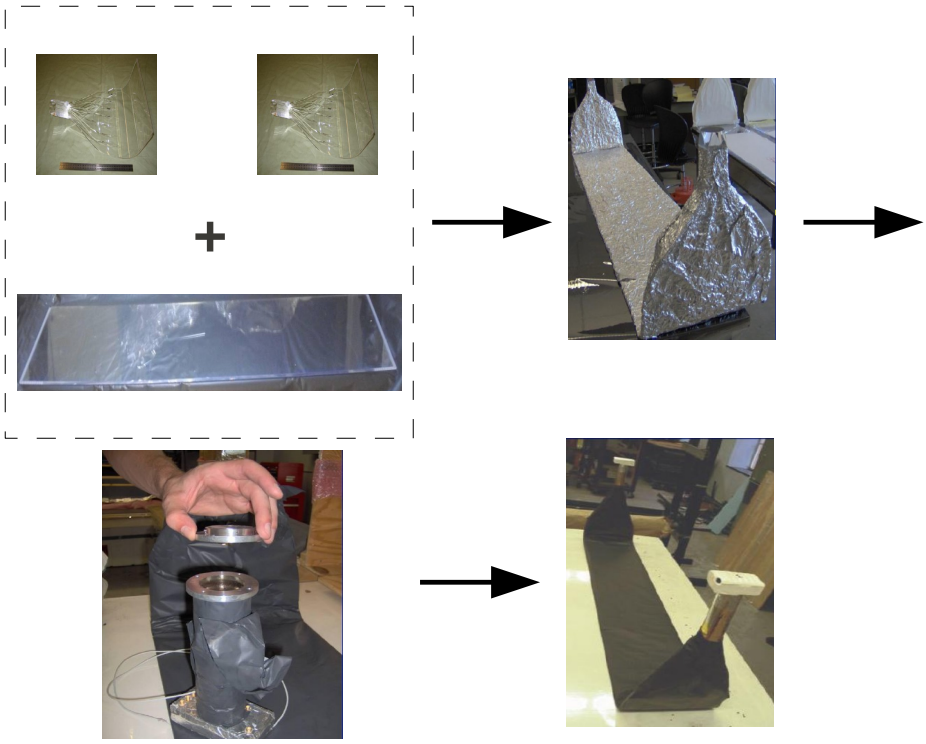

Figure 4.1. A schematic view of the TCD scintillator paddle construction process. Light guides are glued to the scintillator using BC-600 optical epoxy. The scintillator is then wrapped in aluminum foil. PMTs are attached to the light guides using custom designed aluminum rings. The entire paddle assembly is made light-tight using black Dupont Tedlar. The bottom right figure shows a final paddle assembly, with potted PMT bases seen attached to each end of the paddle.

output impedance of the emitter followers create a stiff voltage reference with minimal power dissipation. Large "bucket" capacitors are added in parallel with the dynode chain in order to provide a fast source of charge to dynodes during large pulses. In addition to the anode, dynodes 12, 11, 10, 9, and 7 are also added to the readout. Because dynodes early in the chain operate at a much lower gain than those later in the chain, early dynode taps remain unsaturated at large signal levels.

High voltage (around 3 kV) is supplied to each tube via an external 4A12-P4-F Ultravolt high-voltage power supply [113]. Reynolds 167-2896 high-voltage, vacuum-rated cable [114] is used to transmit high voltage to the PMT base. Due to power constraints, adjacent flight PMTs are required to share a common Ultravolt supply, and so are gain matched prior to being grouped together.

The high altitude at which CREAM/BACCUS flies presents a unique difficulty for high voltage systems, since the minimum ambient pressure at which dielectric breakdown occurs (~ 3 torr) sits well in the range of the atmospheric pressures experienced by the payload. In order to ensure robust high voltage operation, the PMT base boards are first lightly coated in Emerson

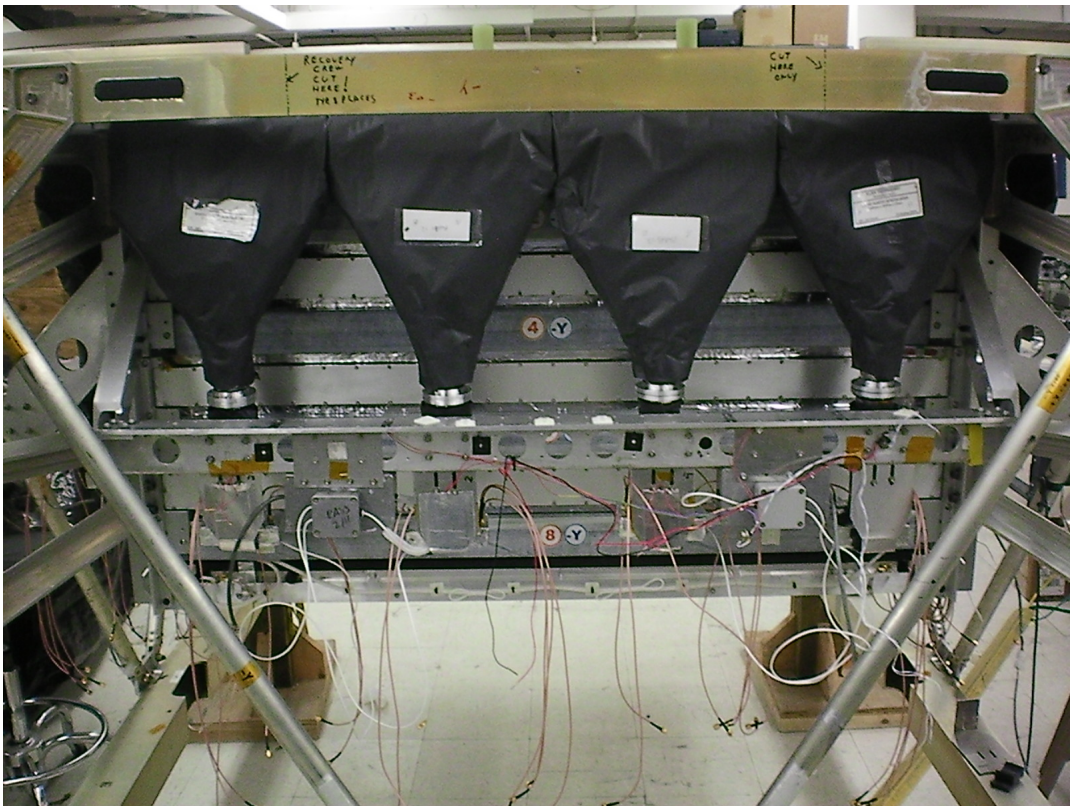

Figure 4.2. The TCD paddles integrated into the upper half of the BACCUS instrument. The aluminum PMT attachment rings can be seen pressing the light guides to the PMTs. The weight of the PMTs is supported by holding brackets connected to the TCD outrigger arms on each side of the instrument.

and Cumming's clear S11 primer [115] and then cast in Emerson and Cumming's Stycast 1266 high voltage potting compound [116], which has a rated dielectric strength of 15.7 kV/mm. The potted assemblies are then taken through four thermal cycles in a 24 hour period, with the temperature extremes of this cycle ranging between -20°C and +50°C. This aggressive thermal cycling helps aggravate differential thermal expansion between the PMT base boards and the potting compound, hence ensuring any flaws in the potting process are caught before flight. The potted assemblies are then monitored for a minimum of one week at maximum high voltage in a vacuum chamber whose pressure is slowly cycled once per day between 1 torr and 10 torr.

Because external magnetic fields can cause changes in PMT gain, all potted tubes are wrapped in two layers of 0.005 in thick high-permeability magnetic shielding foil, known as "mu-metal". The potted PMT bases are also wrapped in an aluminum tape with conductive adhesive. This tape serves the dual purpose of providing electrical shielding to the PMT base and preventing charge accumulation on the surface of the potting compound. The final assemblies are wrapped in 2 layers of Tedlar for light tightness. Figure 4.4 shows the TCD PMTs before and after being potted and wrapped.

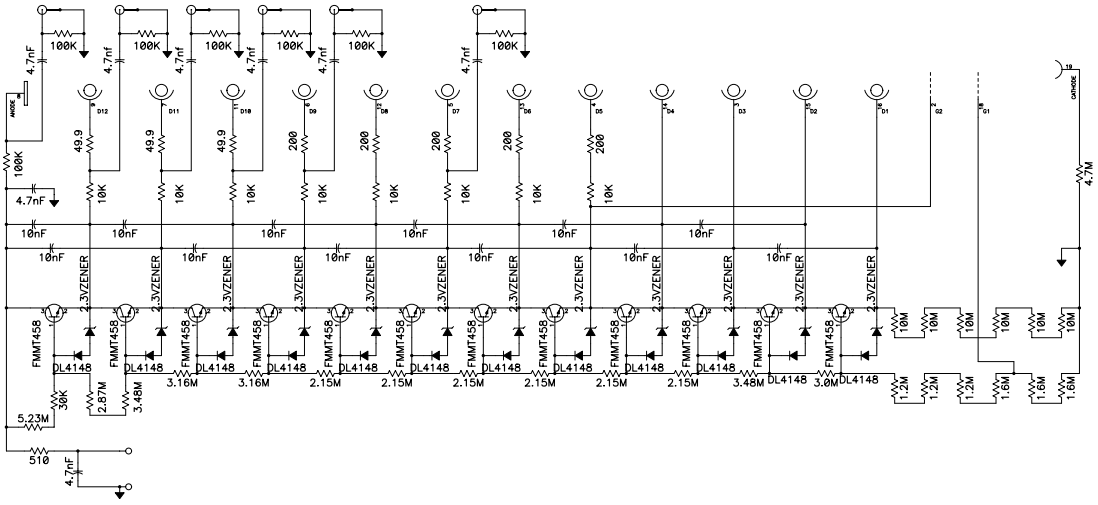

Figure 4.3. PMT active divider schematic

Figure 4.4. A TCD PMT before and after being potted and wrapped (with mounting ring also attached).

4.3 Overview of the TCD Readout Electronics

The TCD readout electronics are arranged such that two PMTs share a common stack of boards, known as a "concentrator stack", or simply a "concentrator". The arrangement of the TCD concentrator stacks and PMTs is shown in Figure 4.5. Looking down on the top of the instrument, PMTs are numbered between 0 and 15, starting at the -Y corner of the +X side of the TCD and working counterclockwise around the instrument. Concentrator stacks are named according to their position on the instrument, with "PX", "PY", "MX", and "MY" corresponding to the +X, +Y, -X, and -Y sides of the instrument, respectively. A final letter designation is added to the end of each concentrator stack name, and is assigned by looking toward the center of the instrument from the side of interest, and giving concentrator stacks on the left side an "L" suffix and those on the right side an "R" suffix.

The concentrator stacks PXL, PXR, PYL, PYR, MXL, MXR, MYL, and MYR all reside on the TCD outrigger arms, and are the concentrator stacks which read out the TCD's 16 PMTs. The S3 detector is also viewed by TCD PMTs and is read out by a TCD concentrator stack known simply as "S3". This concentrator resides on the +y side of the CREAM palette. Starting with the CREAM 2 flight, the eight PMTs of the CD detector were also read out by a newly dedicated TCD concentrator stack, labelled simply as "CD". The CD concentrator stack resides on the TCD outrigger arms, directly between the MXL and MXR concentrator stacks.

Each concentrator stack contains a power distribution board, two peak detector boards (one for each PMT), two time to digital converter (TDC) boards (one for each PMT), and a local trigger board. All boards within a given concentrator stack are linked through a parallel electronics bus, known as the concentrator stack's "Local Bus". The local bus is physically propagated on Samtec's 50-pin, 0.1 in-pitch, dual-row, board-to-board stackable header. In addition to the previously listed boards, the PXR concentrator stack also contains two extra boards in its stack. These are the "TCD Master Trigger Boards", and they define the formation of a TCD trigger event. Aside from receiving a CLEAR command along PXR's local bus, these boards are completely autonomous and do not affect the operation of the other PXR electronics boards in any way.

All boards are designed with a common 6 in $\times$ 4 in form factor and are stacked together in an anodized aluminum frame with bolt-on side panels. This enclosure was custom designed to dissipate heat and provide electrical shielding for the TCD concentrator stacks. Concentrator stack side panels are coated with white Sherwin-Williams appliance epoxy so as to reflect ambient heat during flight. Figure 4.6 shows a concentrator with its side panels removed, so that its stack of electronics boards are visible.

Electronics boards for the concentrator stacks were populated in-house and tested on the lab bench both before and after being subjected to a 24 hour thermal stress test used to identify infant mortality in these freshly-fabricated circuits. Because of the significant power dissipation of the MCF-5272 microcontroller on the stack controller boards, a heat sink was attached to this chip by thermal epoxying a small square of copper foil onto it and thermally strapping the

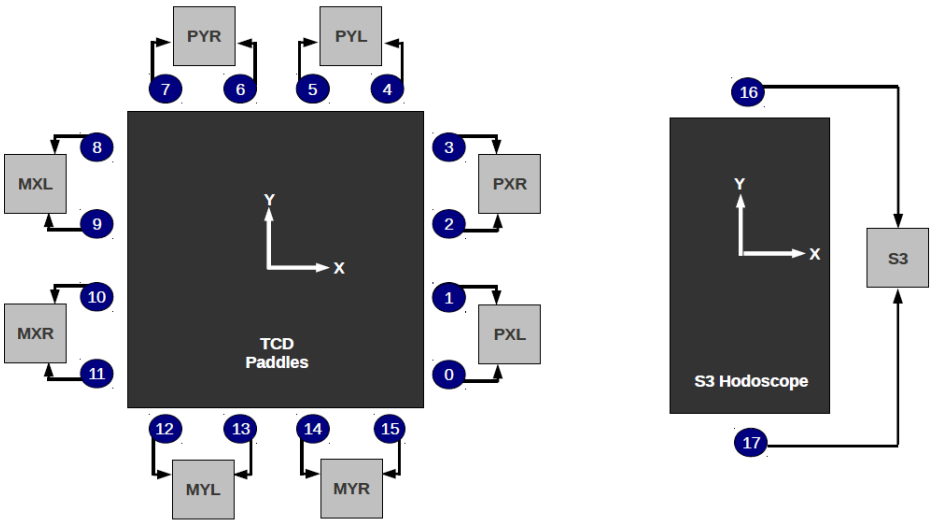

Figure 4.5. Overview of the PMT readout scheme by the TCD concentrator stacks.

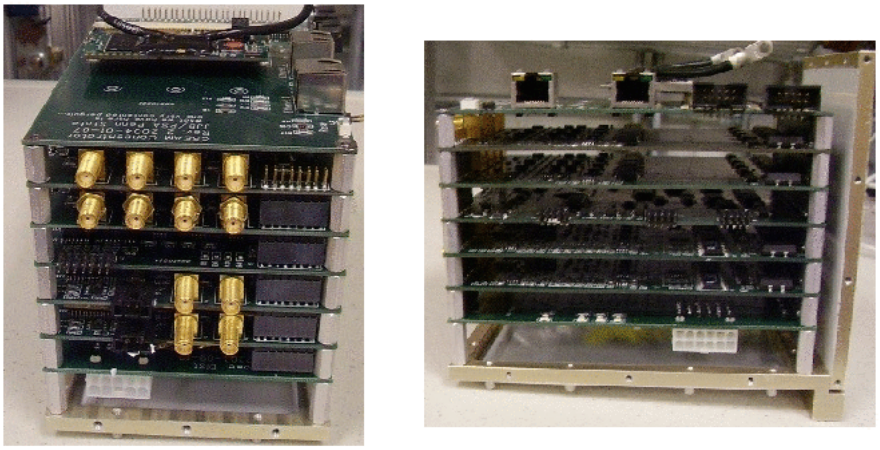

Figure 4.6. An assembled TCD concentrator stack with its panels removed in order to show the readout electronics. From bottom to top: power distribution board, time-to-digital converter 0 board, time-to-digital converter 1 board, local trigger board, peak detector 0 board, peak detector 1 board, and stack controller board.

foil to the concentrator stack's enclosure. For the BACCUS flight, an additional operational thermal test was performed on all concentrator stacks which had previously been flown. This test consisted of four thermal cycles in a 24 hour period, with temperature extremes ranging between -20°C and +50°C. This additional operational thermal test ensured that the now aging concentrator stacks were still functional over the entire range of CREAM flight temperatures.

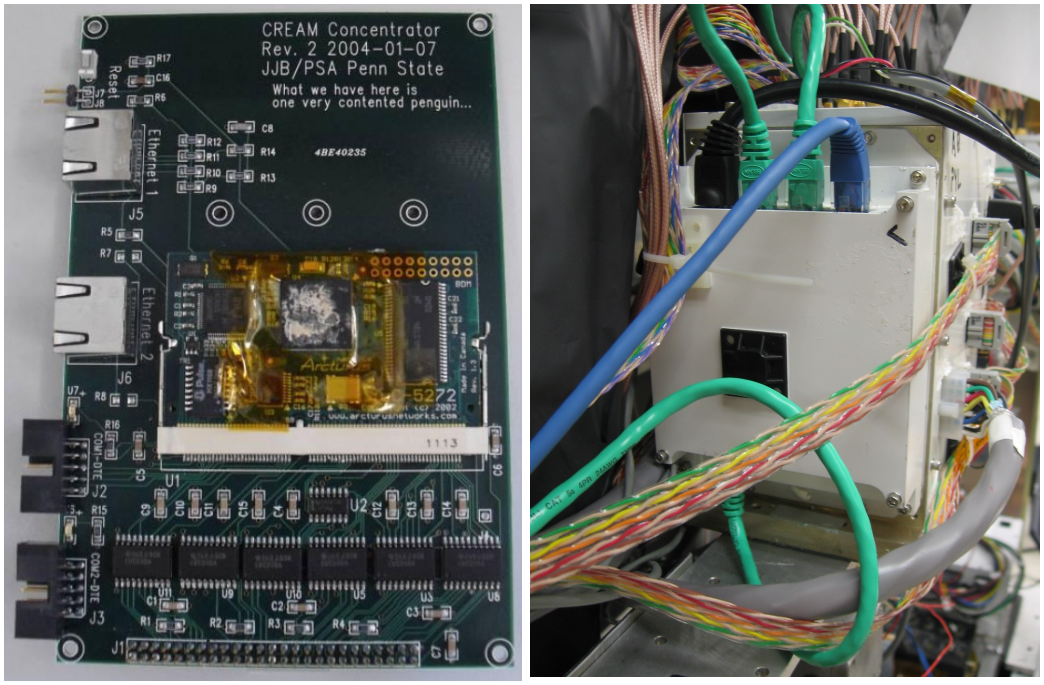

Figure 4.7. A CREAM I–V stack controller board and Parvus Ethernet switch.

4.4 The TCD Stack Controller Boards

The TCD stack controller board is tasked with controlling its concentrator stack's local bus and managing the data stream of command and event packets for its concentrator stack. The stack controller boards were designed as simple carrier boards for the Arcturus Networks MCF-5272 microcontroller module [117]. This board is shown on the left side of Figure 4.7.

All TCD boards interface to the local bus through bi-directional, tri-state buffers. The stack controller board arbitrates control of the local bus through the use of six control lines which activate the tri-state buffers of only one board at a time, determining whether its buffers are used in input or output mode according to whether data is to be written-to or read-from the selected board. Once the control lines have selected the appropriate board, eight address lines select the active component (*e.g.* ADC or DAC) with which the stack controller will communicate. Data words are transmitted as 16-bit wide words on the concentrator's local bus.

For the CREAM I–V missions, the MCF-5272's 10/100 Ethernet capabilities were used to form a data link between each TCD concentrator stack and the SFC. A block-diagram of the TCD network is shown in Figure 4.8. Concentrators closest to the +y side of the CREAM instrument uplink through an Ethernet switch "piggy-backed" on the PYL concentrator, while those on the -y side of the CREAM instrument uplink through an Ethernet switch piggy-backed

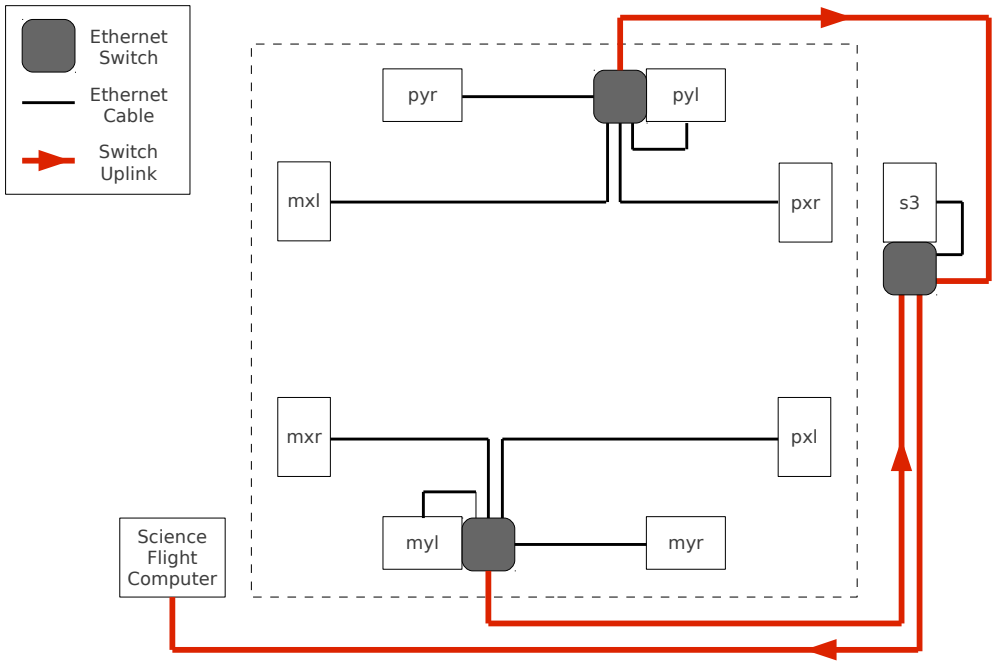

Figure 4.8. The CREAM 1-5 Ethernet-based readout scheme. Concentrators on the +y and -y sides of the instrument plug into separate Ethernet switches, which piggy back on the PYL and MYL concentrators. These switches uplink to a third Ethernet switch, which piggy backs on the S3 concentrator. This final switch uplinks to the CREAM SFC.

on the MYL concentrator. The uplink port of these switches then connects to a third Ethernet switch, piggy-backed on the S3 concentrator. The S3 concentrator switch also receives data from the S3 and CD concentrators and uplinks to the CREAM SFC. The Ethernet switch model used is the Parvus military grade PRV-1059 4-port 10/100 Ethernet switch [118].

Each MCF-5272 module comes preloaded with uClinux-2.4.2. The uClinux operating system is a special port of the Linux kernel for microcontroller platforms that do not include memory management modules. The MCF-5272 modules store a program image for each concentrator in non-volatile flash memory, from which the firmware image is loaded at boot time. Upon booting, each concentrator performs a series of startup routines which calibrate its ADCs and initialize its DACs. Each concentrator then initiates two parallel processes. The ***cServer*** process handles command and status query requests from the SFC, while the ***eServer*** process reads digitized event data from all TCD peak detectors and TDCs upon reception of an event interrupt. All communication between the CREAM SFC and the TCD concentrators is based on TCP/IP protocols. On the SFC side, the ***cClient*** routine sends command and status queries to each concentrator, while the ***eClient*** routine reads event data from each concentrator, parsing it into a single compressed data packet for storage on the flight hard drive.

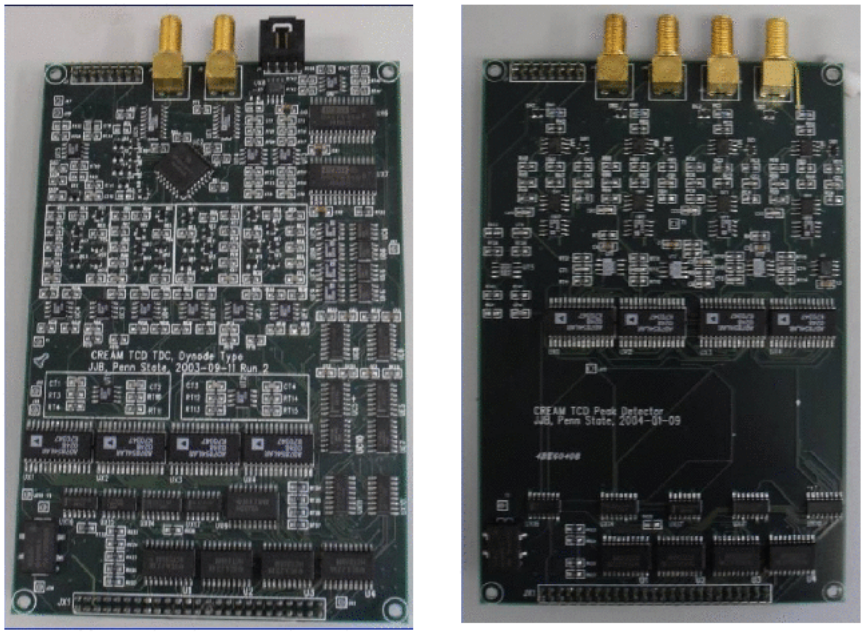

Figure 4.9. The TDC (left) and peak detector (right) boards.

4.5 The TCD Front-End Analog Electronics

An overview of the measurements taken by the TCD's TDC and peak detector circuits was already provided in Section 2.2. Here, the discussion will focus on the hardware-implementation details of these circuits. Figure 4.9 shows a TDC board (left) and a peak detector board (right).

4.5.1 The TDC Boards

A simplified schematic of a single channel from the TDC circuit is shown in Figure 4.10. The PMT's anode or dynode signal (*IN*) feeds the input of the AD96687, a very fast emitter-coupled logic (ECL) comparator. When this signal's level passes the threshold level *THR*, the comparator generates a leading edge which clocks the ECL 100E131 D flip-flop into its *ON* state. The digital electronics (represented as the "Reset and Trigger System" in this schematic) latch this flip-flop level and present it as the *VALID* bit of a trigger status word read out as part of the TCD event data packet. This bit also generates the discriminator crossing bit, *DISC*, which feeds into the formation of the TCD trigger. The *THR* threshold levels are tuned so that TDC0 and TDC1 (which readout the anode) have thresholds at ~ 0.2 MIP and ~ 1 MIP, while TDC2 and TDC3 (which monitor the 11th dynode) have thresholds at ~ 20 MIP and ~ 3.5 MIP. The *DISC* bits generated from the firing of TDC1 and TCD2 are used in coincidence across multiple TCD PMTs to form the TCD's ZLO and ZHI triggers.

The clocking of flip-flop U2 also switches on transistor Q1, which causes the differential amplifier formed by Q2 and Q3 to create a charging path for capacitor C1 through the current source

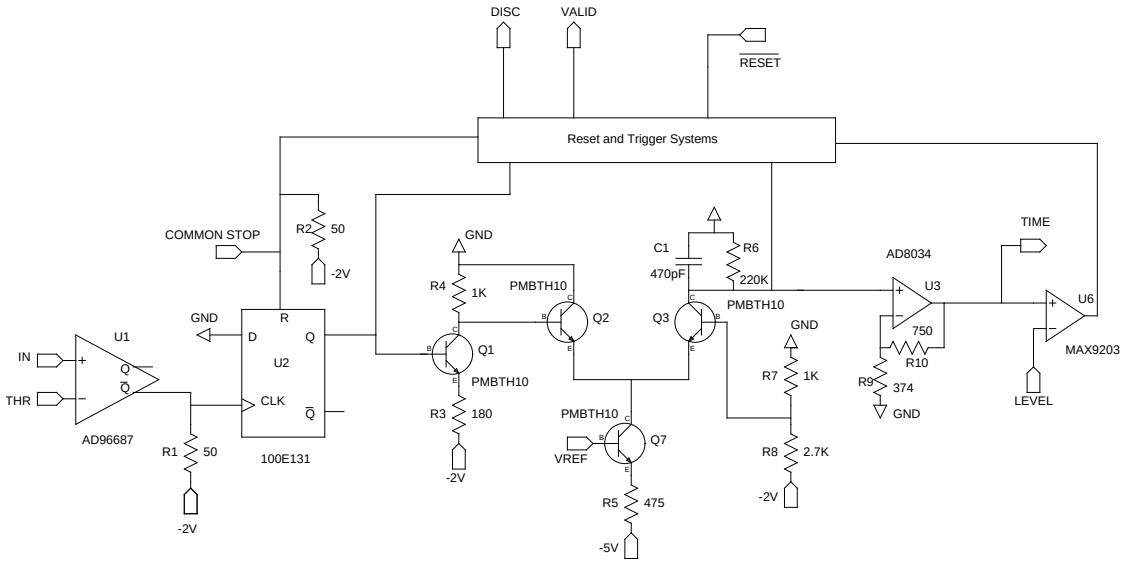

Figure 4.10. Simplified TDC circuit.

formed by Q7. Because C1 is charged through a current source, the voltage across it is directly proportional to the time over which it has been charging. The voltage on C1 is then inverted and amplified through the inverting amplifier formed by the fast AD8034 operational amplifier U3. The output of this operational amplifier, shown as the *TIME* signal in the schematic, is digitized as the TDC timing data. In normal operation, all TDCs in the TCD are stopped simultaneously upon the formation of a TCD coincidence trigger (*i.e.*, *RAW ZLO* or *RAW ZHI*), via the *COMMON STOP* signal. The voltage across C1 is then reset once timing data has been digitized via the *RESET* signal. In the case when a TCD coincidence trigger is not formed, the TDCs are reset locally when the *TIME* signal surpasses the predefined *LEVEL* value. Digitization of timing data is performed through Analog Devices's AD7854L 12-bit, parallel sampling ADC, with one ADC dedicated to each TDC channel. Threshold levels are set via Burr Brown's DAC7625 DAC.

4.5.2 The Peak Detector Boards

A simplified schematic of a single channel from the peak detector circuits is shown in Figure 4.11. The *DYNODE* signal represents the PMT dynode feeding the peak detector circuit, while the *PEAK* signal represents the output to be digitized. It's worth noting that component U1 is a 1 GHz bandwidth MAX4225 current-feedback amplifier (CFA) which, unlike the more common voltage-feedback amplifier (VFA), has a low impedance inverting input, with the output slewing positively for current sinking into the inverting input and the output slewing negatively for current sourcing from the inverting input. When no PMT pulse is present, the *DYNODE* signal and *PEAK* signal are at ground potential. When the *DYNODE* signal begins to rise due to the presence of a positive going dynode pulse, current sinks into the inverting input of U1-A,

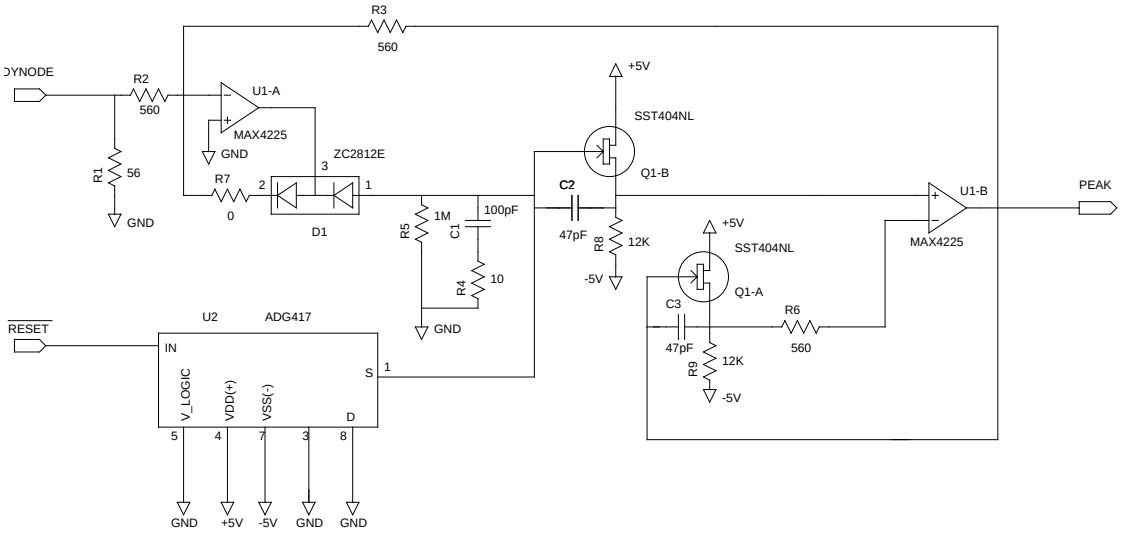

Figure 4.11. Simplified peak-detector circuit.

hence causing its output to move toward the negative rail. This creates a forward bias between terminals 1 and 3 on diode D1 and hence charges capacitor C1. The voltage on C1 is fed into the voltage follower formed by CFA U1-B and JFETs Q1-A and Q1-B. Hence, the *PEAK* signal slews in the negative direction of the *DYNODE* signal when the *DYNODE* signal is increasing. When the *DYNODE* signal has passed its maximum value, the inverting input of U1-A begins to source current out of its inverting input, thereby causing its output to swing toward the positive rail, reverse biasing terminals 1 to 3 of D1, and hence allowing the voltage on C1, which is buffered to the *PEAK* signal, to remain fixed at a level proportional to the maximum voltage applied by the *DYNODE* signal. The voltage level on the *PEAK* signal is then digitized by the TCD readout electronics. The hold time of the voltage on C1 is created by the RC combination of R5 and C1, which has an RC time constant of ~ 100 μs. The peak detectors are reset by the ADG417 switch U2 once their data has been digitized and read out. Digitization of peak detector data is performed through Analog Devices's AD7854L 12-bit, parallel sampling ADC, with one ADC dedicated to each peak detector channel.

4.5.3 The CD Pulse Shaping Board

Because the peak detector boards are designed to handle positive going PMT dynode pulses, an intermediate board was required in order to invert and shape the CD PMT's negative going pulses for its peak detector circuits. This board, known as the "CD pulse shaping board", contains 8 channels for integrating, inverting, filtering, and amplifying the CD PMT signals to levels appropriate for the TCD peak detector circuits. The schematic for one channel of this shaping circuit is shown in Figure 4.12. In addition, this board contains an input for an analog threshold voltage, which is compared to the sum of all CD PMT signals in a discriminator. The

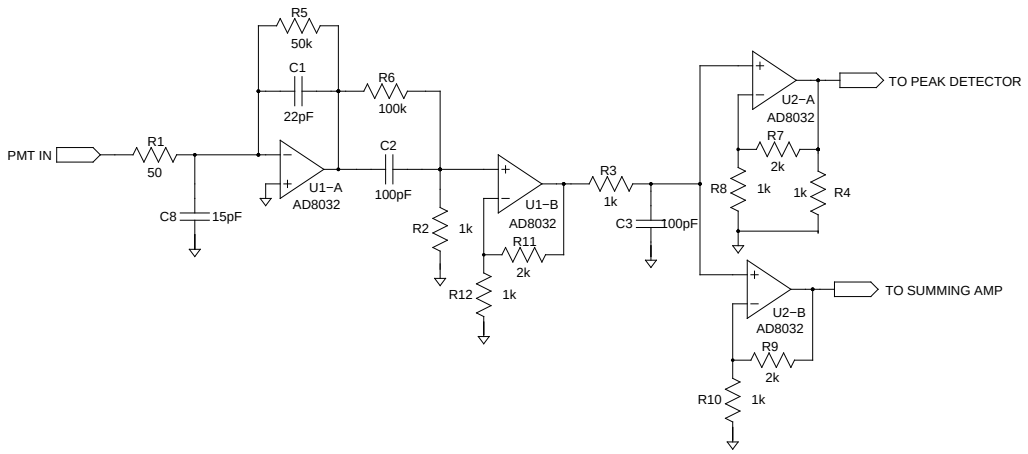

Figure 4.12. One channel of the CD pulse shaping board.

output of this discriminator forms the CD trigger signal, which is used in forming the TCD's *RAWZhi* flag trigger, as will be discussed in the next section.

4.6 The TCD Trigger System

The TCD's role in helping form CREAM instrument triggers was already overviewed in Sections 2.2 and 2.7.2. Here, the discussion will focus on implementation details internal to the TCD.

Each TCD concentrator stack's trigger circuits are located on the so-called "local trigger board". This board sends and receives important trigger formation signals to and from the TCD master trigger boards, while also controlling the sequencing of event data digitization, readout, and event register clearing. As previously discussed, the TCD master trigger boards reside as additional electronics on the PXR concentrator. The TCD master trigger boards form a coincidence from all concentrator stacks' local trigger signals, distribute trigger confirmation signals back to the local trigger boards, and interface with the CREAM instrument's master trigger board, which contains the CREAM instrument's ultimate trigger formation logic.

Signal flow for the TCD's trigger system is shown in Figure 4.13. Logical OR'ing of *ZLO_DISC* and *ZHI_DISC* discriminator flags from the concentrators on each side of the instrument are generated by the concentrator stacks' local trigger boards. A three-fold coincidence is formed based on the disciminator flags from the four sides of the instrument in the TCD master trigger electronics. A three-fold coincidence on ZLO_DISC plus an S3 discriminator flag generates the RAWZLo trigger flag to the CREAM instrument master trigger board, while a three-fold coincidence on ZHI_DISC plus a CD trigger generates the RAWZHi trigger flag to the CREAM instrument master trigger board. Activation of either the RAW_ZLO or RAW_ZHI signals generates the *RAW_COINCIDENCE* signal to all the TCD concentrators. If the CREAM instru-

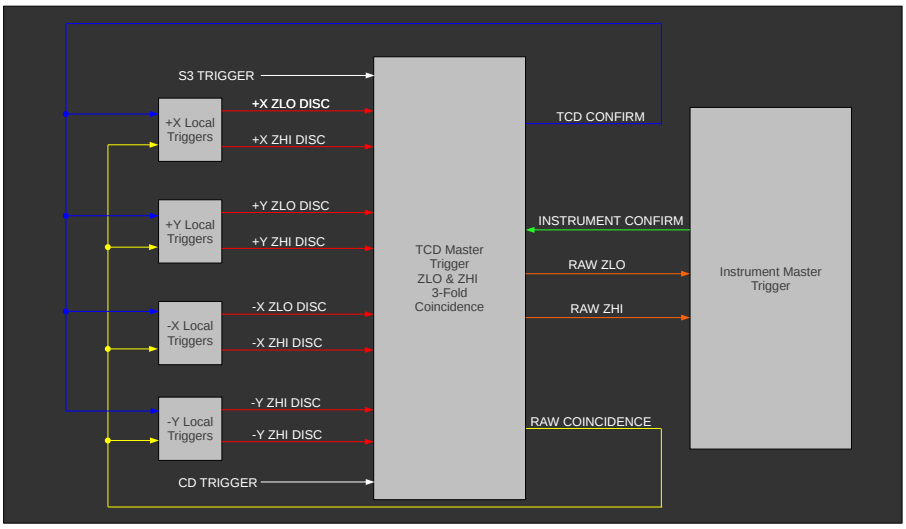

Figure 4.13. Simplified block diagram for the TDC trigger circuit.

ment master trigger board decides to readout the current event, it responds with an *INSTRUMENT_CONFIRM* signal, which gets latched and redistributed to the TCD concentrators as a *TCD_CONFIRM*. The reception of this TCD_CONFIRM signal causes the TCD local trigger boards to begin the digitization of TDC and peak detector data, subsequently transferring the TCD data packet to the CREAM SFC. If the TCD local trigger boards do not receive an instrument confirm within ~ 1 μs, they reset all TDC and peak detector circuits and return to the idle state.

All trigger signals between the concentrator stacks and the TCD master trigger electronics use LVDS signaling over 110 Ω twist-n-flat data cable on dual-row, 0.1 in pitch, rectangular berg connectors. Trigger signals between the TCD master trigger electronics and the CREAM instrument electronics use LVDS signaling over 110 Ω shielded twisted pair on LEMO push-pull connectors.

4.7 The TCD Power System

The TCD concentrator electronics require ± 5 V power levels for analog circuits and +5 V, +3.3 V, and -2 V power levels for digital circuits. In addition, the TCD PMTs require +12 V to power their Ultravolt power supplies. These power levels are down converted from the CREAM instrument's supplied +31 V power at a common TCD power converter box, which is shown on the left of Figure 4.14. TCD voltages are down converted using Vicor's rugged series of industrial-grade DC-DC converters [119]. The analog and PMT power levels also include in-line Vicor ripple attenuation modules [120]. These converted voltages are then fed to the TCD concentrator stacks through two identical power fanout boards, one of which is shown on the right side of Figure 4.14,

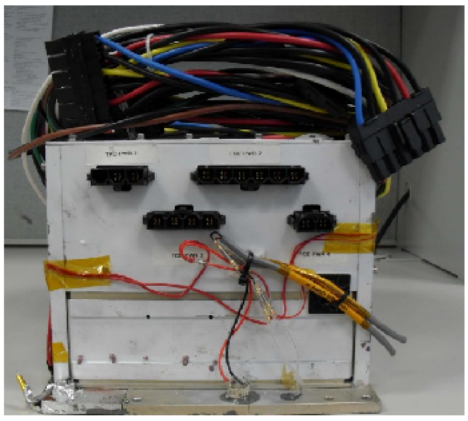

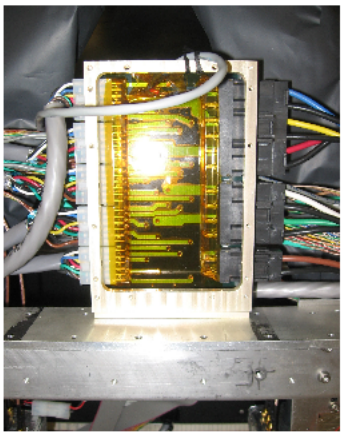

Figure 4.14. The TCD power box and power fanout boards.

through AWG12 gauge wire. Such a large diameter wire gauge is chosen to minimize voltage drops due to the large currents flowing through these long cables. One power fanout board is located on each side of the +y and -y sides of the TCD, with each concentrator receiving its power through a direct connection between the nearest power fanout board and its stack's power distribution board. The power distribution board on each concentrator stack is a simple 2-layer board which provides board level bypass capacitors and a connection point between incoming power and the local bus.

4.8 The TCD Housekeeping

Housekeeping signals are critical indicators of instrument health during flight. In addition to monitoring the values of all TCD power rails and PMT HVs, the TCD power converter box temperature, S3 switch temperature, S3 concentrator temperature, MYR concentrator stack temperature, and MYR PMT temperature are all monitored. National Semiconductor LM35 temperature sensors are used, which output 10 mV/°C. These housekeeping signals are fed into the CREAM instrument housekeeping board, which is part of CREAM's common electronics system. During flight, housekeeping sensors are readout at a rate of once every 5 s, and are monitored regularly at the CREAM SOC during flight.

Chapter 5

The BACCUS TCD Readout Electronics

5.1 Motivation and Goals For a New TCD Readout Design

The CREAM I–V Ethernet based microcontroller readout scheme has the advantages of a ready-made development platform (*i.e.*, the Arcturus MCF-5272 Coldfire microcontroller module with built in uClinux), well defined communication protocols (*TCP/IP* over Ethernet), off-the-shelf network hardware (Parvus 4-port Ethernet switches), and modularity in stack design. As previously described, this scheme requires the SFC to interface with each of the 10 concentrator stacks as separate command and data servers. While such a scheme is advantageous in large-scale experiments, reaping the full performance benefits of such a distributed acquisition system requires that data collection and event definition be completely decoupled processes in the CDAQ. This violates the CDAQ design philosophy of requiring all CREAM detectors to readout data simultaneously, only upon formation of an instrument trigger. Such a lock-step requirement keeps the CDAQ software free from the accumulation of a large number of parallel threads and processes, making it much simpler to debug, manage, and upgrade for future missions. However, this requirement also significantly increases the time to readout the TCD, costing ∼10 ms per event under normal conditions, with a live time fraction of ∼50% when the ZHI trigger rate is not pre-scaled.

Furthermore, subtleties in the interplay between the TCD trigger system, the CREAM master trigger electronics, and the CDAQ led to the occurrence of common glitches, wherein the CDAQ would receive indication of a TCD trigger from the CREAM instrument master trigger board, but the TCD would not respond with data. Such errors occurred in ∼2% of all events, and typically cost between 25 ms and 100 ms per error. The variability in deadtime due to such glitches adds difficulty to the analysis of data for an experiment like CREAM, where live time is an important factor in determining the absolute normalization of cosmic ray spectra. Figure

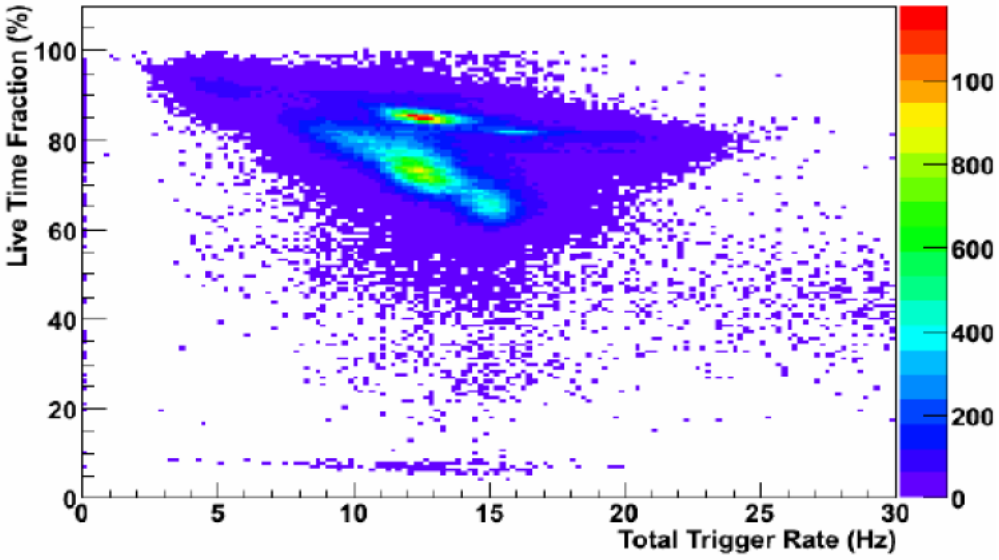

Figure 5.1. The CREAM II live time plot, created by Y. S. Yoon. Two different populations are seen. The higher live time population represents events which are formed from calorimeter triggers. The lower live time population represents events which were formed from TCD triggers [121].

5.1 shows CREAM II instrument live time as a function of trigger rate. Note that there are two separate populations. The population with higher live time and lower variability corresponds to events which hit the SCD and calorimeter, and may or may not include the TCD. The population with lower live time and higher variability corresponds to events which hit only the TCD.

Because of the aforementioned difficulties with the TCD's readout scheme, the TCD group decided to forego the CREAM VI flight in an effort to re-design the communications system between the TCD concentrators and the SFC[1]. The design goals in this effort were:

1. To create a single USB 2.0 link between the SFC and the TCD
2. To create a small, uniform deadtime during TCD event readout
3. To reuse the TCD's existing front-end, trigger, and power systems, while not increasing TCD weight, space, or power consumption

The remainder of this chapter will describe in some detail the hardware and software/firmware technical aspects of this new readout scheme, and serves as the main documentation for this new readout in the continuing CREAM program.

[1]This turned out to have been a fortuitous decision, as the CREAM VI campaign was prematurely terminated after a short, 6 day flight, due to a failure of the balloon flight termination mechanism while the payload was over the far side of Antarctica. Recovery of the flight components was difficult, and the fragile and exposed TCD scintillators could have been easily damaged.

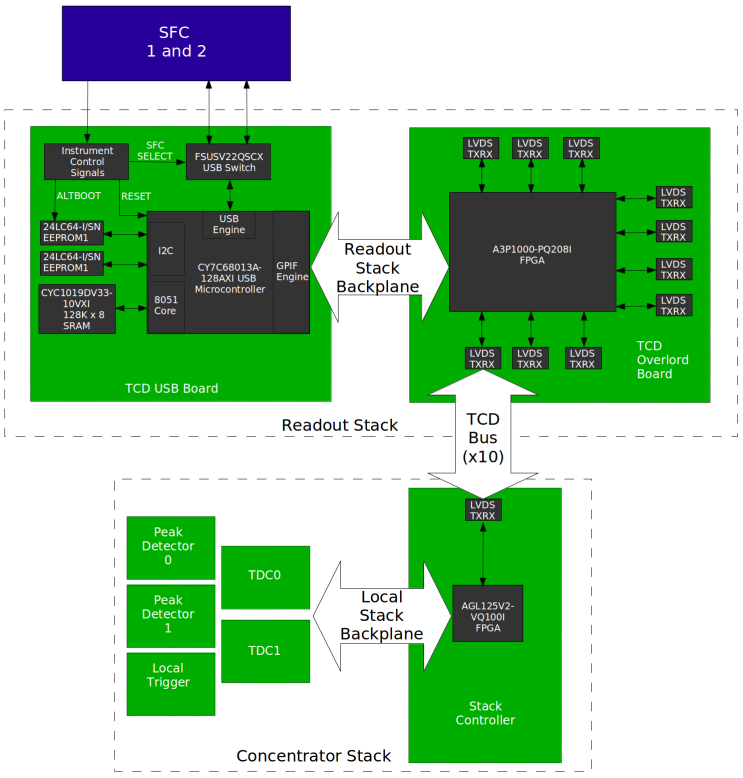

Figure 5.2. Overview of the new TCD readout scheme.

5.2 Overview of the New TCD Readout Scheme

A block diagram of the new TCD readout scheme is shown in Figure 5.2. In the new scheme, the SFC's single point of interface with the TCD is through a new stack of boards, known as the ***TCD Readout Stack***. Two boards reside inside the TCD Readout Stack—the ***TCD USB Board*** and the ***TCD Overlord Board***.

The TCD USB Board manages communication with the SFC via redundant USB 2.0 datalinks and a handful of digital control lines. It writes commands to, and receives status and event data from, the TCD Overlord Board via a parallel bus, shown as the ***Readout Stack Backplane*** in Figure 5.2. The Readout Stack Backplane interface protocol is described fully in Section 5.4.4.

The TCD Overlord Board serializes the commands it receives from the TCD USB Board and transmits these serialized commands to the appropriate concentrator stack. It also de-serializes command responses and event packets from each concentrator stack, presenting them to the TCD USB Board over the Readout Stack Backplane. Communication between the TCD Overlord Board and each concentrator stack happens through ten separate point-to-point, 12 MHz, full-duplex serial links, shown as the ***TCDBus*** in Figure 5.2. The routing of the TCDBus and the TCD's USB 2.0 datalinks is diagrammed in Figure 5.3. The TCDBus interface protocol is described fully in Section 5.4.4.

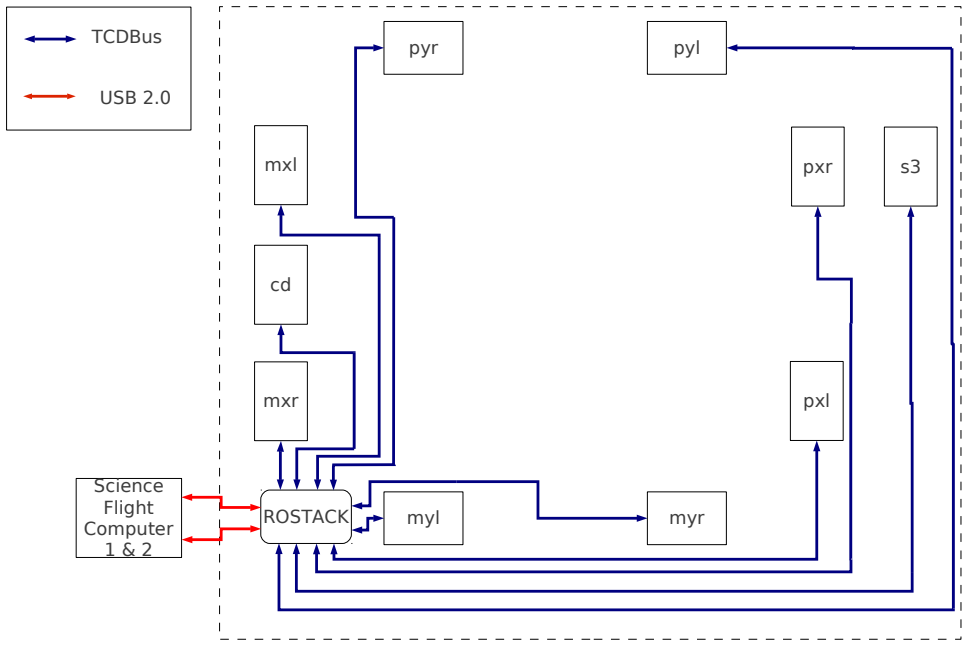

Figure 5.3. The *TCDBus*.

Inside each concentrator stack, the ***TCD Stack Controller Board*** manages incoming and outgoing serial communication with the TCD Readout Stack, while also providing the control logic for its peak detector, TDC, and local trigger boards. For the BACCUS TCD, the other boards in the concentrator stack are identical to those which were described in Chapter 4. Figure 5.4 shows the new TCD readout electronics as designed for the BACCUS TCD.

5.3 New TCD Readout Hardware

This section will provide a hardware-level description of the three new boards commissioned for the new TCD readout—the TCD USB Board, the TCD Overlord Board, and the TCD Stack Controller Board.

5.3.1 The TCD USB Board Hardware

The TCD USB Board is shown in Figure 5.5. Its USB 2.0 functionality is based around the CY7C68013A-128AXI [122]. Commonly referred to as the FX2LP, this chip is an industrial-grade, USB 2.0-capable microcontroller, manufactured by the Cypress Semiconductor Corporation. In addition to providing a USB 2.0 transceiver with an automated serial interface engine (SIE), the FX2LP comes with a myriad of other on-board features. Notable for this work are the 16 kB on-board SRAM program memory, the four double-buffered 512 kB USB endpoint FIFOs, the extended 8051 microcontroller core, the high-speed 16-bit general programmable interface

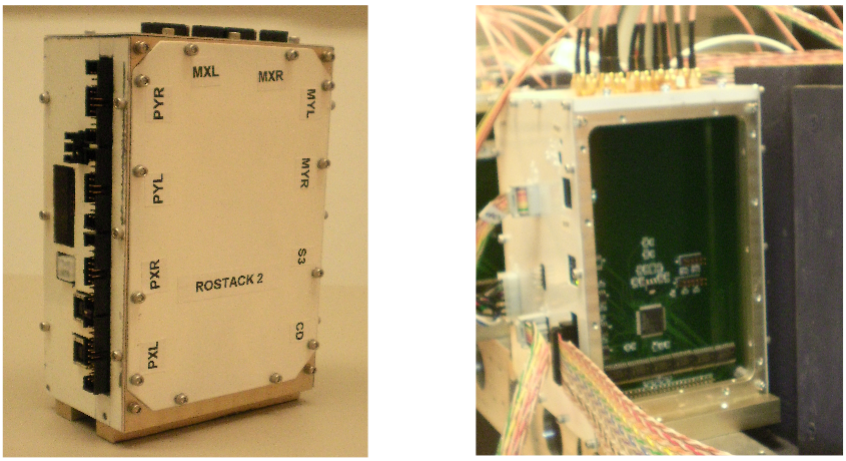

Figure 5.4. The new TCD readout electronics. The figure on the left shows the TCD Readout Stack. The figure on the right shows a concentrator stack with its side panel removed, allowing the new TCD Stack Controller Board to be seen.

(GPIF), several general purpose I/O (GPIO) ports, and an RS-232 port useful during firmware development and debugging. With ease of firmware updates in mind, the FX2LP's configuration was chosen to be "soft", meaning its firmware is uploaded through its USB link following power on.

While the FX2LP forms the heart of the TCD USB Board, several supporting integrated circuits (ICs) are also required. Two 24LC64-I/SN electrically erasable and programmable read-only memory (EEPROM) chips provide critical boot parameters (*i.e.*, USB product ID, vendor ID, and boot instructions) to the FX2LP after a system reset. Because BACCUS incorporates redundant SFCs, the TCD USB Board is designed to communicate through either of two USB-B style connectors, with one connection servicing each flight computer. The USB signals are physically routed through the FSUSB22QSCX, an industrial-grade, high-speed USB switch manufactured by Fairchild Semiconductor. The CY7C1019DV33-10VXI, an industrial grade, 128 KB SRAM manufactured by the Cypress Semiconductor Corporation, was connected to the FX2LP's external address and data lines, thereby allowing access to the 8051's full 64 kB address space. While the FX2LP's firmware is currently small enough that all code can easily reside in on-board memory, the addition of an external SRAM provides expansion capabilities for the future.

The TCD USB Board receives +3.3 V power externally, via a 4-pin Molex mini-fit Jr. receptacle. As previously mentioned, it stacks as the lower of the two boards on the Readout Stack Backplane. This backplane is implemented over SAMTEC 50-pin and SAMTEC 10-pin dual-row, stackable headers with 0.1 inch pitch.

The BACCUS common electronics system provides several instrument control signals to the TCD over a DB-9 instrument control connector. These signals and their associated pin assignments are detailed in Table 5.1. The ***RESET*** signal provides a global reset to the TCD.

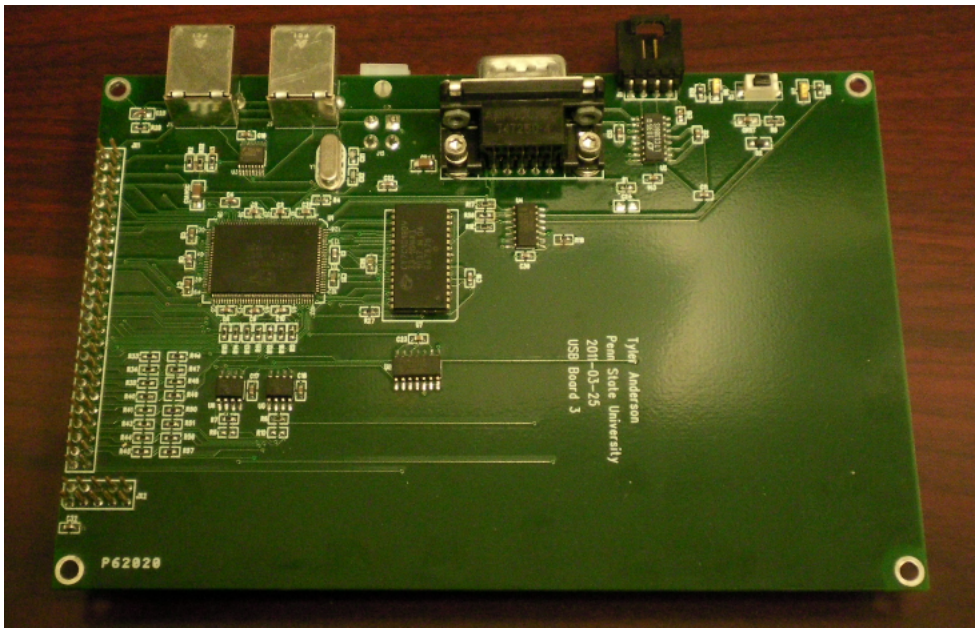

Figure 5.5. The TCD USB Board.

Signal Name	DB9 pin
RESET	1
+5 V (unused)	2,3
SFC2	6
ALTBOOT (unused)	7
GND	8,9

Table 5.1. Instrument control signals.

Activation of the ***SFC2*** signal selects the secondary USB link as active. The ***ALTBOOT***[2] signal causes the FX2LP to boot from its secondary I2C EEPROM. An additional +5V power rail is also supplied for optional power to the USB circuitry, but is unused in the current incarnation of the TCD USB Board. All instrument control signals are active high +5V signals. The 74LVC14, a hex, Schmitt-triggered inverter with +5V tolerant inputs, is used to level shift the instrument control signals to +3.3 V levels.

5.3.2 The TCD Overlord Board Hardware

The TCD Overlord Board (Figure 5.6) is the single TCD flight board which routes, serializes, and de-serializes communication between the FX2LP on the USB Board and the FPGA on each Stack Controller Board. The TCD Overlord Board's control logic resides on the A3P1000-PQ208I, a one million gate, industrial-grade, low-power, non-volatile flash FPGA from Microsemi's ProASIC3 series [123]. Microsemi's flash-based FPGA's are unique in that the FPGA's logic cell

[2]While this feature is useful for some detector systems, it is unnecessary for the TCD, and so, the ALTBOOT signal is ignored.

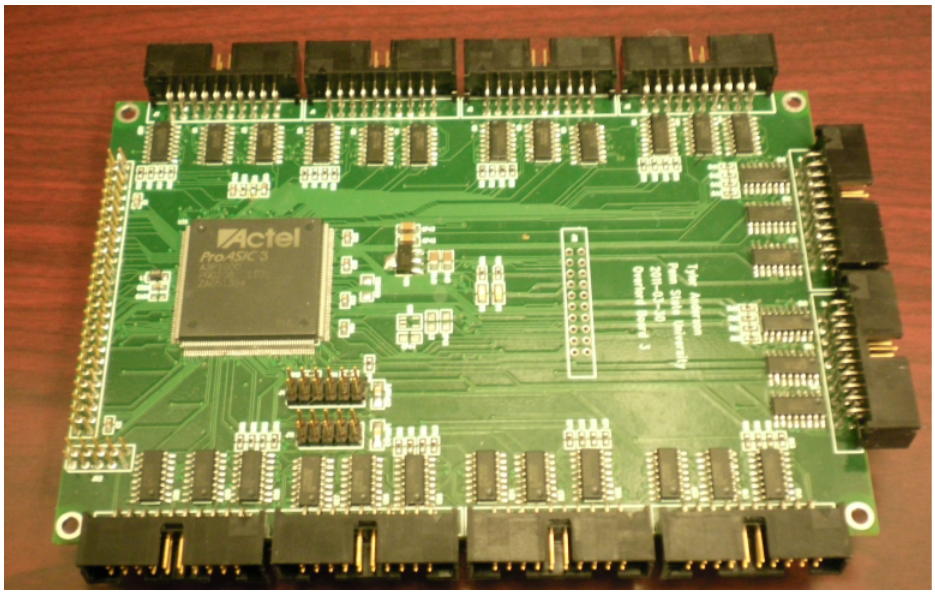

Figure 5.6. The TCD Overlord Board.

configurations and interconnects are stored as flash memory components, and hence offer all the advantages of an anti-fuse device (*e.g.*, live at power up and non-volatile configuration), while still allowing reprogrammability. The A3P1000 is programmed via a simple Joint Test Action Group (JTAG) connection, using Microsemi's FlashPRO-4 programmer.

All I/O banks in the A3P1000 were configured to follow the LVCMOS logic standard, and operate on +3.3 V power, which the A3P1000 receives directly from the TCD USB Board. The ADP3338ACK-1.5-R7 linear regulator is employed to generate the A3P1000's required +1.5 V core voltage.

As already mentioned, the TCD Overlord Board communicates with each concentrator stack via the point-to-point serial TCDBus. All signals on the TCDBus utilize the Low Voltage Differential Signaling (LVDS) standard. The Overlord Board uses National Semiconductor's DS90LV031 LVDS transmitters and the DS90LV032 LVDS receivers as a physical interface to the TCDBus. The TCDBus is transmitted over 110 Ω twist-n-flat ribbon cable with keyed, 20-pin, dual-row, shrouded rectangular connectors on each end. Table 5.2 lists all signals on the TCDBus. The TCDBus signaling protocol is detailed fully in Section 5.4.4.

5.3.3 The TCD Stack Controller Board Hardware

The TCD Stack Controller Board is shown in Figure 5.7. Its logic design resides on a AGL125V2-VQ100I, an industrial-grade, flash-based FPGA from Microsemi's low-power IGLOO series [124]. A power-on reset is obtained through the DS1818R-10+T&R, an industrial grade power-on reset circuit with pushbutton capability. This chip holds the AGL125 FPGA in reset for 150 ms after sensing that the +3.3V rail has reached a stable value. This reset can also be induced via an

Signal Name	Connector Pin	Description
SSPKN±	1, 2	Slave Speak Enable (active low)
MISO±	3, 4	Master In Slave Out
SCLK±	5, 6	Slave Clock
IRQN±	7, 8	Event Interrupt (active low)
MSPKN±	9, 10	Master Speak Enable (active low)
MOSI±	11, 12	Master Out Slave In
MCLK±	13, 14	Master Clock
Unused	15, 16	N/A
RESETN±	17, 18	Reset concentrator stack (active low)
FLUSHN±	19, 20	Return to IDLE state (active low)

Table 5.2. TCDBus signals.

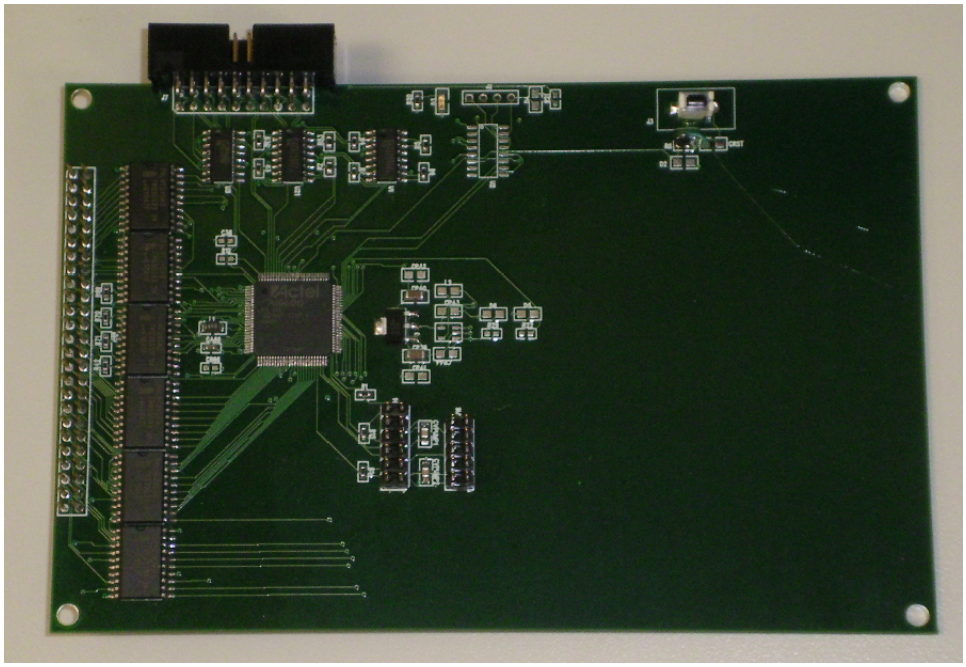

Figure 5.7. The TCD Stack Controller Board.

on-board pushbutton switch. The AGL125 is programmed using Microsemi's FlashPro4 through a 10 pin, dual-row JTAG connector.

As with the TCD Overlord Board, the TCD Stack Controller Board's TCDBus interface is implemented via National Semiconductor's DS90LV031 LVDS transmitters and DS90LV032 LVDS receivers. While the AGL125's I/O banks run on LVCMOS logic levels, powered by +3.3 V logic, its core runs on +1.5 V power. The +3.3 V rail is obtained directly from the stack's power distribution board, while +1.5 V is derived from the concentrator stack's main power via the on board ADP3338ACK-1.5-R7 LDO linear regulator. The Stack Controller Board connects to the concentrator stack's Local Bus via a Samtec 50-pin, board-to-board header. Interface to this bus is governed by the use of 74LVC245 bi-directional bus buffers.

Bit	31	30–28	27–24	23–16	15–0
Content	ERROR	ACTION	TARGET	PARAM	DATARG

Table 5.3. TCD command and response packet format.

5.4 BACCUS TCD Software, Firmware, and Logic Code

This section describes all new code developed for the BACCUS TCD. This includes the communication protocols and interface software written for the CDAQ and ground support equipment (GSE) computers, firmware written for the FX2LP microcontroller, and the Very High Speed Integrated Circuit Hardware Description Language (VHDL) logic designed for the TCD Overlord Board's A3P1000 FPGA and the TCD Stack Controller Board's AGL125 FPGA.

5.4.1 TCD Command, Response, and Event Data Packet Protocols

The TCD implements a command/response verification scheme, such that the reception of a command from the SFC generates a TCD response indicating whether the command was executed properly. TCD command and response packets both adhere to the same 32-bit packet format, which is detailed in Table 5.3. Bit 31 is the ***ERROR*** bit, which is always set to "0" in command packets, but may be set to "1" in a response packet if the command received was un-executable. Bits 30–28 are the ***ACTION*** bits, which designate the overall type of execution to be carried out. Table 5.4 enumerates all possible ACTION values. Bits 27–24 are the ***TARGET*** bits, and choose the destination TCD concentrator stack for the command. Table 5.5 enumerates all possible TARGET values. Bits 23–16 are the ***PARAM*** bits, and represent the TCD parameter to which the command is addressed. Table 5.6 enumerates all possible PARAM values. Bits 15–0 are the ***DATARG*** bits, which specify the data argument (*i.e.*, the numerical value) for the command.

Commands with ACTION = NOP are useful for checking concentrator stacks for connectivity. The TARGET electronics stack responds to a NOP with all bit values in the DATARG inverted. All TARGET values listed in Table 5.5 are valid for use with NOP. During command execution, the PARAM component of the command is ignored, and so can be entered as NA = "not applicable".[3]

Commands with ACTION = GET query the status of the TCD parameter specified by PARAM for the electronics stack specified by TARGET. The TARGET electronics stack responds to a GET with the current value of PARAM in the DATARG position. For TARGET values PXL–CD, PARAM values THR00–DISC3 form valid commands. For TARGET = ROSTACK, only PARAM = CLEV or PARAM = STKMSK are valid. All other combination are deemed invalid, and so, response packets for such commands would echo the original command but have the ERROR bit set to "1".

[3]Actually, since PARAM is ignored, anything can be entered.

Commands with ACTION = SET set the value of the TARGET electronics stack's PARAM parameter to the value specified in DATARG. The TARGET concentrator first executes the routine to set the PARAM parameter to DATARG, and responds with DATARG replaced by the new value for the parameter. In the case of PARAM corresponding to a DAC (*i.e.*, THR00 through DISC3), the response value is actually the physical value read back from the DAC after setting it, and so provides proof that the DAC correctly received its new setting. Valid TARGET/PARAM combinations are the same as those specified for GET.

Commands with ACTION = INIT cause the TARGET electronics stack to initialize all parameters to the default values listed in Table 5.6. INIT is only valid with TARGET = PXL–CD. PARAM is ignored. DATARG is also ignored, and so can be set to "0".

The command "SOFTRESET ROSTACK NA 0" sends the equivalent of a power-on reset to all FPGAs by causing the FX2LP to pulse the SOFT_RESETN line.

The command "FLUSH ROSTACK NA 0" causes the FX2LP to pulse the FLUSHN line, which synchronously causes the state machines in all TCD FPGAs to return to the idle state.

Commands with ACTION = CLEAR cause the TARGET concentrator stack to allow trigger boards to return to the idle state. PXL–CD are valid TARGETs if PARAM = CLEARLT. Such commands cause the TARGET concentrator stack to clear its local trigger board, hence freeing it to re-trigger for the next event. When TARGET = PXR and PARAM = CLEARMT, the PXR concentrator stack's master trigger board clears, thus allowing the whole TCD to form new instrument triggers (see Section 4.6). Other combinations are invalid. DATARG is ignored with CLEAR commands. Note that each concentrator stack's local trigger board is cleared automatically after the event packet has been transmitted, and so the SFC never uses the option to clear the local trigger board while in an automated acquisition mode. However, the SFC issues the command to clear the master trigger board at the end of overall instrument event collection, thereby enforcing the lock-step acquisition requirement discussed in Section 5.1.

The PARAM values CLEV and STKMSK are special parameters which are only valid when ACTION = SET or GET and TARGET = ROSTACK. CLEV represents the number of IRQN flags (*i.e.*, the event interrupts sent from the concentrator stacks to the Readout Stack when triggered) that must be registered before reading out an event. For example, the command "SET ROSTACK CLEV 2" sets CLEV such that reception of an IRQN from any two concentrator stacks triggers event readout. The default value for CLEV is 3. STKMSK is a bit mask, whereby all communication and signaling on the TCDBus connecting to any one of the ten concentrator stacks may be inhibited by setting the bit position corresponding to the TARGET for that stack to 0. For example, "SET ROSTACK STKMSK 0x03EF" inhibits communication with the MXL concentrator.

TCD event packets are passed to the CDAQ on request, when the CDAQ registers an instrument trigger. Unlike response packets, TCD event packets do not pass "header" information (*i.e.*, the ACTION, TARGET, and PARAM) with each "event item" (*e.g.*, ADC values, event numbers, *etc.*). Instead, the TCD passes the CDAQ a single, 440 byte packet, with the contents of each 16-bit word in the packet storing the value of a pre-designated event item. This pre-defined

ACTION	Bits 30–28	Description
NOP	000	Stack controller echos NOP with DATARG inverted.
GET	001	Query the value of a parameter.
SET	010	Set the value of a parameter to DATARG.
INIT	011	Initialize all parameters to default. DATARG ignored.
EVENT	100	Identifies an event packet.
SOFTRESET	101	Reset all FPGAs.
FLUSH	110	Return all FPGAs to their default state.
CLEAR	111	Clear event triggers. DATARG ignored.

Table 5.4. All TCD actions.

TARGET	Bits 27–24	Description
PXL	0000	+x left side concentrator
PXR	0001	+x right side concentrator
PYL	0010	+y left side concentrator
PYR	0011	+y right side concentrator
MXL	0100	-x left side concentrator
MXR	0101	-x right side concentrator
MYL	0110	-y left side concentrator
MYR	0111	-y right side concentrator
S3	1000	S3 detector
CD	1001	CD detector
ROSTACK	1010	Readout stack

Table 5.5. All TCD targets.

event format is elucidated in Table 5.7. Sets of identical event items are ordered consecutively by concentrator TARGET number, such that, for example, the 20 bytes of the PD00 item contain PXL PD00, PYL PD00...CD PD00, *etc.*

5.4.2 CDAQ and GSE TCD Readout Software

A set of C++ base classes was developed for commanding and reading out the TCD. These classes were written generically, such that they were easily incorporated into the SFC's CDAQ. These classes also form the basis for a separate TCD diagnostic software package developed specifically for reading out the TCD during hardware development and troubleshooting.

5.4.2.1 TCD Base Classes

The class ***TCD2Usb*** provides all hardware level functionality for the TCD's USB interface via calls to the *libusb-0.1.12* API. This includes initializing the USB connection, loading the FX2LP's firmware, claiming and releasing the USB software interface, and reading from and writing to the USB endpoint FIFOs. Errors encountered by the TCD2Usb class while attempting to interface to the TCD generate messages, which can be re-directed to the system log by upper-level code.

TARGET = PXL through CD			
Parameter	Bits 23–16	Description	Default DATARG
THR00	0x00	PMT0 TDC0 Threshold	4095
THR01	0x01	PMT0 TDC1 Threshold	4095
THR02	0x02	PMT0 TDC2 Threshold	4095
THR03	0x03	PMT0 TDC3 Threshold	4095
LEVEL0	0x04	PMT0 TDC max value	3000 (150 ns)
HV00	0x05	PMT0 HV control	0 (PMT0 off)
HV10	0x06	PMT1 HV control	0 (PMT1 off)
THR10	0x07	PMT1 TDC0 Threshold	4095
THR11	0x08	PMT1 TDC1 Threshold	4095
THR12	0x09	PMT1 TDC2 Threshold	4095
THR13	0x0A	PMT1 TDC3 Threshold	4095
LEVEL1	0x0B	PMT1 TDC max value	3000 (150 ns)
HV01	0x0C	Spare DAC	0 (unused)
HV11	0x0D	Spare DAC	0 (unused)
DISC0	0x0E	TDC00/TDC10 Coincidence	800 (PMT0 or PMT1)
DISC1	0x0F	TDC01/TDC11 Coincidence	800 (PMT0 or PMT1)
DISC2	0x10	TDC02/TDC12 Coincidence	800 (PMT0 or PMT1)
DISC3	0x11	TDC03/TDC13 Coincidence	800 (PMT0 or PMT1)
CLEARLT	0x12	Clear local trigger board	N/A
CLEARMT	0x13	Clear master trigger board	N/A

TARGET = ROSTACK			
Parameter	Bits 23–16	Description	Default DATARG
CLEV	0x15	Coincidence level for EVT_PENDN	3
STKMSK	0x16	Stack mask	0x03FF (all active)

ACTION = NOP or INIT		
Parameter	Bits 23–16	Description
NA	0xFF	Placeholder for PARAM when ignored

Table 5.6. All TCD parameters.

The class ***TCD2Cmd*** parses outgoing command packets to ensure they represent one of the valid combinations described in Section 5.4.1. In addition, for PARAM = HV00, the TCD2Cmd class checks that DATARG<1750, which corresponds to a PMT high voltage of 3 kV—the maximum allowable for the XP2020 PMTs. Invalid commands generate an error messages and are not transmitted to the TCD.

The ***TCD2Evt*** class examines the TCD's raw data packet (see Table 5.7) and allows for optional packet compression before writing it to disk. When the CDAQ is operated in flight mode, this packet compression option is selected, since it is important to conserve space on the flight hard drive. The format of this compressed packet is shown in Table 5.8. The first two bytes of the compressed packet store the total size (in bytes) of the packet after compression. This is followed by a single 32-bit event number, which is determined via the results of a majority voter algorithm implemented on the ten event numbers collected from the TCD concentrator stacks. The next two bytes contain a "good mask", which stores a "1" in the TARGET bit

Element	Packet Position	EVENTID	Description
PD00	19–0	0x8	Peak Detector PMT0, Channel 0
PD01	39–20	0x9	Peak Detector PMT0, Channel 1
PD02	59–40	0xA	Peak Detector PMT0, Channel 2
PD03	79–60	0xB	Peak Detector PMT0, Channel 3
PD00	99–80	0xC	Peak Detector PMT1, Channel 0
PD10	119–100	0xD	Peak Detector PMT1, Channel 1
PD12	139–120	0xE	Peak Detector PMT1, Channel 2
PD13	159–140	0xF	Peak Detector PMT1, Channel 3
TDC00	179–160	0x0	Time-to-Digital Converter PMT0, Channel 0
TDC01	199-180	0x1	Time-to-Digital Converter PMT0, Channel 1
TDC02	219–200	0x2	Time-to-Digital Converter PMT0, Channel 2
TDC03	239–220	0x3	Time-to-Digital Converter PMT0, Channel 3
VALID0	259–240	NA	Valid Bits for TDC00–TDC03
TDC10	279–260	0x4	Time-to-Digital Converter PMT1, Channel 0
TDC11	299–280	0x5	Time-to-Digital Converter PMT1, Channel 1
TDC12	319–300	0x6	Time-to-Digital Converter PMT1, Channel 2
TDC13	339–320	0x7	Time-to-Digital Converter PMT1, Channel 3
VALID1	359–340	NA	Valid Bits for TDC10–TDC13
STATUS	379–360	NA	Trigger Status Bits
ECOUNT	399–380	NA	Event counter
EVTNO	439–400	NA	Event number

Table 5.7. TCD event packet format.

position corresponding to concentrators which have at least 1 "valid" ADC value.[4] A value equal to one less than the number of valid items from each good concentrator stack is then stored in consecutive data nybbles.[5] Next, valid ADC values from the original packet are stored in 16-bit words, with the highest nybble of each word storing the "EVENTID" for the item (see the third column of Table 5.7) and the lower 12-bits storing the corresponding ADC value. The final two bytes of the compressed packet store the result of a cyclic redundancy check performed on the compressed data packet. The resulting compressed TCD event data packet varies in size between 12 bytes and 154 bytes, depending on the number of valid ADC values.

In the CDAQ, the TCD2Usb, TCD2Cmd, and TCD2Evt base classes are all encapsulated in the wrapper class, ***HTCD2***, which acts as the CDAQ's single point of interface to the TCD.

5.4.2.2 The TGACS Package

The TCD GSE ACquisition Software (TGACS) package was developed for the purposes of hardware development and troubleshooting during the TCD's integration. Based on the base classes described previously, TGACS contains several programs which allow for standalone commanding and reading out of the TCD. The ***command*** program allows mnemonic commands to be issued

[4] In this context, a valid peak detector ADC value is greater than 450 ADC units, while a valid TDC value is greater than 200 TDC units and has corresponding VALID bit value equal to 1.

[5] One less than the number of valid items is stored since this allows the numbers 1–16 to be represented by a 4-bit number.

Byte	Bits	Description
1 to 0	15–0	Number of bytes in packet
5 to 2	31–0	Majority voted event number
7 to 6	15–0	Good mask: 1 in TARGET bit position if some good data, else 0
8	7–4	Number of valid items for first good concentrator - 1
8	3–0	Number of valid items for second good concentrator - 1
etc.		
N+1 to N	15–0	EVENTID & 1st valid 12-bit ADC value
N+3 to N+2	15–0	EVENTID & 2nd valid 12-bit ADC value
etc.		
Last 2 bytes		CRC word

Table 5.8. Format of compressed TCD event packet written to disk.

to the TCD from a terminal (*e.g.*, "SET PXL THR10 100"). The ***getconf*** program queries the status of all TCD parameters, printing the results in tabular form. The ***event*** program reads out TCD event data and writes the resulting 440 byte event packets to an ASCII file. The ***text2root*** program reads in these raw data files and converts them to CERN's ROOT "TTree" format, from which ADC distributions and other analysis plots are easily obtained.

5.4.3 USB Board Firmware

All firmware developed for the FX2LP was compiled using the Small Device C Compiler [125]. The ***fx2lib*** libraries were also incorporated in order to handle some of the FX2LP's more mundane tasks [126].

Figure 5.8 diagrams the steps taken by the FX2LP's firmware after power up. If the USB Board is to be used in debugging mode, the RS-232 interface is enabled. The FX2LP's USB endpoint FIFOs are then initialized. EP1OUT is initialized as a 64 byte USB receiving FIFO, while EP1IN is initialized as a 64 byte sending FIFO. EP1OUT is used for receiving commands from the SFC, while EP1IN is used for sending commands to the SFC. Both EP1IN and EP1OUT are configured for "manual commit mode", meaning that incoming command packets and outgoing response packets require active retrieval from the endpoint FIFOs by the firmware running on the 8051 core. In this case, the advantage of manual commit mode is that the FX2LP's 8051 microcontroller can examine and check the contents of these packets before passing them along to their destination. EP6IN is configured as a 512 byte USB sending FIFO, which is dedicated to sending the TCD's event data to the SFC. In order to maintain low detector dead time, this endpoint is setup in "auto commit mode", meaning that incoming event data is directly handed to the FX2LP's SIE for transmission to the SFC.

The FX2LP's GPIF engine is then initialized with configuration data. The FX2LP's GPIF interface is essentially a programmable state machine with 6 control outputs, 6 ready inputs, a 9-bit address bus, and a 16-bit data bus. In the case of the TCD readout stack, the FX2LP uses its GPIF interface to parse the command, response, and event FIFOs presented to it by the TCD Overlord Board's FPGA.

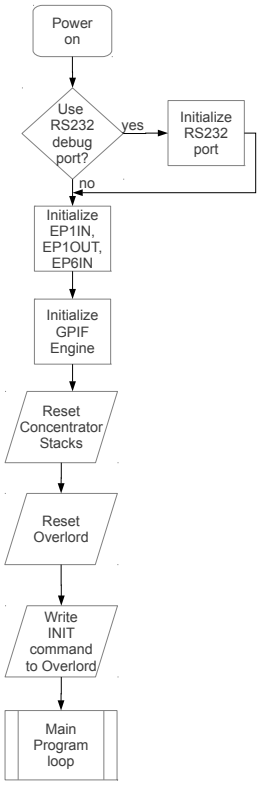

Figure 5.8. The TCD USB Board firmware's power on sequence.

Reset lines are then pulsed to each concentrator stack and to the TCD Overlord Board's FPGA. The issuing of this reset is only a precaution, since the POR circuit servicing each TCD FPGA will have already provided a reset when the TCD is powered ON. The FX2LP then issues the INIT command to all concentrator stacks, causing each stack to initialize its parameters to the default values listed in Table 5.6.

After initialization has completed, the firmware remains in a tight loop, alternately polling for either incoming commands from the SFC or reception of the ***EVT_PENDN*** flag from the TCD Overlord Board, which, as will be described in Section 5.4.4, indicates event data has been collected. Figure 5.9 details the main loop's execution.

5.4.4 Overlord Board FPGA Logic

As with all ProASIC3 FPGAs, the configuration of the TCD Overlord Board's A3P1000 FPGA is stored in non-volatile flash memory. All low-level logic modules for the A3P1000 were written in VHDL and implemented in Microsemi's Libero 9.1 IDE [127]. Top-level modules were assembled using Microsemi's *Smart Design*, a utility which writes HDL code based on connections defined graphically in a canvas. The Libero software suite uses vendor specific versions

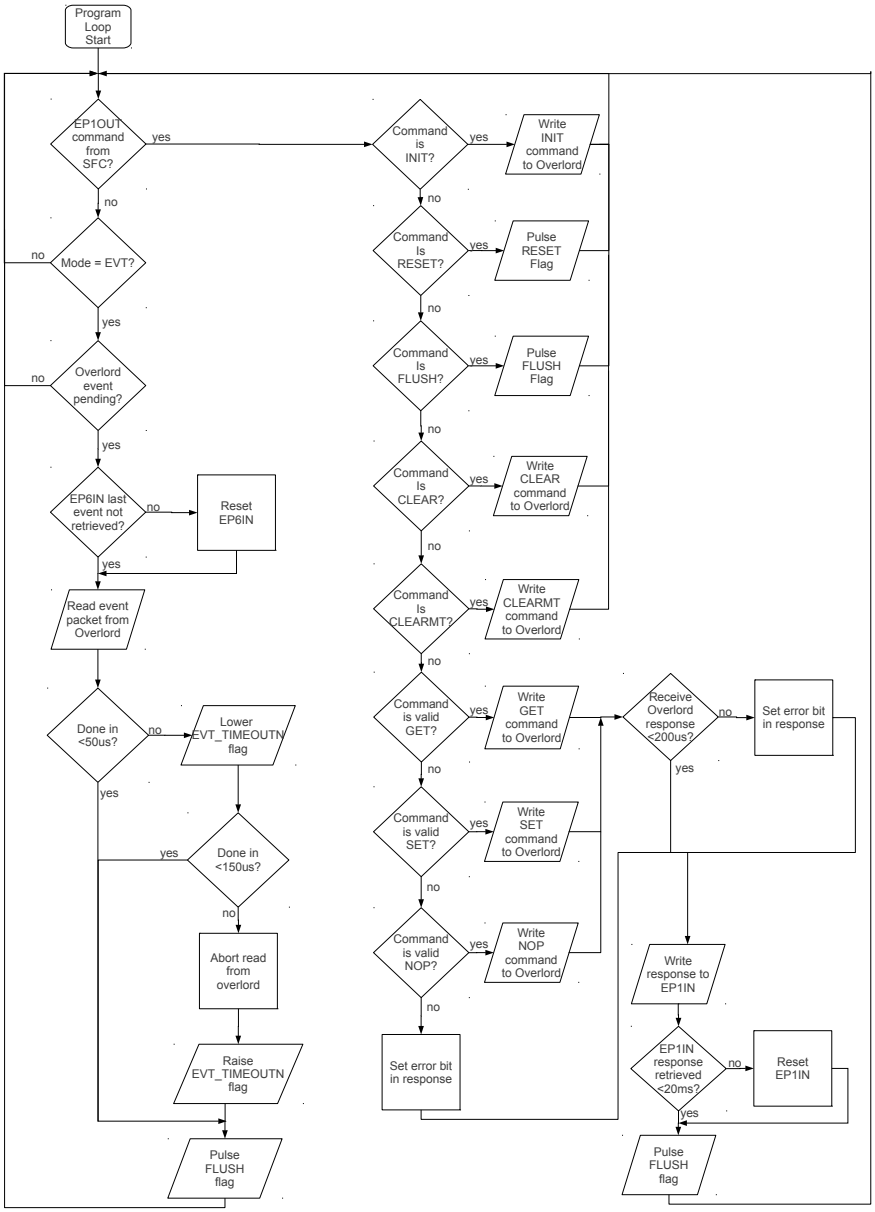

Figure 5.9. The FX2LP's main loop.

Signal Name	FX2LP Pin	Direction	Description
CMD_WEN	GPIF CTL0	out	Command write enable
EVT_REN	GPIF CTL1	out	Event read enable
RSP_REN	GPIF CTL2	out	Response read enable
RWN	GPIF CTL3	out	Read/Write bus direction
OLPC_WRN	GPIF CTL4	out	Parameter module write enable
RSP_RDYN	GPIF RDYN0	in	Overlord response data waiting
EVT_RDYN	GPIF RDYN1	in	Overlord has event data waiting
GPIFADR[8:0]	GPIF GPIFADR[8:0]	out	Overlord memory address
FD[0:15]	GPIF FD[15:0]	in/out	Databus to overlord
EVT_TIMEOUTN	GPIO PORTA1	out	Forces event read
RSP_TIMEOUTN	GPIO PORTA2	out	Forces response read
SOFT_RESETN	GPIO PORTA3	out	Reset the overlord
FLUSHN	GPIO PORTA5	out	Return all stack to IDLE
EVT_PENDN	GPIO PORTA6	in	Event trigger has been generated
EVT_COLLECTN	GPIO PORTA7	out	FX2LP is collecting an event

Table 5.9. The TCD USB Board/TCD Overlord Board GPIF/FIFO interface. Direction is specified relative to the FX2LP.

of Mentor Graphic's *ModelSim* for both pre-layout and post-layout simulations, Synposis's *Synplicity Synplify Pro ME* for logic synthesis, and Microsemi's *Designer* for I/O assignment and place-and-route.

Figure 5.10 is a block diagram of the internal and external interfacing of all logic modules residing in the TCD Overlord Board's A3P1000 FPGA. The A3P1000 presents a 16-bit, bi-directional data bus between itself and the GPIF interface of the FX2LP, which is shown as the *Readout Stack Backplane* in Figure 5.2. The FX2LP's GPIF engine acts as the master of this bus, writing to it in order to issue commands to the TCD concentrator stacks or Overlord FPGA, and reading from it when notified of pending command responses or event packets. Table 5.9 lists all lines which comprise the interface between the FX2LP's GPIF interface and the Overlord Board's FPGA. The FX2LP controls the directionality of the interface's data bus using the ***R/WN*** read/write strobe.

Referring back to the block diagram of Figure 5.10, the FX2LP selects the ***CMD_FIFO*** command FIFO by activating the ***CMD_WEN*** command enable strobe. The 32-bit commands from the FX2LP are written to this 16-bit FIFO in two write stages, with the higher 16-bits written first. The status of the ***CMD_FIFO_EMPTY*** empty flag is monitored by the ***CMD_CONTROL*** module, and commands are retrieved once the non-empty condition is detected.

Once a new command has been retrieved, the CMD_CONTROL module appends an 8-bit ***TAG*** onto the command packet.[6] The CMD_CONTROL module then calculates an odd par-

[6]This TAG byte is generated by a running counter inside the CMD_CONTROL module, whose count is incremented as the last step of processing each command, and whose count is reset to 0 when the FX2LP activates the ***FLUSHN*** flag at the end of each command/response cycle. By passing TAG back to the Overlord in the corresponding response packet, the Overlord's receiver control module is able to present these responses back to the FX2LP in same order as they were dispatched by simply writing them to the TAG memory address.

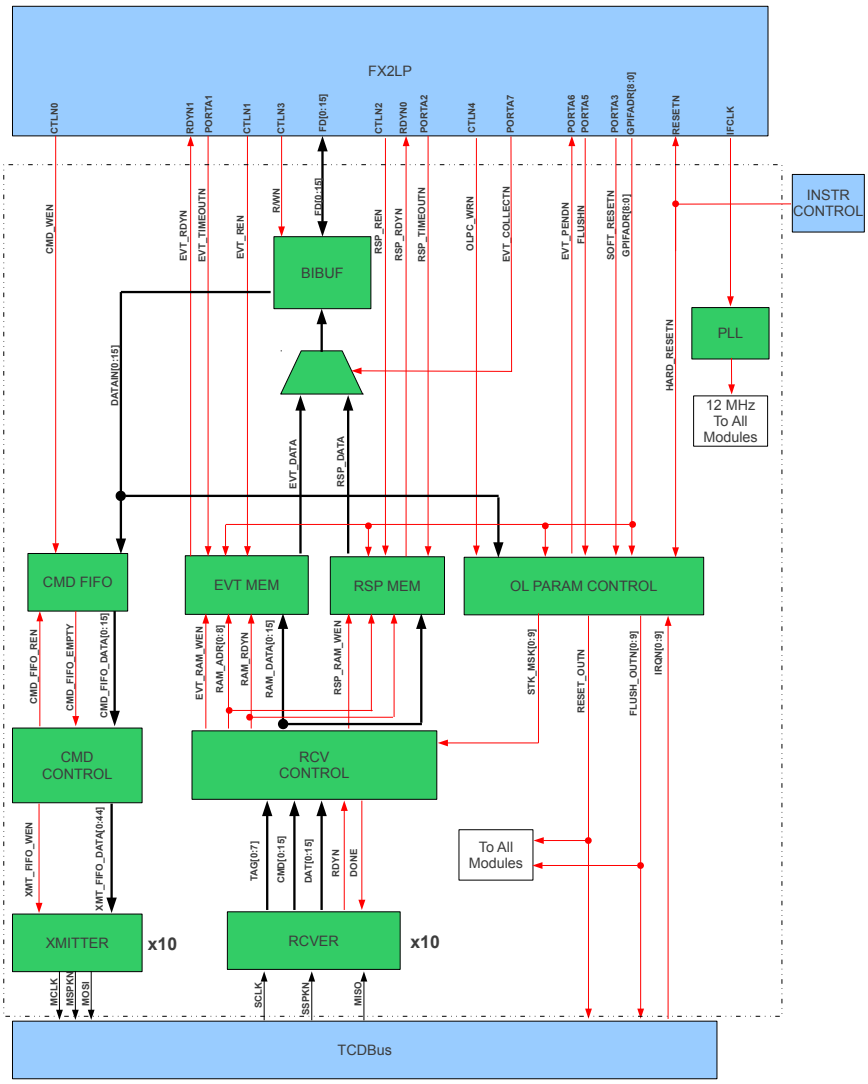

Figure 5.10. Block diagram of the Overlord FPGA logic design. The boundaries of the FPGA are shown inside the dash-dot box. Green blocks represent VHDL logic modules. Thin red lines represent control signals. Thick black lines represent the path of dataflow.

Bit	44	43–36	
Content	TAG Parity	TAG	
Bit	35	34	33–31
Content	ACTION Parity	ERROR	ACTION
Bit	30	29–26	
Content	TARGET Parity	TARGET	
Bit	25	24–17	
Content	PARAM Parity	PARAM	
Bit	16	15–0	
Content	DATARG Parity	DATARG	

Table 5.10. The TCDBus packet format.

ity bit for each of TAG, ACTION, TARGET, PARAM, and DATARG, and arranges the resulting elements according to the 45-bit TCDBus packet format shown in Table 5.10. The CMD_CONTROL module writes the resulting TCDBus packet to the ***XMITTER*** serial transmitter module corresponding to the command's destination concentrator stack, as indicated by the TARGET component of the command.

As previously described, the TCDBus is a full-duplex, 12 MHz, point-to-point serial data link between each concentrator stack and the TCD Readout Stack. On the Overlord, serialization is managed by the XMITTER transmitter module, while de-serialization is managed by the ***RCVER*** receiver module. Both modules utilize standard shift register techniques for serialization and de-serialization. The Overlord transmits serial data on the TCDBus using a three-wire protocol which includes the ***MSPKN*** "master speak" line, the ***MCLK*** "master clock" line, and the ***MOSI*** "master out slave in" line.

Figure 5.11 shows the transmitter module algorithm, while Figure 5.12 shows a timing diagram for TCDBus packet transmission. The MSPKN line transitions LOW for one clock cycle, indicating the start of a packet. Data bits are then shifted out "little endian" (*i.e.*, the least significant bit of the packet goes first) on the MOSI line following the falling edge of each MCLK clock transition. After all 45 bits have been transmitted, the MSPKN line transitions HIGH, indicating the end of transmission for the packet.

Figure 5.13 shows the RCVER receiver module algorithm. The Overlord's receiver works in a complementary manner to the transmitter, operating on a three-wire interface consisting of a ***SSPKN*** "slave speak" line, a ***SCLK*** "slave clock" line, and a ***MISO*** "master in slave out" line. Concentrator stacks follow a transmission protocol identical to that shown in Figure 5.12, with MSPKN exchanged for SSPKN, MCLK exchanged for SCLK, and MOSI exchanged for MISO. The receiver module shifts in the TCDBus's 45-bit little endian data packets and performs an odd-parity check on each received command component. If an error is detected in the parity check, or if less than 45 bits are shifted in during consecutive clock cycles, the packet is dropped.[7] Note that, while the transmitter module shifts data bits out on the clock's falling

[7]The FX2LP will eventually timeout waiting for a response to the dropped command. The CDAQ detects this timeout, and writes a corresponding error message to the system log.

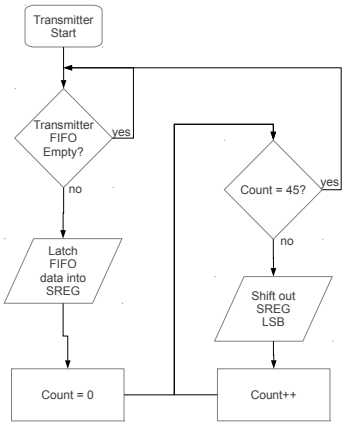

Figure 5.11. Diagram of the transmitter algorithm.

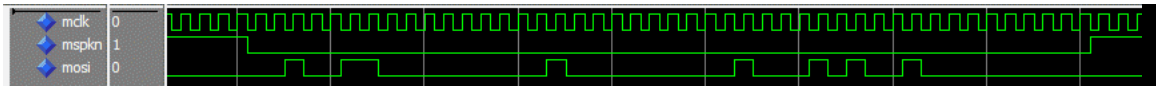

Figure 5.12. Timing diagram of the serial transmission protocol between the TCD overlord and a concentrator stack, as predicted by *ModelSim*. The command "NOP PXL THR00 0" is being transmitted.

edge, the receiver module latches these data bits on the clock's rising edge. Using opposite clock edges for transmission and reception should theoretically improve reliability, since waiting the extra 1/2 clock cycle before latching bit values should reduce the effects of transmission line reflections and clock/data signal skew.[8]

The Overlord's ***RCV_CONTROL*** receiver control module monitors the ***RDYN*** ready lines from each RCVER module for the arrival of new data packets. When a new data packet is detected, RCV_CONTROL retrieves the packet and writes the DATARG of packets with ACTION = EVENT to the ***EVT_MEM*** event RAM block. For packets with ACTION = NOP, GET, or SET, the full 32-bit response packet is written to the ***RSP_MEM*** response RAM block. For both event and response packets, the RCV_CONTROL module writes packets to the memory location corresponding to the packet's TAG, thereby enforcing a pre-determined internal ordering of elements in the packets presented to the FX2LP.

The FX2LP is notified of pending responses by the ***RSP_RDYN*** response ready flag. It reads from RSP_MEM using the ***RSP_REN*** read enable strobe and addresses this RAM block using the ***GPIFADR[8:0]*** GPIF address lines.

Likewise, the FX2LP is notified of pending event data in EVT_MEM by the ***EVT_PENDN*** event pending flag. The FX2LP reads event packets from the EVT_MEM RAM block using

[8]The careful impedance matching and low-skew cables used for the TCDBus likely renders such precautionary tactics unnecessary.

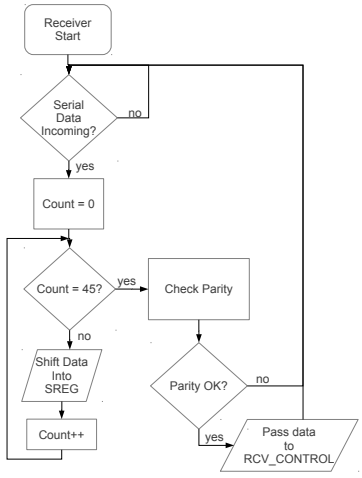

Figure 5.13. Diagram of the receiver algorithm.

the ***EVT_REN*** strobe and addresses this RAM block using the GPIFADR[8:0] GPIF address lines. Response and event data paths to the FX2LP are multiplexed, with the FX2LP's ***EVT_COLLECTN*** event collect control line choosing the active path.

The ***OL_PARAM_CONTROL*** module forms the ***EVT_PENDN*** event pending flag, which signals the FX2LP to read event data from the EVT_MEM event RAM block. As discussed in Section 5.4.1, this flag is formed from the multi-fold coincidence of the IRQN interrupt flags transmitted from each concentrator stack over the TCDBus after triggering. The IRQN coincidence level for formation of EVT_PENDN is programmable by setting the parameter, CLEV. The FX2LP writes a new value for CLEV to OL_PARAM_CONTROL by using the ***OLPC_WRN*** strobe, and setting GPIFADR[8:0] = 0x001.

Likewise, OL_PARAM_CONTROL also maintains the value of STKMSK, which, as discussed in Section 5.4.1, may inhibit all signals from the TCDBus of a given concentrator. The FX2LP writes a new value for STKMSK to OL_PARAM_CONTROL by again using the OLPC_WRN, but this time setting GPIFADR[8:0] = 0x002.

The OL_PARAM_CONTROL module also provides some simple "glue" logic for the FX2LP. It synchronizes the asynchronous FLUSHN signal into the FPGA's clock domain via the standard technique shown in Figure 5.14, creating the synchronized ***FLUSH_OUTN***. It also ANDs the ***HARD_RESETN*** generated at power ON and the ***SOFT_RESETN*** fired on command by the FX2LP, resulting in a single ***RESET_OUTN***. FLUSH_OUTN and RESET_OUTN are then distributed to all logic modules and to all concentrator stacks via the TCDBus.

The TCD Overlord Board uses a single, 12 MHz clock, which derives from the 12 MHz ***IFCLK*** GPIF interface clock provided by the FX2LP. The IFCLK line is fed into the A3P1000's internal phase-locked loop module, and distributed to all logic modules via low-skew clock networks. It's worth noting that timing analysis performed on the Overlord Board's final logic design indicates

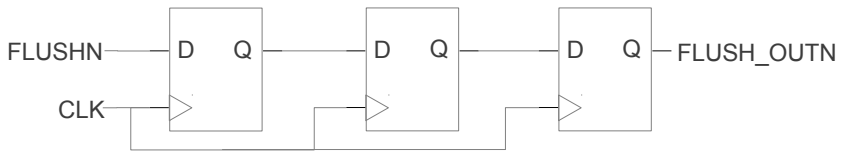

Figure 5.14. The D-flip flop synchronizer strategy.

theoretical clock frequencies in excess of 40 MHz, but in the end, a 12 MHz clock was chosen because it reduced power consumption while still far exceeding the BACCUS TCD's design goals.

5.4.5 Stack Controller Board FPGA Logic

The logic for the TCD Stack Controller Board's AGL125 FPGA was developed using the same Microsemi Libero 9.1 IDE as was described in Section 5.4.4. As with the Overlord Board's code, top-level modules were assembled using Microsemi's *Smart Design*, while low-level modules were written in VHDL.

Figure 5.15 is a block diagram of the internal and external interfacing of all logic modules residing in the TCD Stack Controller Board's FPGA. The XMITTER and RCVER modules perform the tasks of serialization and de-serialization for interface with the TCDBus, and are nearly identical to the modules described in Section 5.4.4. In complement to the Overlord Board, the Stack Controller Board transmits on the TCDBus via the three-wire SCLK, SSPKN, and MISO lines, while it receives from the TCDBus on the three-wire MCLK, MSPKN, and MOSI lines.

The control logic for the concentrator stack resides in the ***CONTROLLER*** module, whose primary responsibilities are to read from the RCVER receiver module, write to the XMITTER transmitter module, and control the other boards in the concentrator stack through a bi-directional bus buffer, ***BIBUF***, which interfaces to these other boards over the Local Bus.

In order to read from the Local Bus (*e.g.*, execute a GET command), the FPGA first simultaneously sets the address lines, ***A[8:1]***, and chip select lines, ***CSN[3:0]***, corresponding to the parameter of interest. It then sets the ***OEN*** output enable line LOW. Figure 5.16 shows a screen capture from a logic analyzer probing the Local Bus during a read cycle.

Likewise, in order to write to the Local Bus (*e.g.*, execute a SET command) the FPGA sets the address lines and chip select lines for the desired parameter, while also placing the 16-bit data word to be written on the data bus. It then pulses the ***R/WN*** read/write strobe LOW. Table 5.11 lists the A[8:1] address line and CSN[3:0] chip select combinations corresponding to each concentrator stack parameter.

Figure 5.17 shows the algorithm for the main loop in the Stack Controller FPGA. The FPGA alternates polling for either a new command from the receiver or the reception of an IRQN from

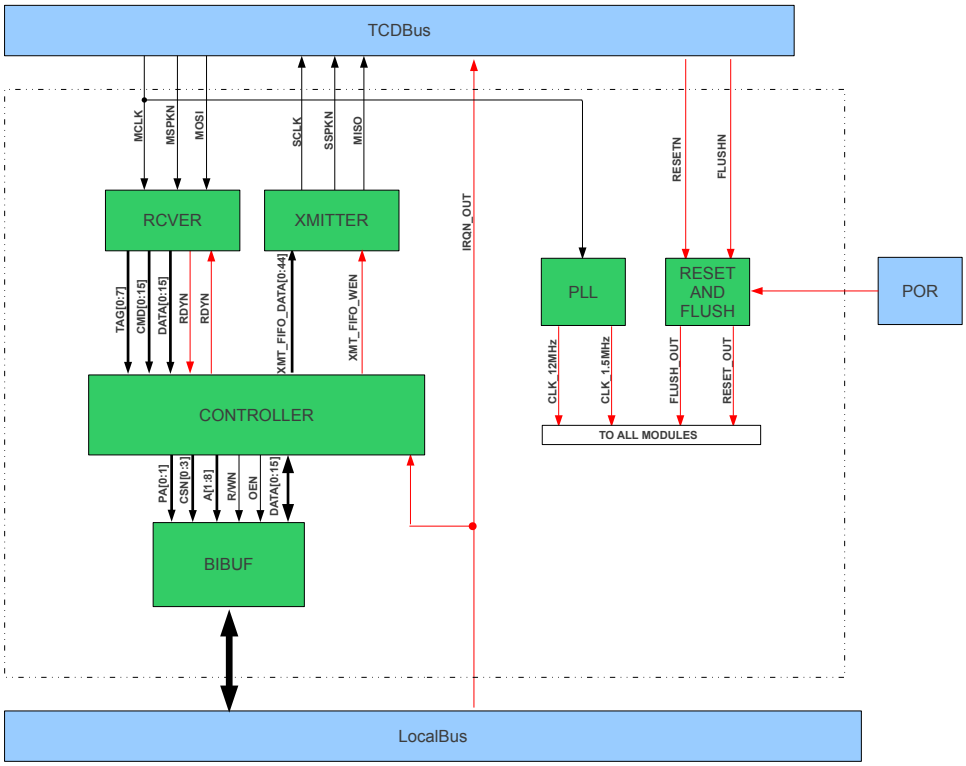

Figure 5.15. Block diagram of Concentrator Stack FPGA logic design. The boundaries of the FPGA are shown in side the dash-dot box. Green blocks represent VHDL logic modules. Thin red lines represent control signals. Thick black lines represent the path of dataflow.

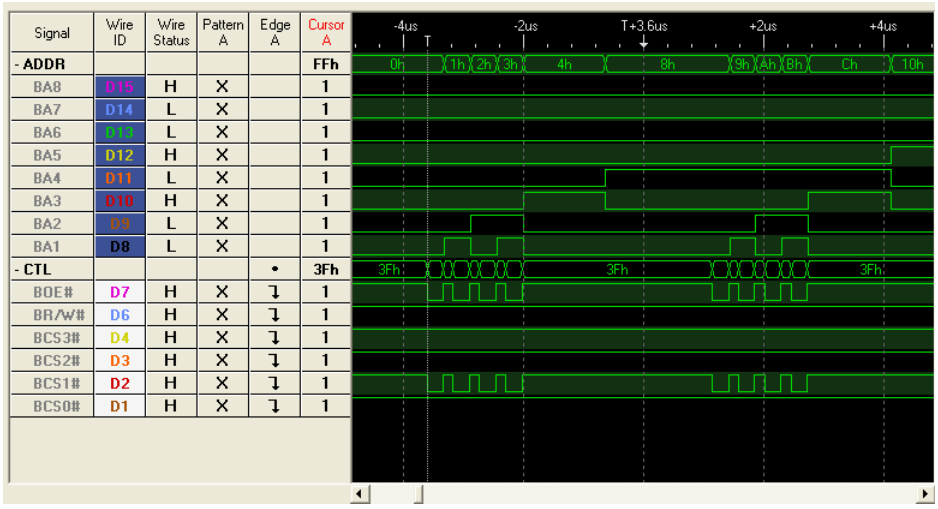

Figure 5.16. Screen capture from a logic analyzer probing the Local Bus during event collection.

Parameter	CSN[3:0]	A[8:1]	Parameter	CSN[3:0]	A[8:1]
THR00	0111	00000000	PD00	1101	00000000
THR01	0111	00000001	PD01	1101	00000001
THR02	0111	00000010	PD02	1101	00000010
THR03	0111	00000011	PD03	1101	00000011
LEVEL0	0111	00000100	PD10	1101	00001000
HV00	0111	00000110	PD11	1101	00001001
HV01	0111	00000111	PD12	1101	00001010
THR10	0111	00010000	PD13	1101	00001011
THR11	0111	00010001	TDC00	1011	00000000
THR12	0111	00010010	TDC01	1011	00000001
THR13	0111	00010011	TDC02	1011	00000010
LEVEL1	0111	00001100	TDC03	1011	00000011
HV10	0111	00001110	TDC10	1011	00000100
HV11	0111	00001111	TDC11	1011	00001001
DISC0	1110	00000100	TDC12	1011	00001010
DISC1	1110	00000101	TDC13	1011	00001011
DISC2	1110	00000110	EVTNOLSB	1110	00000010
DISC3	1110	00000111	EVTNOMSB	1110	00000011

Table 5.11. The TCDBus packet content.

the Local Bus. The FPGA executes all valid commands in the manner described in Section 5.4.1, writing responses to the XMITTER when appropriate. Event acquisition proceeds by reading each element of the event in the manner described previously. (See Figure 5.16 and Table 5.11).

The Stack Controller FPGA phase locks its internal 12 MHz clock to the MCLK clock received over the TCDBus. This phase-locked 12 MHz clock is then distributed to all logic modules via low-skew clock networks. In addition, a secondary 1.5 MHz phase-locked clock signal is used in several counters in the CONTROLLER module, allowing simple enforcement of wait times on the order of 100 ms. As with the Overlord Board's logic design, it's worth noting that, while the timing analysis performed on the Stack Control Board's final FPGA logic design indicates theoretical clock frequencies in excess of 40 MHz, a 12 MHz clock was chosen because it reduced power consumption while still far exceeding the BACCUS TCD's design goals.

The simple ***RESET_AND_FLUSH*** module synchronizes the FLUSHN signal from the TCDBus into the Stack Controller FPGA's clock domain, using the synchronizer circuit of Figure 5.14. This creates the ***FLUSH_OUTN*** signal, which synchronously causes all modules to return to their idle state. The (active low) POR signal is also AND'ed with the RESETN signal from the TCDBus, creating the ***RESET_OUTN*** signal, which acts as an asynchronous reset for all modules.

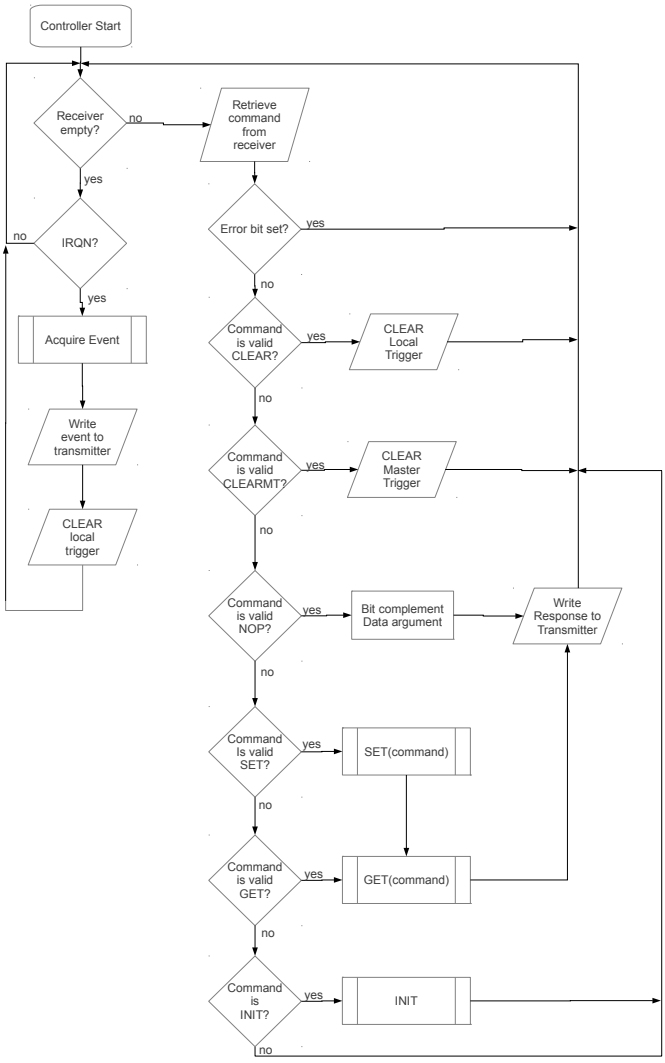

Figure 5.17. Diagram of the stack controller algorithm.

Component	Required	Refurb + New = Total	Note
TCD PMT Assemblies	8	6 + 2 = 8	no more XP2020s
S3 PMT Assemblies	2	2 + 1 = 3	no more XP2020s
USB Board	1	0 + 4 = 4	New to BACCUS TCD
Overlord Board	1	0 + 4 = 4	New to BACCUS TCD
Stack Controller Board	10	0 + 15 = 15	New to BACCUS TCD
TDC Board	18	16 + 8 = 22	Legacy design
Peak Detector Board	20	17 + 8 = 22	Legacy design
Local Trigger Board	10	9 + 4 = 13	Legacy design
Power Distribution Board	10	10 + 4 = 14	Legacy design
Master Trigger Boards	1	1 + 0 = 1	Legacy design
CD Pulse Shaper Board	1	2 + 0 = 2	Legacy design
Power Converter Box	1	1 + 0 = 1	Costly
Power Fanout Boards	2	3 + 0 = 3	Legacy design

Table 5.12. Components manufactured and refurbished for the BACCUS TCD.

5.5 The BACCUS TCD Construction, Verification, and Integration

The TCD's existing PMTs, front-end electronics, trigger system, and power system were re-verified and re-furbished following the CREAM V flight. Table 5.12 lists all new components manufactured for the TCD. New TCD components were manufactured for most items, such that most TCD components have spares. However, no spare TCD PMT assemblies exist due to an unavailability of XP2020 PMTs.[9] Furthermore, a spare TCD Power Convert Box was not manufactured, due to prohibitive cost. However, the TCD Power Converter Box is highly ruggedized, and its components have an expected lifetime well beyond the expected length of the BACCUS flight.

All new and refurbished components were subjected to the vacuum and thermal stress tests discussed in Chapter 4. In addition, all newly designed TCD electronics for the BACCUS flight underwent operational tests in a vacuum chamber set for a pressure of ∼3 torr—very near the ambient pressure typically experienced in flight. All electronics stacks were also subjected to an "operational" thermal test, whereby the operation of the concentrator stacks was continuously monitored and verified during an 8 hour thermal cycle ranging in temperature between +50°C and -20°C. The totals in Table 5.12 reflect only those components which passed all stages of verification.

Two stackable wooden platforms were built for setting up and testing the BACCUS TCD readout electronics at Penn State. This test setup is pictured in Figure 5.18. The TCD was fully cabled and powered, and the software, firmware, and FPGA logic were thoroughly tested and

[9]Photonis's PMT division was shutdown in 2009, and normal wear-and-tear of the original supply of PMTs from CREAM I had reduced the stock of XP2020 PMTs to the minimum necessary. ET Enterprises now offers a replacement PMT roughly equivalent to the XP2020, but it has a different recommended voltage divider configuration, which would have required further circuit customization.

Figure 5.18. The BACCUS TCD test platform at Penn State.

debugged before shipping and integrating the TCD Readout Electronics into the overall payload at the University of Maryland.

Figure 5.19 shows a screenshot from a logic analyzer viewing activity on the Readout Stack Backplane from the BACCUS TCD. Reading out the TCD with TGACS on the TCD's diagnostic laptop, the mean acquisition time for a given event is near $\sim$250 μs, with a typical RMS deviation of $\sim$2%. This yields a 4 kHz maximum TCD readout rate and an expected TCD instrument live time greater than 99%, given the typical 30 Hz HiZ TCD trigger rate experienced in past flights. Thus, the goal of creating a TCD readout scheme with a small, uniform deadtime has been accomplished.

The BACCUS TCD was delivered to the University of Maryland in January 2012. Integration with the CDAQ was completed in March of that year. Figure 5.20 shows ground muon data taken by the BACCUS TCD during instrument checkout at the Columbia Scientific Ballooning Facility, several weeks before the instrument began its sea voyage to Antarctica. Pairs of PMTs have been tuned so as to center the mean position of the muon peak near 1000 ADC channels. While PMTs 4 and 12 have a somewhat anomalously low gain, our limited supply of XP2020s meant the inclusion of these low-gain PMTs in the BACCUS TCD was required. The enhanced large-signal tail from some high-gain PMTs (*e.g.*, PMT3) has existed for all TCD flights, and is caused by a well understood non-linearity in the XP2020's dynode 12. This non-linearity has no effect on dynodes 10, 9, and 7, which cover the range of signals for the $Z > 3$ to $Z \sim 26$ particles

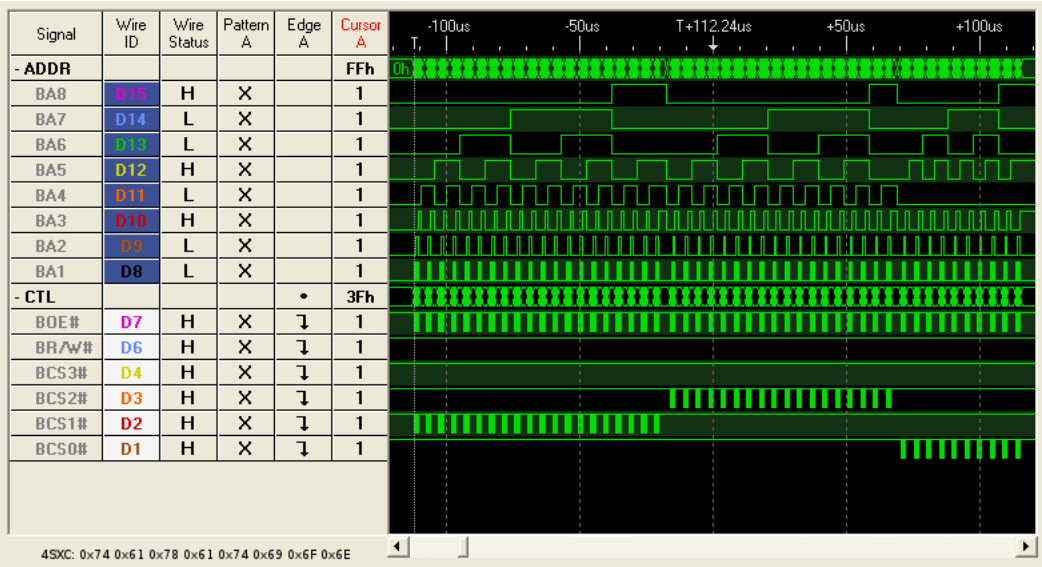

Figure 5.19. Acquisition of a single TCD event.

of interest for the BACCUS flight. In any case, a scheme exists to correct for this non-linearity in offline analysis [54].

All aspects of the TCD have been verified as fully working, and the TCD is ready for the 2013-2014 BACCUS mission in Antarctica.

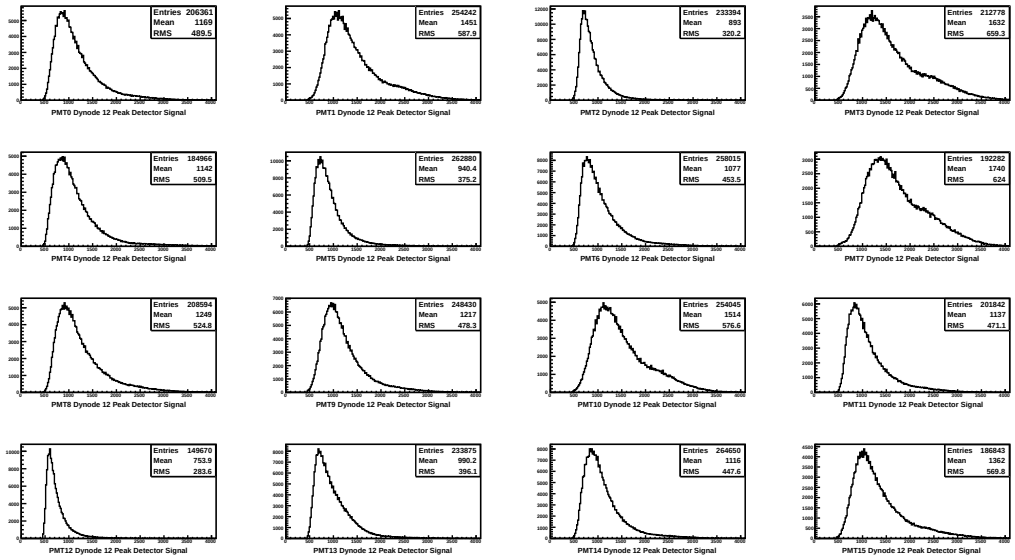

Figure 5.20. Muon data taken by the BACCUS TCD in July of 2013.

Chapter 6

Calibration of the ISS-CREAM Prototype BSD

The ISS-CREAM mission was discussed from the perspective of a project overview in Chapter 3. As was mentioned there, ISS-CREAM will take on the new science goal of measuring the cosmic-ray electron spectrum above 100 GeV. The ISS-CREAM Boronated Scintillator Detector (BSD), a detector system originating from the CREAM project's Pennsylvania State University group,[1] aims to enhance the ISS-CREAM calorimeter's electron identification ability by measuring the late-time neutron activity produced by cosmic-ray induced showers.

Here, the measurement techniques associated with the BSD will be reviewed, its characterization and qualification will be described, and results of a November 2012 test of a prototype version of this detector in the CERN H2 beam line will be presented.

6.1 The BSD Measurement Technique

The BSD derives its electron/hadron discrimination power from the fact that, for showers which produce similar amounts of total energy deposit in the ISS-CREAM calorimeter, those which are hadronically induced generate several times more neutrons than those originating from electrons. Figure 6.1 demonstrates this fact qualitatively, comparing oscilloscope screenshots obtained by measuring the late time signals output by a BSD PMT exposed to 150 GeV electrons (left, yellow) and 350 GeV pions (right, cyan) during the CERN 2012 beam test. Clearly, there is significantly more late-time signal for pions than for electrons.

The BSD's primary detector medium is a 60 cm $\times$ 60 cm $\times$ 3.8 cm slab of Eljen Technology's EJ-254 boron-loaded plastic scintillator [128]. The BSD's scintillator is loaded with 5% elemental

[1] The BSD collaboration also includes the CREAM groups at NASA Goddard Space Flight Center and Northern Kentucky University.

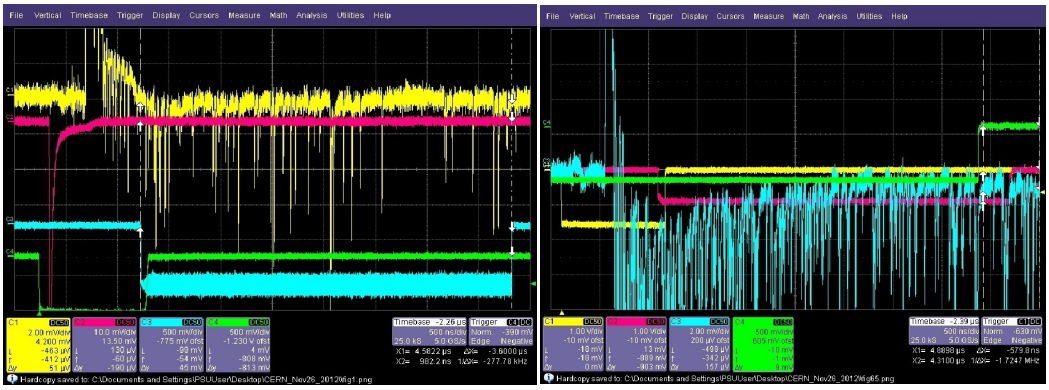

Figure 6.1. Left: Anode signal from a gated BSD PMT assembly during a 150 GeV electron run (yellow trace). Right: Anode signal from a gated BSD PMT assembly during a 350 GeV pion run (cyan trace). Note that the large positive going signals seen in each case are due to "switching transients" (described in Section 6.3.1). The integration window for the charge-integrating ADC measurement (discussed later) is also shown for electrons (cyan) and pions (magenta).

boron, by weight. Naturally occurring boron has a 20% isotopic abundance of ^{10}B, leading to an overall ^{10}B loading of 1%.

Upon entering the BSD, neutrons which were first produced by cosmic-ray showers in the ISS-CREAM calorimeter may undergo the capture process

$$^{10}B + n \rightarrow {}^{7}Li + \alpha + \gamma \tag{6.1}$$

with a capture probability which follows a decaying exponential of time constant

$$\tau = (N(^{10}B)\sigma V)^{-1} \tag{6.2}$$

where $N(^{10}B)$ is the number density of ^{10}B, σ is the cross section for capture, and V is neutron velocity. Below 200 keV, the neutron capture cross section scales as V^{-1}, leading to an energy independent time constant, which evaluates to 2.74 μs for a 1% ^{10}B loading. Such a time profile manifests in the BSD as an exponentially-decaying probability for the BSD's PMTs to detect the photons which are generated by the scintillation of the ^{7}Li and α reaction products of the neutron capture. This is evident in the oscilloscope trace shown on the right side of Figure 6.1, where, starting at the second horizontal time division, the frequency of the many thin spikes (*i.e.*, the single photoelectron pulses) can be seen to fall off exponentially with a time constant in

the range of a few microseconds.[2] Various attempts to investigate the time-based characteristics of neutrons in the BSD are discussed in Section 6.4.4.

Literature values for the scintillation yield resulting from a single neutron capture suggest that the light level is equivalent to that produced by a 76 keV electron [129], leading to a predicted 570 photons/capture for EJ-254's stated 7500 photons/MeV light yield. A measurement of the the neutron-capture light yield of EJ-254 is discussed in Section 6.4.3.1.

6.2 Design and Construction of the Prototype BSD

A prototype version of the BSD was built, with the goal of verifying its electron/hadron identification abilities in the CERN H2 beam line. Presented here are the details of the construction of the prototype BSD's PMT assemblies and detector box and a measurement of the collection efficiency for the combined system.

6.2.1 Prototype PMT Assemblies

Hamamatsu's R1924A PMTs [130] were selected for measuring the light output of the BSD.[3] GEANT4 simulations of the ISS-CREAM BSD predict that the large number of charged particles generated in the first 100 ns of the calorimeter's shower (henceforth referred to as the "early shower") create large signals in the BSD, with each PMT being exposed to between 10^4 and 10^6 photons. Laboratory testing with the R1924A PMTs revealed that such large signals tend to induce significant PMT afterpulsing, extending up to 2 μs in duration, with amplitudes rivaling those predicted for the BSD's delayed neutron signal.

In order to eliminate this afterpulsing background, "dynode gating boards" were incorporated into the PMT assemblies which hold the potential applied to PMT dynodes 1 and 2 at -12 V, thus inhibiting the injection of photoelectrons[4] into the PMT's multiplier stage from its (grounded) photocathode. When supplied with an external +5 V dynode ON (***DON***) logic signal, the dynode gating boards switch the potentials applied to each of dynodes 1 and 2 to their normal high voltage within 300 ns. This dynode gating strategy allows the BSD's PMTs to measure delayed neutron capture signals in the BSD's scintillator block, while being effectively "blind" to the large signals present during the early shower. This technique of PMT dynode gating, which has history in laser stimulated fluorescence measurements [132], was found to completely remove even the largest of early shower signals, with a "cut-off ratio" (*i.e.*, the ratio of the number of

[2]Such decaying-exponential behavior is not as easily discernable in the example 150 GeV electron oscilloscope trace shown on the left-side of Figure 6.1 because the overall number of photoelectrons produced there is small. However, as will be shown in Section 6.4.4, it can be made more evident by averaging signal profiles over many events.

[3]These are rugged PMTs, with an excellent flight history on the TIGER [131] LDB mission. Their 2.54 cm diameter provides a good match to the 3.8 cm thickness of the BSD's scintillator, and their 300 nm to 650 nm spectral response overlaps well with EJ-254's 425 nm maximum emission wavelength.

[4]A photoelectron is defined as an electron which is ejected from a PMT's photocathode as a result of the photoelectric effect occurring in the photocathode's material. The probability for an incident photon to undergo the photoelectric effect is known as the photocathode "quantum efficiency", and is roughly 25% for the semi-transparent, bialkali photocathode used in the R1924A.

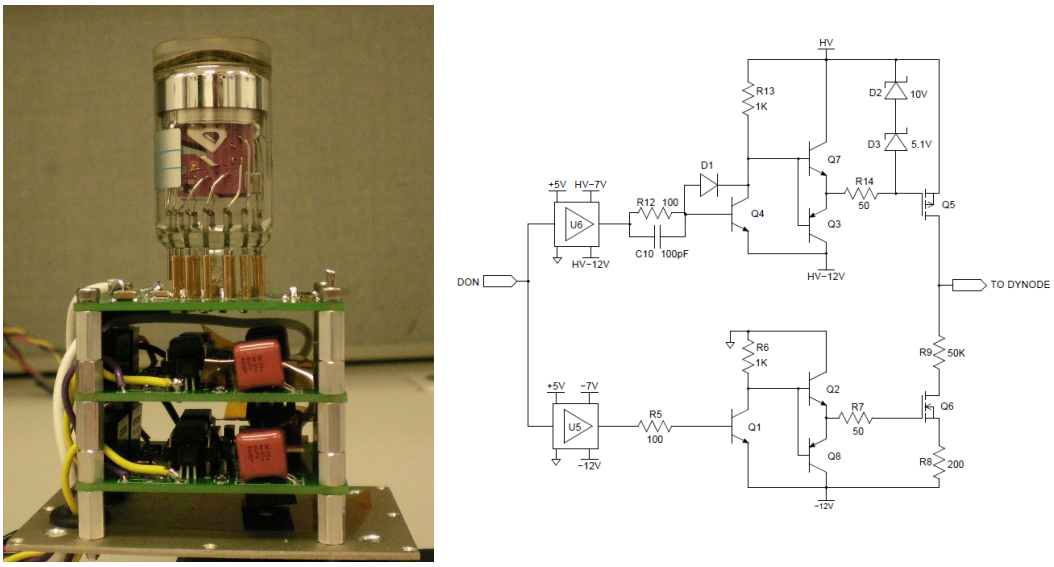

Figure 6.2. Left: a PMT assembly with its sidewalls removed. The R1924A plugs in to a socketed high voltage divider board (top board). Two dynode gating boards, positioned as the bottom two boards in the stack, switch the potentials applied to dynodes 1 and 2 from -12V during the initial calorimeter shower to their full high voltage values within 300 ns. Right: schematic for the dynode gating circuit.

photons which would be seen by the PMT in the early shower to the number of photoelectrons seen after 400 ns) near 10^6.

The left side of Figure 6.2 shows a prototype BSD PMT assembly. The high voltage bias for dynodes 3 through 10 was supplied using a resistive divider with a socketed PMT connection, seen as the top board in the stack. Two identical dynode gating boards, seen as the lower two boards in the stack, switch the high voltage[5] to each of dynodes 1 and 2. The resulting stack of three prototype BSD PMT base boards is mounted together in a 3 inch $\times$ 2 inch anodized aluminum enclosure with removable sidewalls. This enclosure serves the combined purposes of electrically shielding the PMT base boards and providing a rigid mechanical structure for mounting the assembly in the detector box.

The right side of Figure 6.2 shows the dynode gating board's high-voltage switching circuit. Switching the potential applied to the dynodes between -12 V and a positive high voltage (typically between 200 V and 400 V, depending on the target gain for the PMT) is accomplished through the use of "totem-pole" configured, high-voltage Metal-Oxide-Semiconductor Field-Effect Transistors (MOSFETs) Q5 and Q6, each of which are controlled by drive circuits whose reference potential is tied to the MOSFET's source terminal. The DON signal, which initiates the switching action, is level shifted and protected from the circuit's high voltage via U5 and U6, which are Avago Technologies HCPL-7720 optocouplers, which have an inherently

[5]When the main high-voltage divider was run at 1200 V, dynode 2 was switched from -12 V to 370 V and dynode 1 was switched from -12 V to 278 V.

small (∼40 ns) propagation delay [133]. All floating references are derived from a combination of zener diodes and RECOM Power's 2 kV isolated RM-Series 0.25 W DC/DC converters [134].

Note that by applying a steady +5 V to the DON input of the dynode gating board, PMTs are made constantly sensitive to incoming photon signals, and so behave identically to PMTs whose dynode high-voltage bias is provided via a standard resistive divider. PMTs operated is such a manner will hence be referred to as "unswitched", while those operated via a pulsed DON signal will be referred to as "switched".

6.2.2 Prototype BSD Detector Box

The prototype BSD detector box is shown in the upper part of Figure 6.3, with its lid removed. The scintillator was wrapped in three layers of ultra-reflective PTFE in order to maximize light collection. The wrapped scintillator was then secured in a delrin frame, which was mounted in a custom-designed wooden box. The lower part of Figure 6.3 shows the scheme for mounting the PMT assemblies in the box and optically coupling them to the scintillator. RTV615 disks of 1 inch diameter and 1/8 inch thickness were glued to the faces of the prototype BSD PMTs. Holes were drilled in the PMT assembly's aluminum enclosure, which were fitted onto threaded rods protruding from the delrin frame. Jam nuts press the back of the PMT assembly's aluminum enclosure toward the scintillator, such that thorough wetting of the scintillator-optical cookie interface is assured. BNC and SHV bulkhead connectors mounted on aluminum feedthrough plates bring external power into the box, while LEMO bulkhead connectors bring PMT anode signals out of it.

For the purpose of interpreting PMT signals in the context of number of photons generated in the scintillator, it is useful to measure the "PMT collection efficiency" (*i.e.*, the number of photoelectrons seen by a PMT per photon generated in the scintillator) for the PMTs in the prototype BSD detector box. Figure 6.4 shows the naming scheme and high voltage settings for the PMTs used for this collection efficiency measurement. The two sides of the instrument from which the PMTs view the scintillator are referred to as the "A side" and the "B side", and PMTs are assigned names according to the convention depicted in the figure. PMT high voltages were set to 1200 V (near the maximum for the R1924A PMTs), and the PMTs were run in unswitched mode (*i.e.*, DON constantly high). PMT 1A was not present during this test. The position which might have been occupied by a PMT 7B was instead taken by a set of two red LEDs, which were used for liveness testing and calibration.

As a first step, the charge output corresponding to detection of a single photon was measured for each PMT. This was accomplished via the method of single photoelectron characterization. A pulse was applied to one of the detector box's LEDs and its amplitude and width were adjusted such that firing the LED caused the PMT to output a signal roughly 50% of the time. The resulting charge pulses from the PMT's anode represent the emission of a single photoelectron from the PMT's photocathode. Charge integration[6] was triggered from a pick-off of the LED's

[6]The "windowed area" feature of a Lecroy Waverunner 104MXi oscilloscope was used to perform charge integration for this PMT collection efficiency measurement. It calculates the integral of each trace (in units of

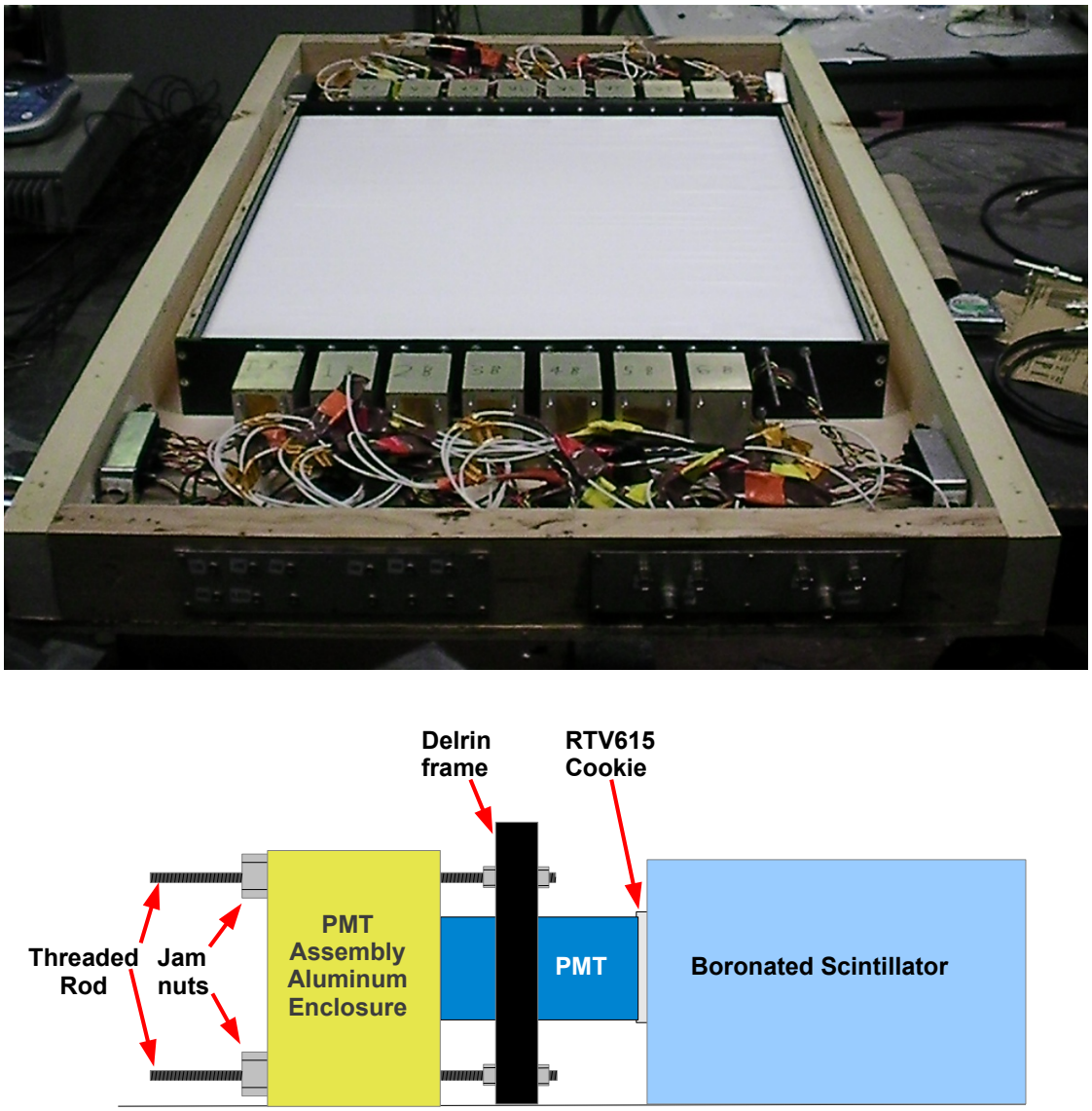

Figure 6.3. Top: the prototype BSD detector box with its lid removed. The scintillator can be seen wrapped in PTFE, mounted in the delrin frame inside the wooden box. PMTs view the scintillator from two sides, with feedthroughs bringing power and signal lines into and out of the box. Bottom: scheme for optically coupling the PMTs to the scintillator. The PMT's aluminum enclosure is slid onto threaded rods which attach to the delrin frame, and jam nuts are used to compress the RTV cookie against the scintillator.

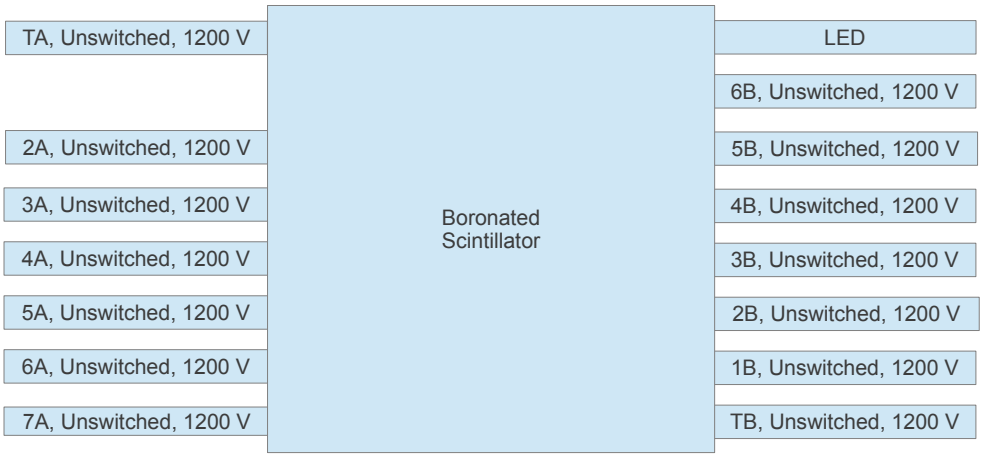

Figure 6.4. PMT setup for measuring collection efficiency in the prototype BSD.

drive signal. The left side of Figure 6.5 shows an example of the resulting charge distribution for PMT 4A. Two populations are seen. The left-most population, known as the "pedestal", represents the background created by channel offsets and electrical noise in the case when no photoelectrons are ejected from the PMT's photocathode. The right-most population corresponds to the case when a single photoelectron is produced. The distribution is fitted to a double Gaussian, and the difference in the fit means of the two Gaussians is taken as the charge produced by a single photoelectron (PE), here 0.909 pC.

Next, the BSD was set to trigger on muons vertically incident on the center of the scintillator block. Figure 6.6 shows the setup. Two 1 cm-thick scintillator paddles (shown as "trigger paddles" in Figure 6.6) of dimensions 23 cm $\times$ 30 cm were placed $\sim$76 cm above and below the center of the BSD, respectively. The coincidence of signals from these two scintillators was used to trigger read out of the BSD's PMTs. With this configuration, the maximum variation in signal size due to pathlength is a negligible 3%. The right side of Figure 6.5 shows the resulting muon distribution from PMT 4A. The distribution was fitted to a Landau function, and the Landau function's most probable value was taken as the PMT's charge output for a muon, here 72.0 pC. The ratio of muon charge ouput to single photoelectron charge output then gives the number of photoelectrons detected by the PMT per incident muon, here 80 photoelectrons, here 79 PE.

Atmospheric muons are highly relativistic. Because scintillator has a relatively flat response above the point of minimum ionization, muons can be taken as minimum ionizing particles (MIPs) to good approximation. For polyvinyltoluene (the base material in EJ-254), a MIP

Volt-seconds) via a rectangular approximation, with a rectangle width equal to the oscilloscope's sampling period (100 ps). Dividing the result by the 50Ω termination resistance of the oscilloscope gives the total charge contained in the pulse, in units of Coulombs. Charge values obtained from this oscilloscope windowed area method have been compared to those from the CAMAC 2249W charge integrating ADC module used in the CERN beam test (see Section 6.3.1). Both methods have been found to agree within errors. In this case, the oscilloscope's windowed area feature is preferred because it allows real-time monitoring of measurement quality, and its charge resolution is somewhat better than that of the 2249W.

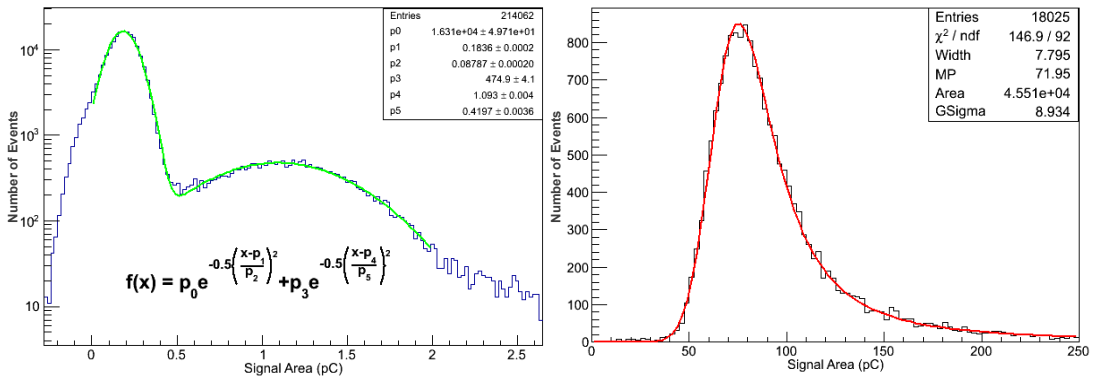

Figure 6.5. Left: an example distribution resulting from the single photoelectron measurement for PMT 4A. A double Gaussian fit identifies the pedestal (left population) and the single photoelectron peak (right population). Right: the distribution of muon signals for PMT 4A. The result has been fitted to a Landau distribution. With a single PE signal of 1.093 - 0.184 = 0.909 pC, a muon pulse with a most probable value of 72.0 pC thus corresponds to 79 PE.

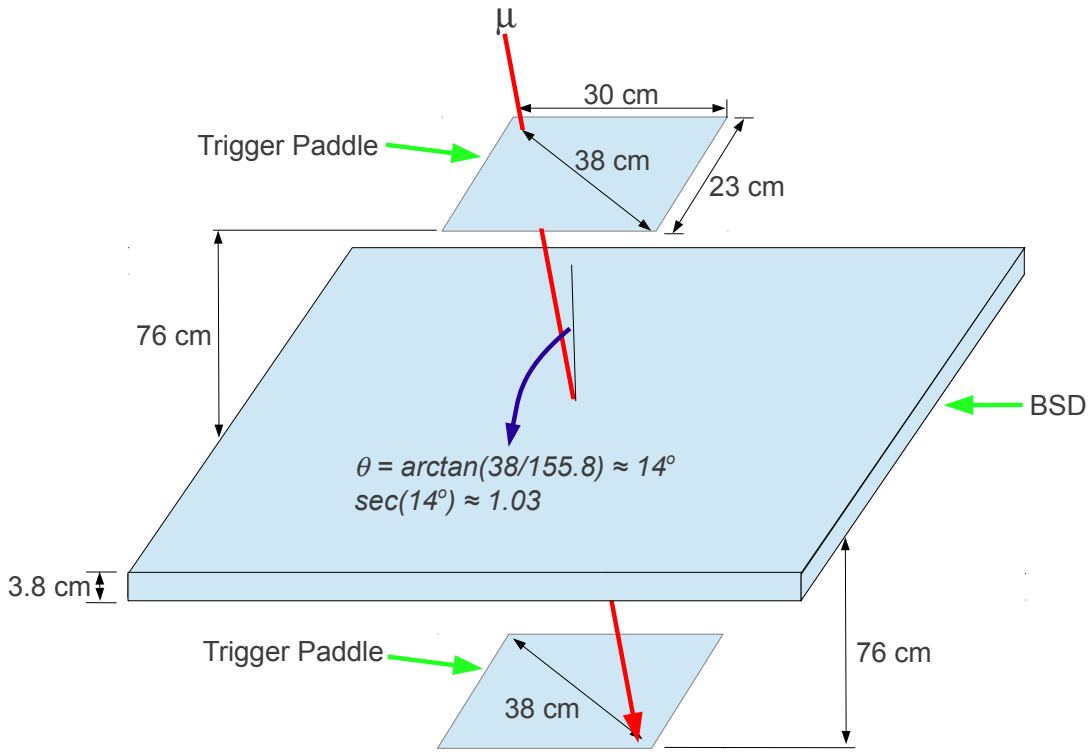

Figure 6.6. Trigger geometry for atmospheric muon measurements in the prototype BSD. The muon trajectory which corresponds to the maximum pathlength through the scintillator is shown. Dimensions are not to scale.

PMT	PEs	Col. Eff.	PMT	PEs	Col. Eff.
TA	56	0.10%	6B	59	0.10%
2A	63	0.11%	5B	67	0.12%
3A	89	0.16%	4B	85	0.15%
4A	78	0.14%	3B	78	0.13%
5A	69	0.12%	2B	57	0.10%
6A	56	0.10%	1B	58	0.11%
7A	51	0.09%	TB	58	0.10%

Table 6.1. Number of photoelectrons and the corresponding collection efficiencies for a vertically incident muons through the center of the prototype BSD.

deposits $\sim$2 MeV cm^2/g [8]. Since the density of EJ-254 is $\sim$1 g/cm^3, and the BSD's boronated scintillator is 3.8 cm thick, $\sim$7.6 MeV of energy is deposited by vertically incident muons. Given EJ-254's 7500 photon/MeV light yield, a muon produces $\sim 5.7\times10^4$ photons.

For each PMT, taking the ratio of the number of photoelectrons detected for vertically incident muons to the overall number of photons it produces yields a measurement of the PMT's collection efficiency. Table 6.1 shows the photoelectron signals and resulting collection efficiencies for each prototype BSD PMT, as measured for vertically incident muons in the center of the detector. The BSD's collection efficiency ranges from $\sim$0.09% at its corners to $\sim$0.16% near the center—a reasonable variation given the extra travel distance necessary for a photon to arrive at a corner PMT and geometric differences in totally internally reflected trajectories which lead to eventual photon detection by any given PMT.

The measured collection efficiency can be double checked by an order-of-magnitude hand calculation.[7] Assuming photons are uniformly incident on all points of the BSD's surface, 11.2% exit the edges of the scintillator (the fraction of total area represented by the edges). Of those which exit the top of the detector, assume 50% are re-directed to the scintillator's edges due to reflections on the scintillator's PTFE wrapping. This means 55.6% of all photons exit the scintillator from the edges. The R1924A has a minimum active photocathode area of 3.8 cm^2, meaning a single PMT collects 0.4% of the light exiting the edges of the scintillator, or 0.2% of the total light generated. The R1924A has a quantum efficiency near 25% for scintillation light, so the estimated collection efficiency is 0.05%, which matches the measured 0.09%–0.16% collection efficiency within an order of magnitude.

6.3 Calibration of the Prototype BSD in the CERN H2 Beam Line

In November of 2012, the prototype BSD was shipped to CERN and calibrated alongside the ISS-CREAM calorimeter in the H2 beam line. Here, the detector's setup and readout will be outlined. The reduction of data from this beam test will also be described. Finally, a measurement of the

[7] Thanks to BSD collaborator Jason Link of NASA Goddard Space Flight Center for teaching me this "back-of-the-envelope" method of estimating collection efficiency.

Figure 6.7. The prototype BSD detector mounted behind the ISS-CREAM instrument calorimeter pallet in the CERN H2 beamline.

prototype BSD's hadronic rejection power, as derived for 125 GeV electron and 350 GeV pions, will be presented.

6.3.1 CERN Mechanical Positioning and PMT Configuration

Figure 6.7 shows the prototype BSD detector box in the CERN H2 beam line. The prototype BSD detector box was held 11.4 cm behind the ISS-CREAM instrument pallet on a unistrut frame, with the BSD centered on the beam line. Long power and signal cables were routed from the sides of the prototype BSD detector box to Nuclear Instrumentation Module (NIM) triggering and timing electronics and to Computer Automated Measurement and Control (CAMAC) digitization modules.

Figure 6.8 depicts the naming scheme, PMT assembly positioning, high-voltage settings, and read out mapping used for the prototype BSD during the CERN beam test. PMTs were read out using a CAMAC 2249W 12-channel, 11-bit charge-integrating ADC module, which has a charge resolution of 0.25 pC/count. PMTs 1A–6A and 2B–5B were run at 1200 V in switched

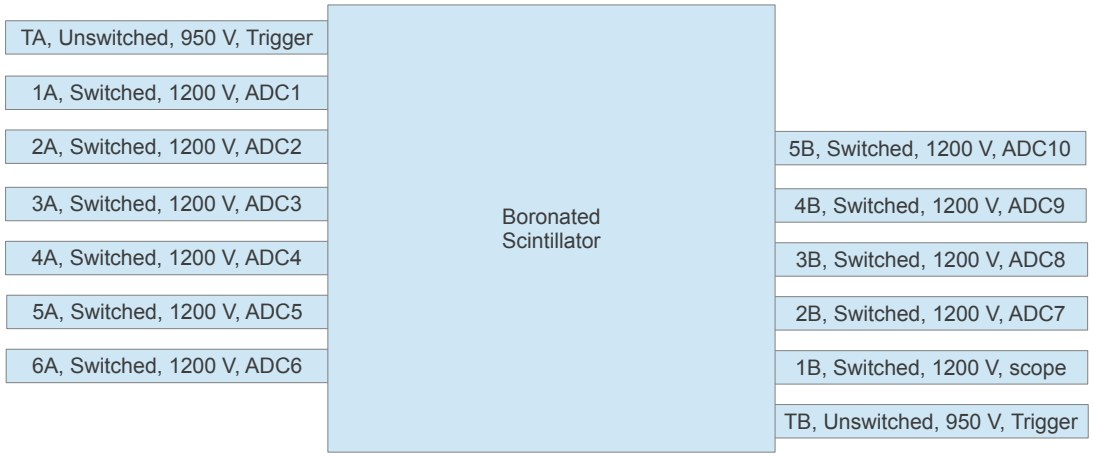

Figure 6.8. PMT setup for the prototype BSD tests at CERN.

high voltage mode and provide the BSD's primary dataset for characterizing late shower activity in the BSD. PMT 1B was also run at 1200 V in switched high voltage mode, but was read out into one channel of the LeCroy Waverunner 104MXi Oscilloscope, thereby providing a visual indicator of instrument health and allowing a means of studying the late shower's timing profile. PMTs TA and TB were run at 950 V in unswitched high voltage mode and were used to trigger the BSD.

Figure 6.9 shows a timing diagram of the BSD's event sequence, while Figure 6.10 shows a block diagram for the electronics used in the prototype BSD calibration. A NIM coincidence module was used to trigger event readout on the coincidence of unswitched PMTs TA and TB, with thresholds set at the 1/2 MIP level. A coincidence between TA and TB caused a NIM gate/delay generator to activate the DON logic signal. DON was fed into each PMT dynode gating board, thereby initiating the switching-ON of the high voltage to dynodes 1 and 2 for the 10 gated PMTs.

Each gated PMT anode signal was fed into its respective channel of the 2249W module. A second gate/delay generator fired the ***INTEGRATE*** signal, which caused the 2249W to integrate the total charge from each gated PMT anode during the window where neutron captures should dominate light production in the BSD. In principle, this period begins approximately 400 ns after the start of the shower. However, for the CERN configuration, the INTEGRATE signal was delayed by 900 ns in order to completely avoid residual baseline distortion from the "switching transient".[8] Despite this increased delay, each gated PMT still saw sufficient signal in order to fully parameterize the late time neutron activity of each event. The gated PMT

[8]The switching transient was caused by the capacitive coupling of the gated PMT's switched high voltage onto the anode. Under normal conditions, the gated PMT's switching transient is narrow enough that integration can begin very near to the 400 ns minimum delay. However, the long cables which were required for the CERN beam test significantly delayed trigger formation and widened the switching transient's width, hence causing a large delay (900 ns) in the start of the BSD's integration window. The BSD's flight geometry allows for significantly shorter cables, and so, a much earlier start of the integration window will be possible there.

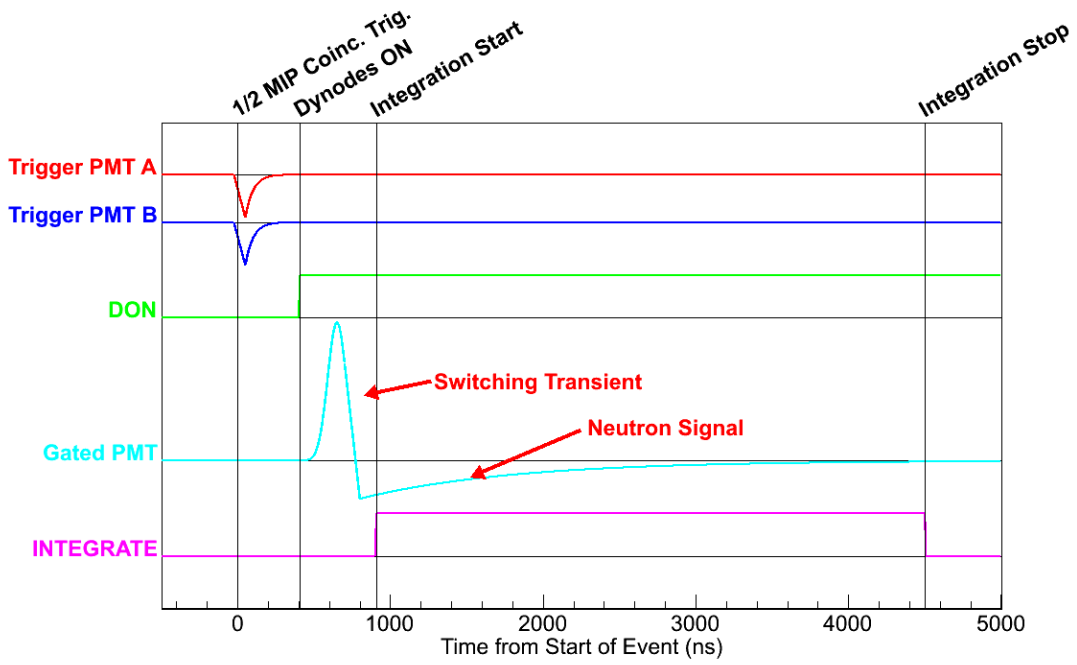

Figure 6.9. The triggering and event sequence for the CERN beam test. The smooth exponential representing the late-time neutron signal in the BSD illustrates average behavior. Real single-event traces exhibit photoelectron statistics, such as those shown in Figure 6.1.

signals were integrated for a total of 3600 ns. Re-triggering of the BSD was inhibited for 500 μs after each event in order to allow the gated PMTs to fully return to their OFF state (125 μs minimum).

Because the BSD's NIM and CAMAC readout electronics had a significantly lower dead time than those used for the calorimeter (500 μs vs 10 ms), the BSD naturally read out many more events than the calorimeter. Event matching between the calorimeter and the BSD was performed offline using a latched 32-bit event number (***EVTNO***), distributed to both the calorimeter readout electronics and the BSD by the calorimeter trigger system. As additional assurance of event matching, a flag was latched if both the BSD's trigger (***TRIG***) and the calorimeter's trigger (***EXT_TRIG***) were active within 5 μs of when the BSD's trigger formed.

6.3.2 Data Reduction

The CERN H2 beam line was tuned for electrons at energies of 50, 75, 100, 125, 150, and 175 GeV. Protons were unavailable at the time of this beam test. However, for the purpose of characterizing and calibrating the BSD, pions provide a good hadronic substitute, as they are known to create calorimeter showers similar to those generated by protons. The H2 beam line was also tuned for pions at energies of 250, 300, and 350 GeV.

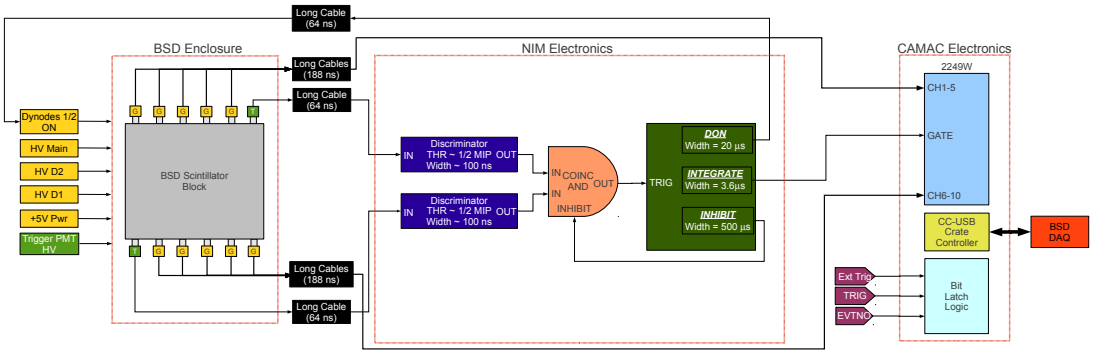

Figure 6.10. A block diagram of the BSD CERN readout electronics.

Events were selected for analysis for which event numbers were found to match and trigger flags were found to be coincident between the calorimeter and BSD data. Figure 6.11 shows BSD event number versus measurement timestamp, with those events which have matching calorimeter and BSD event numbers shown in green. As can be seen, this selection has the expected effect of choosing only those events which were inside the beam spill period (*i.e.*, those periods which have the steeper slope in Figure 6.11).

The ten gated BSD PMTs were pedestal-subtracted, gain-normalized, and summed. The resulting quantity was taken as the BSD's delayed neutron activity signal. Likewise, each of the scintillating fiber ribbons in the calorimeter was pedestal subtracted, and the five ribbons on to which the beam was centered were summed over all calorimeter layers. The resulting sum was taken as the total energy deposit in the calorimeter.

In order to simulate the calorimeter's flight trigger threshold, a cut was applied requiring greater than 40 MeV energy deposit in each of six consecutive calorimeter layers. Figure 6.12 demonstrates the effect of this selection by showing the total calorimeter signal for all electron energy runs before (blue) and after (black) the six-layer cut. Because only six 50 GeV electron events passed the six-layer cut, 50 GeV electrons were excluded from further analysis. As can be seen in Figure 6.12, the six-layer cut has the additional benefit of purifying the electron beam, which is inherently contaminated by low energy pions at the 25% level.[9]

Figure 6.13 shows the resulting energy deposit distributions for electrons and pions in both the BSD and the calorimeter. The BSD's ability to distinguish electrons from hadrons is immediately clear. Even for a broad range of calorimeter signal values, the BSD's pion distributions tend to cluster at larger values of BSD signal than the electron distributions, owing to their elevated neutron production. As will be seen, these differences sharpen even more when the calorimeter's signal range is limited to emulate an energy range selection of the sort that will be carried out with flight data.

[9]The pion beam was filtered by several stages of lead absorbers far upstream of the calibration table, creating an estimated purity better than 95%.

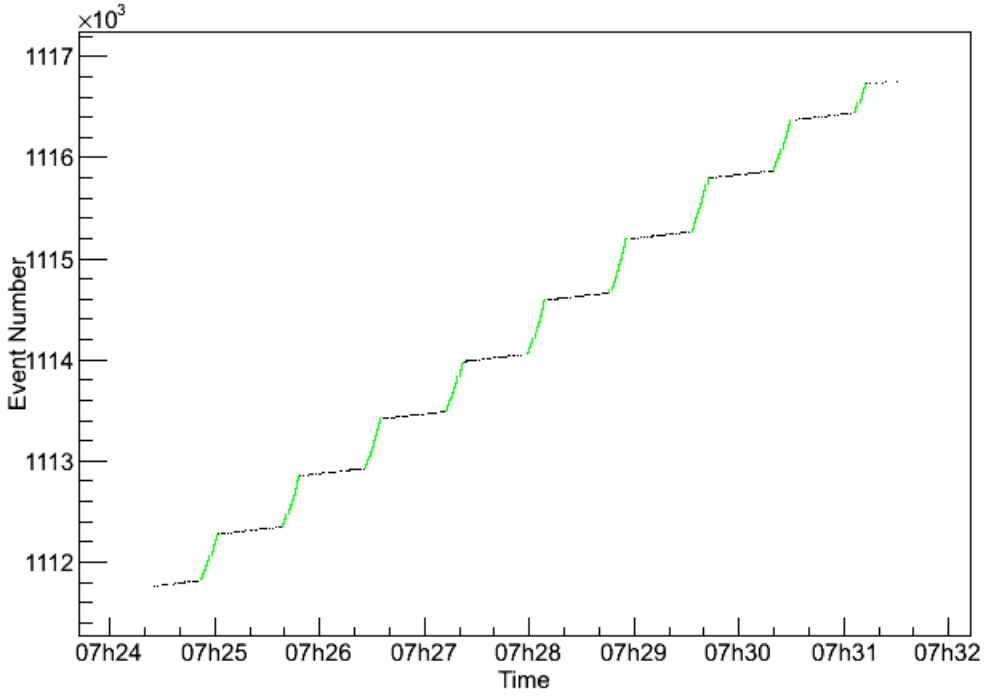

Figure 6.11. BSD event number as a function of event timestamp. Events where BSD and calorimeter data match are shown in green. As expected, these events occur during beam spills.

6.3.3 Prototype BSD Rejection Power

While the overall hadronic rejection power is ultimately an instrument-level concern, it is useful to derive a BSD-only rejection power from the CERN beam test. The left side of Figure 6.14 shows calorimeter signal for 125 GeV electrons (red) and 350 GeV pions (blue). These runs were chosen because their calorimeter signal distribution peaks are well aligned. Thus, 350 GeV pions tend to strongly "mimic" 125 GeV electrons on the basis of calorimeter total energy deposit. This is as expected, since an electromagnetic shower at such an energy is fully contained within the calorimeter, whereas for a hadronic shower a significant amount of energy can leak out of the bottom of the calorimeter. The two vertical lines represent the calorimeter signal range within two standard deviations of the electron peak, thereby defining a zone of maximal particle identity confusion for electrons and pions of these energies. The right side of Figure 6.14 shows BSD signal distributions for 125 GeV electrons (red) and 350 GeV pions (blue), where only those events containing a calorimeter signal within two standard deviations of the electron peak have been included. The vertical line indicates the BSD signal value below which 80% of electrons are retained. The BSD's hadronic rejection power is evident, with the bulk of the pion distribution being excluded by such a cut.

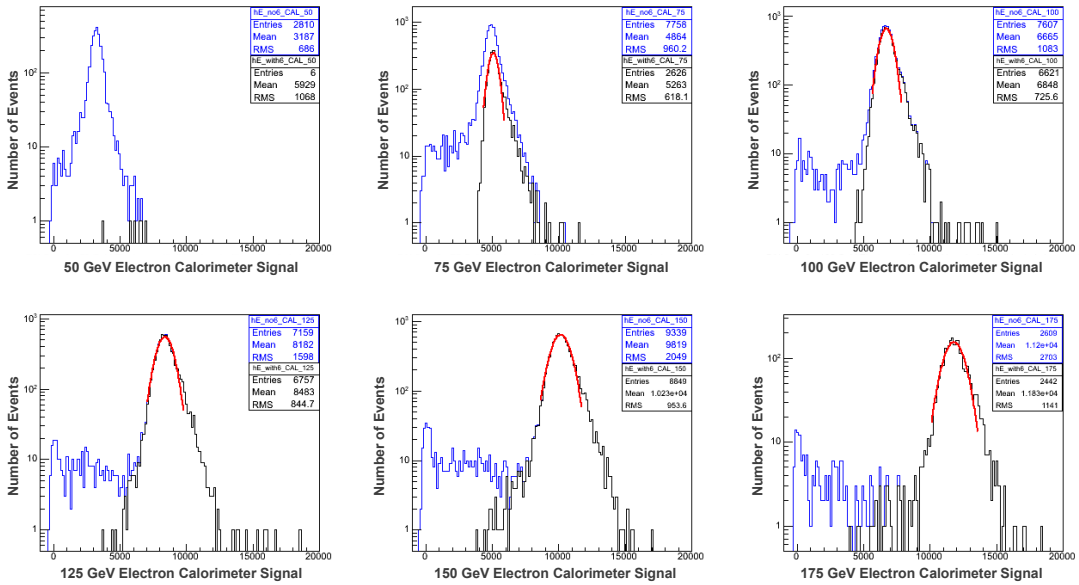

Figure 6.12. Calorimeter signal distributions for 50 GeV–175 GeV CERN electron runs before (blue) and after (black) the six-layer cut. The fitted curves are Gaussians identifying the peaks of the distributions.

The BSD distributions from Figure 6.14 can be used to derive the BSD's hadronic rejection power as a function of electron acceptance by gradually increasing a maximum value of BSD signal and then calculating the resulting hadronic rejection power and electron acceptance for the portion of the electron and pion distribution below this maximum. Here, hadronic rejection power for the BSD is defined as

$$\text{Rejection Power} = \frac{(\text{Fraction of Electrons Accepted})}{(\text{Fraction of Hadrons Not Rejected})} \tag{6.3}$$

Figure 6.15 shows the BSD's hadronic rejection power as a function of electron acceptance as derived from Figure 6.14. The BSD demonstrates a rejection power greater than 100 for an electron acceptance efficiency of 80% or less. Error bars are propagated from the statistics of the BSD electron and pion signal distributions in Figure 6.14.

6.4 Comparison of the CERN Data with GEANT4

A GEANT4 monte carlo simulation of the BSD's beam test configuration has been developed, which includes geometrical modeling of the detectors present during the CERN beam test.[10]

[10]This simulation was developed, and is primarily maintained, by Professor Scott Nutter, an ISS-CREAM collaborator from Northern Kentucky University.

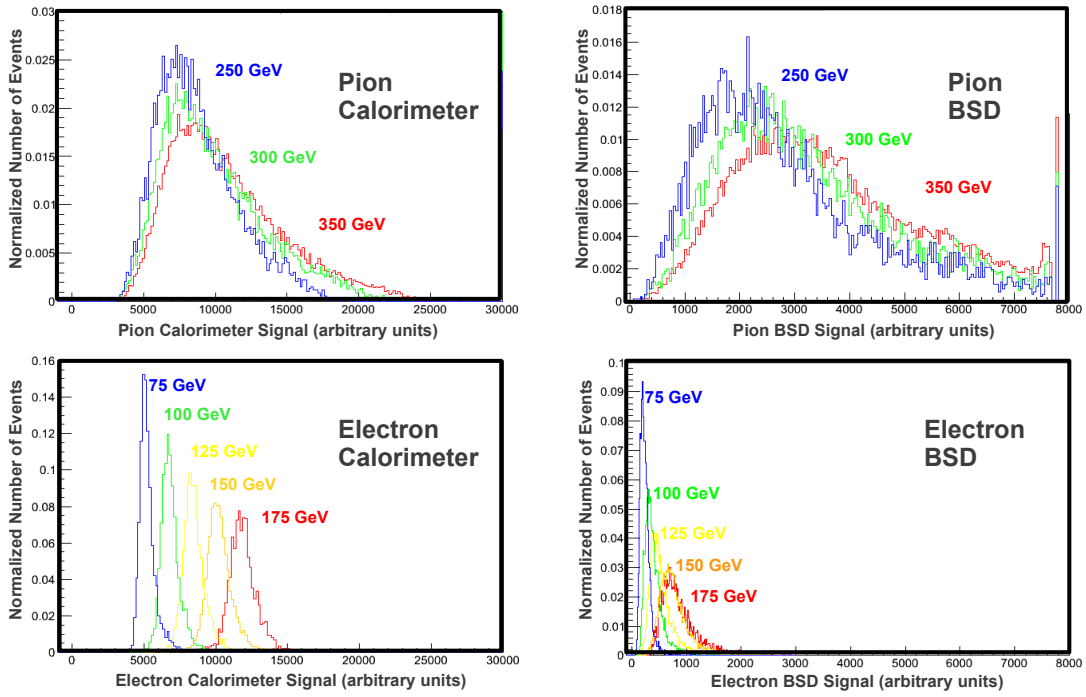

Figure 6.13. Signal histograms for the calorimeter (left) and BSD (right) for pions (top) and electrons (bottom). All distributions are scaled by total number of events.

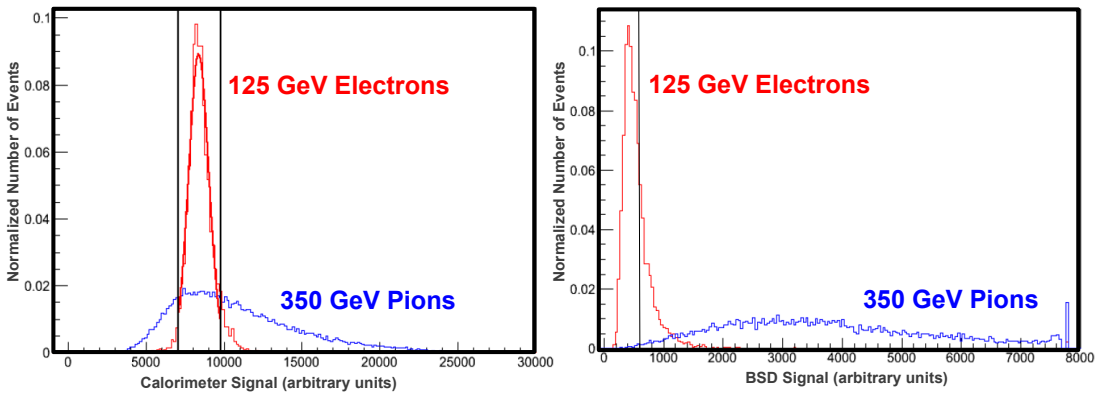

Figure 6.14. Calorimeter (left) and BSD (right) signal distributions for 125 GeV electrons (red) and 350 GeV pions (blue). On the left, vertical lines indicate two standard deviations from the mean of the fitted electron peak. On the right, the BSD signal distributions represent events containing calorimeter signals within two standard deviations of the electron peak's mean, and a vertical line indicates the BSD signal value below which the electron acceptance is 80%. All distributions are scaled by total number of events.

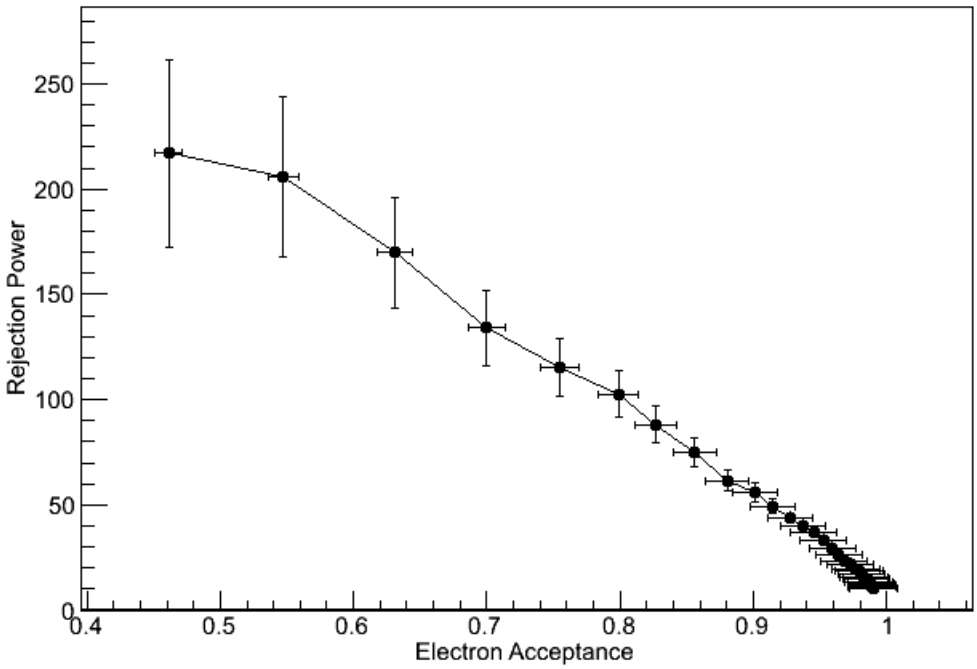

Figure 6.15. BSD hadronic rejection power versus electron acceptance for the 125 GeV electron and 350 GeV pion runs at CERN.

Figure 6.16 shows the detector model. The beam line is incident on the center of the detector systems. The carbon targets, calorimeter, instrument pallet, and prototype BSD are all included in the model. Neutron physics is simulated via the QGSP_BIC_HP physics list, which incorporates the gamut of both elastic and inelastic neutron interaction processes. In this section, comparisons will be made between this simulation's predictions and the results obtained at CERN.

6.4.1 Electron and Pion Distribution Shapes

As a first step in comparing the simulations to the CERN results, the overall shapes of the distributions can be studied, irrespective of their absolute normalizations. Figure 6.17 shows the measured BSD signal distributions for 150 GeV electron runs and 350 GeV pion runs in the CERN beam test (blue), superimposed on top of the monte carlo simulation's predicted distributions (red). Here, the BSD's simulated signal is derived directly from the total number of BSD neutron captures predicted to occur within the 900 ns–4500 ns integration window used during the CERN beam test. Simple Poissonian smearing was added to the simulated distributions in order to account for variations in photon propagation. Neutron capture peaks are visible, indicating that an improved accounting of resolution and background effects needs to be implemented in the

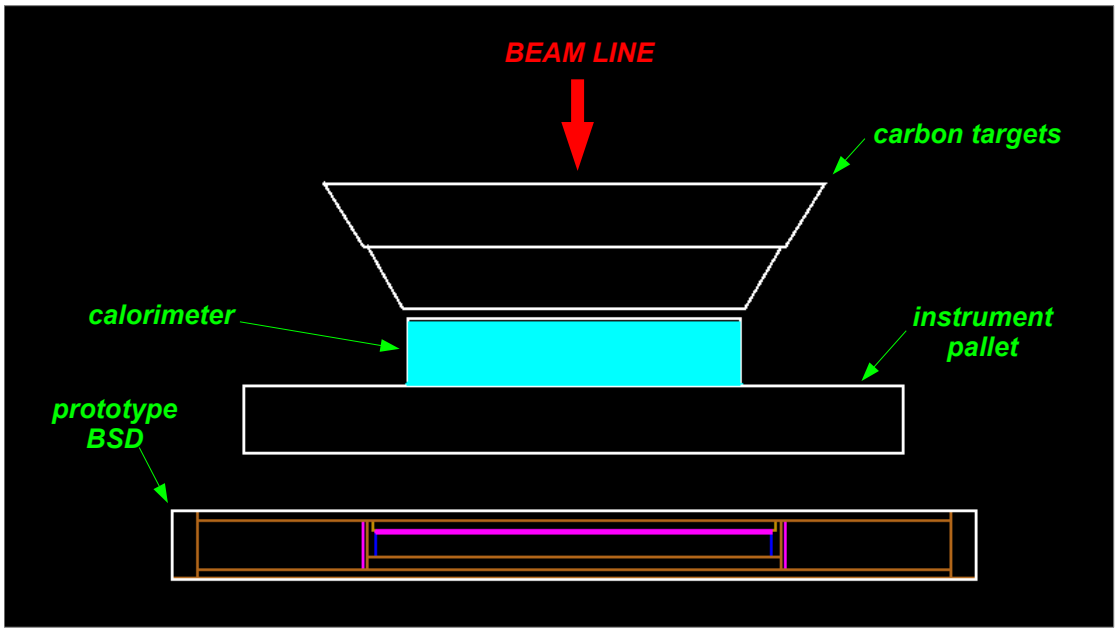

Figure 6.16. The GEANT4 geometry for the CERN beam test. The beam line is incident through the center of the detector. The carbon targets, calorimeter, instrument pallet, and prototype BSD are included in the model.

simulations. However, the rough correspondence in the overall shapes of the distributions is clear.

6.4.2 Signal Magnitudes and Scaling with Energy

Using the prototype BSD collection efficiencies of Section 6.2.2, the absolute magnitude of the signals seen at CERN can be compared with the predictions of the simulations. Referring to Table 6.1, the prototype BSD's overall collection efficiency[11], summed over all ten switched PMTs, is found to be 1.2%. Since each capture produces 570 photons in the BSD (see Section 6.1), a capture should correspond to a 6.8 PEs signal, when summed over all ten PMTs.

Table 6.2 converts the number of neutron captures predicted by the simulation to expected photoelectron signal by multiplying by this 6.8 PE/capture conversion factor. The actual number of photoelectrons measured at CERN is also shown. Clearly, there is large discrepancy—roughly an order of magnitude—between the signal sizes predicted by the simulation and those seen at CERN.

A further comparison is made in Figure 6.18, which plots the BSD signal measured at CERN versus mean number of neutron captures predicted from the GEANT4 simulation for all electron runs 75 GeV–175 GeV (red fit line) and pion runs 250 GeV–350 GeV (blue fit line). In Figure 6.17, a single scale factor was chosen for both electrons and pions so as to best align the electron

[11] PMT 1A was not installed when collection efficiencies were being measured, but its collection efficiency can reasonably be taken as 0.1%.

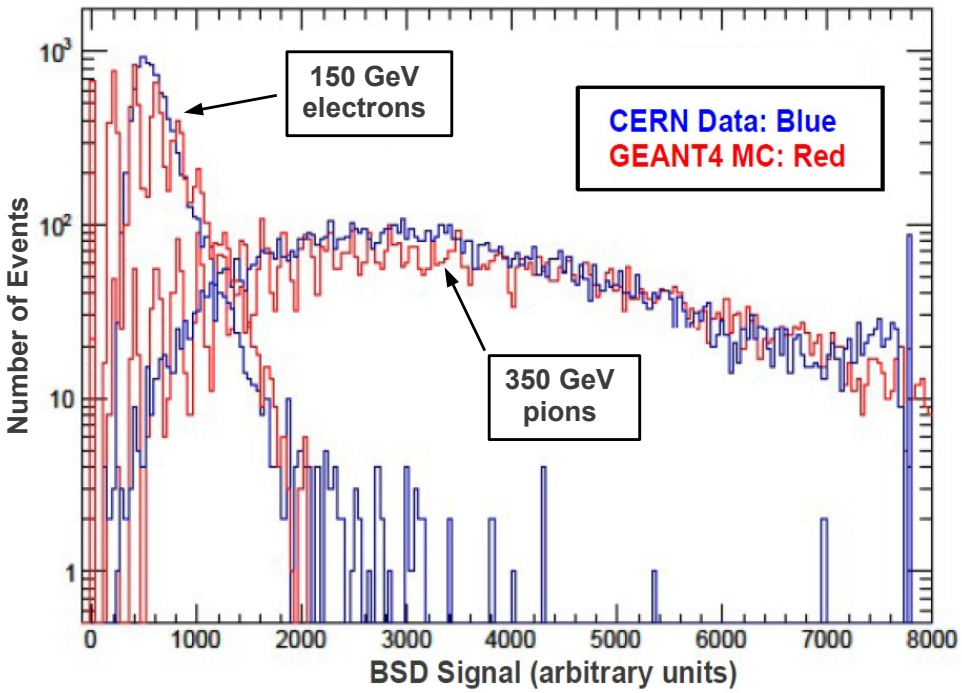

Figure 6.17. Comparison of CERN data (blue) with the GEANT4 simulation (red). The small-scale structure in the simulated distributions results from the fact that sufficient smearing has not yet been fully accounted for and is not expected to be seen in experimental data.

Electron Energy (GeV)	GEANT4 Neutron Captures	Equivalent Photo-electrons	CERN Photo-electrons
75	1.4	9.6	181
100	1.8	12.3	289
125	2.3	15.7	395
150	2.8	19.2	605
175	3.3	22.6	655
Pion Energy (GeV)	**GEANT4 Neutron Captures**	**Equivalent Photo-electrons**	**CERN Photo-electrons**
250	16.3	111.5	1890
300	17.8	121.8	2340
350	18.9	129.3	2681

Table 6.2. Predicted GEANT4 photoelectron signals compared to CERN signals.

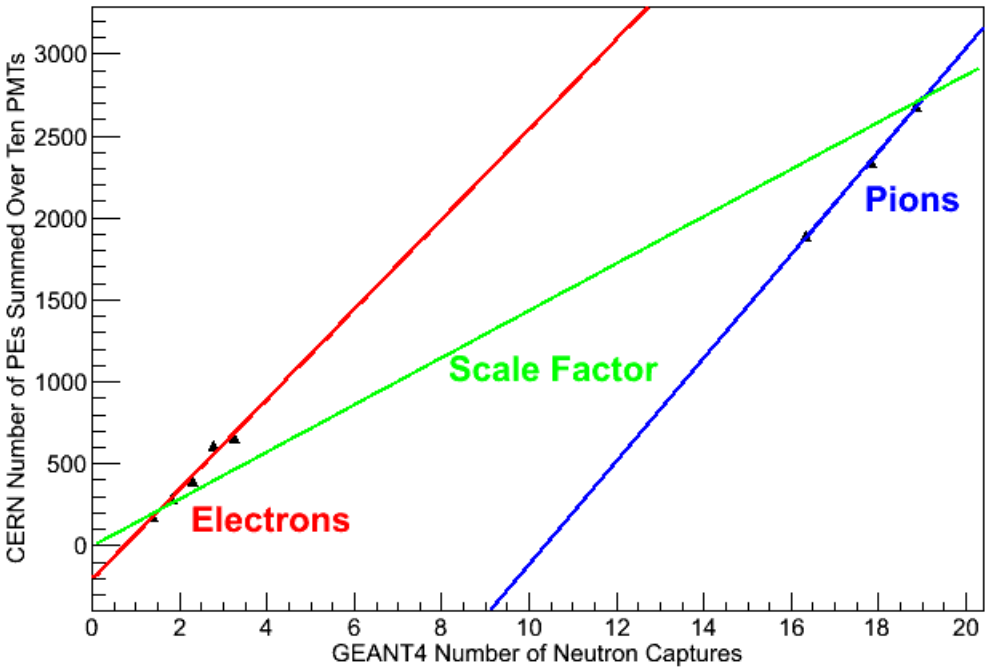

Figure 6.18. CERN BSD signal is plotted versus GEANT4's predicted number of neutron captures in the BSD for 75 GeV–175 GeV electrons (red fit line) and 250 GeV–350 GeV pions (blue fit line). A scale factor (green fit line) is shown which seems to best match GEANT4 150 GeV electrons and 350 GeV pion distributions to those distributions measured at CERN. Such a scale factor was used in generating Figure 6.17.

and pion peak simulated distributions with the CERN data. In Figure 6.18, a line representing this scale factor is drawn in green. Error bars in Figure 6.18 were derived from the standard error of the mean for each of the distributions in Figure 6.13, but the resulting error bars were smaller than the size of the data markers. The systematic error in the BSD's measurement of the CERN data is unknown, since no secondary method of measuring late-time shower activity in the BSD was present during the CERN beam test.

From Figure 6.18, it is clear that the slopes of the fit lines for both electrons and pions are roughly the same, but that the extrapolated y-intercept for the pion data is quite a bit lower than that found for the electron data. The pion data's large y-intercept shift is certainly not caused by non-linearities in the response of the BSD's PMTs or CAMAC readout electronics, since pre-flight calibration of these detector elements indicated a linear response throughout the range of signals encountered during the CERN beam test. The discrepancy is far too large to be attributed to gain drifts in the photomultiplier tubes or the 2249W readout electronics. Large shifts in electronics pedestal also seem an unlikely explanation, since all measurements were taken consecutively, within the same three hour time period. In the end, differences between

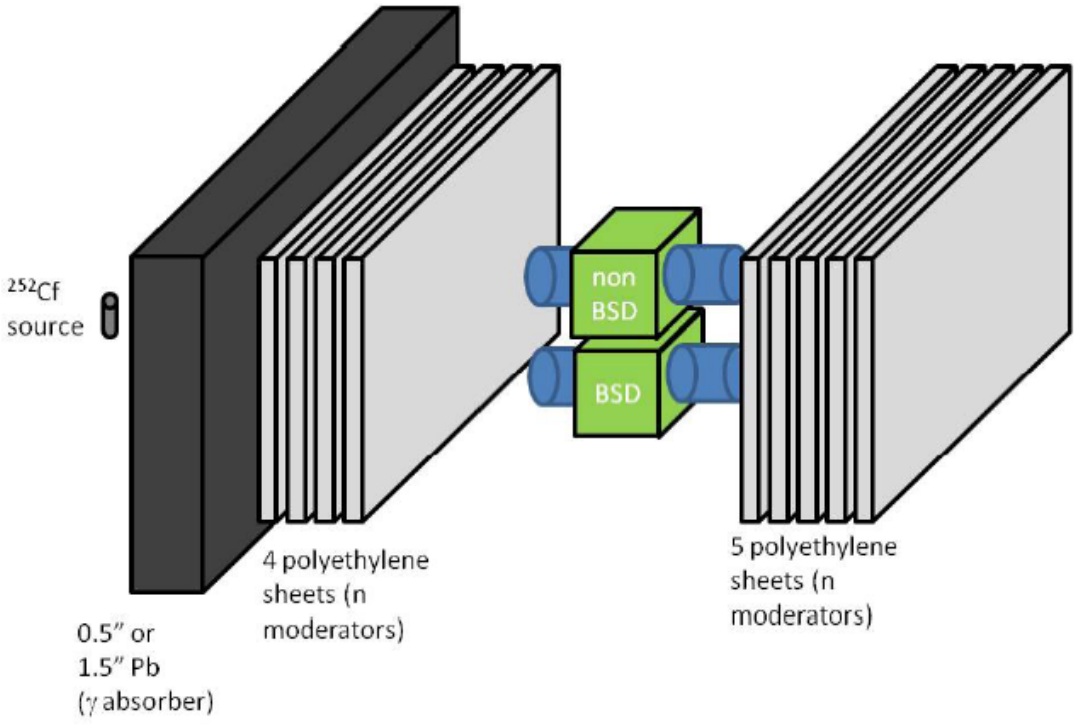

Figure 6.19. Setup for studying the neutron capture spectrum. Four polyethylene sheets are interposed between the source and the scintillator blocks. Coincidence rates are studied as a function of threshold for both cases of 0.5 in lead absorber and 1.5 in lead acting as a gamma-ray absorber.

the electron and pion curves of Figure 6.18 are difficult to explain on the basis of instrumental effects.

6.4.3 Investigation of Discrepancies

Three factors were used in calculating the prototype BSD's expected signal size at CERN—its photon collection efficiency of 1.2%, its light yield of 570 photons/capture, and GEANT4's prediction for its number of neutron captures. As described in Section 6.2.2, the prototype BSD's collection efficiency was carefully measured, and so, seems free of blame. The 570 photon/capture light yield of 5% boron-loaded EJ-254 and the predicted number of neutron captures from the GEANT4 simulation will each be examined below.

6.4.3.1 The Neutron Capture Light Yield

The light output from both a boronated and a non-boronated scintillator block, each of dimensions 5.8 cm × 6.9 cm × 3.8 cm, was studied in the presence of a neutron source in order to determine whether the light yield produced by a single neutron capture was commensurate with the 570 photon/capture expectation. These small blocks were chosen because they sim-

plified measurement setup while also increasing the collection efficiency of a single PMT. The boronated-scintillator block was comprised of the same 5% boron-loaded EJ-254 scintillator formulation which was used in the block tested at CERN[12], while the non-boronated block was cast from EJ-200 [104], the base material for EJ-254.[13]

A ^{252}Cf source with a 4.2 mrem/hr neutron intensity and a 12.0 mrem/hr gamma ray intensity was used in order to generate a neutron flux through the scintillator blocks. Both the neutron and the gamma ray components of the source have a spectrum which peaks in the range of a few MeV. While both the boronated and the non-boronated scintillator blocks should see a significant signal rate due to scattering of the source's fast neutron and gamma ray products, the boronated scintillator should also see an elevated rate due to thermalizing neutrons being captured. Thus, by comparing the signal rates in both the boronated and the non-boronated scintillators, the characteristics of neutron captures can be studied.

The neutron capture spectrum was studied via the setup shown in Figure 6.19. Two R1924A PMT assemblies, run in unswitched mode, were optically coupled to each scintillator block, and the two blocks were stacked on top of each other, such that each had roughly the same exposure to the source. The high voltage applied to each PMT was adjusted so as to gain match all PMTs via their atmospheric muon signal. This gain matching procedure led to a single photoelectron signal with an amplitude of roughly 6 mV. A LeCroy 612AM PMT amplifier was used to increase the PMT signals by a factor of 10. The amplified signals were then fed into a Philips Scientific 710 discriminator module, with a threshold setting of roughly 1/4 PE, thus ensuring sensitivity to the even the smallest of photoelectron signals. The outputs from the discriminator modules were fed into a LeCroy 622 coincidence module, and the ANDs of the discriminator outputs from the two PMTs viewing the same scintillator block were each fed into a channel on a Canberra 512 Dual Counter/Timer module, thus allowing a measurement of the $\geq$1 PE coincidence rate for the two PMTs on each of the boronated and non-boronated scintillator blocks.

The ^{252}Cf source's gamma-ray component was attenuated by the presence of lead shielding. Measurements were taken with lead-shield thicknesses of 0.5 inch and 1.5 inch. In addition, 4 sheets of 1.1 cm-thick polyethylene moderator (4.4 cm total thickness) were interposed between the lead shield and the scintillator blocks. This amount of moderator had been determined to optimize the background-subtracted fractional excess in the coincidence rate of the boronated scintillator over that of the non-boronated scintillator, and so, was taken as the amount of moderator which optimized the signal due to neutron captures over that of neutron scatters. Five additional sheets of polyethylene moderator were also placed behind the scintillator blocks in hopes of thermalizing and capturing some neutrons which otherwise would have missed the scintillator.

The results of the experiment are shown in Figure 6.20 for 0.5 in of lead absorber (left) and 1.5 in of lead absorber (right). The abscissa has been scaled to units of photoelectrons, using the 1 PE/6 mV scale factor. In both cases, the coincidence rate in the boronated scintillator block

[12]Moreover, the manufacturer assured us that this small block of boronated scintillator was hewn from the same raw boronated scintillator slab as our primary detector block.

[13]This measurement was performed by Professor Stephane Coutu of the Pennsylvania State University.

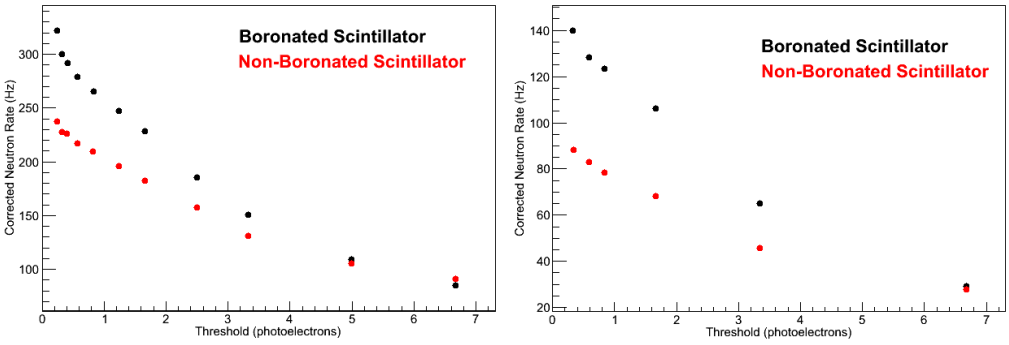

Figure 6.20. Count rate versus photoelectron threshold for 0.5 inch (left) and 1.5 inch (right) lead shielding for both the boronated (black) and non-boronated (red) scintillator samples.

approaches the rate in the non-boronated block near ∼6 PE. Thus, very crudely, the size of the neutron capture signal can be taken as 3 PEs in the small boronated scintillator block.

A single PMT collection efficiency of 0.6% was measured for the PMTs attached to the boronated scintillator block, using the method described in Section 6.2.2. The ∼3 PEs neutron capture signal estimated here can be scaled up for the larger BSD block via the ratio of the collection efficiencies, 3 PE × 1.2%/0.6% ≈ 6 PE, in good agreement with the 6.8 PEs derived from the 76 keV energy deposit predicted in the literature. Thus, the neutron capture light yield of the prototype BSD's EJ-254 scintillator block agrees with expectations and cannot be faulted as the source of discrepancy between the CERN measurements and GEANT4 predictions.

6.4.3.2 Verifying the GEANT4 Physics Model

As has been presented above, the large discrepancies observed in both signal magnitudes and energy-scaling behavior when comparing simulations with measured CERN data cannot be accounted for on the basis of instrumental effects or mis-understandings of a neutron capture's light yield. The next avenue of exploration is to verify GEANT4's neutron capture model. A GEANT4 model was developed whereby the probability was calculated for neutrons to undergo the ^{10}B capture process after having traversed 1 mm of a slab of 5% boron-loaded EJ-254. The 1 mm pathlength was chosen in order to limit energy loss from other, non-capture mechanisms. Simulations were generated for 10^5 neutrons at each of the energies 0.1 eV, 1 eV, 10 eV, 100 eV, 1 keV, and 10 keV. The results were compared to expectations based on literature values for neutron attenuation lengths in scintillator. Figure 6.21 shows the result of this comparison. The resulting capture probabilities agree fairly well, and the large differences observed between simulations and CERN results certainly cannot be attributed to this particular aspect of GEANT4's physics model.

Many other aspects of GEANT4's physics model remain to be verified, especially its neutron production and interaction models. In any case, it is worth noting that, while GEANT4 is well established as a high-energy physics simulation framework, it has only begun to emerge as a tool

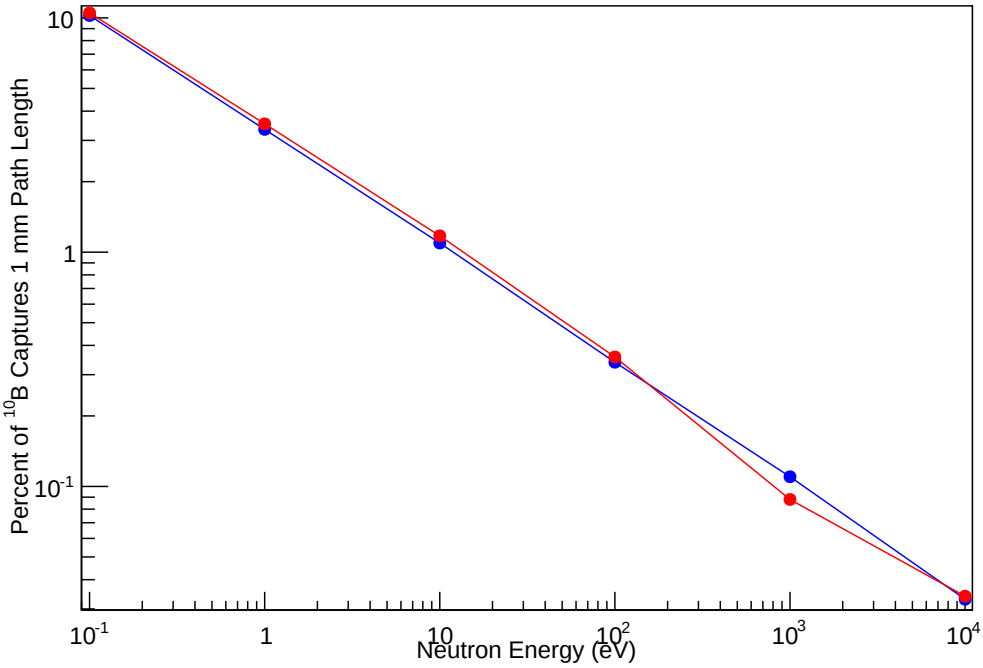

Figure 6.21. The probability of ^{10}B neutron capture after traveling 1 mm in EJ-254, as reported in the literature (blue) [128] and as predicted by GEANT4 (red).

for modelling low-energy neutron interactions. In any case, while the discrepancy associated with the GEANT4 simulations remains unresolved, the higher-than-simulated light yields observed serve well to make the BSD a workable technique on the ISS-CREAM payload.

6.4.4 Time-Dependent Behavior of EJ-254

As has been stated previously, 5% boron-loaded EJ-254 is expected to have a ^{10}B neutron capture-time constant of 2.74 μs, and the GEANT4 simulation suggests that this time constant should be reflected in the timing profile seen by the BSD when viewing calorimeter showers at late times. Both of these assertions have been explored empirically, and the results of this exploratory work are presented below.

6.4.4.1 EJ-254 Neutron Capture Time Constant

A measurement was performed of the neutron capture time constant of EJ-254. This measurement relies on the idea that occasionally, a fast neutron will lose most of its energy in a single interaction with one of the scintillator's protons. The interaction produces scintillation via the recoil motion of the proton. The neutron then has an exponentially decaying probability of undergoing ^{10}B capture, and if it does, a second pulse of light will be emitted. Thus, by measuring

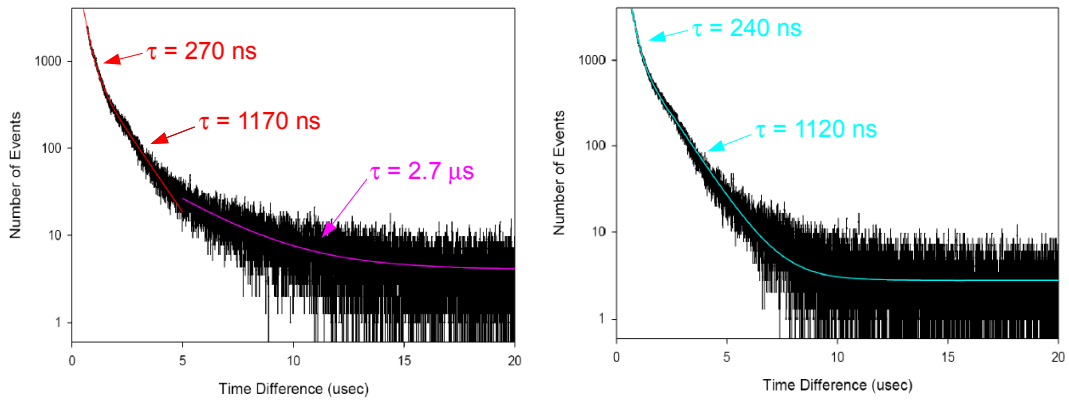

Figure 6.22. The time constants found by the delayed coincidence method for boronated (left) and non-boronated (right) scintillator.

timing differences between consecutive light pulses in boronated scintillator, the time constant associated with the neutron capture process can be measured.

The ^{252}Cf source was used with the setup of Figure 6.19 to measure the time constants associated with neutron capture in the BSD. A 1.5 inch thick lead shield was installed for enhanced gamma-ray absorption, and timing differences were measured between consecutive coincident pulses with delays of up to 10 μs. Figure 6.22 shows the resulting timing distributions for the boronated (left) and non-boronated (right) scintillator blocks. For timing differences less than 5 μs, both distributions exhibit decaying exponential components with time constants in the range 200 ns–300 ns and 1100 ns–1200 ns. While the cause of these two exponential components is somewhat unclear, multiple scattering of fast neutrons provides one plausible explanation. In any case, since this behavior is present in both the boronated and non-boronated block, it is clearly not related to the ^{10}B thermal neutron capture process.

For timing differences greater than 5 μs, the boronated scintillator shows a time constant of 2.71 μs, in agreement with expectations for 5% boron loaded scintillator (see Section 6.1). The non-boronated scintillator displays no evidence of 2.7 μs time-constant behavior, bolstering the argument that ^{10}B neutron captures are the source of this exponential component. The fact that the expected time structure materializes only beyond 5 μs is an artifact of the use of the Californium source here, and does not affect the BSD technique in the ISS-CREAM flight configuration.

6.4.4.2 CERN Late-Shower Time Constant

During the CERN beam test, an attempt was made to characterize the late-shower timing profile measured by the PMTs. Such a measurement is useful for comparison with simulations and verification of the characteristics of the boronated scintillator. Since, the BSD's primary acquisition system (*i.e.*, the CAMAC 2249W charge integrating ADC module and its ten gated PMTs) was

occupied with measuring BSD signals over the full 900 ns to 4500 ns time window, an alternative means of studying the late-shower's timing profile was needed.[14] For this measurement, the windowed area feature of the LeCroy Waverunner's 104MXi oscilloscope (see the footnote in Section 6.2.2.) was used on PMT 1B's trace. The oscilloscope was triggered off of the same NIM trigger flag which triggered the primary acquisition system (see Section 6.3.1). Triggering was inhibited outside of beam spill periods. PMT 1B's signal was broken up into 400 ns "time slices", starting roughly 1 μs after the shower's start. The oscilloscope's windowed area feature was used to log 1000 measurements of the area of PMT 1B's signal in each 400 ns time slice. Using windowed area measurements was deemed preferable to directly captured oscilloscope traces, since the windowed area technique generated many fewer data files, minimized oscilloscope deadtime, and served to naturally smooth out the statistical effects of neutron capture and photon propagation on the expected exponential form of the averaged late-time shower curve.

By plotting the mean signal derived from each time slice versus the midpoint of the corresponding time slice, the shower's time constant should become evident, since, for a given time slice with midpoint t and width $\Delta T = 400$ ns,

$$\int_{t-\Delta T/2}^{t+\Delta T/2} e^{-t'/\tau} dt' = 2\tau \sinh\left(\frac{\Delta T}{2\tau}\right) e^{-t/\tau} \tag{6.4}$$

which is a decaying exponential, with time constant identical to the original shower's time constant.

Signal distributions resulting from the windowed-area measurement of each 400 ns time slice of PMT 1B are shown in Figure 6.23 (150 GeV electrons) and Figure 6.24 (350 GeV pions). For the 150 GeV electron measurements, each time slice distribution was found to fit well to a simple Landau distribution. For the 350 GeV pion measurements, the best fit for the first nine time slices was found to be the sum of a Landau and Gaussian.[15] For these time slices, only the Landau component of the fit function was used in finding the mean. The remaining 350 GeV time slice distributions were found to fit best to a simple Landau distribution.

In the case of 150 GeV electrons, pedestal measurements were taken on each time slice by triggering the oscilloscope "on line", with each time-sliced pedestal distribution showing a good fit to a Gaussian. The resulting differences in peak and pedestal means were taken as the data values for each time slice. In the case of 350 GeV pions, no measurement of pedestal was performed. However, as described below, fitting the resulting data with an additional constant provides some means of accounting for the un-measured pedestal.

[14] Time was limited during the CERN beam test. The beam time allotted for ISS-CREAM was rigidly scheduled, and moreover, the end of ISS-CREAM's beam run coincided with the start of a series of LHC upgrades, which meant the beginning of a two-year shutdown of the LHC. Thus, there was no possibility to extend ISS-CREAM's beam test or negotiate with other groups for more beam time, and so, the primary acquisition system could not be re-purposed to study the late-shower time constant.

[15] The gaussian component was necessary in order account for a second peak in the low-end of the distributions of the early time slices from the 350 GeV pion runs. This peak is believed to be caused by false triggers due to the low threshold settings of the two trigger PMTs. Such false triggers are removed in the primary acquisition system by offline analysis cuts which require coincidence between calorimeter and prototype BSD triggers.

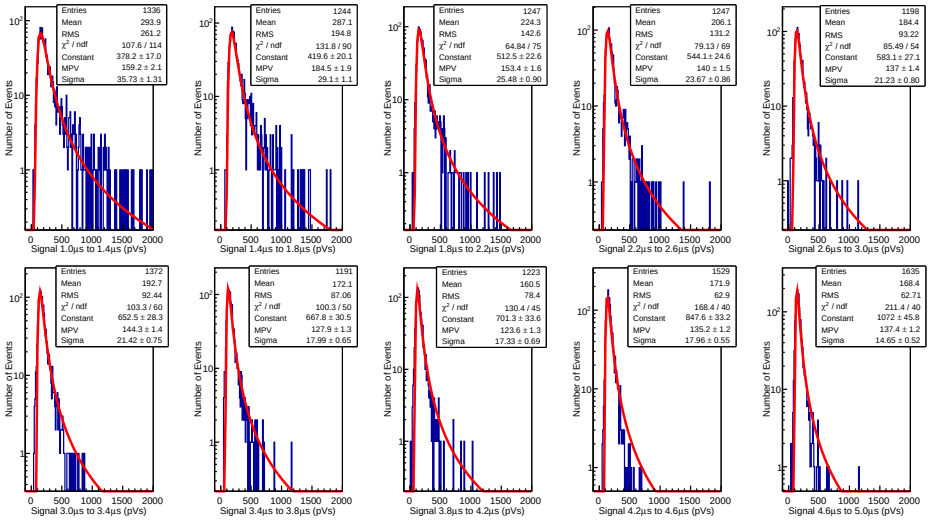

Figure 6.23. Time slices for the 150 GeV electron measurement. Fits to Landau peaks are shown.

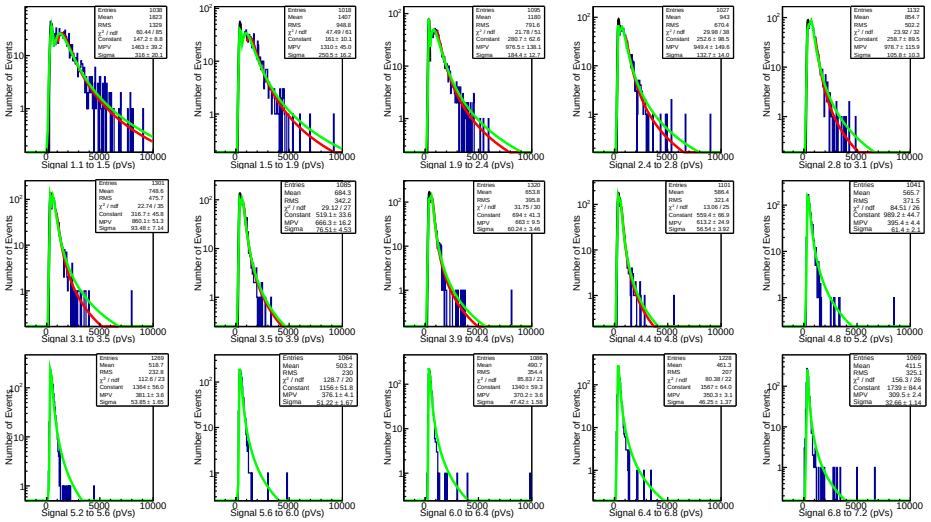

Figure 6.24. Time slices for the 350 GeV pion measurement. Fits to the sum of a Landau and Gaussian are shown for the first nine time slices, while fits to a simple Landau are shown for the remaining time slices.

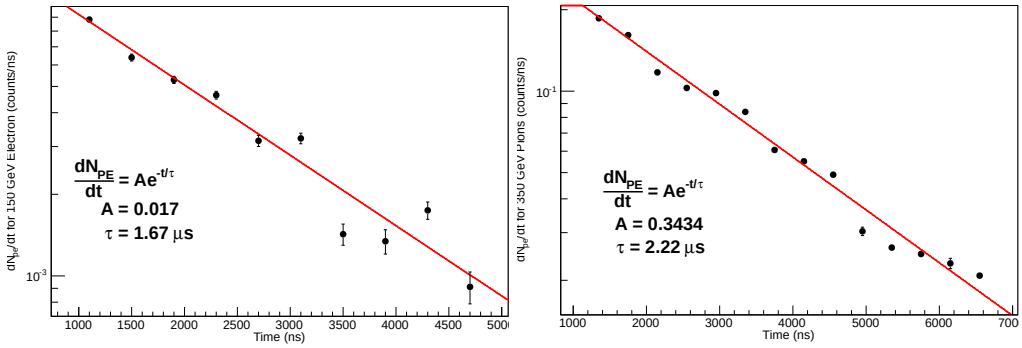

Figure 6.25. The CERN 150 GeV electron (left) and 350 GeV pion (right) timing profiles.

The oscilloscope's windowed area feature natively gives measurements in units of "volt-seconds". The obtained time-sliced means were converted to number of photoelectrons per unit time via the relation

$$\frac{dN_{PE}}{dt} \approx \frac{\mu_s}{GeR\Delta T} \tag{6.5}$$

where μ_s is the distribution mean as described above, G is the measured gain of PMT 1B, e is the electron charge, ΔT is the 400 ns window width, and R is the 50 Ω termination resistance of the channel.

Ordered pairs were formed between the time-sliced means and the midpoint of each time slice, and the result was fitted to the function

$$f\left(t\right) = p_2 + e^{p_0 + tp_1}. \tag{6.6}$$

The p_2 fit parameter represents either residual pedestal, or perhaps, some constant noise component which might have been induced during the beam spill. The value of fit parameter p_2 was subtracted from all ordinate values, and the final results were re-fitted to the equation

$$f\left(t\right) = Ae^{-t/\tau}. \tag{6.7}$$

Figure 6.25 shows the resulting shower profiles for 150 GeV electrons (left) and 350 GeV pions (right). Error bars are calculated as the error in the time sliced distribution fits. The systematic error in the measurement is unknown. The 150 GeV electron data fits to a time constant $\tau = (1.67 \pm 0.04)$ μs (statistical), while the 350 GeV pion data fits to a time constant $\tau = (2.22 \pm 0.02)$ μs (statistical). While the derived time constant values are somewhat smaller than what is predicted by theory, several factors deserve consideration.

First, no method exists of sample purification. As previously discussed, the pion beam was pure at the 95% level, while the electron beam was only pure at the 75% level. Analysis from the primary acquisition system benefited from correlation between BSD and calorimeter events, which allowed implementation of the six-layer cut described in Section 6.3.2. However, because

data logging by the oscilloscope did not allow correlated event reconstruction with the primary acquisition system, implementing any sort of cross-detector clean-up cut was impossible. Thus, the measurement of the time constant, as described here, was highly subject to false triggers, sample impurities, and pathological events whose effects would have been more easily mitigated in analyses using the primary acquisition system.

Second, (and this is especially true for the electron measurement) the time-sliced distributions are not well separated from pedestal, and so, such small signal values are very subject to noise contamination. While the primary acquisition system benefited from the signal-to-noise improvement of summing the signals from ten PMTs, only one PMT was used in the time constant analysis presented here. Furthermore, the pedestal "fit and subtract" method used in this analysis assumed a constant pedestal throughout the time window measurement. If backgrounds drifted or changed significantly across the 3.6 μs integration window, or if they were significantly different outside the beam spill as compared to during it, this might have influenced the final outcome of the time constant determination.

Third, in the case of the pion time constant, the necessity of switching between the sum of a Landau and Gaussian fit function to a pure Landau fit at the tenth time slice introduces a "glitch" in the curve which, while somewhat smoothed out by adjacent points, may introduce some error in the fit result.

Given the uncertainties in the measurement of this time constant from the CERN data, it seems prudent not to attribute too much significance to it. In the end, the measured late-shower time constants for electrons and pions are in the range of expectations (a few microseconds), but attempting to derive meaning beyond this crude assessment may be too much to ask.

6.4.5 Alternative Explanations for the BSD's CERN Signal

Given the discrepancies noted above between GEANT4 predictions of the BSD signal and the results obtained at CERN, questions naturally arise as to whether the late-time signals measured by the prototype BSD at CERN might be attributed, not to neutron captures, but to some other, as yet unidentified, delayed light generation mechanism in the BSD, which is triggered by the calorimeter's shower. At first glance, this explanation seems bolstered by Figure 6.26, which plots the BSD signal measured at CERN versus GEANT4's prediction of energy deposit in the last layer of the calorimeter. Clearly, the slopes of the fit lines for both electrons (red) and pions (blue) are similar, and the y-intercepts of the fit lines are much closer than they were in Figure 6.18. However, identifying an alternative mechanism for late-time light production in the BSD is difficult. Several possibilities for the production of such delayed light are examined below.

6.4.5.1 Late Arriving Photons

The measured late-time light cannot be due to photons created during the first 400 ns of the calorimeter's shower, since the probability of such photons surviving inside the scintillator for the additional 500 ns minimum necessary to arrive at the start of the BSD's integration window

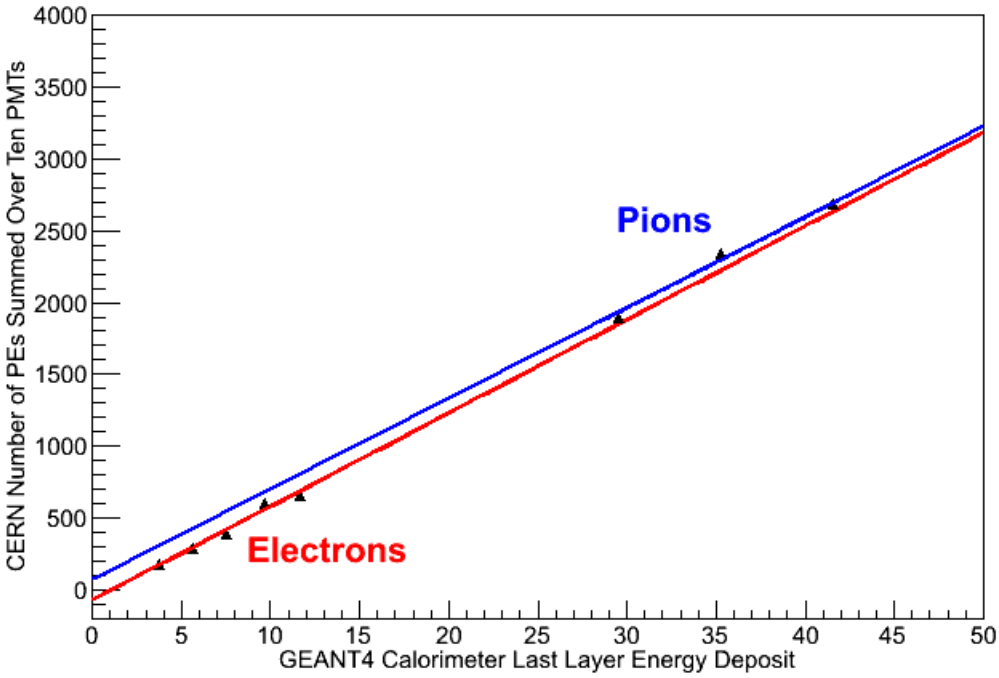

Figure 6.26. CERN BSD total signal as a function of GEANT4's predicted signal in the last layer of the calorimeter. Fit lines are shown for electrons (red) and pions (blue).

is less than 10^{-35}, given EJ-254's bulk attenuation length of 120 cm and its refractive index of 1.58.

6.4.5.2 Late Arriving Charged Particles

It also seems untenable that this light is created by slow moving charged particles which were created in the first part of the shower, since, in traveling from the bottom of the calorimeter to the top of the BSD, such particles would have maximum speeds near $\beta \sim$ (15 cm/500 ns)/(30 cm/ns) $\sim 10^{-3}$. Such low energy charged particles are stopped almost immediately, and hence, would never enter the BSD, let alone deposit enough energy in the BSD to create scintillation light.

An alternative means of generating charged particles which might impinge on the BSD at late times is via the decay products of long-lived excited nuclei in ISS-CREAM's target material. The GEANT4 simulation was used to examine this possibility. Simulations were run for 150 GeV electrons and 350 GeV pions, and charged particles were logged which entered the BSD at times greater than 400 ns after the start of the calorimeter's shower. The probability for one or more charged particles to enter the BSD at times greater than 400 ns in a given event was 2×10^{-4} for the electron runs and 2×10^{-3} for the pion runs. All such late particles were electrons and

positrons, most with kinetic energies less than 1 MeV. Thus, the probability of the incidence of such particles is far too small to explain the BSD signal observed at CERN.

6.4.5.3 Slow Component of Scintillation

One explanation which is not immediately refutable is the existence of a "slow component" of scintillation with a time constant of a few microseconds, and which, while highly suppressed relative to the scintillator's primary fluorescence channel, could have been activated by the large number of charged particles passing through the BSD's scintillator in the early shower.[16] Organic scintillation is triggered by the excitation of π-bonded atomic electrons from the spin-singlet ground state up to higher-energy spin-singlet and spin-triplet energy levels. The primary, or so-called "fast component", of scintillation results from the de-excitation of the excited spin-singlet states to vibrational-excitations of the ground state[17] within a few nanoseconds. The excited spin-triplet states decay much more slowly, and thus, present the possibility of generating a slow component of scintillation. However, in plastic scintillators, such slow components of scintillation are known to be highly suppressed, and thus, difficult to study. Their amplitude and timing profile depend on both the specific chemistry of the scintillator's formulation and the identity of the ionizing particles which generate it [47].

A literature search has been unsuccessful in obtaining data on the amplitude or time constants of potential slow components of scintillation for Eljen technology's EJ-254 boron-loaded scintillator, its base formulation EJ-200 [104], or a similar formulation by Saint-Gobain Crystals, BC-454 [135]. Figure 6.27 shows the most similar dataset which could be found—a plot of the timing profile for BC-422[18] stimulated by a ^{90}Sr beta source [136]. The amplitude of the primary-signal's spike near 200 ns is difficult to read from the plot, but it appears to extend up to 10^6 or beyond. At 900 ns, the start of the BSD's CERN integration window, the amplitude of scintillation has decayed to less than 10^2, so the amplitude suppression of this slow component appears to be at least 10^4. However, whether this result might be extended to EJ-254 is uncertain.

6.4.6 Conclusions on the Comparisons

Given GEANT4's yet unverified ability to correctly model low energy neutron production and interactions, it seems premature to prefer any alternative explanation of delayed light production in the BSD over the idea that the BSD's late-time signal is indeed created by neutron captures. In regards to Figure 6.26, it may turn out to be entirely reasonable that the predicted mean values from the distributions of energy deposit in the last layer of the calorimeter correlate with the overall neutron signal measured in the BSD, since the same primary particle is generating

[16] Such a slow component of scintillation is readily present (and in fact, is often considered a useful feature) in inorganic scintillators, such as BaF_2.

[17] Scintillator would not be transparent to its own radiation if its excitations decayed directly back to the ground state, rather than one of the ground state's vibrationally-excited energy levels.

[18] BC-422 utilizes the same polyvinyltoluene base as EJ-254.

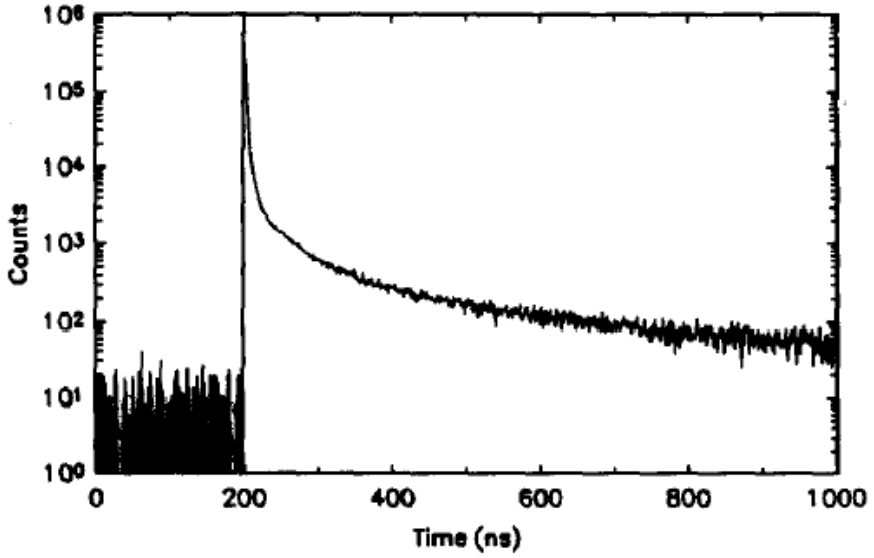

Figure 6.27. The timing profile of BC-422 plastic scintillator when exposed to a ^{90}Sr beta source, from reference [136].

both the "punch-through" component of the shower which creates the signal in the last layer of the calorimeter and the neutron component of the shower which is measured by the BSD. Further work is needed in order to better understand light production in the BSD's scintillator and to verify and refine the GEANT4 model of the BSD.

Hypothetically, if the BSD were to derive its hadronic rejection power from a delayed component of scintillation which is activated by the early shower, then the question naturally arises as to whether this additional hadronic rejection power might be derived from the calorimeter instead by using, for instance, its last layer, which sees an early shower profile very similar to that observed by the BSD. (Less than $0.2X_0$ and $0.03\lambda_I$ separate the two.) In such a case, the BSD would be rendered superfluous.

Figure 6.28 plots the BSD's late time signal versus signal in the calorimeter's last layer. Equal-sized populations of 125 GeV electrons and 350 GeV pions have been selected for the study. The plot on the left considers the calorimeter signal taken as the sum over all non-zero pedestal subtracted last-layer ribbons, and thus, is somewhat representative of signals from the shower's core which penetrates to the deepest layer of the calorimeter. The plot on the right represents the opposite extreme, selecting all ribbons in the last calorimeter layer with signals above pedestal. As can be seen, in both cases, the BSD provides significantly better separation of electron and hadron populations than the calorimeter's last layer. So, whatever the source of the BSD's late light, results from the CERN beam test indicate that the BSD makes a significant contribution to the ISS-CREAM calorimeter's electron/hadron discrimination.

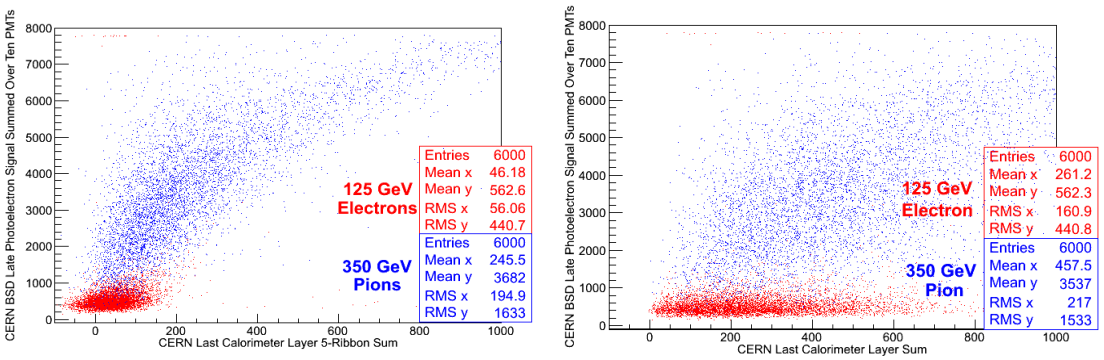

Figure 6.28. CERN BSD signal versus (left) 5-ribbon sum and (right) all ribbons with signal > 0 in the last layer of the calorimeter.

Chapter 7

Design of the ISS-CREAM Flight BSD

The design of the flight BSD will be presented in this chapter. Figure 7.1 shows a Computer-Aided Design (CAD) drawing of the ISS-CREAM instrument. Callouts have been added, identifying visible features of the payload, such as the SCD, calorimeter support structure, and the ISS-CREAM common electronics rack. The flight BSD's system is shown to be comprised of two components—the ***BSD detector box*** and the ***BSD electronics box***. The BSD detector box (brown) mounts underneath of the calorimeter honeycomb plate and, as will be described more fully in Section 7.2, contains the BSD's scintillator block and the PMT assemblies which view it. The BSD electronics box (salmon) mounts to the sidewall of the ISS-CREAM structure and reads out the anode signals from each PMT assembly through a stack of five circuit boards. The design of the BSD electronics box, and the boards inside it, will be described more fully in Section 7.3.

7.1 BSD Design Considerations

Here, the major considerations which drive the design of the BSD will be presented. In later discussions of the specific details of the BSD's detector box and electronics box, aspects of the design which are motivated by these considerations will be highlighted.

Paramount to any flight mission is the goal of minimizing detector size and mass while still providing sufficient structural stability to protect its components. The mechanical design of the BSD has undergone extensive analysis, and its structure has been selectively re-enforced in order to ensure that it can withstand the expected worst-case static and dynamic loadings of the mission.

Careful attention must also be paid to the maximum and minimum temperatures experienced by the payload's components in flight. The constituents of the BSD's design have been analyzed

in order to determine their survival temperature limits (-40°C to 60°C for the detector box and -40°C to 70°C for the electronics box) and operational temperature limits (-20°C to 40°C for both). ISS-CREAM employs a combination of an active thermal cooling system, survival heaters, and carefully constructed and utilized thermal models in order to ensure all elements of its payload remain within their specified temperature range. Furthermore, careful attention has been paid to fragile components (*e.g.*, scintillator, PMTs, etc.) in order to ensure that mis-matches in the coefficient of thermal expansion between adjacent materials will not cause component damage or breakage. Such considerations are also paramount to the safety of the crew and systems of the ISS.

Staying within the BSD's allotted power budget is also important. Early estimates of the total power required for each detector system drove the selection and design of various instrument power converters, as well as the power dissipation requirements of the BSD's thermal model. Adherence to this original power budget is important in order to ensure that the needs of the final detector system can be adequately met.

While graceful degradation and redundancy has been selectively employed for some portions of the BSD, total redundancy is not assured, since doing so would add prohibitive costs to the project. However, many other risk mitigation techniques have been implemented. In the BSD's electronics design, for example, all components were selected with a 60% de-rating factor in voltage and power in order to minimize loading stresses over the course of a three-year mission. Care was also exercised for circuits which contain high voltage (*i.e.*, greater than 50 V) by ensuring that the space between electrodes at differing potentials was large enough to avoid high-voltage breakdown. Also, all circuit boards will be conformally coated with Arathane 5753 [137], which serves the dual purposes of decreasing the risk of high-voltage failures and inhibiting the development of so-called "tin whiskers", a phenomenon whereby lead-less tin alloys operated in vacuum over long periods develop protruding tendrils which can create short circuits, increased noise pickup, and (for components subjected to high voltage) an increased probability of corona arcing [138].[1]

Finally, the enhanced charged-particle radiation which will be encountered during a three-year orbital mission means that the effects of ionizing radiation on electrical components must also be taken into consideration.[2] Of primary concern to ISS-CREAM are so-called "single event effects" (SEEs). SEEs are of two types. Single-event upsets (SEUs) occur when a charged particle passing through a transistor creates enough ionization to momentarily change its state, resulting in a single-bit error. In digital circuits, the effects of SEU are commonly mitigated by the use of triple-modular redundancy (TMR) checks[3] and, to some extent, offline analysis of the data. Single-event latchups (SELs) occur when a charged particle passing through a transistor

[1]The problem of tin whiskers has been exacerbated by the fact that most electronics are now RoHS [139] compliant, thus making it difficult to procure new, commercially-available ICs which utilize tin-lead alloys.

[2]Reference [140] provides an excellent comprehensive overview of the effects of space radiation on microelectronics.

[3]TMR is a technique most frequently used in FPGAs and ASICs, whereby the data path passes through three identical hardware chains. Assuming only one SEU occurs at a time, a majority voter can be used to choose the most common data value from all three paths, thereby removing the data word with the erroneously flipped bit.

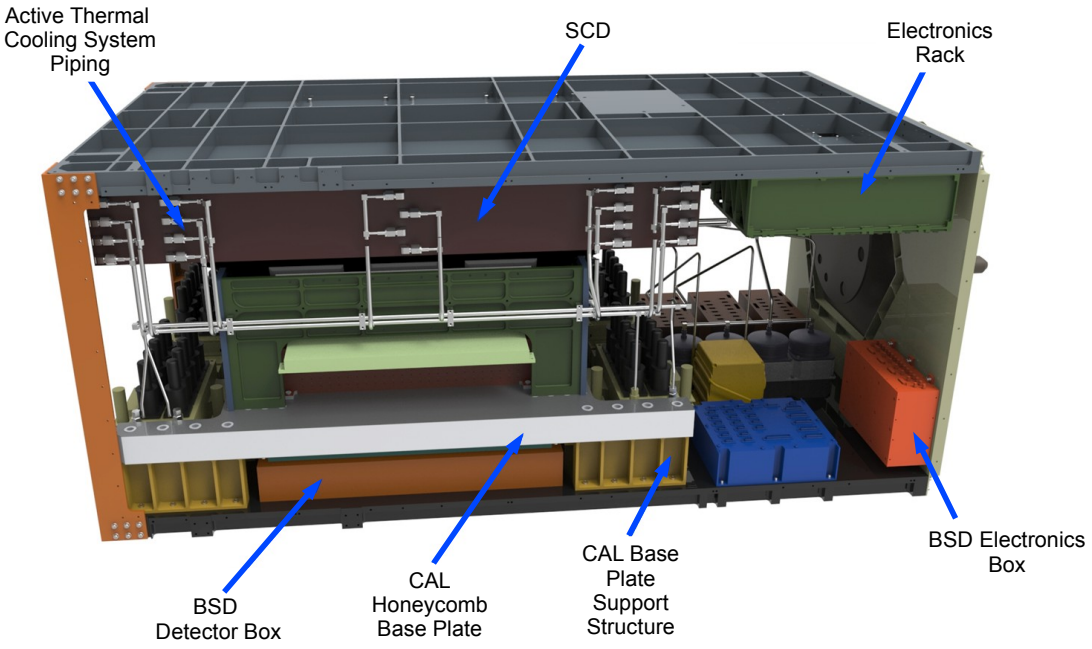

Figure 7.1. CAD Drawing of the ISS-CREAM instrument, depicting the placement of the BSD detector box and BSD electronics box in the overall geometry of ISS-CREAM.

creates enough ionization to cause it to enter a long-term, high-current state. In the case of SELs, normal operation can only be restored by power cycling the latched device. Because commercially available discrete FETs (especially high-voltage or high-power MOSFETs) tend to be much more susceptible to destruction via SEL than devices based on bipolar-junction transistors (BJTs), the BSD utilizes discrete BJT-based circuits whenever practical. For complex ICs (*e.g.*, DACs, ADCs, microcontrollers, FPGAs, operational amplifiers, etc.) ISS-CREAM dictates that each part type must have an SEL test data set which demonstrates non-destructive behavior in the worst-case radiation environment which might be encountered during a three-year mission. Any devices with test data which indicate the occurrence of infrequent, non-destructive SEL must be powered by an automatic shut-off protection circuit, capable of power-cycling the device when it detects an over-current 140% higher than that drawn during normal operation. In the BSD, two such components have been identified as requiring SEL reset circuits—the FX2LP USB microcontroller [122] and the AD7663 ADC [141].

7.2 BSD Detector Box

Figure 7.2 shows a CAD drawing of the BSD detector box (left) and the contents of one corner of the box (right). The main body of the detector box (orange) is machined from a single block of 6061-T6 aluminum, so as to provide enhanced mechanical integrity and a contiguous electrical

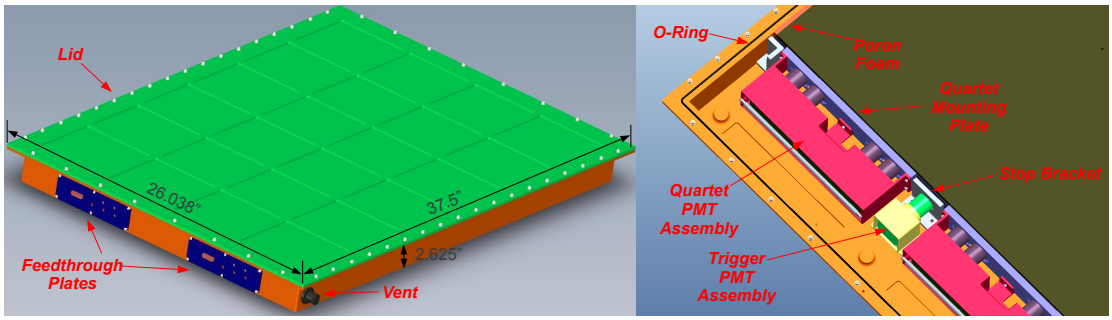

Figure 7.2. Left: a CAD drawing of the BSD detector enclosure. Right: one corner of the BSD detector box showing a quartet PMT assembly and a trigger PMT assembly.

shield. The lid (green) is machined from a single aluminum plate, with pockets selectively hewn out in order to minimize the detector's weight, while still maintaining the lid's structural rigidity. Two opaque, acrylic plates[4] (blue) located on both instrumented sides of the detector box provide feedthroughs for SMA and D-subminiature (DB) 15-pin connectors, which carry PMT anode signals, control signals, housekeeping signals and power into and out of the detector box. The BSD detector box's aluminum lid and body are both anodized in order to allow radiative dissipation of heat. The detector box is conductively coupled to ISS-CREAM's base plate, and closely follows its temperature.

Inside the BSD detector box, the boronated scintillator is viewed by PMT assemblies on two of its sides. The same 60 cm $\times$ 60 cm $\times$ 3.8 cm block of boron-loaded scintillator which was calibrated in the CERN beam test is used in the flight BSD. Poron foam of 0.5 inch thickness sandwiches the scintillator from above, below, and on two of its un-instrumented sides. Poron foam is used because it is compliant enough to allow the scintillator to be installed in the box, while still stiff enough to hold it rigidly, once installed. Poron foam also provides the benefit of significant dampening of the detector box's natural vibrational modes. An embedded O-ring assures the final detector box will be light tight.

At the center of each instrumented side of the detector box, a BSD Trigger PMT assembly views the scintillator, monitoring it for the start of the calorimeter's shower through a hole drilled in an aluminum stop plate. The stop plate compresses 0.5 inch thick poron foam against the scintillator. Meanwhile, at each of the four corners of the two instrumented sides of the scintillator block, a BSD Quartet PMT assembly measures light production in the late shower. Both styles of PMT assemblies are described next.

[4]The use of these electrically insulating feedthrough plates electrically isolates the BSD from ISS-CREAM's support structure, while also eliminating a secondary electrical return path between the BSD's detector box and the electronics box.

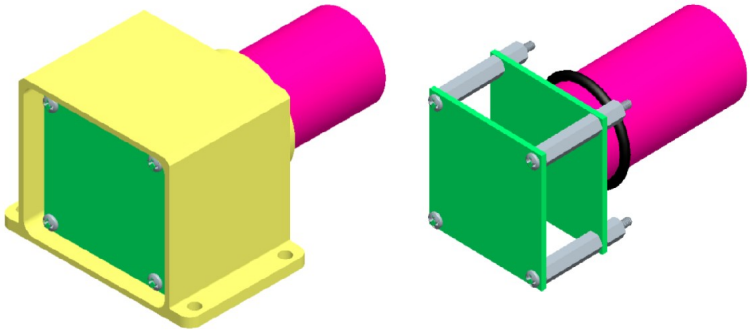

Figure 7.3. CAD drawing of a BSD trigger PMT assembly with (left) and without (right) its aluminum enclosure.

7.2.1 Trigger PMT Assembly

Figure 7.3 shows a CAD drawing of a trigger PMT assembly both with (left) and without (right) its enclosure. Two circuit boards (green) stack together, separated by four 0.5 inch-long aluminum standoffs (gray). The R1924A PMT (pink) fits in a socketed connection on the top board. An aluminum enclosure (yellow) bolts directly to the detector box floor.[5] The aluminum enclosure (yellow) provides shielding and mechanical stability for the PMT assembly.

Figure 7.4 shows the schematic for the trigger PMT's base circuit boards. The division of elements between the bottom and top boards in the stack is denoted in the boxes. The trigger PMT base receives +12 V power and a high-voltage analog control level (***CONTROL***) from the BSD electronics box and sends a housekeeping high-voltage analog monitor level (***MONITOR***) and the PMT's anode signal (***ANODE OUT***) to it. Resistor R23 and capacitor C17 filter high-frequency noise from the incoming control line, while Schottky diode pair U6 protects the circuit from over-voltage. Component U3, an Analog Devices OP97 high-precision operational amplifier [142], regulates the output of an EMCO QH15-12S 1.25 W proportional high-voltage supply [143] via a feedback loop, with a high-voltage-to-control ratio of 400:1. This regulation circuit has been tested and found to be stable at a level better than 0.1% for temperatures ranging from -10°C to 40°C. Component U9 buffers the high voltage monitor line, and has a high-voltage-to-monitor ratio of 1000:1. The overall ripple of the resulting regulated high-voltage is less than 0.01%, and its coupling onto the PMT's output line is imperceptible at the level of sensitivity of the BSD's readout electronics.

High voltage is passed to the top board via a Reynolds 167-2896 high-voltage, vacuum-rated cable [114]. The top board implements a standard high voltage divider, with 1 nF capacitors placed in parallel with the resistors in the last stage of the chain in order to increase the linearity

[5] While the trigger PMTs do view the scintillator through a roughly 0.5 inch air gap, the resulting loss of light is acceptable, given the large number of photons generated in the BSD by the charged particles in the calorimeter's early shower.

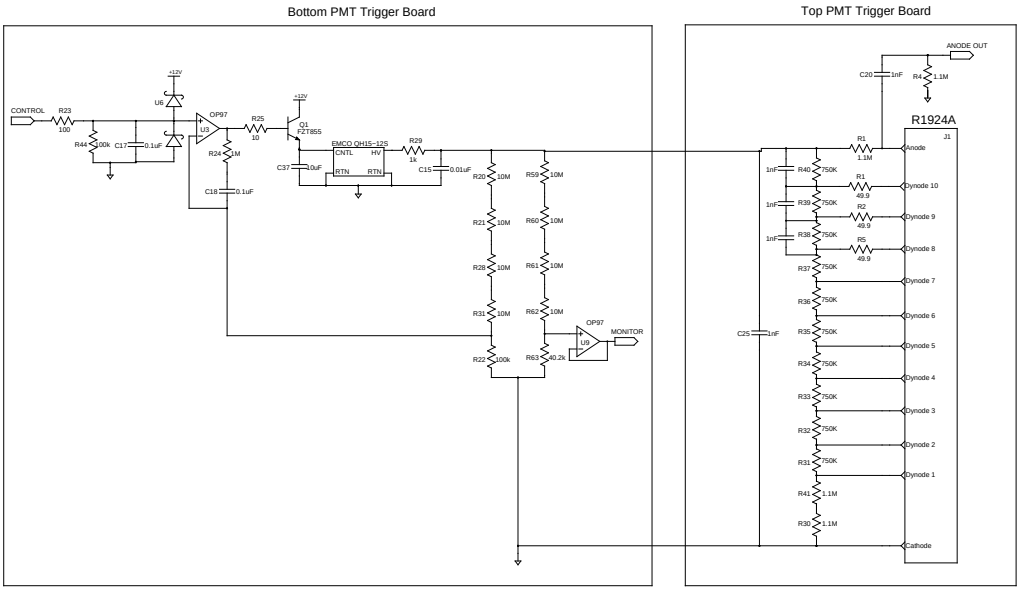

Figure 7.4. Schematic for the trigger PMT base design.

of the PMT's response to large light levels. The PMT's anode signal is output through high-voltage blocking capacitor C20. Each component's power, voltage, and temperature ratings were selected with worst-case criteria in mind.

The gain curve of the R1924A PMT was characterized by measuring the single photoelectron spectrum at a variety of high voltage values. The left side of Figure 7.5 shows the resulting gain curve. The linearity in the response of the R1924A was also explored by interposing Kodak wratten neutral density filters [144] between an LED and a PMT. The right side of Figure 7.5 shows the resulting linearity curve. Non-linearity is apparent above 6000 PE at a high voltage setting of 800 V. Unfortunately, the early shower signals expected to be seen in flight will range as high as 10^5 PE, and so, would exhibit significant saturation, and thus, poor threshold adjustability if no additional considerations were incorporated.

Two options are currently under investigation in order to mitigate the effects of this signal-size mis-match. One option is to have the PMTs view the scintillator through a neutral density filter which attenuates the number of photons seen by the PMT by roughly one to two orders of magnitude, thereby shifting the signal size into a range commensurate with the dynamic range of the current trigger PMT design. Another option is to implement a so-called "tapered base" design, whereby the values of the resistive divider circuit shown in Figure 7.4 are modified in order to enhance the PMT's dynamic range. The experiences of BSD collaborators at NASA's Goddard Space Flight Center on the super-TIGER mission suggest that, with the proper selection of base resistors, signal sizes as large as 2×10^5 PE can be measured linearly [145]. Both possibilities are

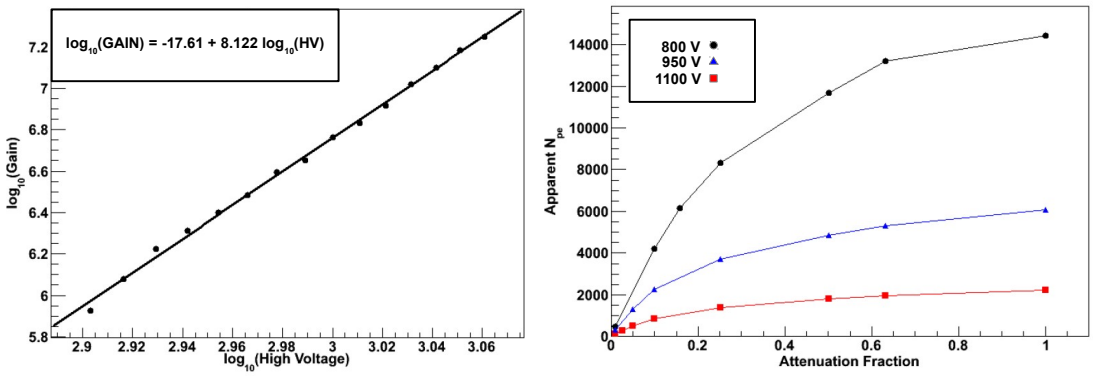

Figure 7.5. Gain (left) and linearity (right) characteristics for the trigger PMT design.

being actively investigated and neither would represent a significant change to the engineering aspects of the BSD.

7.2.2 Quartet PMT Assembly

The left side of Figure 7.6 shows a CAD drawing of a quartet PMT assembly, while the right side shows the prototype version of the base circuit boards and PMTs. A single quartet PMT assembly is comprised of four R1924A PMTs which share a common set of high-voltage supplies and dynode gating circuits. This sharing scheme was implemented in order to minimize the BSD's power consumption. The quartet assembly's aluminum enclosure (fuchsia) bolts directly to an acrylic mounting plate (magenta), which is glued to the scintillator block. Optical coupling of the PMTs to the scintillator block is accomplished via the application of Nusil CV4-2500 RTV [146]. By securing the PMTs directly to the scintillator rather than to the detector box frame, the risk of degrading the optical interface between of the PMTs and the scintillator block via vibrational stresses or differential thermal expansion and contraction is significantly reduced. At the back of the assembly, an aluminum tie-down bar (white) allows management and strain relief of the assembly's cables. Mechanical stability is added to the quartet assemblies by Samtec stackable headers and strategically placed aluminum standoffs. Both quartet boards are fabricated with a 0.125 inch thickness, which allows sufficient resistance to vibrational forces in order to protect the board's components.

Figure 7.7 shows the electrical design for the quartet base circuits. The bottom board generates the main high voltage (1000 V typically) and the high voltage for dynodes 1 and 2 (232 V and 315 V typically) via regulation circuits with a topology identical to that shown in the trigger PMT schematic of Figure 7.4. These high voltage regulation circuits have a high-voltage to control ratio and high-voltage to monitor ratio of 1000:1. The bottom quartet board also receives the DON signal from the readout electronics box. A +12 V to 0 V transition on the DON line initiates switching of the high-voltages applied to dynodes 1 and 2 from -12 V up to their full potentials in roughly 200 ns. The long-tailed pair formed by Q7 and Q8 level shifts DON so that

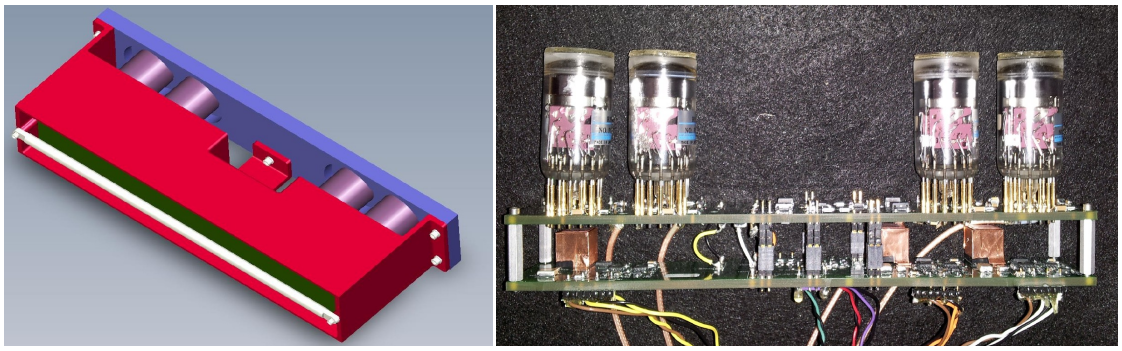

Figure 7.6. Left: a CAD drawing of the BSD quartet PMT assembly. Right: a prototype version of the electronics for this assembly.

it can be used to turn off the lower NPN transistors Q1 and Q3 of the high-voltage totem pole. Meanwhile, the upper PNP transistors Q10 and Q13 of the high-voltage totem pole are turned on by the pulse generated by a buffered DON through high-voltage blocking capacitors C2 and C4.

On the top board, the high voltage bias for dynodes 3 through 10 is generated by a standard resistive divider. Capacitors of value 1000 pF are soldered directly on top of each resistor in the high-voltage divider chain in order to provide a low-impedance path to ground for transients generated by the switched high voltage to dynodes 1 and 2. Board layout was performed carefully in order to minimize capacitive coupling of such transients onto the anode line of the base.

A prototype version of this base design (shown on the right side of Figure 7.6) has been tested extensively. The anode signal output from the PMT has been found to be free of the effects of the switching transient caused by gating the high voltage to dynodes 1 and 2 starting 400 ns after switching, which is sufficient for the requirements of flight. The prototype was found to be reliable over the course of a two month test under vacuum at NASA's Goddard Space Flight Center. Because two quartets view the scintillator from each instrumented side of the box, a total of 16 gated high-voltage PMTs will view the late shower, which leads to an expected 1.9% collection efficiency, or 11 PE per neutron capture in the flight.

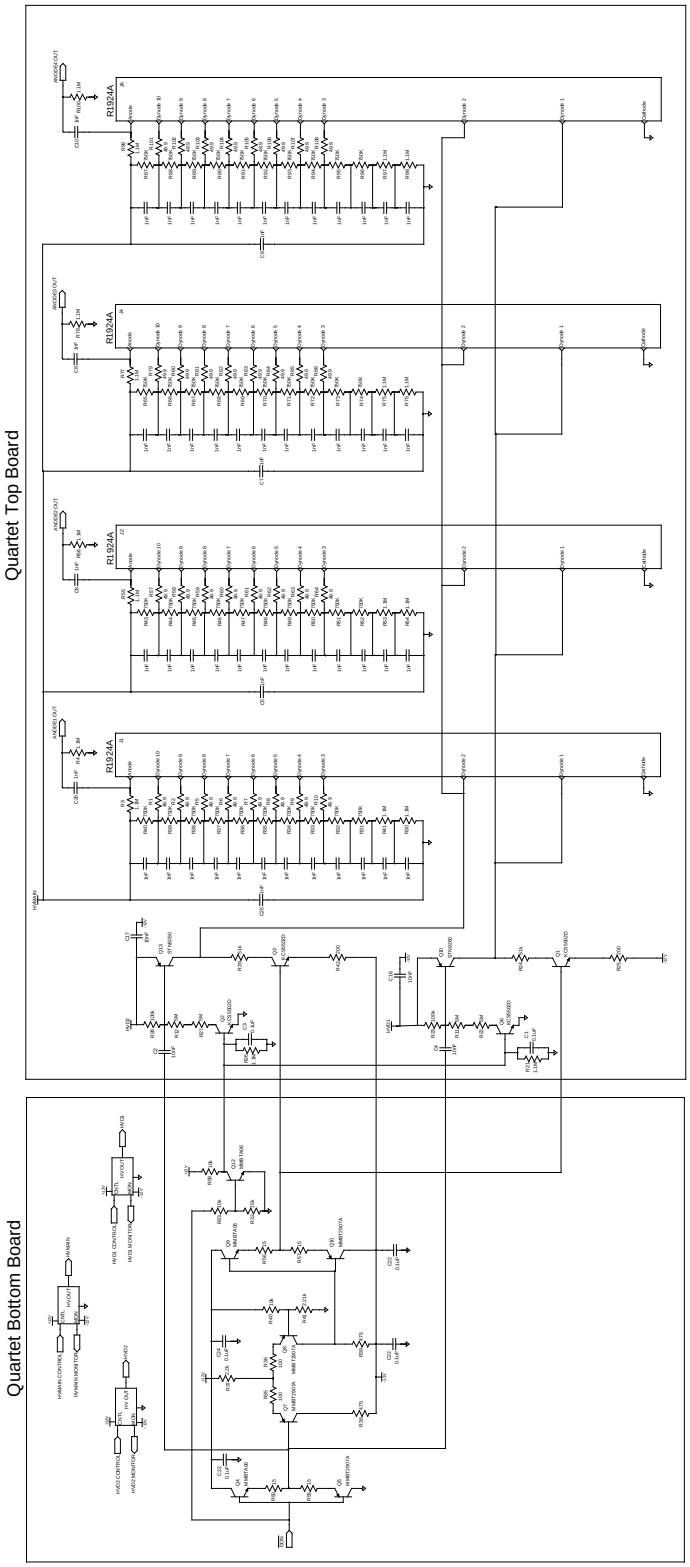

Figure 7.7. Schematic for the quartet PMT base design.

7.3 BSD Electronics Box

Figure 7.8 shows a CAD drawing of the BSD readout box with (left) and without (right) its side walls. Callouts have been added in order to highlight important aspects of the design. On the top of the box, the BSD receives ±5 V and +12V from the calorimeter power module over a DB-9 connector. It sends housekeeping signals to the ISS-CREAM common electronics system over a DB-37 connector. All communication between the BSD and the SFC is via a pair of USB 2.0 links, with the active SFC selecting the appropriate USB link. SMA connectors on the top of the box allow calibration pulses to be sent to LEDs inside the BSD detector box. On one side of the box, SMA ports bring in the anode signals from the detector box, while DB-15 connectors carry power, high-voltage control signals, and high-voltage monitor signals to and from the BSD's PMT assemblies in the detector box.

All D-subminiature connectors are panel-mount style, with flying leads terminating to the circuit board. For these connectors, the flying-lead configuration is preferred since the heavy cables (typically ten or more AWG-24 wires bundled together) which attach to them induce external stresses which are best carried by the walls of the enclosure rather than the solder joints on the circuit board. All SMA connectors are right-angle, board-mount connectors, which is acceptable given the much lighter RG-196 cables which attach to them. Thermal analysis of the BSD electronics box shows that its temperature follows closely to that of the ISS-CREAM sidewall to which it attaches.

The stack of five boards inside the BSD detector box is called out on the right side of Figure 7.8. From top to bottom, these are the power and housekeeping (PHK) board, the control board, and the three front-end electronics (FEE) boards. Boards inside the electronics box connect to each other via Samtec stackable headers which, in addition to strategically placed standoffs, add structural rigidity to these boards. Each circuit board is 0.125 inch thick, with cutouts placed around its periphery in order to allow the flying leads of the panel-mount connectors to pass easily to their destination board. The design and functionality encompassed by each board is presented below.

7.3.1 Control Board

Figure 7.9 shows a block diagram of the BSD control board. The A3P1000 FPGA [123] (shown as the black square at the center of the diagram) is the BSD's single control block which manages *all* communication and control aspects of the system. Power for the FPGA is derived from +5 V received from the power and housekeeping board via Maxim MAX1792 +3.3 V and +1.5 V low-dropout (LDO) linear regulators [147]. The ***POR*** circuit (light blue) provides a 50 ms power-on reset derived from the +1.5 V regulator. The FPGA is programmed via a standard JTAG interface and uses a Statek radiation-hardened CX03M 50 MHz oscillator [148] as its system clock. The ***Spare I/O Header*** brings out unused signal pins from the FPGA. Various drive circuits (yellow blocks) buffer FPGA signals and allow the FPGA to engage in cold sparing with un-powered FEE boards.

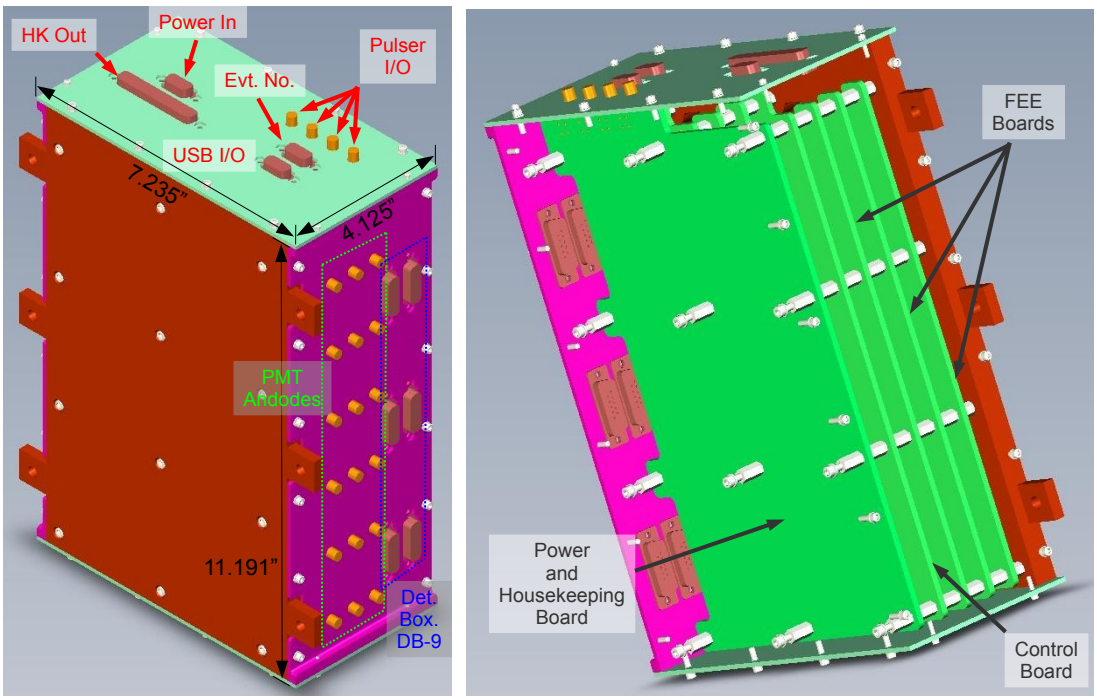

Figure 7.8. The BSD electronics enclosure with (left) and without (right) its side walls.

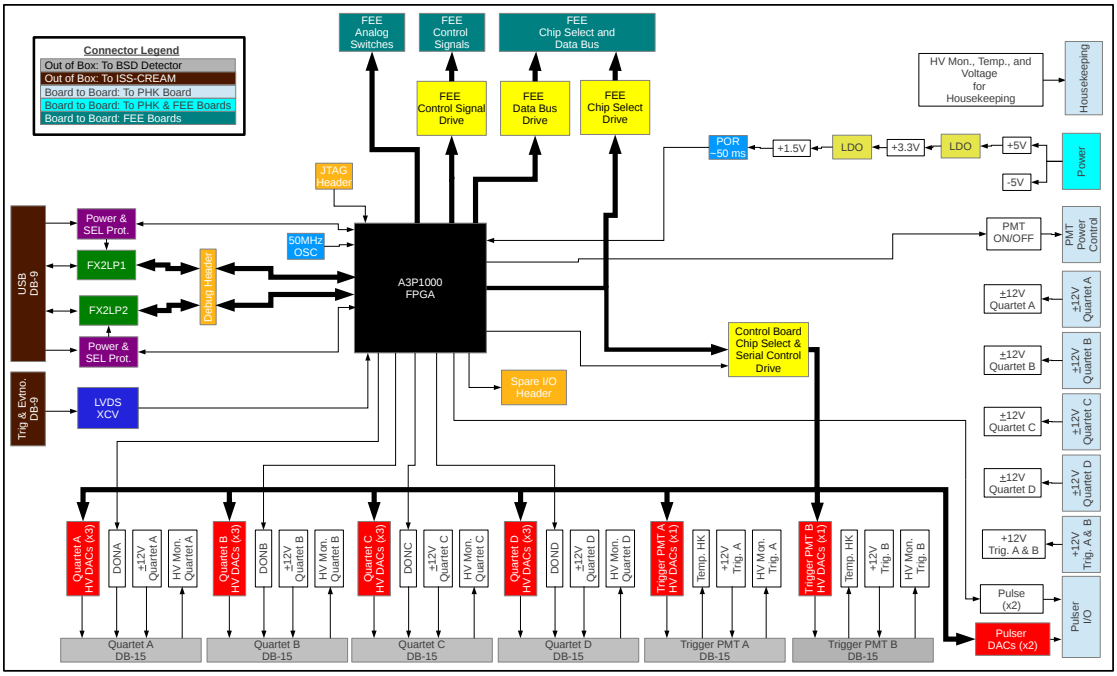

Figure 7.9. Block diagram of the BSD control board.

The control board has two connectors which interface to the ISS-CREAM payload. The ***Trig & Evtno DB-9*** connector (brown) receives an ISS-CREAM instrument event trigger along with a serialized 32-bit event number, identical to that used in the previous balloon flights of CREAM. An SN65LVDT390 LVDS receiver [149] (dark blue) is used to convert the signals carried through this connector to +3.3 V logic levels. The ***USB DB-9*** connector (brown) carries USB 2.0 packets between the BSD and the ISS-CREAM SFCs. The BSD implements its USB functionality via FX2LP USB 2.0 capable microcontrollers [122].[6] In order to reduce the BSD's power consumption, only one FX2LP is powered up at any given time. The active microcontroller is selected externally via a binary control signal propagated through the USB DB-9 connector. Because the FX2LP was found to experience occasional non-destructive latchup in radiation environments, ***Power & SEL Prot*** circuits (purple) monitor the current draw from each FX2LP and initiate an automatic power cycle when an over-current condition is detected. Strategic interface signals between the FPGA and FX2LPs are brought out on a debugging header, shown as the orange ***Debug Header*** block in the figure.

The control board's interface to the three FEE boards is shown as the turquoise blocks at the top of the figure. The FPGA sets the start and stop times of the gated integrators on each FEE board via the ***FEE Analog Switches*** interface. The control board's FPGA receives trigger and status flags from each FEE board and sets the power state of each board via the ***FEE Control Signals*** interface. Finally, it reads out the FEE board's ADCs and DACs via the ***FEE Chip Select and Data Bus*** interface.

The control board's interface to the detector box is primarily through the six DB-15 connectors (gray) shown at the bottom of the figure, each of which carries power, control, and housekeeping signals to their respective quartet or trigger PMT assembly. The FPGA controls the settings of Maxim 5353 DACs [150] which provide the high-voltage control level for the PMT assemblies. The FPGA also fires the DON gating signal for each quartet assembly, which turns on the high voltage applied to dynodes 1 and 2 in order to allow measurement of the calorimeter's late shower. The control board provides direct feedthroughs for ± 12 V power rails and various analog housekeeping signals which flow between the detector box and the power and housekeeping board.

The FPGA provides the power and housekeeping board with logic signals which control the power state of all PMT assemblies, shown as the blue-gray ***PMT Power Control*** block on the right side of the diagram. Finally, the FPGA controls two DACs which set the amplitude of a calibration pulser circuit on the power and housekeeping board. The voltage outputs of these DACs are sent along with logic signals whose width specify the duration of each calibration pulse to the power and housekeeping board over the ***Pulser I/O*** connector.

The control board allows many of the BSD's parameters to be adjusted in flight. Adjustability of the control voltage settings for each PMT assembly, and of the time delay and width of each PMT assembly's DON and FEE gated integrator start and stop pulses, allow optimization of the measurement of late-shower signals. While the values of these parameters will likely be

[6] This combination of FX2LP microcontroller and A3P1000 FPGA is similar to that used by the BACCUS TCD, as described in Chapter 5.

selected during pre-flight tuning procedures, the flexibility afforded by their commandability is convenient. It was decided that the power state of each FEE board and PMT assembly should be set independently by the BSD's FPGA, since doing so would allow any malfunctioning elements of the BSD to be powered off while other elements continued working, thus allowing graceful degradation of the system. A "power-up safe" strategy was implemented so that, if a BSD component failure causes it to draw a current high-enough to activate the ISS-CREAM power system's automatic shut-off of BSD power, this fault condition is automatically removed after power cycling.

7.3.2 Power and Housekeeping Board

Figure 7.10 shows a block diagram of the BSD's power and housekeeping board. ISS-CREAM provides regulated ±5 V and +12 V to the BSD over the ***ISSCREAM Power In DB-9*** connector (brown). A bypass capacitance of 0.1 mF to ground is connected to each incoming power rail (light green). The ±5 V and +12 V rails are distributed to all boards in the BSD electronics stack via Samtec board-to-board power connectors (aqua). The +12 V line is also used in a custom designed DC-DC converter to generate an additional -12 V rail for use in the quartet assemblies. This power converter design is based on Pico Electronics 31141 ultra-miniature DC-DC transformer converter [151]. The resulting ±12 V is passed through an ON/OFF Switch (lavender) to the BSD control board, which, as was discussed in the previous section, passes these voltages directly to the detector box.

The BSD's housekeeping signals are passed to the ISS-CREAM housekeeping system via the ***BSD Housekeeping Out DB-37*** connector. Two external pulser signals from the ISS-CREAM calibration system (***ISS-CREAM Calibration SMA1*** and ***ISS-CREAM Calibration SMA2***) are summed with the internally generated calibration pulses (whose amplitude and timing are set by the control board via the signals on the ***Pulser I/O*** header) and sent to the BSD detector box's ***BSD Calibration LED1*** and ***BSD Calibration LED2***. The possibility of using multiple pulsers with the BSD allows significant flexibility for liveness testing and system calibration during both ground operations and flight.

7.3.3 FEE Board

The BSD utilizes three FEE boards which have identical layouts, but are differentiated on the basis of selection resistors. Figure 7.11 shows a block diagram of the electronics on a single FEE board. As was previously described, the power state, event timing, DAC settings, and readout of all FEE boards are managed by the control board over the ***FEE Control Signals*** interface, the ***FEE Analog Switch*** interface, and the ***FEE Chip Select and Data Bus*** interface, while its ±5 V power rails are received from the power and housekeeping board. Each FEE board contains 6 channels, numbered 0 through 5, with channel 5 also including an optional split to a one-channel discriminator circuit, used by the control board to form the BSD's event trigger. Each channel contains individual power filtering and over-current protection circuits, which, as

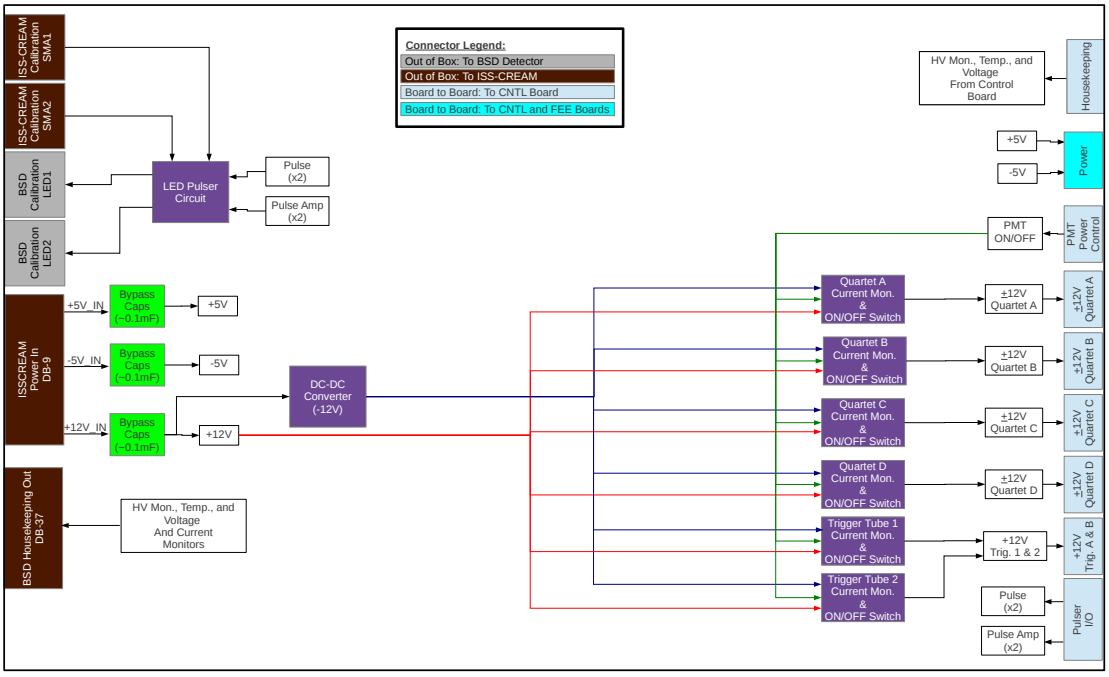

Figure 7.10. Block diagram of the BSD power and housekeeping board.

was mentioned previously, are necessary due to the occasional non-destructive SEL experienced by its AD7663 ADCs.

Figure 7.12 shows a simplified schematic for a single readout channel. The PMT's input signal is delayed through component U1, a Data Delay Devices 50 Ω, 200 ns lumped-delay element [152],[7] which allows the BSD to form its trigger well in advance of receiving the PMT's charge pulse.[8] Components RH1 and RL1 create a 4:1 charge split between the high-gain and low-gain branches of the channel. Note that the parallel resistance of RH1 and RL1 is 50 Ω, thus allowing for cable termination via the "virtual ground" enforced by Analog Devices AD8052 operational amplifiers UH-A and UL-A [153]. UH-A and UL-A perform charge integration through gain capacitors CH1 and CL1. The beginning of the charge integration window is defined by the opening of switches SH1 and SL1. The outputs of UH-A and UL-A are tracked by capacitors CH2 and CL2 and held via the opening of switches SH2 and SL2, thus defining the end of the charge integration window. All switches SH1, SL1, SH2, and SL2 are Maxim MAX4583 Low-Voltage, CMOS analog switches [154], whose opening and closing times relative to the start of the shower are set via commands sent to the control board, as previously described. The voltage of capacitors CH2 and CL2 is amplified and summed with a programmable baseline offset through

[7] While this delay line has only a 17.5 MHz bandwidth, it is composed of only passive reactive elements. Thus, total integrated charge is roughly constant for integration windows of order 1 μs or more.

[8] The 400 ns delay between the early component of the calorimeter's shower and the start of the neutron capture window is plenty of time for the BSD to form its trigger. Thus, the additional 200 ns delay is unnecessary for measuring these signals. However, non-showering cosmic rays provide an excellent calibration signal for the BSD in flight, and the 200 ns delay element is included in order to allow triggering on these calibration events.

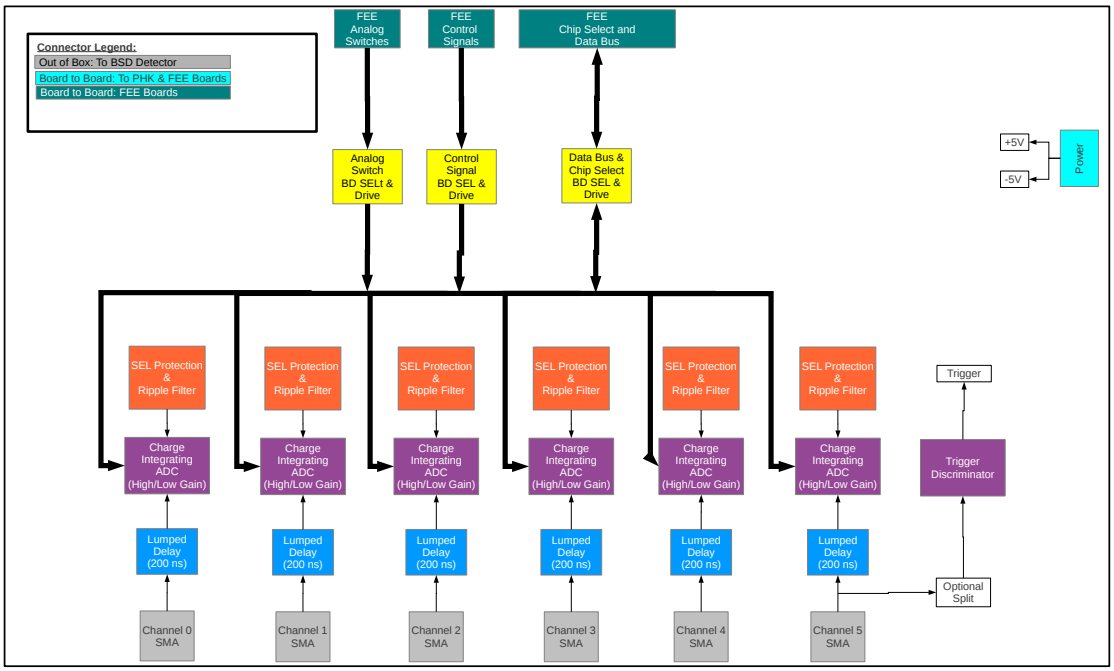

Figure 7.11. Block diagram of the components in the BSD's FEE board.

operational amplifiers UH-B and UL-B. Digitization is performed via an Analog Devices AD7663 unit [141], a 16-bit ADC, operated with a 0 V to 2.5 V input range. Analysis of both the high and low gain branches of the single readout channel shown in the figure yields conversion factors of 0.05 pC/count and 1.4 pC/count, respectively. Because the R1924A PMTs output roughly 1 pC/PE when operated at their maximum 1200 V high voltage, the low-gain branch allows the possibility of resolving signals as small as a single photoelectron, while the high-gain branch allows un-saturated measurement of signals above 8×10^4 PE.[9]

It is worth noting that, while the AD8052 has an offset voltage (1.8 mV typical, 25 mV maximum) and bias current (1.4 μA typical, 3.5 μA maximum) which are somewhat higher than those desired for an integrator, its use was mandatory since it was the only operational amplifier on ISS-CREAM's flight-approved parts list with a slewrate large enough for use in the BSD's front-end electronics. Left un-checked, such large DC offsets can create significant baseline shifts which vary from channel-to-channel and drift with temperature and time. Thus, several compensation techniques have been employed in order minimize this baseline drift in flight. First, the specific component values shown in Figure 7.12 have been selected in order to allow cancellation of the effects of offset voltage and bias current in a well matched set of amplifiers. An effort is currently underway to select a set of AD8052 amplifiers from a larger

[9]This is the late-time signal expected to be seen by a single PMT from a 100 TeV proton shower, as extrapolated from Table 6.2. While the upper range of signals measurable in flight can be increased by roughly two orders of magnitude by decreasing the PMT's high voltage, this will likely be unnecessary. In any case, this provides flexibility to deal with any foreseeable in-flight conditions, such as orbital periods of transit through the South Atlantic Anomaly.

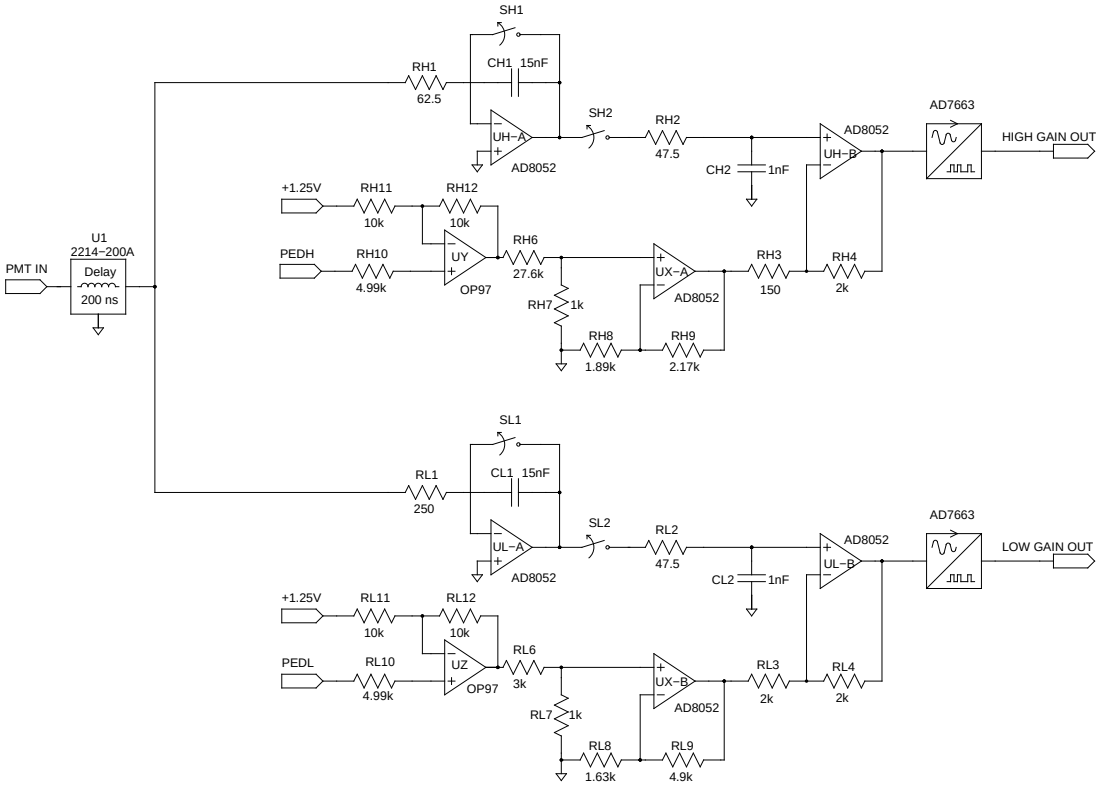

Figure 7.12. Simplified schematic for a single channel of the FEE board.

batch which have offset voltages and bias currents at or below the datasheet's typical value, and to match the characteristics of the amplifiers used in each channel at the 10% level. Furthermore, both the high and low-gain branches of every channel are equipped with an independent DAC, whose output is shown as ***PEDH*** and ***PEDL*** in Figure 7.12, thereby allowing further baseline matching of the channels. Finally, during flight, baseline measurements will be taken at 5 minute intervals in order to allow the effects of temperature and time-dependent baseline drifts to be corrected in offline analysis.

A prototype version of a single branch of the FEE board was built and characterized before finalizing the circuit topology to be used in flight. Its characteristics are shown in Figure 7.13, where the linearity (left) and charge resolution (right) of a single channel (CH3) were measured using a reference charge source. While the specific gain settings of the circuit shown here are somewhat different from those planned for flight, the full-range linearity and asymptotic resolution near 0.02% seen in the figure are good predictors of the characteristics of the final flight design.

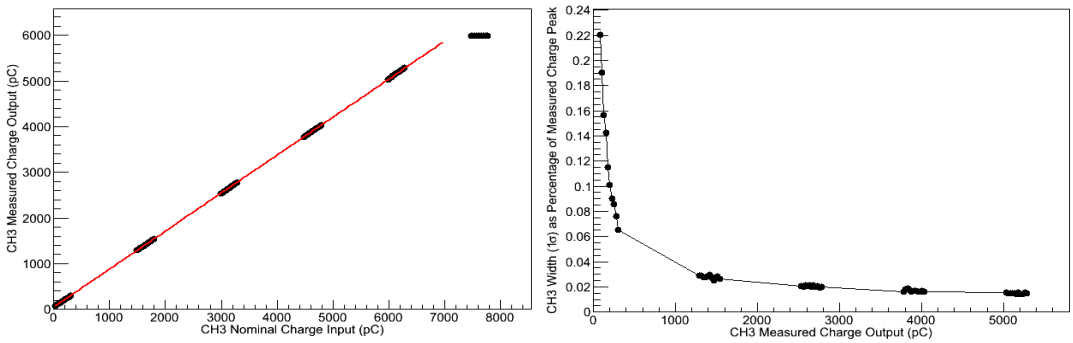

Figure 7.13. Characteristics of one branch of a prototype FEE channel. Left: the linearity characteristics of channel CH3 are plotted as a function of charge input. The charge values obtained for the abscissa are derived from a gain analysis of the circuit. Right: the charge resolution characteristics of CH3 plotted as a function of charge input.

7.4 Conclusion

All major engineering aspects of the BSD which will be flown with ISS-CREAM have been decided, and the design presented in this chapter has successfully passed all of NASA's safety and critical design reviews. The estimated mass and power consumption of the BSD's detector box (40.50 kg, 12.8 W) and electronics box (8.28 kg, 14.7 W) are within the limits for the detector. Current thermal models predict that the temperature limits seen by the BSD will fall well within its survival and operational range. The detector system is currently under construction and is scheduled to be delivered for integration with the payload in January 2014.

Chapter 8

Conclusion

Various aspects of the CREAM project have been presented, including its scientific motivation and its relevance to the open questions of cosmic-ray physics (Chapter 1), its instrument details and measurement techniques (Chapter 2), and its science results and upcoming BACCUS and ISS-CREAM missions (Chapter 3). The details of the CREAM TCD were presented (Chapter 4), and the design and validation of a new set of TCD readout electronics for CREAM's BACCUS mission were described in detail (Chapter 5). The design, construction, and characterization of a prototype version of the ISS-CREAM BSD were presented, and its hadronic rejection power was shown to be greater than 100 for values of electron acceptance efficiency up to 80%. Significant attention has been given to the effort to reconcile the prototype system's measured signal distributions with predictions of its performance by a GEANT4 monte carlo simulation, and a question has been raised as to the potential contribution of a hypothetical slow-component of scintillation. While the final resolution of these questions will require further effort, the BSD's ability to contribute to the overall hadronic rejection power required for ISS-CREAM's electron-spectrum measurement is evident (Chapter 6). The design of the flight BSD has also been reviewed. To date, this design has passed all of its technical reviews and is currently under construction (Chapter 7).

8.1 Personal Research Statement

My involvement with the CREAM project began while preparations for the CREAM III flight were still underway. I worked with the TCD groups at Penn State University and Ohio State University to install and verify the TCD on the CREAM upper structure at the University of Maryland. In addition, I fabricated and verified many spare components for CREAM III, including various readout electronics boards and PMT assemblies. I also served as an instrument operator at the University of Maryland's Science Operations Center (SOC) during the flight.

I served as the TCD instrument expert for the CREAM IV and V flights. This role included fabricating and wrapping new scintillator paddle and light guide assemblies, building and testing new and refurbished PMT assemblies and TCD electronics, integrating the TCD into the CREAM payload, and supporting and monitoring the performance of the TCD during flight. In addition, I spent November–December of 2008 at McMurdo Station, Antarctica, where my activities included performing upgrades on the TCD's CDAQ software, monitoring instrument performance during pre-flight operations, and tuning the TCD's parameters during the high bandwidth, line-of-sight opportunity which occurs during the first few hours of flight. I again served as an instrument operator at the SOC during both CREAM IV and V flights.

I performed all design work related to the new BACCUS TCD readout electronics. In terms of hardware design, this includes the use of Mentor Graphics's *PADS Logic* suite to design and draft the schematics and PCB layouts for the new boards discussed in Section 5.3. I also defined all the command and event protocols discussed in Section 5.4.1, developed the CDAQ and TGACS software discussed in Section 5.4.2, and designed the FX2LP firmware and FPGA logic discussed in Sections 5.4.3 through 5.4.5.

I led the hands-on effort to refurbish and repopulate the supply of BACCUS TCD hardware components, including manufacturing the new components listed in Table 5.12, and overseeing all stages of vacuum testing, thermal cycling, and total system verification.

I acted as the on-site TCD instrument expert during the January-March 2012 integration of the TCD into the BACCUS payload, working on everything from mechanical installation to final system checkout and verification. Since that time, I have provided a few small software/firmware patches and served as a remote consultant for the BACCUS instrument team.

I worked as part of the BSD's science team to test the prototype BSD system at Goddard Space Flight Center's Pulsed Neutron Facility and in CERN's H2 beam line. While this was a multi-faceted endeavor, I was especially involved in the efforts to inspect, wrap, and install the EJ-254 scintillator in the prototype BSD's detector box, characterize the prototype BSD detector system's light response and PMT gain measurements, work out the specifics of the prototype BSD's NIM-based trigger/timing and CAMAC-based acquisition system, and support the detector during the beam test. I performed all analyses related to characterizing the BSD's CERN performance and hadronic rejection power, as presented in Chapter 6. I've worked closely with Professor Nutter from Northern Kentucky University in reconciling these results with the predictions of the ISS-CREAM instrument simulation.

I led the effort to design and characterize ISS-CREAM's BSD PMT assemblies. This includes the design, drafting, and testing of both the prototype gated-dynode assemblies used at CERN and the quartet and trigger PMT assemblies to be used in flight. I also worked closely with the BSD's electronics design lead, Dr. John Mitchell of NASA Goddard Space Flight Center (GSFC), on the design and characterization of the BSD's readout electronics.

In addition to my work on the CREAM project, I have also worked on the Cosmic Ray Electron Synchrotron Telescope, a balloon-borne instrument which searches for cosmic-ray electrons with energies >2 TeV via the X-ray synchrotron radiation signature detected in a 32 x 32 array

of barium fluoride crystals as these electrons traverse earth's magnetic field. Specifically, I contributed to the design and construction of CREST's novel charged-particle veto system, whereby wavelength-shifting optical fibers are embedded into ∼2.6 m long scintillator paddles in order to capture scintillation light, piping it to a fiber-optic light guide for collection in a PMT. This included working with CREST's veto system group to develop the procedure for gluing these fibers into scintillator paddles, cleaning and wrapping the resulting paddles, preparing the surfaces for optical coupling, and characterizing the light output from the final paddle assemblies. Also, I worked to support a 2009 test flight of the CREST instrument out of Fort Sumner, New Mexico, including assembling, calibrating, and deploying an array of temperature and pressure sensors and working as a member of the CREST on-site pre-launch team.

Bibliography

[1] Hess, V. F. (1912). "Observations of the Penetrating Radiation on Seven Balloon Flights." *Physikalische Zeitschrift*, **13**, pp. 1804–1091.

[2] Rossi, B. (1964). *Cosmic Rays*. McGraw-Hill, Inc., New York, New York.

[3] Millikan, R. A. and Cameron, G. H. (1926). "High Frequency Rays of Cosmic Origin III. Measurements in Snow-Fed Lakes at High Altitudes." *Phys. Rev.*, **28**, pp. 851–868.

[4] Anderson, C. D. (1933). "The Positive Electron." *Phys. Rev.*, **43**, pp. 491–494.

[5] Simpson, J. A. (1983). "Elemental and Isotopic Composition of the Galactic Cosmic Rays." *Annual Review of Nuclear and Particle Science*, **33**(1), pp. 323–382.

[6] Smith, M. W. E., *et al.* (2013). "The Astrophysical Multimessenger Observatory Network (AMON)." *Astroparticle Physics*, **45**, p. 56.

[7] Cronin, J. W., Gaisser, T. K., and Swordy, S. P. (1997). "Cosmic Rays at the Energy Frontier." *Scientific American*, **276**, pp. 44–49.

[8] Beringer, J., *et al.* (2012). "Review of Particle Physics." *Phys. Rev. D*, **86**, p. 010001.

[9] Beatty, J. J. and Westerhoff, S. (2009). "The Highest-Energy Cosmic Rays." *Annual Review of Nuclear and Particle Science*, **59**, pp. 319–345.

[10] Ichimura, M., *et al.* (1993). "Observation of heavy cosmic-ray primaries over the wide energy range from 100 GeV/particle to 100 TeV/particle: Is the celebrated "knee" actually so prominent?" *Physical Review D*, **48**, pp. 1949–1975.

[11] Takahashi, Y. (1998). "Elemental abundance of high energy cosmic rays." *Nuclear Physics B - Proceedings Supplements*, **60**(3), pp. 83 – 92.

[12] Derbina, V. A., *et al.* (2005). "Cosmic-Ray Spectra and Composition in the Energy Range of 10-1000 TeV per Particle Obtained by the RUNJOB Experiment." *The Astrophysical Journal*, **628**, pp. L41–L44.

[13] Evans, L. (2007). "The Large Hadron Collider." *New Journal of Physics*, **9**(9), p. 335.

[14] Seo, E. S., *et al.* (1991). "Cosmic Ray Proton and Helium Spectra During the 1987 Solar Minimum." In "Proceedings of the 22nd International Cosmic Ray Conference," Dublin, Ireland.

[15] Ave, M., *et al.* (2008). "Composition of Primary Cosmic-Ray Nuclei at High Energies." *The Astrophysical Journal*, **678**(1), p. 262.

[16] d'Enterria, D., *et al.* (2011). "Constraints from the first LHC data on hadronic event generators for ultra-high energy cosmic-ray physics." *Astroparticle Physics*, **35**(2), pp. 98 – 113.

[17] Hillas, A. M. (2005). "Can diffusive shock acceleration in supernova remnants account for high-energy galactic cosmic rays?" *Journal of Physics G: Nuclear and Particle Physics*, **31**(5), p. R95.

[18] Berezinsky, V., Gazizov, A., and Grigorieva, S. (2006). "On astrophysical solution to ultrahigh energy cosmic rays." *Physical Review D*, **74**(4), p. 043005.

[19] Greisen, K. (1966). "End to the Cosmic-Ray Spectrum?" *Phys. Rev. Lett.*, **16**, pp. 748–750.

[20] Zatsepin, G. T. and Kuz'min, V. A. (1966). "Upper Limit of the Spectrum of Cosmic Rays." *Soviet Journal of Experimental and Theoretical Physics Letters*, **4**, p. 78.

[21] Ave, M., *et al.* (2008). "Composition of Primary Cosmic-Ray Nuclei at High Energies." *The Astrophysical Journal*, **678**(1), p. 262.

[22] Strong, A. W., Moskalenko, I. V., and Ptuskin, V. S. (2007). "Cosmic-Ray Propagation and Interactions in the Galaxy." *Annual Review of Nuclear and Particle Science*, **57**, pp. 285–327.

[23] Gaisser, T. K. (1990). *Cosmic Rays and Particle Physics*. Cambridge University Press, Cambridge, Great Britain.

[24] Stanev, T. (1990). *High Energy Cosmic Rays*. Springer-Verlag, Heidelberg, Germany.

[25] Vladimirov, A. E., *et al.* (2011). "GALPROP WebRun: An internet-based service for calculating galactic cosmic ray propagation and associated photon emissions." *Computer Physics Communications*, **182**, pp. 1156–1161.

[26] Ptuskin, V. (2012). "Propagation of galactic cosmic rays." *Astroparticle Physics*, **3940**(0), pp. 44 – 51. ISSN 0927-6505. Cosmic Rays Topical Issue.

[27] Fermi, E. (1949). "On the Origin of the Cosmic Radiation." *Physical Review*, **75**(8), pp. 1169–1174.

[28] Yanasak, N., *et al.* (2001). "Cosmic-ray time scales using radioactive clocks." *Advances in Space Research*, **27**(4), pp. 727 – 736.

[29] Simpson, J. A. and Garcia-Munoz, M. (1988). "Cosmic-Ray Lifetime in the Galaxy: Experimental Results and Models." *Space Science Reviews*, **46**(3), pp. 205–224.

[30] Hillebrandt, W. and Niemeyer, J. C. (2000). "Type IA Supernova Explosion Models." *Annual Review of Astronomy and Astrophysics*, **38**, pp. 191–230.

[31] Janka, H.-T., *et al.* (2007). "Theory of core-collapse supernovae." *Physics Reports*, **442**, pp. 38–74.

[32] Ellison, D. C., *et al.* (2010). "Efficient Cosmic Ray Acceleration, Hydrodynamics, and Self-Consistent Thermal X-Ray Emission Applied to Supernova Remnant RX J1713.7-3946." *The Astrophysical Journal*, **712**, pp. 287–293.

[33] Abdo, A. A., *et al.* (2011). "Observations of the Young Supernova Remnant RX J1713.7-3946 with the Fermi Large Area Telescope." *The Astrophysical Journal*, **734**, p. 28.

[34] Acero, F., *et al.* (2013). "Gamma-ray signatures of cosmic ray acceleration, propagation, and confinement in the era of CTA." *Astroparticle Physics*, **43**, pp. 276–286.

[35] Ginzburg, V. L. and Syrovatskii, S. I. (1964). *The Origin of Cosmic Rays*. Macmillan, New York.

[36] Longair, M. S. (1992). *High Energy Astrophysics: Volume 2*. Cambridge University Press, Cambridge, Great Britain.

[37] Bell, A. R. (1978). "The acceleration of cosmic rays in shock fronts. I." *Monthly Notices of the Royal Astronomical Society*, **182**, pp. 147–156.

[38] Kittel, C. and Kroemer, H. (1980). *Thermal Physics, 2nd Ed.*. W. H. Freeman and Co., New York, New York.

[39] Lucek, S. G. and Bell, A. R. (2000). "Non-linear amplification of a magnetic field driven by cosmic ray streaming." *Monthly Notices of the Royal Astronomical Society*, **314**, pp. 65–74.

[40] Antoni, T., *et al.* (2005). "KASCADE measurements of energy spectra for elemental groups of cosmic rays: Results and open problems." *Astroparticle Physics*, **24**, pp. 1–25.

[41] Biermann, P. L. (1993). "Cosmic rays. 1. The cosmic ray spectrum between 10 GeV and 3×10^6 GeV." *Astronomy and Astrophysics*, **271**, p. 649.

[42] Jokipii, J. R. (1987). "Rate of energy gain and maximum energy in diffusive shock acceleration." *The Astrophysical Journal*, **313**, pp. 842–846.

[43] Binns, W. R., *et al.* (2005). "Cosmic-Ray Neon, Wolf-Rayet Stars, and the Superbubble Origin of Galactic Cosmic Rays." *The Astrophysical Journal*, **634**, pp. 351–364.

[44] Binns, W. R., *et al.* (2007). "OB Associations, Wolf Rayet Stars, and the Origin of Galactic Cosmic Rays." *The American Astronomical Society*, **130**, pp. 439–449.

[45] "BC-400, BC-404, BC-408, BC-412, BC-416 Premium Plastic Scintillators." `http://www.phys.ufl.edu/courses/phy4803L/group_I/muon/bicron_bc400-416.pdf`.

[46] "XP2020 Photomultiplier Datasheet." `http://my.et-enterprises.com/pdf/XP2020.pdf`.

[47] Leo, W. R. (1994). *Techniques for Nuclear and Particle Physics Experiments: A How-to Approach*. Springer-Verlag, Heidelberg, 2nd edition.

[48] Sternheimer, R., Berger, M., and Seltzer, S. (1984). "Density effect for the ionization loss of charged particles in various substances." *Atomic Data and Nuclear Data Tables*, **30**(2), pp. 261 – 271.

[49] Agostinelli, S., *et al.* (2003). "GEANT4 - A Simulation Toolkit." *Nuclear Instruments and Methods A*, **506**, pp. 250–303.

[50] Sternheimer, R. M. (1952). "The Density Effect for the Ionization Loss in Various Materials." *Phys. Rev.*, **88**, pp. 851–859.

[51] Birks, J. B. (1951). "Scintillations from Organic Crystals: Specific Fluorescence and Relative Response to Different Radiations." *Proceedings of the Physical Society. Section A*, **64**(10), p. 874.

[52] Conklin, N. B. (2009). "The Boron-to-Carbon Ratio From the First Cosmic Ray Energetics and Mass Balloon Campaign." *The Pennsylvania State University*.

[53] Ahlen, S., Cartwright, B., and Tarle, G. (1977). "Return to unsaturated response of polymeric scintillators excited by relativistic heavy ions." *Nuclear Instruments and Methods*, **147**, pp. 321–328.

[54] Mognet, S. I. (2009). "Measurement of H, He, C, and O Cosmic Ray Primaries: Preliminary Results from the CREAM II Experiment." *The Pennsylvania State University*.

[55] "A users guide to the H2 beam line in the North Area at CERN." `http://nahandbook.web.cern.ch/nahandbook/default/h2/1%20General.htm`.

[56] Ahn, H., *et al.* (2009). "The Cosmic Ray Energetics and Mass (CREAM) timing charge detector." *Nuclear Instruments and Methods in Physics Research Section A: Accelerators, Spectrometers, Detectors and Associated Equipment*, **602**(2), pp. 525 – 536.

[57] Beuville, E., *et al.* (1989). "A Low-Noise, Low-Power Analog CMOS Signal Processor for Multi-Element Silicon Particle Detectors." *CERN/EF*, **89**(9), pp. 1–34.

[58] Boyle, P., Swordy, S., and Wakely, S. (2003). "Comparison of a transition radiation detector response with numerical simulations." In "Proceedings of the 28th International Cosmic Ray Conference," pp. 2233–2236. Tsukuba, Japan.

[59] Jackson, J. D. (1998). *Classical Electrodynamics*. John Wiley and Sons, New York, 3rd edition.

[60] Ahn, H., *et al.* (2008). "Measurements of cosmic-ray secondary nuclei at high energies with the first flight of the CREAM balloon-borne experiment." *Astroparticle Physics*, **30**(3), pp. 133 – 141.

[61] Adams, J. (1999). "CR-1 Chip: Custom VLSI Circuitry for Cosmic Rays." In "Proceedings of the 26th International Cosmic Ray Conference," p. 69. Salt Lake City, USA.

[62] Park, I., *et al.* (2007). "Silicon charge detector for the CREAM experiment." *Nuclear Instruments and Methods in Physics Research Section A*, **570**(2), pp. 286 – 291.

[63] Park, I., *et al.* (2004). "Heavy ion beam test results of the silicon charge detector for the CREAM cosmic ray balloon mission." *Nuclear Instruments and Methods in Physics Research Section A*, **535**(12), pp. 158 – 161.

[64] Ahn, H. S., *et al.* (2010). "Discrepant Hardening Observed in Cosmic-ray Elemental Spectra." *The Astrophysical Journal Letters*, **714**(1), p. L89.

[65] Ahn, H., *et al.* (2007). "The Cosmic Ray Energetics And Mass (CREAM) instrument." *Nuclear Instruments and Methods in Physics Research Section A*, **579**(3), pp. 1034 – 1053.

[66] Toker, O., *et al.* (1994). "VIKING, a CMOS low noise monolithic 128 channel frontend for Si-strip detector readout." *Nuclear Instruments and Methods in Physics Research Section A*, **340**(3), pp. 572 – 579.

[67] Lee, M. H., *et al.* (2005). "Electronics for the CREAM calorimeter and hodoscopes." In "Proceedings of the 29th International Cosmic Ray Conference," p. 409. Pune, India.

[68] Ahn, H., *et al.* (2006). "Performance of CREAM Calorimeter: Results of Beam Tests." *Nuclear Physics B*, **150**(0), pp. 272 – 275.

[69] Marrocchesi, P. S., *et al.* (2005). "Beam test calibration of the balloon-borne imaging calorimeter for the CREAM experiment." In "Proceedings of the 29th International Cosmic Ray Conference," p. 309. Pune, India.

[70] Yoon, Y. S., *et al.* (2008). "Calibration of the CREAM-I calorimeter." In "Proceedings of the 30th International Cosmic Ray Conference," pp. 421–424. Merida, Mexico.

[71] Han, J. H. (2011). "Calibration of the CREAM calorimeter with beam test data." In "Proceedings of the 32nd International Cosmic Ray Conference," p. 392. Beijing, China.

[72] Gallin-Martel, L., *et al.* (2003). "The read-out electronics of the AMS prototype RICH detector." *Nuclear Instruments and Methods in Physics Research Section A*, **504**(13), pp. 273 – 275.

[73] Mangin-Brinet, M., *et al.* (2007). "CHERCAM: A Cherenkov imager for the CREAM experiment." *Nuclear Instruments and Methods in Physics Research Section A*, **572**(1), pp. 410 – 412.

[74] Buenerd, M., *et al.* (2007). "CHERCAM: The Cherenkov Imager of the CREAM Experiment, Results in Z=1 Test Beams." In "Proceedings of the 30th International Cosmic Ray Conference," Merida, Mexico.

[75] Zinn, S.-Y., *et al.* (2006). "Design, Implementation, and Performance of CREAM Data Acquisition Software." *Nuclear Physics B*, **150**(0), pp. 304 – 307.

[76] Yoon, Y. S., *et al.* (2011). "Cosmic-ray Proton and Helium Spectra from the First CREAM Flight." *The Astrophysical Journal*, **728**(2), p. 122.

[77] Ahn, H. S., *et al.* (2009). "Energy Spectra of Cosmic-ray Nuclei at High Energies." *The Astrophysical Journal*, **707**, pp. 593–603.

[78] "FLUKA: A Multi-Particle Transport Code." `http://www.slac.stanford.edu/pubs/slacreports/slac-r-773.html`.

[79] Adriani, O., *et al.* (2011). "PAMELA Measurements of Cosmic-Ray Proton and Helium Spectra." *Science*, **332**, p. 69.

[80] Ahn, H. S., *et al.* (2006). "The energy spectra of protons and helium measured with the ATIC experiment." *Advances in Space Research*, **37**, pp. 1950–1954.

[81] S. Haino, *et al.* (2013). "Precision Measurements of the Proton Flux with AMS." In "Proceedings of the 33rd International Cosmic Ray Conference," Rio de Janeiro, Brazil.

[82] Shikaze, Y., *et al.* (2007). "Measurements of 0.2 20 GeV/n cosmic-ray proton and helium spectra from 1997 through 2002 with the BESS spectrometer." *Astroparticle Physics*, **28**, pp. 154–167.

[83] Derbina, V. A., *et al.* (2005). "Cosmic-Ray Spectra and Composition in the Energy Range of 10-1000 TeV per Particle Obtained by the RUNJOB Experiment." *The Astrophysical Journal*, **628**, pp. L41–L44.

[84] Takahashi, Y. (1998). "Elemental Abundance of High Energy Cosmic Rays." *Nuclear Physics B Proceedings Supplements*, **60**, pp. 83–92.

[85] Tibet Asγ Collaboration, *et al.* (2011). "Cosmic-ray energy spectrum around the knee obtained by the Tibet experiment and future prospects." *Advances in Space Research*, **47**, pp. 629–639.

[86] Wefel, J. P., *et al.* (2008). "Revised Energy Spectra for Primary Elements (H - Si) above 50 GeV from the ATIC-2 Science Flight." In "Proceedings of the 31st International Cosmic Ray Conference," Lódź, Poland.

[87] Mueller, D., *et al.* (1991). "Energy spectra and composition of primary cosmic rays." *The Astrophysical Journal*, **374**, pp. 356–365.

[88] Engelmann, J. J., *et al.* (1990). "Charge composition and energy spectra of cosmic-ray nuclei for elements from Be to Ni - Results from HEAO-3-C2." *Astronomy and Astrophysics*, **233**, pp. 96–111.

[89] Obermeier, A., *et al.* (2011). "Energy Spectra of Primary and Secondary Cosmic-Ray Nuclei Measured with TRACER." *The Astrophysical Journal*, **742**, p. 14.

[90] Ptuskin, V., Zirakashvili, V., and Seo, E.-S. (2010). "Spectrum of Galactic Cosmic Rays Accelerated in Supernova Remnants." *The Astrophysical Journal*, **718**, pp. 31–36.

[91] Ptuskin, V., Zirakashvili, V., and Seo, E.-S. (2013). "Spectra of Cosmic-Ray Protons and Helium Produced in Supernova Remnants." *The Astrophysical Journal*, **763**, p. 47.

[92] Biermann, P. L., *et al.* (2010). "The Origin of Cosmic Rays: Explosions of Massive Stars with Magnetic Winds and Their Supernova Mechanism." *The Astrophysical Journal*, **725**, pp. 184–187.

[93] Stanev, T. (2012). "Explosions of massive stars with magnetic winds: cosmic ray acceleration." *Mem. S.A.It.*, **83**, p. 110.

[94] Zatsepin, V. I. and Sokolskaya, N. V. (2006). "Three component model of cosmic ray spectra from 10 GeV to 100 PeV." *Astronomy and Astrophysics*, **458**, pp. 1–5.

[95] Yuan, Q., Zhang, B., and Bi, X.-J. (2011). "Cosmic ray spectral hardening due to dispersion in the source injection spectra." *Phys. Rev. D*, **84**, p. 043002.

[96] Thoudam, S. and Hörandel, J. R. (2012). "Nearby supernova remnants and the cosmic ray spectral hardening at high energies." *Monthly Notices of the Royal Astronomical Society*, **421**, pp. 1209–1214.

[97] Thoudam, S. and Hörandel, J. R. (2013). "Revisiting the hardening of the cosmic ray energy spectrum at TeV energies." *Monthly Notices of the Royal Astronomical Society*, **435**, pp. 2532–2542.

[98] Panov, A. D., *et al.* (2008). "Relative abundances of cosmic ray nuclei B-C-N-O in the energy region from 10 GeV/n to 300 GeV/n. Results from ATIC-2 (the science flight of ATIC)." In "Proceedings of the 30th International Cosmic Ray Conference," pp. 3–6. Merida, Mexico.

[99] Aguilar, M., *et al.* (2010). "Relative Composition and Energy Spectra of Light Nuclei in Cosmic Rays: Results from AMS-01." *The Astrophysical Journal*, **724**(1), p. 329.

[100] Oliva, A., *et al.* (2013). "Precision Measurement of the Cosmic Ray Boron-to-Carbon Ratio with AMS." In "Proceedings of the 33rd International Cosmic Ray Conference," Rio de Janeiro, Brazil.

[101] Ahn, H. S., *et al.* (2010). "Measurements of the Relative Abundances of High-energy Cosmic-ray Nuclei in the TeV/Nucleon Region." *The Astrophysical Journal*, **715**(2), p. 1400.

[102] Seo, E., *et al.* (2013). "Cosmic Ray Energetics and Mass for the International Space Station (ISS-CREAM)." In "Proceedings of the 33rd International Cosmic Ray Conference," Rio de Janeiro, Brazil.

[103] Park, J., *et al.* (2013). "Results of Tests and Simulations for the Top Counting Detector and Bottom Counting Detector of the ISS-CREAM Experiment." In "Proceedings of the 33rd International Cosmic Ray Conference," Rio de Janeiro, Brazil.

[104] "EJ-200 Plastic Scintillator Datasheet." http://www.eljentechnology.com/images/stories/Data_Sheets/Plastic_Scintillators/EJ200%20data%20sheet.pdf.

[105] Anderson, T., *et al.* (2013). "The ISS-CREAM Boronated Scintillator Detector." In "Proceedings of the 33rd International Cosmic Ray Conference," Rio de Janeiro, Brazil.

[106] Malinin, A. t. (2013). "A Transition Radiation Detector for the BACCUS Experiment." In "Proceedings of the 33rd International Cosmic Ray Conference," Rio de Janeiro, Brazil.

[107] "Light Guides and Waveshifter Bars." http://www.detectors.saint-gobain.com/Optical_Components.aspx.

[108] "BC-600 Optical Cement." http://www.detectors.saint-gobain.com/uploadedFiles/SGdetectors/Documents/Product_Data_Sheets/BC600-Data-Sheet.pdf.

[109] "RTV615." http://www.momentive.com/Products/ShowTechnicalDataSheet.aspx?id=10333.

[110] "BC-630 Silicone Optical Grease." http://www.detectors.saint-gobain.com/uploadedFiles/SGdetectors/Documents/Product_Data_Sheets/SGC_Detector_Assembly_Materials_Data_Sheet.pdf.

[111] "Dupont Tedlar PVF Film." http://www2.dupont.com/Tedlar_PVF_Film/en_US/.

[112] "3M 966 Clear Adhesive Transfer Tape." http://solutions.3m.com/wps/portal/3M/en_US/Adhesives/Tapes/Products/?N=4294955752+5000130&Nr=AND%28hrcy_id%3AGSCNJ5WVFDgs_930HFQWH1D_N2RL3FHWVK_GPD0K8BC31gv%29&rt=d.

[113] "F Series High Voltage Ripple Stripper Biasing Supplies." http://www.ultravolt.com/uv_docs/FSeriesDS.pdf.

[114] "Teledyne Reynolds High Voltage Coaxial Shielded Cable." http://www.teledynereynolds.com/product/0wireandcable/9hvcsc.asp.

[115] "Emerson and Cummings Clear S-11 Primer." http://www.ellsworth.com/emerson-and-cuming-primer-s-11-nc-clear-1-lb-jar/.

[116] "Emerson and Cummings Stycast 1266." http://www.ellsworth.com/emerson-and-cuming-stycast-1266-part-a-epoxy-clear-9oz-can/.

[117] "Arcturus Networks uC5272." http://www.arcturusnetworks.com/products/uC5272/.

[118] "PRV-1059 5-Port PC/104 10/100 Fast Ethernet Switch." http://www.parvus.com/Product/overview.aspx?prod=PRV-1059.

[119] "VI-J00, VE-J00 Half Brick DC-DC Converters." http://cdn.vicorpower.com/documents/datasheets/ds_vi-j00.pdf.

[120] "VI-RAM/VE-RAM Ripple Attenuator Modules." http://cdn.vicorpower.com/documents/datasheets/ds_vi-ram.pdf.

[121] Yoon, Y. S. (2010). "Proton and Helium Spectra from the First Flight of the CREAM Balloon-Borne Experiment." *The University of Maryland*.

[122] "EZ-USB FX2LP." http://www.cypress.com/?id=193.

[123] "Microsemi's ProASIC3 FPGA Series." http://www.microsemi.com/products/fpga-soc/fpga/proasic3-overview.

[124] "Microsemi's IGLOO FPGA Series." http://www.microsemi.com/products/fpga-soc/fpga/igloo-overview.

[125] "SDCC - Small Device C Compiler." http://sdcc.sourceforge.net/.

[126] "fx2lib." http://sourceforge.net/projects/fx2lib/.

[127] "Microsemi's Libero SOC." http://www.microsemi.com/products/fpga-soc/design-resources/design-software/libero-soc.

[128] "EJ-254 Boron-Loaded Plastic Scintillator Datasheet." http://www.eljentechnology.com/images/stories/Data_Sheets/Loaded_Scintillators/EJ254%20data%20sheet.pdf.

[129] Drake, D., Feldman, W., and Hurlbut, C. (1986). "New electronically black neutron detectors." *Nuclear Instruments and Methods in Physics Research Section A*, **247**(3), pp. 576 – 582.

[130] "Hamamatsu R1924A Photomultiplier Tube Datasheet." http://www.hamamatsu.com/resources/pdf/etd/R1924A_TPMH1280E01.pdf.

[131] Rauch, B. F., *et al.* (2009). "Cosmic Ray origin in OB Associations and Preferential Acceleration of Refractory Elements: Evidence from Abundances of Elements $_{26}$Fe through $_{34}$Se." *The Astrophysical Journal*, **697**, pp. 2083–2088.

[132] Martini, F. D. and Wacks, K. P. (1967). "Photomultiplier Gate for Stimulated-Spontaneous Light Scattering Discrimination." *Review of Scientific Instruments*, **38**(3=7), pp. 886 – 888.

[133] "40 ns Propagation Delay, CMOS Optocoupler." http://www.avagotech.com/docs/AV02-0876EN.

[134] "RECOM 0.25 W, SIP4, Single Output DC/DC Converter. Isolated to 2 kV." http://www.recom-power.com/pdf/Econoline/RM.pdf.

[135] "Natural Boron-Loaded Premium Plastic Scintillators." http://www.detectors.saint-gobain.com/uploadedFiles/SGdetectors/Documents/Product_Data_Sheets/BC454-Data-Sheet.pdf.

[136] Flournoy, J. (1993). "Measurement of decay times of fast scintillating fibers." *Radiation Physics and Chemistry*, **41**(12), pp. 389 – 394. ISSN 0969-806X.

[137] "Arathne 5753-A/B (LV) Urathane Casting Compound." http://www.centralcoating.com/PDF/Arathane-5753.pdf.

[138] "NASA Tin Whiskers (and Other Metal whiskers) Homepage." http://nepp.nasa.gov/whisker/.

[139] "Restrictions of Hazardous Substances Directive (RoHS)." http://www.mel.nist.gov/msid/SSP/standard_landscape/RoHS.html.

[140] L. D. Edmonds, C. E. Barnes, and L. Z. Scheick (2000). *An Introduction to Space Radiation Effects on Microelectronics*. http://parts.jpl.nasa.gov/docs/JPL00-62.pdf.

[141] "AD7663, 16-Bit, 250 kSPS CMOS ADC." http://www.analog.com/static/imported-files/data_sheets/AD7663.pdf.

[142] "OP-97, Low Power, High Precision Operational Amplifier." http://www.analog.com/static/imported-files/data_sheets/OP97.pdf.

[143] "Q Series Isolated, Proportional DC to HV Converters." http://www.emcohighvoltage.com/pdfs/qseries.pdf.

[144] "Kodak Neutral Density No. 96 Filters." http://www.analog.com/static/imported-files/data_sheets/OP97.pdf.

[145] Sasaki, M., 1, and 2 (2013). "Super-TIGER 2012/2013 In-flight Instrument Performance and Preliminary Results." In "Proceedings of the 33rd International Cosmic Ray Conference," p. 421. Rio de Janeiro, Brazil.

[146] "CV4-2500 Controlled Volatility RTV Silicone." http://www.silicone-polymers.co.uk/pdf2007/CV4-2500P.pdf.

[147] "500 mA Low-Dropout Linear Regulartor in μMAX." http://datasheets.maximintegrated.com/en/ds/MAX1792.pdf.

[148] "Surface Mount Miniature Quartz Crystals." http://www.statek.com/products/pdf/10109.pdf.

[149] "High Speed Differential Line Receivers." http://www.ti.com/lit/ds/symlink/sn65lvdt390.pdf.

[150] "Low-Power, 12-Bit Voltage-Output DACs with Serial Interface." http://datasheets.maximintegrated.com/en/ds/MAX5352-MAX5353.pdf.

[151] "Ultra Miniature DC-DC Transformer Converters, Input 12 V." http://www.picoelectronics.com/plugin/pe50_51.htm?PartNo=31141.

[152] "20-Tap DIP Delay Line." http://www.datadelay.com/datasheets/2214.pdf.

[153] "AD8051/AD8052/AD8054 Rail-to-Rail Amplifier." http://www.analog.com/static/imported-files/data_sheets/AD8051_8052_8054.pdf.

[154] "Low-Voltage CMOS Analog Multiplexers/Switches." http://datasheets.maximintegrated.com/en/ds/MAX4581-MAX4583.pdf.

Vita

TYLER B. ANDERSON

tba109@psu.edu

EDUCATION:

Ph.D. in Physics, *The Pennsylvania State University*, 2013.

B.S. in Electrical Engineering with Physics and Mathematics Minor, *Geneva College*, 2006.

SELECTED PUBLICATIONS

T. Anderson *et al*. (2013), "The ISS-CREAM Boronated Scintillator Detector", In *Proceedings of the 33rd International Cosmic Ray Conference."* Rio de Janeiro, Brazil.

E. S. Seo *et al*. (2013), "Cosmic Ray Energetics And Mass for the International Space Station (ISS-CREAM)", In *Proceedings of the 33rd International Cosmic Ray Conference.* Rio de Janeiro, Brazil.

J. M. Park *et al.* (2013), "Results of Tests and Simulations for the Top Counting Detector and Bottom Counting Detector of the ISS-CREAM Experiment", In *Proceedings of the 33rd International Cosmic Ray Conference.* Rio de Janeiro, Brazil.

Y. S. Yoon *et al.* (2011), "Proton and Helium Spectra from the CREAM-III Flight", In *Proceedings of the 32nd International Cosmic Ray Conference.*" Beijing, China.

J. H. Han *et al.* (2011), "Performance of the CREAM-V and CREAM-IV calorimeters in flight", In *Proceedings of the 32nd International Cosmic Ray Conference.*" Beijing, China.

L. Derome *et al.* (2009), "Preliminary Results of the CREAM-III Cherenkov Camera", In *Proceedings of the 31st International Cosmic Ray Conference.* Łódź, Poland.

SELECTED TALKS

T. Anderson (2013), **"**Exploring the Cosmic-Ray Spectrum", *American Association of Physics Teachers Western Pennsylvania Regional Meeting*. Erie, Pennsylvania.

T. Anderson (2013), "The ISS-CREAM Boronated Scintillator Detector", *The 33rd International Cosmic Ray Conference: Experimental Methods Section*. Rio de Janeiro, Brazil.

T. Anderson (2013), "Electronics Design of the Boronated Scintillator Detector", *NASA's Critical Design Review of the ISS-CREAM Boronated Scintillator Detector.* College Park, Maryland (by teleconference).

T. Anderson (2009), "Cosmic Rays and Penguins: My Science Adventures in Antarctica", *Young Scholars of Central Pennsylvania Fifth and Sixth-Grade Science Assembly*. State College, Pennsylvania.

SELECTED AWARDS

NASA Earth and Space Sciences Fellowship (NESSF), 2011-2013.

David C. Duncan Graduate Fellowship, 2010.

Pennsylvania Space Grant Consortium Fellowship (PSGC), 2009-2010.

Valedictorian, Geneva College, Class of 2006.

Suma Cum Laude, Geneva College, Engineering Class of 2006.

Alpha Chi Honor Society Member, 2003-2006.